The Effect of Zr and ZrB$_2$ additions to NdFeB alloys

By

Chun-Hsin Kuo

A thesis submitted to the University of Birmingham
for the degree of

Doctor of Philosophy

School of Metallurgy & Materials
College of Engineering and Physical Sciences
The University of Birmingham
Birmingham B15 2TT
England
September 2010

Synopsis

Alloy compositions near to stoichiometric $Nd_2Fe_{14}B$ produced under normal casting conditions, with subsequent isothermal heat treatments and with sintering have been characterised. The possible mechanisms for removing the soft magnetic phase, free α-Fe, via additions of 0.6 at% of Zr or 1.0 at% of ZrB_2 have been investigated by EPMA (Electron Probe Microanalysis) and TEM (Transmission Electron Microscopy). 1.0 at% of ZrB_2 has been found to be very effective in suppressing the formation of free α-Fe dendrites during solidification, but the excessive ZrB_2-type needles formed in the NdFeB alloy may have a deleterious effect on the magnetic properties. However, the coercivity of the NdFeB sintered magnets can be improved to some extent by addition of Zr or ZrB_2 to the composition $Nd_{12.68}Fe_{77.91-80.91}B_{6.41-8.41}Zr_{0-1}$ (at%) due to the smaller and more uniform grains of the $Nd_2Fe_{14}B$ phase (~6.5 μm) in the sintered magnets.

Both SEM (equipped with WDX) and TEM (equipped with EDX) have been employed to investigate ZrB_2 needles in $Nd_{12.68}Fe_{77.91-80.91}B_{6.41-8.41}Zr_{0-1}$ (at%) alloys. It is found that suppression of free α-Fe dendrites in both Zr-containing NdFeB alloys resulted from different solidification routes. Since the sequences of formation of the ZrB_2-type needles in Zr-containing alloys are different, the $Nd_2Fe_{14}B$ grain growth is inhibited via different mechanisms.

Meanwhile, evidence for the high temperature solubility of Fe in ZrB_2 needles is found for both Zr-containing NdFeB alloys. Chemical analysis shows that the ZrB_2-type needles in the NdFeB alloys are composed mainly of B (~70 at%) and Zr (~20 at%) with a small but significant amount of Fe (~7 at%), a formula which can be expressed as $(Zr_{1-x}, Fe_x)B_2$ (x~0.3).

Acknowledgements

This dissertation would not have been completed without the support of many wonderful individuals. In particular, I would like to acknowledge the enthusiasm and dedication of my thesis director and academic advisors, Professor I. P. Jones and Professor I. R. Harris. I am deeply grateful for both of their valuable guidance and constant encouragement throughout my graduate career.

I would also like to express my sincere gratitude to many other members in the department for their interest in and feedback on my research. Dr. Rengen Ding always offered insightful suggestions and gave significant contribution to boost my knowledge in electron microscopy and enhance my analysing skills. His energy, wit and wisdom will always remain in my heart. Dr. Andy Williams provided numerous insights on different facets of the magnet development, which have profoundly influenced my work. Dr. Miha Zakonit always offered much helpful input, and was always willing to lend an attentive ear and a critical eye.

Many friends and colleagues have contributed in countless ways to my dissertation. My sincere thanks go to Dr. Ming Chu for offering training in TEMs, to Mr. Paul Stanley and Mrs. Lesley Tomkins for offering training in SEMs, and to Mr. John Lane for assisting in producing the special grinding tools.

I am grateful to all technical staff of Met & Mat; particularly to Mick, Tony, Paul and Anne, for their support and help.

I am also grateful to my lab-mates: Hilda, Yihsuan, Hiroto, Chuanwei, and Anqi for making our Lab 13 a lovely studying environment. Special thanks go to Drs. Yau Yau Tse, Yulung Chiu, Biswajit Paik, Fernando Barradas, Jian Chen, Yong Li, Fei Wang, Santiago Corujeira and Mr. Salahadin Adrwish for their friendship and unfaltering encouragement over the years of my academic pursuit.

I would like to thank my parents and Department of Metallurgy and Materials for providing financial support.

Finally, a crucial debt is owed to my family: to my mom, Mrs. Huei-Hsiung Chen, my dad, Prof. Tung-Ying Kuo, my sister, Dr. Li-Jen Kuo, and my brother in law, Dr. Lo Chih-Ping, for their ceaseless effort to give me the best possible support in every aspect of my life, even though there have been many thousands of miles between us.

To

My parents and all my family

Chun-Hsin Kuo

November 2010

Contents

List of Figures

List of Tables

List of Abbreviations

BEI   Backscattered Electron Image

BF   Bright Field TEM micrograph

DF   Dark Field TEM micrograph

DP   Diffraction Pattern

EDX   Energy Dispersive X-ray analysis

EPMA   Electron Probe Microanalysis

FIB   Focussed Ion Beam milling

HAADF   High Angle Annular Dark Field

HD   Hydrogen Decrepitation

HDDR   Hydrogenation Disproportionation Desorption and Recombination reaction

HT   High Tension

ICP   Inductively Coupled Plasma

SADP   Selected Area Diffraction Pattern

SEI   Secondary Electron Image

SEM   Scanning Electron Microscopy

TEM   Transmission Electron Microscopy

WDX   Wavelength Dispersive X-ray analysis

XRD   X-ray Diffraction

ZAF   Atomic number-Absorption-Fluorescence

1   Introduction

1.1   The Historical Development of Magnets

The history of permanent magnets originates from a naturally occurring stone, lodestone. This special stone was found mostly in the Province of Magnesia in Macedonia, from which the term "magnetism" was derived. The earliest record of magnetic materials and the first application as a compass were in China around 200 B.C. (Parker, 1990).

The first scientific experimental investigation of magnetism was by Gilbert in 1600 on lodestone (Fe_3O_4). He studied terrestrial magnetism and magnetic induction and observed that magnets lose their magnetism when heated. In 1825, Sturgeon invented the electromagnet and discovered the magnetic field, which is generated by an electric current through coils. In 1880, Warburg showed the first hysteresis loop for iron.

Further developments concerning magnetic phenomena have occurred since the 19th century: the relationship between an internal and external magnetic field in ferromagnetic materials was discovered by Weiss, magnetostriction by Joule, the Curie law by Curie and hysteresis by Ewing. In the 20th century, scientists developed the physical concept of magnetism, involving quantum mechanics with theories of electron spin and exchange forces, to explain the phenomena of magnetism. During this period, Néel discovered diamagnetism.

Great advances in permanent magnet technology occurred at the beginning of the 20th century. Many new magnetic materials were discovered and the maximum energy product improved considerably with the discovery of each material. The sequential development of the various magnetic materials is associated with their energy product, $(BH)_{max}$.
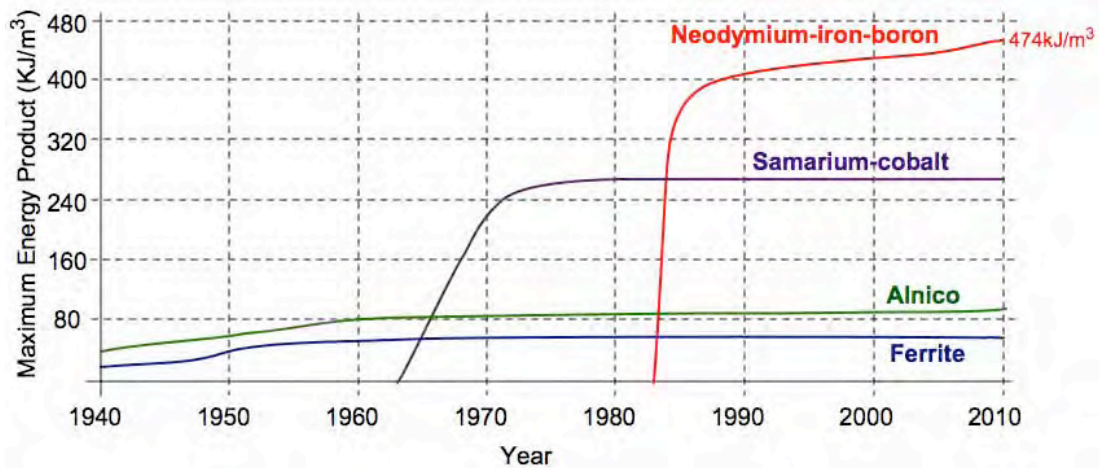
Figure 1.1 Variation of (BH)$_{max}$ with time via various types of magnetic material. (adapted from www.magnetweb.com)

The first magnet discovered with a useful energy product in the earlier part of the 20th century was carbon steel. Its performance was improved by the addition of chromium and tungsten. A significant improvement of this magnet appeared in 1917 when Honda, Masumoto and Tanakada substituted 35% cobalt into tungsten steel magnets. These cobalt steel magnets improved the (BH)$_{max}$ to ~8kJm^{-3} (Honda and Shimizu, 1903, Shimizu and Tanakadate, 1906).

The next significant advance was the development of Alnico magnets. Alnico magnets were developed from cobalt magnets in 1932 by Mishima. Alnico alloys are composed primarily of aluminum, nickel and cobalt (hence the term al-ni-co) with the addition of iron, copper and, sometimes, titanium. They can be magnetized to produce permanent magnetic fields. Alnico alloys have Curie points around 800°C (Mishima, 1932). They were improved considerably by subsequent microstructural modification. The use of directional casting techniques by Lutejin and De Vos in 1956 led to the development of columnar Alnico. Alnicos were also produced in anisotropic form with an energy product of 80 kJm^{-3} relying on fine precipitates and shape anisotropy (Luteijn and De Vos, 1956).

In the early 1950s, Ba-ferrite with a hexagonal magnetoplumbite type structure was

discovered. Snoek and associates at Philips Research Laboratories developed ferrite magnets based on $(Ba, Sr)Fe_{12}O_{19}$ using a powder metallurgy process. The original Ba-ferrite gave an improved energy product of 32 kJm^{-3}. These ferrites were the first major example of material which used magnetocrystalline anisotropy as the basis for their coercivity. Although, because of their ferrimagnetism, the magnetizations of the ferrites are low compared to that of the Alnicos, their high coercive force ensured that they found widespread use. The ease of processing, without the need for a protective coating, and the low cost of the raw materials make the ferrite magnets very cheap to produce (Stijntjes and Van Loon, 2008).

In the following decade, materials with intrinsically high anisotropies were developed from hexagonal structured rare earth (RE)-transition metal alloys. The use of the RE elements was based upon their high magnetic moments and uniaxial magneto-anisotropy, which could be used in conjunction with ferromagnetic materials (Fe, Co & Ni). In 1967, Karl Strnat produced the first commercially viable RE-based hard magnetic material, $SmCo_5$, with a maximum energy product of 160 kJm^{-3} (Strnat et al., 1967). A decade later, another compound emerged, based on the fomula Sm_2Co_{17}, with a maximum energy product of 240 kJm^{-3} (Tawara and Strnat, 1976). Up to now, $SmCo_5$ has the highest uniaxial magnetocrystalline anisotropy, achieved by careful control of the microstructure together with additions such as iron, copper and zirconium.

In 1970s, due to some political and pricing issues concerning cobalt, researchers began to look for other raw materials to replace cobalt in the fabrication of the magnets. In the late 1970s, an investigation into boron stabilized Nd-Fe compounds by a Russian group initiated the discovery of the NdFeB ternary compound. In 1983, Sumitomo Special Metals of Japan and, independently, General Motors of the USA identified the crucial compound as $Nd_2F_{14}B$ and developed suitable processing routes to make permanent magnets (The Rare-Earth Magnetic

Association, 2008). The two different routes for producing the Nd-Fe-B alloy were the powder metallurgy route (eventually the same as that of $SmCo_5$), developed by Sumitomo, and a nano-crystalline melt spinning route adopted by General Motors. Sagawa reported a maximum energy product of 290 kJm^{-3} for sintered magnets (Sagawa et al., 1984). Croat at General Motors developed Nd-Fe-B bonded magnets with a maximum energy product of 112 kJm^{-3} (Croat et al., 1984). A distinct improvement obtained from this kind of magnet is in the amount of magnetic flux delivered by the magnet at much lower cost. The coercive forces attainable in Nd-Fe-B type magnets are not however superior to those of SmCo based magnets.

The properties of sintered Nd-Fe-B based magnets were improved further through optimising processing parameters and minor alloy additions to the starting material. In 1998 Kaneko developed magnets with a maximum energy product of 431 kJm^{-3} by controlling the oxygen content and particle size distribution of the powder (Kaneko, 2000). Advanced Technologies of Sumitomo Special Metals have developed a new grade of sintered Nd-Fe-B-type magnet producing a maximum energy product of 444 kJm^{-3}. After various improvements in both the heat treatment and processing of NdFeB based alloys, permanent magnets with a record maximum energy product of 474 kJm^{-3} (B_r=1.555T, H_{CJ}=653kA/m) were produced (Xie et al., 2006).

The newest Nd-Fe-B permanent magnets have magnetic properties superior to other magnetic materials at room temperature. This has made them popular for many applications, gradually replacing ferrite- and Sm-type magnets. However, the application of Nd-Fe-B permanent magnets is limited to low operating temperatures and non-humid environment because of its low Curie temperature (312°C), poor corrosion resistance and poor temperature coefficients of coercivity and remanence.

1.2 Introduction to the Project

Nd-Fe-B magnets are based on the hard magnetic phase, $Nd_2Fe_{14}B$, which, for sintered magnets has a typical starting composition of $Nd_{15}Fe_{77}B_8$ (at %) known as 'Neomax'. The Neomax composition is the one most widely used to develop new process for the NdFeB magnets and improve the magnetic properties. Shifting this alloy composition closer to that of the stoichiometric composition ($Nd_{11.76}Fe_{82.35}B_{5.88}$, at%) is an effective way to maximize the volume of the hard magnetic $Nd_2Fe_{14}B$ phase in the material and hence to improve the magnetic properties (particularly B_r). However, this causes the conventionally cast, near stoichiometric type alloys to contain a large proportion of free α-Fe dendrites, dispersed within the $Nd_2Fe_{14}B$ matrix phase. The free α-Fe is a soft magnetic phase and therefore has a deleterious effect on the permanent magnetic properties (particularly the H_{cj}). Previous studies by Fujita et al (2000), Shaaban (2005) and Kirby (2006) have reported that the amount of free α-Fe can be eliminated by the formation of a ZrB_2-type needle phases within the NdFeB alloy. However, the influences of ZrB_2-type needles on the NdFeB magnet and the mechanism whereby magnetic properties are influenced by the formation of ZrB_2-type needles have not been fully studied. The objective of this project is to elucidate the effect of the ZrB_2 on both the free α-Fe content and subsequently on the magnetic properties.

The work reported in this thesis starts with the characterisation of conventional cast ingots of a near stoichiometric composition ($Nd_{12.68}Fe_{77.91-80.91}B_{6.41-8.41}Zr_{0-1}$, at%). An attempt is made to investigate the phase distribution during processing and to understand the possible mechanisms for the reactions during the processing. As zirconium additions were believed to influence the coercivity, the impact on the resulting magnetic properties is also discussed.

References for Chapter 1

Croat J. J., Herbst J. F., Lee R. W. & Pinkerton F. E. 1984. Pr-Fe and Nd-Fe-based materials: A new class of high-performance permanent magnets (invited). *Journal of Applied Physics,* 55**,** 2078-2082.

Honda K. & Shimizu S. 1903. *Phil. Mag.,* 5**,** 650.

Kaneko Y. 2000. *Proceedings of the 16th International Workshop on Rare-Earth Magnets and Their Applications, Sendai, Japan,.*

Luteijn A. I. & De Vos K. J. 1956. *Philips Res. Rept. ,* 11.

Mishima T. 1932. On the new high magnet "M.K." steel. *Ohm,* 19.

Parker R. J. 1990. *Advances in permanent magnetism*, Wiley-interscience publications.

Sagawa M., Fujimura S., Yamamoto H., Matsuura Y. & Hiraga K. 1984. Permanent magnet materials based on the rare earth-iron-boron tetragonal compounds. *IEEE Transactions on Magnetics,* 20**,** 1584-1589.

Shimizu S. & Tanakadate S. 1906. *Toyko Sugaku Buturi Kiji,* 3.

Stijntjes T. & Van Loon B. 2008. Early Investigations on Ferrite Magnetic Materials by J. L. Snoek and Colleagues of the Philips Research Laboratories Eindhoven. *Proceedings of the IEEE,* 96**,** 900-904.

Strnat K., Hoffer G., Olson J., Ostertag W. & Becker J. J. 1967. A Family of New Cobalt-Based Permanent Magnet Materials. *Journal of Applied Physics,* 38**,** 1001-1002.

Tawara Y. & Strnat K. 1976. Rare earth-cobalt permanent magnets near the 2-17 composition. *IEEE Transactions on Magnetics,* 12**,** 954-958.

The Rare-Earth Magnetic Association. 2008. *Patents and History-History of Rare-Earth Magnets* [Online]. Available: http://www.rareearth.org/magnets_patents_history.htm [Accessed].

Xie H. Z., Zhao J. T. & Yu Y. J. 2006. New Achievements in NdFeB Mass Production. *Journal of Iron and Steel Research, International,* 13**,** 324-330.

2 Literature Review

2.1 Magnetism

2.1.1 Origin of Magnetic Field

A magnetic field is created whenever there is an electrical charge in motion. There are two kinds of electron motion, orbital and spin, and each has a magnet moment associated with it.

The orbital motion of an electron around a nucleus may be likened to a current in a loop of wire having no resistance; both are equivalent to a circulation of charge. As shown in Figure 2.1, a wire with a current passing through will have a magnetic field generated in its perpendicular plane. This field will decrease in strength with the distance from the wire.

Spinning electrons also generate a magnetic field, which is countered by a couple from another electron of opposite spin. In a complete electronic shell, the spin magnetic moment for all the electrons has no net contribution to the magnetic moment of an atom. Only the electrons in partially filled shells are responsible for the atomic moments and give rise to magnetism.

2.1.2 Units of Magnetism

There are two sets of unit system commonly employed to quantify magnetic parameters: The Gaussian or C.G.S (centimetre-grams-second) system and System International or M.K.S. (metre-kilogram-second) system. The C.G.S. system of units has been generally accepted for over 100 years. Today, the SI system is widespread and used in engineering and technical areas. Units throughout this thesis will be expressed in the SI system whenever this is possible. However, as a comparison, the conversions and relationships between the two systems are

given in Table 2.1.
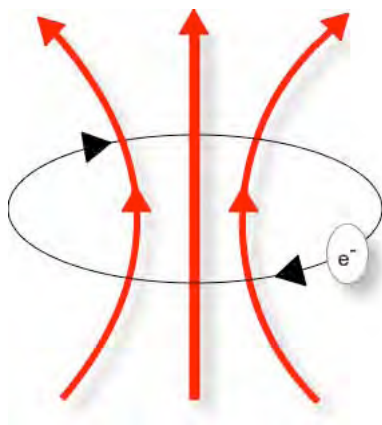
(a)
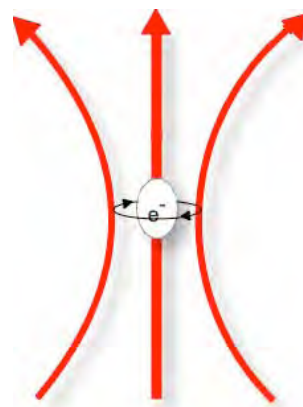
(b)
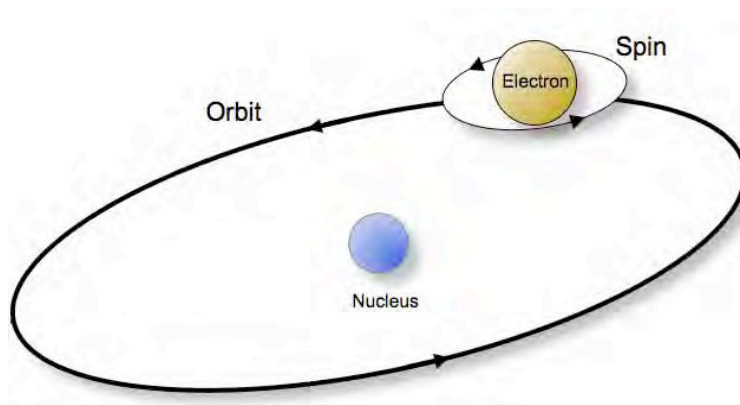
(c)

Figure 2.1 Origin of magnetism: (a) orbital magnetic moment (b) spin magnetic moment (c) The orbit of a spinning electron about the nucleus of an atom. (adapted from (Skomski and Coey, 1999))

Table 2.1 Magnetic terms with their symbols and units in C.G.S. and S.I. systems (Parker, 1990).

Terminology and Symbols	Units in CGS	Units in SI	Unit Conversion
Magnetic Field, H	Oersted (Oe)	Am^{-1}	$1Oe=79.58 \ Am^{-1}$
Magnetisation per unit volume, M	emu	$JT^{-1}m^{-3}$	$1emu \ cm^{-3}=10^{3} \ JT^{-1}m^{-3}$
Magnetisation per unit mass, $\sigma=M/\rho$	$Erg \ Oe^{-1}g^{-1}$	$JT^{-1}kg^{-1}$ or $Am^{2}kg^{-1}$	$1 \ Erg \ Oe^{-1}g^{-1}= 1 \ JT^{-1}kg^{-1}$
Permeability of free space, μ_0	Unity	$4\pi*10^{-7}$ Weber $A^{-1}m^{-1}$	
Induction in free space, B	$B=H$; Gauss (G)	$B=\mu_0 H$; Tesla (T)	$1G=10^{-4}T$
Susceptibility per unit volume, $\chi=M/H$			$CGS=10^{7}$ SI
Bohr magnetron, $\mu_B=e\hbar/2m$	$9.2732*10^{-21}$ $erg.Oe^{-1}$	$9.2732*10^{-24}JT^{-1}$	$1 \ erg.Oe^{-1}= 10^{3}JT^{-1}$
Maximum Energy Product, $(BH)_{max}$	MGOe	kJm^{-3}	$1MGOe=7.958kJm^{-3}$

2.1.3 Magnetic Quantities

The magnetic flux per unit area is referred to as the magnetic induction B and in vacuum is defined as:

$$B = \mu_0 \cdot H$$

Equation 2-1

where H is the magnetic field and μ_0 the permeability of free space. A magnetic induction B of 1 tesla generates a force of 1 newton per metre on a conductor carrying a current of 1 Ampere perpendicular to the direction of the induction. When a material is placed in a magnetic field H, the overall atomic moment within the material is affected by the external

magnetic field. The effect of such an external field is excited magnetic moments within the exposed material. The magnetic moment per unit volume is defined as the magnetisation M. This magnetic moment creates a field of induction of its own which will affect the applied field H. Therefore, the overall behaviour of the system can be described as:

$$\overline{B} = \mu_0 \cdot (\overline{H} + \overline{M})$$

Equation 2-2

The magnetic susceptibility χ, also known as bulk or volumetric susceptibility, is dimensionless and represents the degree of magnetisation of a material in response to a magnetic field. It can be expressed as:

$$\chi = \frac{M}{H}$$

Equation 2-3

The value of the susceptibility is an important criterion that can be used to distinguish several kinds of magnetism in a material as well as characterising their behaviour. There are five main classes of magnetism; paramagnetism, diamagnetism, ferromagnetism, ferrimagnetism and antiferromagnetism. For example, if χ is positive and small, the material is said to be paramagnetic, if χ is negative, the material is said to be diamagnetic.

Another parameter that demonstrates the magnetic response of a material and its strength is the permeability μ. Absolute permeability μ can be defined as:

$$\mu = \frac{B}{H}$$

Equation 2-4

Combining equations 2.3.2 and 2.3.3 gives:

$$B = \mu_0 \cdot H \cdot (1 + \chi) = \mu_0 \cdot \mu_r \cdot H$$

Equation 2-5

where μ_r is the relative permeability of the material. Combining equations 2.4 and 2.5 gives:

$$\mu = \mu_0 \cdot \mu_r$$

Equation 2-6

μ, μ_r or χ may be employed to characterise the magnetic response of a material within a magnetic field.

Another important parameter is the magnetic polarisation J [Tesla]. This value is the magnetisation of a material and can be expressed as:

$$J = \mu_0 \cdot M$$

Equation 2-7

2.1.4 Magnetic Domains

Magnetic domains were hypothesised by the French physicist Pierre-Ernest Weiss in 1907. He proposed the existence of magnetic domains to explain how a ferromagnetic material with spontaneous magnetisation can exist in a demagnetised state. He postulated that a ferromagnetic body must be composed of some regions called Weiss domains, each of which is magnetised to a saturation level, but the direction from domain to domain is such that the net magnetisation is zero (Weiss, 1907).

Subsequently, the existence of domains was observed experimentally by Barkhausen. He showed that the magnetisation of a ferromagnetic sample increased under a continuously increased applied magnetic field. Sudden discontinuous jumps in magnetization may be detected by a coil of wire wound on the ferromagnetic material, the sudden transitions in the magnetic field of the material produce pulses of current in the coil that, when amplified, produce a series of clicks in a loudspeaker. He proposed that these effects corresponded to the

rotation of magnetisation in domains (Barkhausen, 1919). Further research on domains, reported by Bloch showed that domains are separated by walls of finite thickness (Bloch, 1932).

2.1.5   Domain Wall

A domain is a small volume or region with a size typically between 10^{-12} and 10^{-8}m^3. Each domain is spontaneously magnetised in one direction so that the substance may have a net magnetisation of zero if these directions are completely random. The domain wall has an energy associated with it and has the equilibrium spacing where the sum of the appropriate energies is at a minimum, which then gives rise to a multi-domain specimen. Figure 2.2 shows schematically the breaking up of one domain into several domains to reach a lower energy state. A single domain structure that is spontaneously magnetised in one direction, as presented in Figure 2.2 (a), creates a large magnetostatic energy associated with the demagnetising field resulting from the existence of magnetic free poles at the end surfaces.

The magnetostatic energy is reduced when a single domain breaks down into more domains through the formation of 180° domain walls as presented in Figure 2.2 (b). Furthermore, if the magnet forms N domains, then the magnetostatic energy is reduced by 1/N. For example Figure 2.2 (c) represents a quarter of the magnetostatic energy of Figure 2.2 (a). Figure 2.2 (d) represents a closure domain structure where the magnetostatic energy is zero.
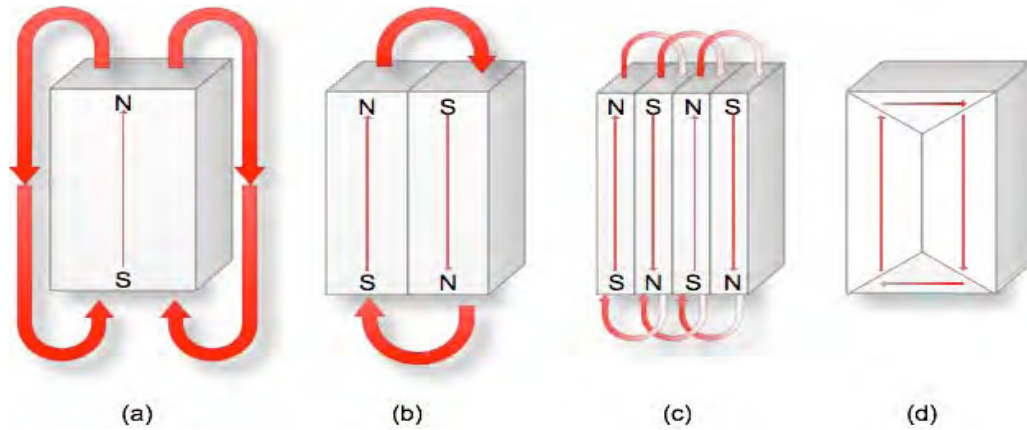
Figure 2.2 Schematic illustration of the break up of magnetisation into domains. (adapted from (Campbell, 1994))

These closure domains can be present in materials that do not possess a strong uniaxial anisotropy. A schematic representation of a planar 180° wall is shown in Figure 2.3. The change in direction of the magnetisation is very gradual rather than being in one discontinuous jump across a single atomic distance. The energy of a domain wall is simply the difference between the moments before and after the domain wall was created. The width of the domain wall varies with the opposing energies that create it, i.e. the magnetocrystalline anisotropy energy and the exchange energy, both of which want to be as low as possible so as to be in a more favourable energetic state.

The anisotropy energy is lowest when the individual magnetic moments are aligned with the crystal lattice axes, therefore reducing the width of the domain wall. The exchange energy is reduced when the magnetic moments are aligned parallel to each other.
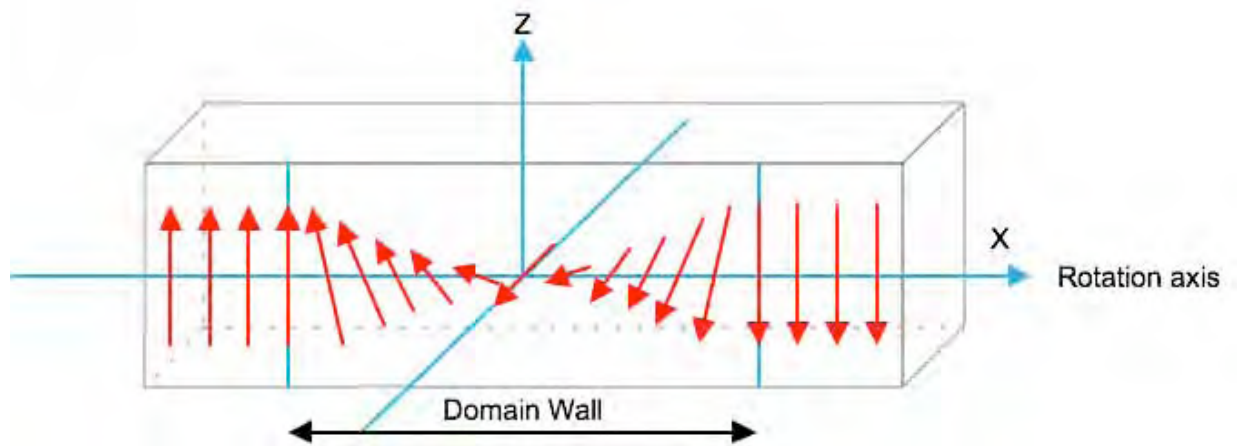
Figure 2.3 Schematic structure of a 180 degree domain wall (adapted from (Coey, 1996)).

2.1.6 Magnetic Anisotropy

Anisotropy is a term used to describe the dependence of the magnetic properties of a material when exposed to an applied magnetic field. A magnetically isotropic material has no preferential direction for its magnetic moment in a zero field, while a magnetically anisotropic material will align its moment to an easy axis. Therefore, the nature of the magnetic anisotropy is an important factor in determining the suitability of magnetic material for a particular application.

The anisotropy can be either intrinsic to the material, as a result of its crystal structure or shape, or it can be induced by a careful choice of processing methods. Anisotropy is related to the lattice structure and to the physical properties of the material. Two kinds of anisotropy are reviewed in this section.

2.1.6.1 Magnetocrystalline Anisotropy

The magnetocrystalline anisotropy is the energy required to deflect a magnetic moment in a single crystal from the easy to the hard direction. The easy and hard directions arise from the interaction of the spin magnetic moment with the crystal lattice (spin-orbit coupling).

Uniaxial anisotropy is the simplest form of magnetocrystalline anisotropy. It is created when the orbital electrons couple with the lattice. A state of minimum energy exists in a domain when the magnetisation vector (M_s) lies along one of its preferred directions. The applied field that is required to rotate all the magnetic moments of a single crystal as one unit to a magnetically hard direction is called the anisotropy field H_a and is defined as:

$$H_a = \frac{2K}{M_s}$$
<div align="right">Equation 2-8</div>

where M_s is the saturation magnetisation and K is the anisotropy constant, which depend on the material and on the temperature. The temperature dependence of H_a is a result of thermal disordering and of the changing influence of the sublattice anisotropies.

The energy involved in the rotation of the internal magnetisation from the easy axis to the applied magnetic field is called the anisotropy energy and is designated as E_a. It strongly depends on the crystal structure. In a simple cubic system such as iron, the anisotropy energy E_a is defined by:

$$E_a = K(\cos^2\theta_1 \cos^2\theta_2 + \cos^2\theta_1 \cos^2\theta_3 + \cos^2\theta_3 \cos^2\theta_1)$$
<div align="right">Equation 2-9</div>

where K is the anisotropic constant of the material and θ_1, θ_2 and θ_3 the angles between the magnetisation and the three crystal axes.

The schematic in Figure 2.4 shows how the anisotropy energy is related to the direction of magnetisation. It can be seen that a higher applied field is required to magnetise along the hard directions with a higher energy state than magnetisation in the easy direction. In the example of iron, which has a body centred cubic crystal structure (BCC), the anisotropy energy is a minimum when the magnetisation is parallel to <100>.
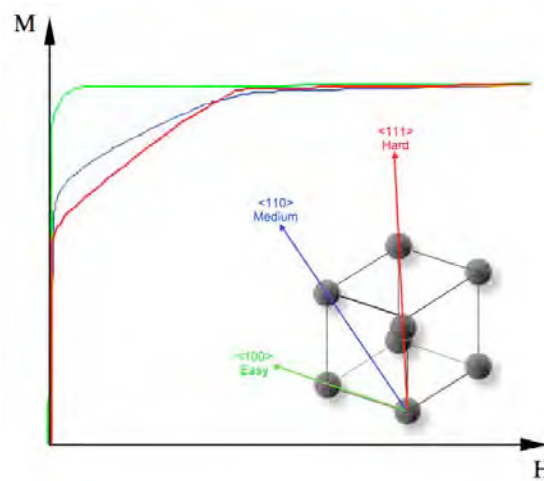
Figure 2.4 Magnetisation curve for single crystal of iron (adapted from (Jiles, 1998))

2.1.6.2   Shape Anisotropy

Shape anisotropy relies on the physical shape, such as the shape of a grain in a material. A magnetised sample will produce a magnetic charge at the surface. This surface charge distribution, acting in isolation, is itself another source of a magnetic field, called the demagnetizing field. It is called the demagnetizing field because it acts in opposition to the magnetization that produces it. For a spherically shaped, randomly aligned polycrystalline specimen that has no crystal anisotropy, the magnetisation will be the same in any direction. Therefore a will have no shape anisotropy. However, in a thin needle shaped specimen, the demagnetising field will be less if the magnetisation is along the long axis than if it is along one of the short axes. This produces an easy direction of magnetisation along the long axis. The energy associated with the shape anisotropy is the magnetostatic energy E_{as}, which can be written as:

$$E_{as} = K_s \sin^2 \theta \hspace{4cm} \text{Equation 2-10}$$

where K_s is the shape anisotropy constant and θ is the angle between the magnetisation and the easy direction.

2.1.7   Magnetic Response of Solids

Figure 2.5 illustrate the change in domain structure of a multi-domain material during magnetisation. With increasing magnetic field firstly the domains that are aligned with respect to the external field grow at the expense of the misaligned domains. At the beginning this is a reversible process, but then subsequently an irreversible one. As the field is increased to a moderate strength, the second mechanism becomes significant; this is reversible domain rotation until the magnetic moments are aligned parallel to the applied field- also called the point of saturation.
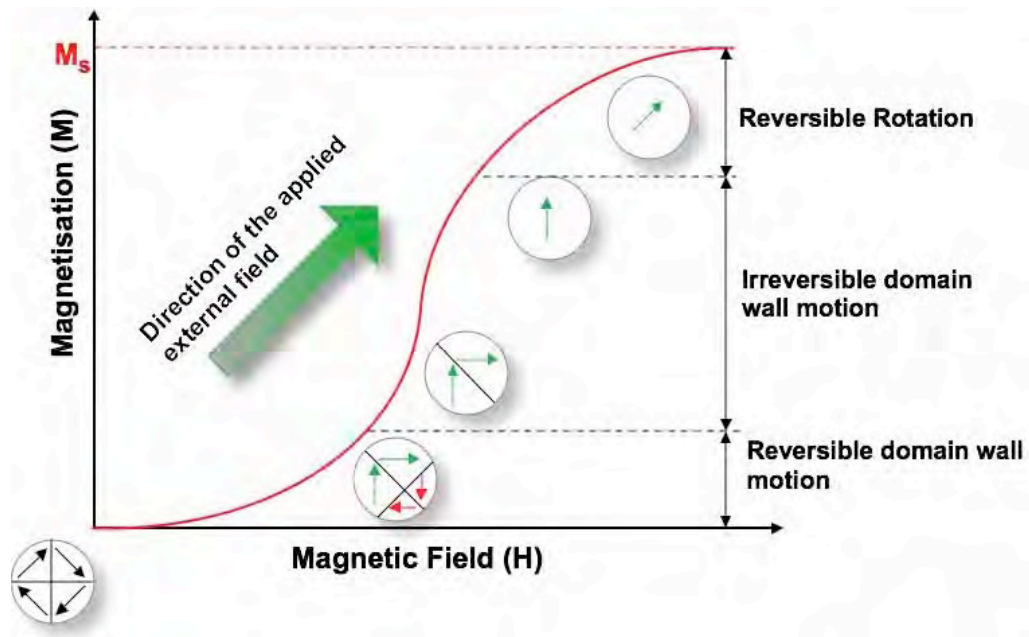
Figure 2.5 Influence of an external magnetic field on domain structure (adapted from (Wyatt and Dew-Hughes, 1974)).

The most common method of representing the bulk magnetic properties of ferromagnetic and ferrimagnetic materials is the hysteresis loop. The hysteresis loop is a plot of the resultant magnetic induction B (or magnetisation, M) for various applied fields H, as shown in Figure 2.6. The sequence is that the magnet material starts at the origin in an unmagnetised state, and the magnetic induction follows the curve from 0 to B_s as the applied field is increased

in the positive direction. The value of magnetic induction (B) at B_s is called the saturation induction, and the curve of B from the demagnetised state to B_s is called the normal induction curve.

When the applied magnetic field, H, is reduced to zero after the saturation, the magnetic induction reduces from B_s to B_r – the residual induction. The reverse field required to reduce the induction to zero is called the coercivity, H_c. Depending on the value of coercivity, ferromagnetic materials are classified as either hard or soft. A hard magnet needs a large applied magnetic field to reduce its induction to zero (or conversely to saturate the magnetisation). A soft magnet is easily saturated and also easily demagnetised.

As B is dependent upon the applied field, B will continue to increase with applied field whereas the magnetisation will achieve saturation at some point. The saturation induction (B_s) will also be related to the temperature.
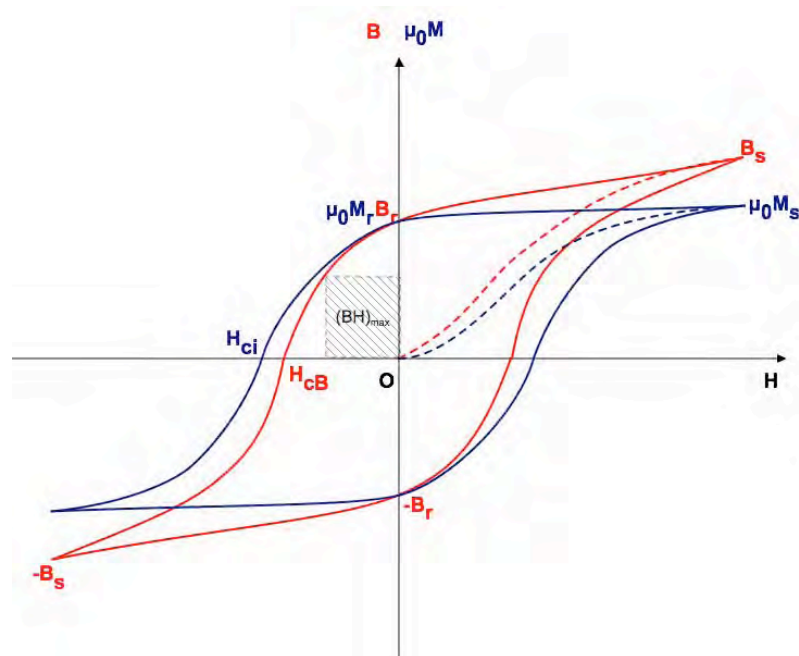
Figure 2.6 Schematic representation of the B(H) red and μ_0M(H) blue hysteresis loop for hard magnetic materials. The dashed curves represent the initial magnetisation and the rectangle the energy product (BH)$_{max}$.

BH$_{max}$ represents the point at which the product of B and H are at a maximum. At this point, the energy density of the magnetic field into the air gap surrounding the magnet, is at a maximum. The higher this product, the smaller the magnet needs to be in order to generate and equivalent force.

2.1.8 Coercivity of Magnetic Materials

Coercivity is a term used to describe a capability of the magnetic material to resist a reduction in magnetisation caused by its own demagnetising field or the reverse field during the magnetisation-demagnetisation process. The reversal of magnetisation in magnetic materials is due to the movement of domain walls or the rotation of the magnetisation vectors. Therefore, the saturation magnetisation of a magnet is an intrinsic property and will be dependent on the composition of the magnet without being influenced by any other factor. Magnetic properties such as the remanence and the coercivity, on the other hand, are affected by microstructure changes. In particular, we are interested in the coercivity; the ability of the magnet to retain its magnetic properties in the presence of demagnetising field. The relationship between the microstructural features and the coercivity can be expressed as:

$$H_a = \frac{\alpha(T)2K}{M_s} - N_{eff}M_s \qquad\qquad \text{Equation 2-11}$$

where H$_a$ is the actual coercivity, α(T) << 1.0 is a temperature dependent microstructural parameter which is enhanced by a fine, uniform grain size. K is the anisotropy constant, M$_s$ is the saturation magnetisation and N$_{eff}$ is the demagnetisation factor. The following sections will examine the various coercivity mechanisms.

2.1.8.1 Domain Wall Pinning

Domain wall pinning can result from the presence of fine precipitates in the material.

Precipitates within the grains, or at the grain boundaries, can obstruct domain wall movement and make the reverse domains difficult to propagate through the grains. It will therefore increase the coercivity.

In the 2/17-type magnets (Sm$_2$ (Co, Fe, Cu, Zr)$_{17}$), for instance, pinning is achieved by the presence of a fine distribution of a SmCo$_5$-type phase, which has a much lower domain wall energy than that of the majority 2/17-type phase. The domain walls are therefore pinned within the SmCo$_5$-type cellular precipitates and reversal of the magnetisation is difficult. Substitution of iron, copper and zirconium is made for cobalt and forms a coherent cellular SmCo$_5$ type structure with Zr-containing needles (Kumar, 1988). The coherency strains around these second phase particles cause the motion of domain walls to be hindered.

2.1.8.2 Domain Nucleation

The nucleation-type coercivity mechanisms depend upon the ease of nucleating reverse domains. This method is used to optimise the coercivity in the sintered NdFeB and SmCo$_5$ magnets. By modifying the microstructure, it is possible to make reverse domains more difficult to nucleate and thus improve the coercivity. The microstructure can be modified by a selected processing technique during sintering and annealing for the production of uniform, fine and smooth grains.

Reverse domains are easily nucleated when the grains are imperfect, with defects such as cracks, pores and sharp edges. Reducing grain damage and smoothing grain boundaries increases the field required for domain nucleation and therefore increases the coercivity. When a reverse field is applied after the material reaches saturation, a high resistance to demagnetisation ensues due to the difficulty in nucleating reverse domains.

2.1.8.3   Magnetisation Behaviour of Different Coercivity Mechanisms

Two types of coercivity mechanism can be determined from the shape of the first quadrant of the magnetisation curve as shown in Figure 2.7. For pinning, the magnetisation increases slowly with increasing field, as the domains need to overcome the pinning field, which is not constant throughout the material: hence the gradient changes until there is a sharp rise when the pinning field has been overcome entirely. For the nucleation-type mechanism, however, the magnetisation increases rapidly with the application of a magnetic field due to easy growth and the rotation of the domains into the direction of the applied field until saturation is achieved.
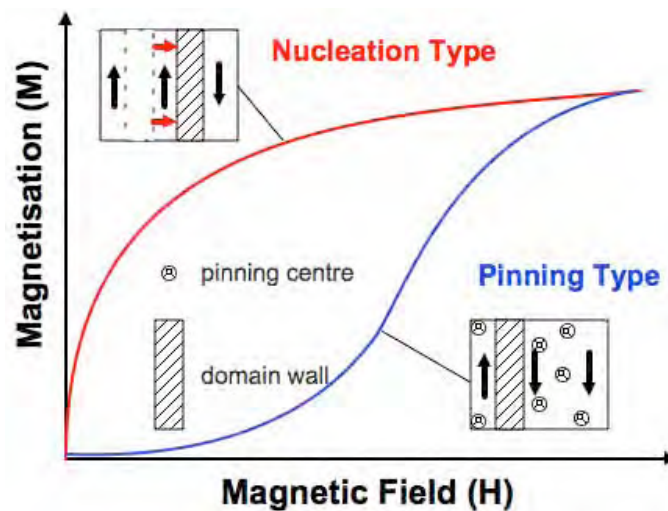
Figure 2.7 The magnetisation curves for the nucleation and pinning types of coercivity.

2.1.9   Type of Magnetism

Figure 2.8 illustrate the types of magnetic behaviour of each element at room temperature. All materials can be classified in terms of their magnetic behaviour into one of five major categories, depending on their bulk magnetic susceptibility, χ, as shown in Table 2.2. The two most common types of magnetism are diamagnetism and paramagnetism.

Figure 2.8 A periodic table showing the type of magnetic behaviour of each element at room temperature.

2.1.9.1 Paramagnetism

In a paramagnetic material, an external magnetic field results in a weak magnetisation in the same direction as the applied field and therefore the value of χ is small and positive. The susceptibility of these materials is in the range as 10^{-3} to 10^{-5}. A paramagnetic effect is created by a net magnetic alignment of unpaired electrons that align with the applied field. At low magnetic fields, the magnetization is linearly proportional to the applied field but deviations occur at higher magnetic fields when the magnetisation begins to saturate. In the case of the material possessing localized moments, the paramagnetic effect decreases with increasing temperature and this can be described by the Curie Law:

$$\chi = \frac{C}{T}$$

Equation 2-12

where C is the positive Curie constant and T is the absolute temperature, both measured in K.

Table 2.2 Summary of different types of magnetic behaviour.

Type of Magnetism	Reason	Spontaneous Magnetisation	Structure	Critical Temperature	Magnitude of χ	Example
Diamagnetism	filled up electron shell	none	compensation of the spin moments	none	-10^{-6} to -10^{-5}	Ag, Au, Bi, Cu, H_2, N_2
Paramagnetism	unfilled electron shell	none	random distribution	none	10^{-5} to 10^{-3}	Sn, Pt, Al, W, O_2
Ferromagnetism	unfilled inner electron shell	below T_c a universal curve above T_c none	parallel spin alignment in domains	Curie temperature T_c	10^2 to 10^5	Co, Fe, Ni
Antiferromagnetism	unfilled inner electron shell; close atom distances; NaCl structure	none	two ferromagnetic sublattices of equal spin moments	Néel temperature T_N	10^{-5} to 10^{-3}	CoO, FeO, NiO, CrF_3, FeF_3, CoF_3
Ferrimagnetism	unfilled inner electron shell; spinelstructure	below T_c nonuniversal curve above T_c none	two ferromagnetic sublattices of unequal spin moments	Curie temperature T_c	10^2 to 10^5	MeO·Fe_2O_3 (Me: Ba, Sr, Fe, Ni, Co)

2.1.9.2 Diamagnetism

In a diamagnetic material, an external magnetic field results in a weak magnetisation in the opposite direction as the applied field and therefore the value of χ is small and negative. Typically, values of the susceptibility for these materials are in the range $\sim 10^{-5}$ to -10^{-6}. Under a magnetic field the total magnetic moments align in such a way that opposes the external magnetic field.

2.1.9.3 Ferromagnetism

Ferromagnetic materials possess a permanent magnetic moment in the absence of an external field. In a ferromagnetic material, an external magnetic field causes the magnetic moments to align parallel to the external field. A point of saturation is reached when further increase of the external applied field causes no increase in the magnetisation. A ferromagnetic material has a parallel alignment of atomic moments whereby the substance is spontaneously magnetised in the absence of an external magnetic field. The alignment of the magnetic moments is disturbed by thermal agitation and the magnetisation of the material drops eventually to zero with increasing temperature. Ferromagnetic materials have positive and large values of χ below the Curie temperature (T_c), typically between 50 and 14000.

Above the Curie point, the susceptibility is inversely proportional to the temperature difference from the Curie point. This is called the Curie-Weiss law:

$$\chi = \frac{C}{(T - \theta)}$$

Equation 2-13

where θ is a constant (positive or negative) with units K. The extra term θ comes from the Weiss theory, which explains the interactions between neighbouring magnetic moments, which are localised at atomic or ionic sites.

Ferromagnetic materials are usually compared in terms of their saturation magnetisation.

2.1.9.4 Ferrimagnetism

Ferrimagnetic materials exhibit spontaneous magnetisation, but there are opposing atomic moments, which are unequal. This happens when the sublattice consists of different materials or ions: for example: Fe^{2+} and Fe^{3+} in ferrites. Unlike ferromagnetic materials, the magnetic behaviour is very similar to ferromagnetism, except that ferromagnetic susceptibilities do not follow the Curie-Weiss Law until relatively high temperatures are reached-up to two times its T_c. Typical values for the susceptibility of ferrimagnetic materials are between 50-10000.

2.1.9.5 Antiferromagnetism

Antiferromagnetic materials exhibit a small positive susceptibility, which is similar in magnitude to those of paramagnetic materials. Typical values for the susceptibility of antiferromagnetic materials are 10^{-3} to 10^{-5}. Magnetic moments are aligned in a regular pattern with neighbouring moments pointing in opposite directions. The onset of antiferromagnetism is characterised by the Néel temperature. Below the Néel temperature the atomic moments are spontaneously magnetised as in ferromagnetic materials. Above the Néel temperature the material behaves like a typical paramagnet with a random arrangement of magnetic moments.

2.2 The Production of NdFeB Magnets

The production route for sintered NdFeB magnets is a multistage process which can be divided by two major steps: casting of NdFeB alloys and followed by sintering of NdFeB magnets, where any one step can critically affect the quality of the final product.

2.2.1   Casting of NdFeB Alloys

2.2.1.1   Vacuum Induction Melting

The NdFeB alloys are produced mainly by the vacuum induction melting and casting route. Rare earth alloys produced from vacuum induction melting has an advantage of less oxygen (less than 200 ppm). The alloy components in pure form, Fe, Nd and Fe-B are melted together under vacuum by induction heating and cast into thin metal moulds or water cooled copper. The microstructure and phases present in the cast alloys are strongly influenced by the alloy composition, melting temperature and solidification behaviour of the melt during casting.

In order to obtain good magnetic properties, the amount of $Nd_2Fe_{14}B$ phase present needs to be maximised. Therefore the Nd content needs to be kept as low as possible in the starting composition, i.e. as near to the stoichiometric composition as possible.

NdFeB alloys having the stoichiometric composition have several advantages including:

1. Less oxidisation because of less Nd in the alloy

2. Higher content of hard magnetic phase ($Nd_2Fe_{14}B$), which would give better remanence but lower coercivity

3. Less grain growth due to less diffusion through the grain boundary phase

However, NdFeB alloys with stoichiometric composition require an appropriate melting and cooling technique to minimise the formation of free α-Fe dendrites. Utilizing a modified casting technique, such as a water cooled book mould with small thickness or spread casting on a water cooled copper plate with no boundaries would effectively suppress the Fe dendrites (Ma and Bounds, 1991). It has been shown that stoichiometric alloys require rapid solidification processing, for examples melt spinning (Ogilvy et al., 1984) or strip casting

(Bernardi and Fidler, 1998), to suppress the formation of free α-Fe.

2.2.1.2 Strip Casting

Strip casting is one of the steps in the process of making magnets. The strip casting process for NdFeB alloys involves a quenching technique where the molten alloys are poured onto a rotating roller, so that flake-shaped alloys are produced. The technique allows the rare earth content of the alloy to be decreased to ~11 at% as compared to 16 at% for the conventional casting process, without the formation of free Fe (Kaneko, 2000). The isothermal homogenisation process, which is required to dissolve the free Fe, can be avoided from the production of NdFeB magnets. Meanwhile, NdFeB alloys prepared by the strip casting method (as a kind of ' rapid solidification') provide a good dispersion of the Nd-rich phase and smaller columnar structures of the hard magnetic $Nd_2Fe_{14}B$ phase (Bernardi and Fidler, 1998), which leads to a high density of fine cracks after hydrogen decrepitation and produce magnets with a higher remanence.

2.2.1.3 Mechanical Alloying

Mechanical alloying is a way to produce the powder as a starting material for making magnets. Schultz at Siemens first demonstrated the application of mechanical alloying of rare earth magnet alloys (Schultz et al., 1991). During the process, elemental Nd, Fe and B (or Fe_2B) powders are combined and milled for ~4 days in a high-energy ball mill. This extensive milling produces the powder with an ultrafine-layered microstructure of Fe and Nd with the submicron B particles embedded within the layer. After annealing at 720°C for ~30 minutes, finer $Nd_2Fe_{14}B$ grains can be produced by a solid-state diffusion reaction. The powder would then process into magnet by the powder metallurgy route which will be discussed in following sections.

2.2.2 Sintering of NdFeB Magnets

As long as the NdFeB alloys (either in bulk or powders) are ready, there are two major routes to produce commercial NdFeB magnets in the following process: powder metallurgy to make oriented sintered magnets and melt spinning to make directly coercive ribbon or flake. Details of each route will be discussed in the following sections.

2.2.2.1 Powder Metallurgy Route

Powder metallurgy, which involves a sequence of orienting, pressing and sintering operations on finely divided alloy powders, has long been employed in the commercial production of ferrite and samarium-cobalt magnets. Sagawa et al. were the first to apply such methods to NdFeB magnets (Sagawa et al., 1984a). The main steps in the sintering production route are shown in Figure 2.9.
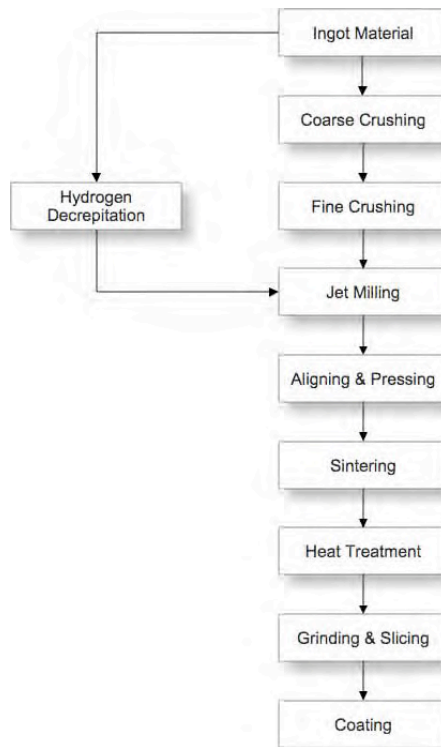
Figure 2.9 Processing route for rare earth sintered magnets (Harris and McGuiness, 1991).

Initially, the ingot material must firstly be broken up either by a mechanical route using a jaw crusher (Sagawa et al., 1984a) or by a chemical route using hydrogen (Harris et al., 1985) - this is called Hydrogen Decrepitation (HD). The HD process is carried out at room temperature under hydrogen pressures of ~1 bar or greater. During the HD process, hydrogen reacts with the Nd-rich grain boundary phase and is absorbed by the $Nd_2Fe_{14}B$ matrix grains (McGuiness et al., 1989). In both cases, cracking occurs due to differential lattice expansion and the resulting HD material is extremely friable. This allows the following milling time to be reduced considerably with significicant cost and energy savings compared to conventional jaw crushing. Some of the main technical advantages of the HD process were summarised by (Harris and McGuiness, 1991). Figure 2.10 shows a schematic of The HD-route for the production of sintered NdFeB-type magnets.
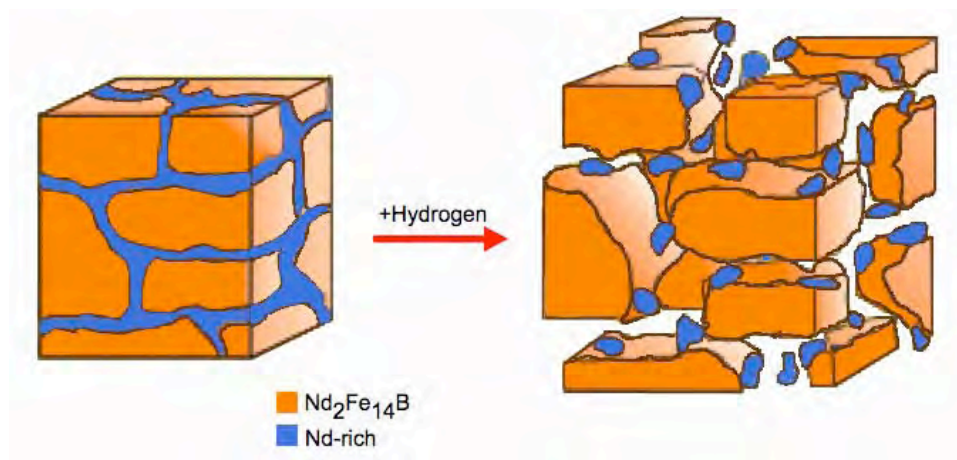
Figure 2.10 A schematic diagram of the Hydrogen Decrepitation Process for Nd-Fe-B alloys (Williams et al., 1991).

After the HD process, the alloy is then milled, using either an attritor mill or a jet mill, to a fine powder with a particle size of 3~7 µm. After milling, the powder is aligned in a magnetic field of at least 636.62 kA/m (Kawai et al., 1990) and pressed to a green compact either isostatically, or uniaxially, parallel or perpendicular to the alignment field.

2.2.2.2   The Effect of Sintering

Variable parameters in the sintering profile, temperature and material composition would have an effect on the resultant microstructure and magnetic properties in sintered NdFeB magnets. The sintering of the NdFeB magnets is carried out in either an inert atmosphere or under vacuum. At around 660°C, the Nd-rich grain boundary eutectic phase melts (Durst et al., 1987) and this liquid aids sintering, at this low melting point liquid acts as a sintering aid enabling liquid phase sintering and associated mechanisms of mass transport and deification. During the heating, the hydrogen would be desorbed from the pre-milling HD process alloy (Williams et al., 1991). Sintering is commonly carried out for one hour at temperatures between 1040-1100 °C, depending on the exact composition, before cooling to room temperature.

Cooling from the sintering temperature is followed by an annealing treatment for an hour at ~850°C and then at 550 °C (Ping et al., 2006, Fedorov et al., 2009) to improve the coercivity by smoothing the grain boundaries and reducing the number of sites for reverse domain nucleation.

2.2.2.3   Melt Spinning Route

A fine-grained $Nd_2Fe_{14}B$ powder can be produced via rapid solidification, as shown in Figure 2.11. The production of magnets from the Nd-Fe-B material using this technique was first reported by Croat (Croat et al., 1984).

The melt spinning technique consists of melting the alloy in a crucible either under an inert gas or in vacuum in order to keep the oxidation level to a minimum. The melt is ejected through a small orifice onto the surface of a rapidly revolving water-cooled copper wheel. Nearly single-phase $Nd_2Fe_{14}B$ ribbons are produced typically 30-50 µm thick, 1.5-3.0 mm wide

and 1-l0 mm in length (Herbst et al., 1986). Melt spinning achieves a solidification rate as high as 10^6 K/s, and the rate can be varied by changing the surface velocity of the spinning wheel, Vs.

The solidification rate strongly determines the microstructure and magnetic properties of the melt-spun ribbons. At an optimum solidification rate, the ribbons contain equiaxed $Nd_2Fe_{14}B$ grains with diameter varying from 20-100 nm. These ribbons are magnetically isotropic due to the random distribution of c-axes as observed by Mishra (Mishra et al., 1986). At lower rates, ribbons consist of larger grains and exhibit low coercivity.

However, totally amorphous material which exhibits negligible coercivity and energy product can be fabricated if the melt spun ribbons are prepared at too high a solidification or quench rate.

Fabrication of useful magnets requires consolidation of the brittle melt spun ribbons into a compact shape. The ribbons are processed into magnets through three processing routes named Magnequench (MQ) as shown in Figure 2.11.
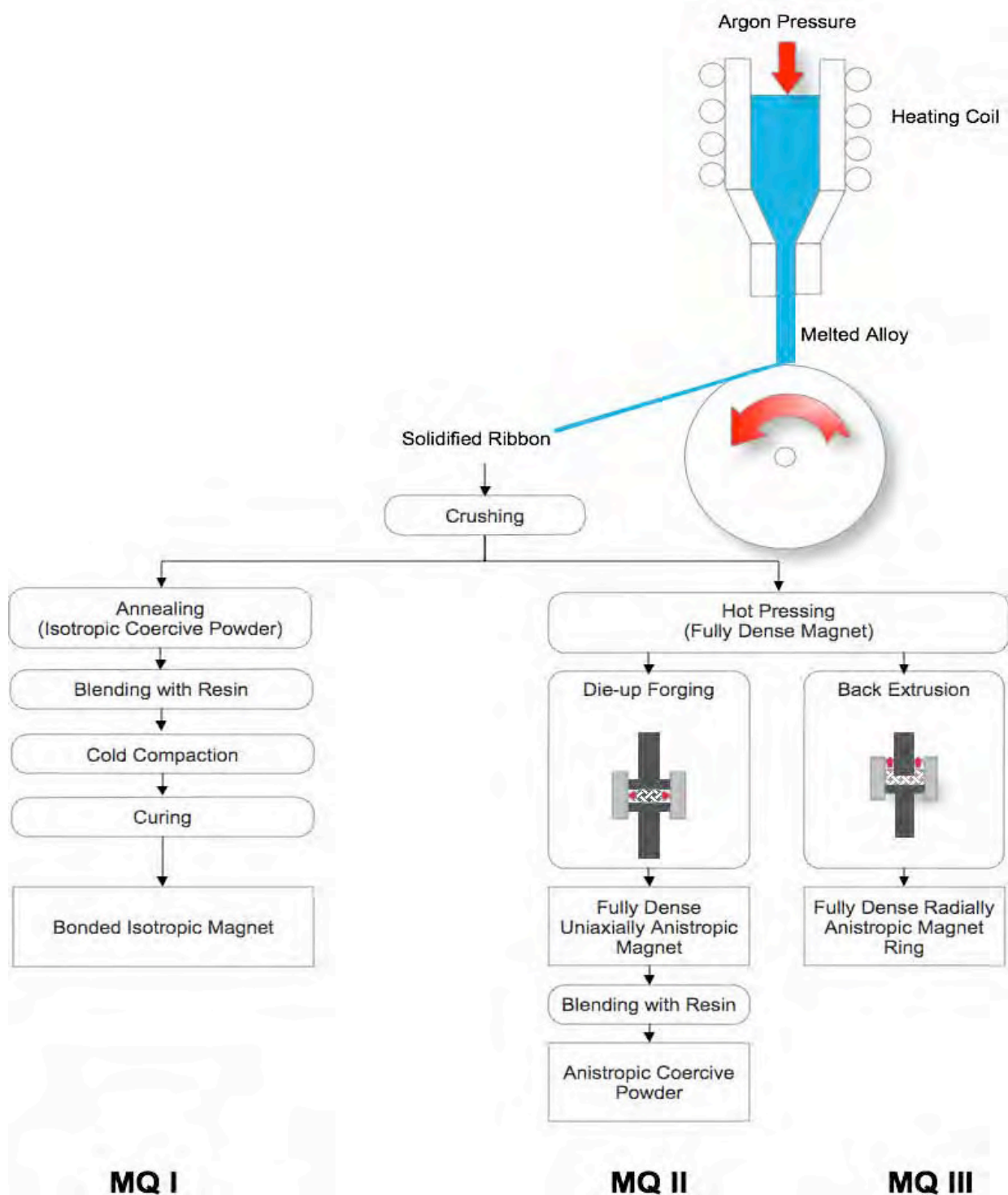
Figure 2.11 A schematic diagram of a melt spinning device and the Magnequench process using melt spun materials.

2.2.2.4 HDDR Process

Powders obtained by grinding sintered NdFeB magnets lose coercivity quickly with diminishing particle size and are unsuitable for the preparation of bonded magnets. Takeshita reported a "hydrogenation-dehydrogenation" treatment of Nd-Fe-B ingots (Takeshita and Nakayama, 1989). The treatment consisted of heating the alloy up to between 750 and 900°C for l-3 hours under 1 atm of hydrogen. This was followed by evacuating at the same temperature for 0.5~1 hour, cooling by quenching in argon gas and subsequent use in bonded magnets. This process was described in terms of a hydrogenation disproportionation desorption and recombination reaction (HDDR) (McGuiness et al., 1989).

Figure 2.12 is a schematic presentation for the microstructure of NdFeB alloy after each stage of the HDDR procedure. The first stage of the HDDR process is the hydrogenation of the bulk material, which results in decrepitation and forms a mixture of $NdH_{2.7}$ and $Nd_2Fe_{14}BH_{2.9}$. The disproportionation reaction then occurs at elevated temperature. This results in the $Nd_2Fe_{14}B$ reacting with hydrogen to form a very fine divided crystalline mixture of $NdH_{2.1}$, Fe and Fe_2B within the confines of the original coarse grain structure. Under vacuum, the intimate mixture of iron, ferroboron and neodymium hydride becomes thermodynamically unstable and reverts to the more stable $Nd_2Fe_{14}B$. The newly recombined $Nd_2Fe_{14}B$ grains are very fine (0.3 µm) and randomly orientated. Thus, the HDDR process converts the coarse-grained cast alloys into a material with an ultrafine grain size. Some detailed studies of the microstructures of HDDR by HREM and TEM were carried out later (Gutfleisch et al., 1995, Tomida et al., 1999).

Cast $Nd_{16}Fe_{76}B_8$ Alloy

$Nd_2Fe_{14}B$

Nd-rich

Expose to Hydrogen. Hydrogen Decrepitation breaks the alloy into a powder.

Hydrogenation

$Nd_2Fe_{14}BH_{2.9}$

$NdH_{2.7}$

On heating in hydrogen the $Nd_2Fe_{14}B$ disproportionates at ~650°C, to give Fe, $NdH_{1.1}$ and Fe_2B

Disproportionation

Very fine mixture of Fe, $NdH_{2.1}$ and Fe_2B

Material is held at 800 °C in hydrogen to ensure full disproportionation. The chamber is then evacuated to desorb the hydrogen, with the recombination of Nd, Fe and Fe_2B resulting in the nucleation of very fine grains of $Nd_2Fe_{14}B$.

Desorption

Very fine mixture of Fe, Nd and Fe_2B with $Nd_2Fe_{14}B$

Material is held at 800°C in vacuum to allow full recombination.

Recombination

Fine grained $Nd_2Fe_{14}B$

Figure 2.12 A schematic of the Hydrogen Decrepitation Process for an NdFeB alloy. (Harris and McGuiness, 1991)

2.3 Nd-Fe-B Alloys

2.3.1 Phase Diagram

Chaban et al. were the first to report the existence of a stable NdFeB ternary phase (Chaban et al., 1979), but the potential of this system for application as permanent magnets was not recognized. Among other earlier research, Stadelmaier (Stadelmaier et al., 1984) and Matsuura (Matsuura et al., 1985) also investigated the projection of the liquidus surface and identified several liquid compositions that were present at equilibrium in the Nd-Fe-B system.

In 1995, Hallemans et al. presented a complete review that gave an insight into the phases of the relevant composition region and the development of the phase diagram (Hallemans et al., 1995). This review paper involved a thermodynamic calculation based on all the experimental phase diagrams and chemical data in the literature. A calculated isothermal section at 25°C of the NdFeB phase diagram is shown in Figure 2.13.
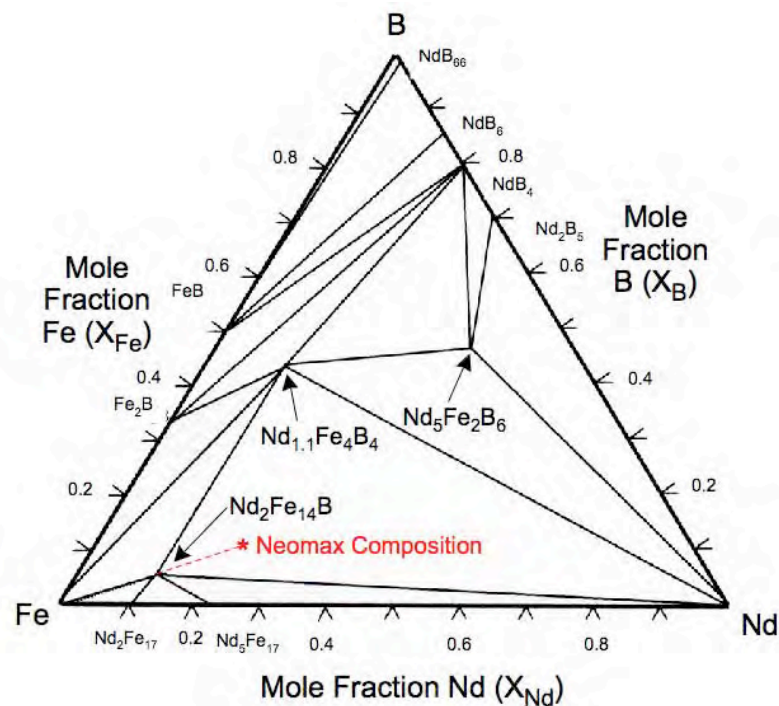
Figure 2.13 Isothermal section of the Nd-Fe-B system at 25°C. (Hallemans et al., 1995)

The Fe-rich region is the most relevant part of the phase diagram for the production of the hard magnetic $Nd_2Fe_{14}B$ phase. The asterisk in Figure 2.13 indicates the position of the 'Neomax', $Nd_{15}Fe_{77}B_8$ composition. This composition lies in a large phase field and is an equilibrium mixture of the three phases $Nd_2Fe_{14}B$ (φ), $Nd_{1.1}Fe_4B_4$ (η) and Nd-rich (ε). The dashed line from the iron corner indicates the plane of the vertical section through the ternary phase diagram where it is possible to see the $Nd_2Fe_{14}B$ phase. The calculated isopleth Fe-$Nd_2Fe_{14}B$ where the Nd: B ratio is 2:1 is shown in Figure 2.14.
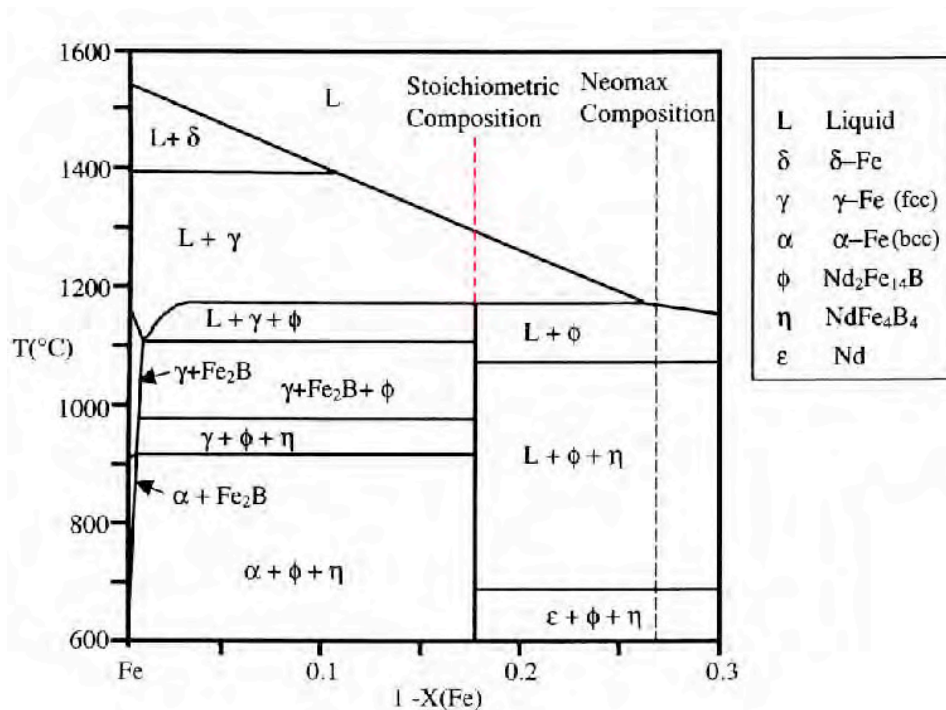
Figure 2.14 Calculated isopleths Fe-Nd$_2$Fe$_{14}$B (Hallemans et al., 1995).

The appropriate vertical section can be determined when the maximum temperature of the melt is kept near the liquidus temperature and allowed to cool slowly. At the stoichiometric composition of $Nd_2Fe_{14}B$ i.e. it is $Nd_{11.76}Fe_{82.35}B_{5.88}$ (marked by the red dashed line) the phase does not melt congruity and on slow cooling leads to the formation of primary crystallites of α-Fe. The $Nd_2Fe_{14}B$ phase then forms partially when the liquidus temperature reaches the

peritectic reaction at 1181°C;
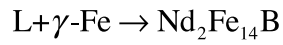
$$L+\gamma\text{-Fe} \rightarrow Nd_2Fe_{14}B \qquad\qquad \text{Equation 2-14}$$

A prolonged peritectic reaction between the primary Fe phase and the liquid phase increases the volume fraction of the $Nd_2Fe_{14}B$. Most casting processes do not allow the peritectic reaction to go to completion and the liquid does not dissolve all the Fe. During the cooling period, the composition of the remaining liquid changes along the liquidus line, becoming richer in Nd and B. The Fe undergoes a structural transition from γ (f.c.c.) to α (b.c.c.) at 922°C. Thus, most alloys of the stoichiometric composition contain a substantial fraction of α-Fe dendrites in the microstructure resulting from non-equilibrium cooling. Since α-Fe is a soft ferromagnetic phase, it is detrimental to the hard magnetic properties. Figure 2.15 shows an BSE image from as cast NdFeB alloy.
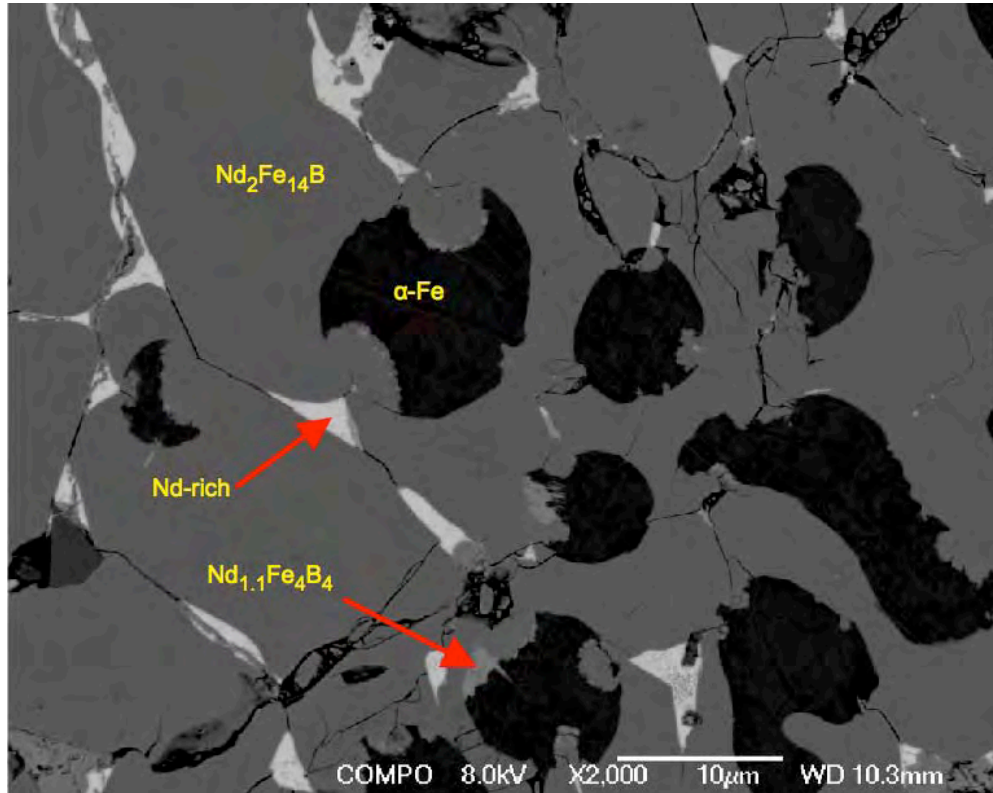
Figure 2.15 BSE image from as-cast NdFeB alloy.

2.3.2 $Nd_2Fe_{14}B$ Phase

$Nd_2Fe_{14}B$ (φ) is the main phase present in Nd-Fe-B magnets. It is a hard magnetic phase which is responsible for the high saturation magnetisation and remanence of the alloy. The first structural determination of the $Nd_2Fe_{14}B$ phase was made by Herbst (Herbst et al., 1984) using neutron diffraction. In the same year, crystallographic results based on x-ray diffraction data from Boller (Boller and Oesterreicher, 1984), Givord (Givord et al., 1984) and Shoemaker (Shoemaker et al., 1984) confirmed this. Sagawa also showed that $Nd_2Fe_{14}B$ has an atomic structure of space group $P4_2/mnm$ (Sagawa et al., 1984b), as illustrated in Figure 2.16.

The φ phase should be noted that, for clarity, the (c/a) ratio has been exaggerated in Figure 2.16. $Nd_2Fe_{14}B$ has a unit cell of tetragonal structure with a= 0.88 nm and c=1.22nm and contains four formula units or 68 atoms. Buschow (Buschow et al., 1985) showed that $Nd_2Fe_{14}B$ is virtually a line compound (i.e. it has a very narrow homogeneity range). Within the structure there are six nonequivalent iron sites, two rare-earth sites and one boron site. These have been named using various nomenclatures by different authors; Figure 2.16 uses the system of Herbst (Herbst et al., 1984). The line–compound nature of $Nd_2Fe_{14}B$ means that it has, so far, proved impossible to produce a precipitation hardened magnetic alloy based on the (φ)– phase. In this structure, the 'easy' direction of magnetization is parallel to the c-axis of the unit cell. That is because the iron and neodymium magnetic moments are aligned parallel (ferromagnetically) to each other and the c-axis, producing a net magnetization at room temperature.

It has six crystallographically equivalent iron sites ($16k_1$, $16k_2$, $8j_1$, $8j_2$, 4e, 4c), two crystallographically inequivalent neodymium sites (4f, 4g) and one boron site (4f). In this system, the 16 in $16k_1$ signifies that there are 16 equivalent sites of that kind present in the unit

cell. The top half of Figure 2.16 is a mirror image of the bottom half of the cell, with the planes at $z = 0$ and $z = 1/2$ being mirror planes. All of the Nd and B atoms, but only 4 of the iron atoms in the unit cell, are found on these mirror planes; the rest of the iron atoms form networks of atoms between the mirror planes. The $Fe(k_1)$, $Fe(k_2)$, $Fe(j_1)$ and $Fe(e)$ sites make up two slightly distorted hexagonal arrays, one of which is rotated by $\sim 30°$ relative to the other. Sandwiched between these two layers are the $Fe(j_2)$ atoms which are located above or below the centres of the hexagons.
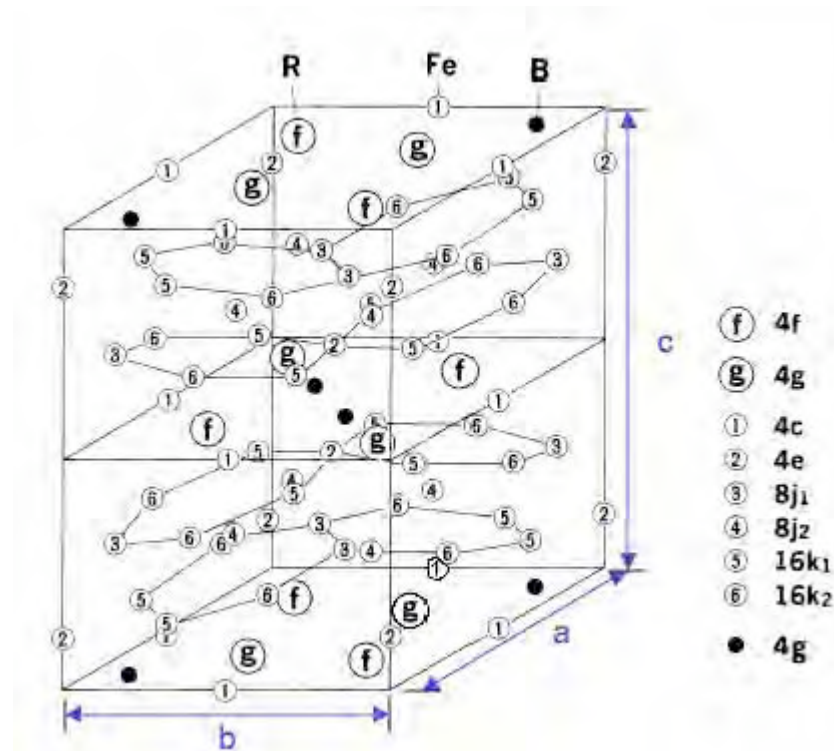
Figure 2.16 The Unit Cell of Nd$_2$Fe$_{14}$B (Herbst et al., 1984). (Note: a=b≠c)

The unit-cell parameters and the positional coordinates of the atoms are arranged and shown in Table 2.3.

Table 2.3 Published and standardized data sets from four independent structure determinations of tetragonal $Nd_2Fe_{14}B$ (Gelato and Parthe, 1987).

I: Boller & Oesterreicher (1984); II: Givord, Li & Moreau (1984); III: Shoemaker, Shoemaker & Fruchart (1984); IV: Herbst, Croat, Pinkerton & Yelon (1984).

	I $a = 8{\cdot}792, c = 12{\cdot}174$ Å			II $a = 8{\cdot}792, c = 12{\cdot}190$ Å			III $a = 8{\cdot}804, c = 12{\cdot}205$ Å			IV $a = 8{\cdot}792, c = 12{\cdot}19$ Å		
	x	y	z	x	y	z	x	y	z	x	y	z
Published data												
Nd(1)	0·267	0·267	0	0·3572	0·3572	0	0·14278	0·14278	0	0·266	0·266	0
Nd(2)	0·140	−0·140	0	0·7698	0·2302	0	0·73016	0·26984	0	0·139	−0·139	0
Fe(1)	0·224	0·568	0·128	0	0	0·116	0	½	0	0·224	0·568	0·128
Fe(2)	0·040	0·360	0·174	0	½	0	0·72417	0·06755	0·37248	0·039	0·359	0·176
Fe(3)	0·097	0·097	0·200	0·0978	0·0978	0·2942	0·46273	0·14037	0·32374	0·097	0·097	0·205
Fe(4)	0·318	0·318	0·250	0·3184	0·3184	0·2550	0·18236	0·18236	0·25434	0·318	0·318	0·247
Fe(5)	0	0	0·107	0·5670	0·2245	0·3735	0·40210	0·40210	0·29551	½	½	0·113
Fe(6)	0	½	0	0·1397	0·5370	0·1759	0	0	0·38522	0	½	0
B	0·367	−0·367	0	0·124	0·124	0	0·37736	0·37736	0	0·368	−0·368	0
Standardized data, all with Wyckoff sequence $k^2 j^2 g f^2 e c$												
Fe(1) in 16(k)	0·040	0·360	0·326	0·0370	0·3603	0·3241	0·03727	0·35963	0·32374	0·039	0·359	0·324
Fe(2) in 16(k)	0·068	0·276	0·128	0·0670	0·2755	0·1265	0·06755	0·27583	0·12752	0·068	0·276	0·128
Fe(3) in 8(j)	0·097	0·097	0·300	0·0978	0·0978	0·2942	0·09790	0·09790	0·29551	0·097	0·097	0·295
Fe(4) in 8(j)	0·318	0·318	0·250	0·3184	0·3184	0·2550	0·31764	0·31764	0·25434	0·318	0·318	0·253
Nd(1) in 4(g)	0·233	0·767	0	0·2302	0·7698	0	0·23016	0·76984	0	0·234	0·766	0
B in 4(f)	0·133	0·133	0	0·124	0·124	0	0·12264	0·12264	0	0·132	0·132	0
Nd(2) in 4(f)	0·360	0·360	0	0·3572	0·3572	0	0·35722	0·35722	0	0·361	0·361	0
Fe(5) in 4(e)	0	0	0·393	0	0	0·116	0	0	0·11478	0	0	0·113
Fe(6) in 4(c)	0	½	0	0	½	0	0	½	0	0	½	0

Sagawa et al. reported that boron plays a direct role in expanding the Fe-Fe interatomic distances and/or decreasing the number of iron nearest neighbours, but stabilizes the structure and causes a higher Curie temperature (312°C) in comparison to that of the Nd-Fe binary compounds (Sagawa et al., 1984a).

Transmission electron microscopy studies by Fidler have shown that the $Nd_2Fe_{14}B$ phase is free from imperfections (Fidler and Knoch, 1989).

2.3.3 $Nd_{1.1}Fe_4B_4$ Phase

The B-rich $Nd_{1+\varepsilon}Fe_4B_4$ phase is a non-ferromagnetic boride phase. It was first reported and assigned the formula $NdFe_4B_4$ by Chaban et al. (Chaban et al.). Sagawa and Matsuura suggested that this boron-rich phase may be represented by $Nd_2Fe_7B_6$ which has a tetragonal lattice with a = 0.72 nm and c = 2.740 nm (Sagawa et al., 1984a, Matsuura et al., 1985). Bezinge proposed that the composition of the phase is $NdFe_{3.3}B_{3.7}$ after microprobe analysis (Bezinge et al., 1985). Following work on X-ray diffraction it led to the description of this

phase as a FeB primitive tetragonal lattice superimposed on a RE body centred tetragonal lattice (Givord et al., 1984). However, further work by Buschow suggested that the phase has a slight composition range concerning the ratio of Fe:Nd, and hence the composition is often represented by the formula $Nd_{1+\varepsilon}Fe_4B_4$, where $\varepsilon \sim 0.1$(Buschow et al., 1985).

$Nd_{1+\varepsilon}Fe_4B_4$ is paramagnetic at ambient temperature but undergoes a ferromagnetic transition at 15K (Givord et al., 1984). The phase forms below 1100°C in Nd-Fe-B type alloys with Nd and B in excess of the stoichiometric composition ($Nd_{11.76}Fe_{82.35}B_{5.88}$, at%); an excess in Nd and B prevents the presence of free iron in the as cast state.

The crystal structure of $Nd_{1+\varepsilon}Fe_4B_4$ was described by Bezinge (Bezinge et al., 1985) as consisting of two interpenetrating metal sublattices of incommensurate periods with identical a-spacing, but different although parallel c-spacings. One sublattice has a Fe-B primitive tetragonal sublattice with a $P4_2/mcn$ space group and a = 0.71 nm and c_{Fe} = 0.39 nm. The Fe:Nd ratio can vary with the commensurability of the Fe_4B_4 and Nd sublattices of the long chain structure so that the formula which has been reported as $Nd_{1+\varepsilon}Fe_4B_4$ is approximate. Since its Curie temperature is 15 K, it is not a ferromagnet at room temperature and hence dilutes the magnetic properties of the magnets.

Transmission electron microscopy studies by Mishra (Mishra et al., 1986) and Fidler (Fidler, 1987) have shown that the $Nd_{1+\varepsilon}Fe_4B_4$ phase has a high density of dislocations and planar defects.

2.3.4 Nd-rich Phase

The paramagnetic Nd-rich phase is important to the magnetic properties of the NdFeB material (Otsuki et al., 1990, Vial et al., 2002). The phase is reactive towards hydrogen and

therefore enhances decrepitation and grain refinement during powder processing. In sintered magnets, this phase isolates the grains and thus enhances the coercivity by smoothing the surfaces, so that the potential for nucleation of reverse domains is reduced. The phase also assists in densification at lower temperature via liquid phase sintering and minimizes the grain growth.

The Nd-rich phase was first reported as an f.c.c. structure which contains 85-95 at% of Nd and 5-15 at% Fe with a trace amount of boron in sintered Neomax magnets, but was not found in the NdFeB ternary equilibrium phase diagram by Sagawa et al (Sagawa et al., 1984b). This difference has been attributed to the higher oxygen content in the grain boundaries of the sintered magnet (0.017 wt% in the ingots compared to up to 0.63 wt% in the sintered magnets) (Tang et al., 1988). Matsuura reported from X-ray analysis that this phase has a double hexagonal close packed (d.h.c.p.) structure in the ingot material (Matsuura et al., 1985).

Most rare earth metals contain oxygen which unintentionally introduced when they are processed. This additional oxygen means that the alloy system should be considered as a quaternary system (Nd-Fe-B-O) and additional phases may well be presented (Durst et al., 1987). The formation of the f.c.c. Nd-rich phase is a result of the higher oxygen content compared with that of the d.h.c.p. phase, and this also results in an increase in the amount of the $Nd_{1+\varepsilon}Fe_4B_4$ phase present. This was found to be important to the sintering behaviour of the NdFeB alloy (Kim, 1988). The formation of the f.c.c. phase containing oxygen has been shown to be very important to the behaviour of the NdFeB magnet and, if it is retarded, the sintering reaction does not proceed properly to produce a fully dense magnet (Gutfleisch et al., 1995). From the literature, it appears that the Nd-rich regions are rather complex. Four kinds of structure have been reported as shown in Table 2.4.

Table 2.4 The crystal structure and lattice parameters of all reported Nd-rich phases (Wang and Li, 2005).

Phase	Prototype	Space Group	Lattice parameters(nm)	References
DHCP-Nd_2O_3	unknown	HCP	a= 0.365-0.37 ; c=1.18	a, b
FCC-NdO	NaCl	Fm$\bar{3}$m	a=0.507-0.524	b, c
Complex-Nd_2O_3	unknown	FCC+BCC	a_{FCC}=0.52 a_{BCC}=1.04	c, d
h-Nd_2O_3	La_2O_3	P$\bar{3}$ml	a= 0.383 ; c= 0.600	e

a) Fidler et al. (Fidler), b) Tang et al. (Tang et al.), c) Lemarchand et al. (1990), d) Jin et al. (1993), e) Grier et al. (1998)

Makita reported the Nd-rich phase to be f.c.c (a = 0.548 nm) and there were two orientation relationships between the f.c.c. grain boundary phase and $Nd_2Fe_{14}B$ in optimally heat treated NdFeB sintered magnets: (110)tetra // (110)fcc, [001]tetra // [223]fcc, or (110)tetra // (010)fcc, [001]tetra // [102]fcc (Makita and Yamashita, 1999). The high intrinsic coercivity of the NdFeB sintered magnets may be due to the occurrence of such an ordered structure at the interfaces between these phases.

TEM studies showed that the soft Nd-rich phase contained a high density of defects (Fidler, 1987, Fidler and Knoch, 1989).

As stated previously, it is thought that the extra oxygen incorporated during processing is responsible for the replacement of the d.h.c.p structure by f.c.c.. Many authors have also observed a body centred cubic (b.c.c.) structure (Hiraga et al., 1985). This was later shown to be an artifact of sample preparation (Hirosawa and Tsubokawa, 1990), whereby ion beam thinning of T.E.M. samples had resulted in oxidation of the material. Oxide inclusions have also been observed in the Nd-rich phase: these have been shown to include Nd_2O_3 and B_2O_3 (Holc et al., 1990).

2.3.5   Other Phases

2.3.5.1   α-Fe Phase

In the ternary Nd-Fe-B system, a number of other phases may exist. Free iron is often found in the microstructure of cast alloys that are low in rare earth content. It can be the first solidification product to form from the melt during casting. Under equilibrium conditions it would undergo a peritectic reaction with the liquid to form $Nd_2Fe_{14}B$. However, in practice this reaction does not go to completion. Free iron can prevent the complete milling of the alloy to a fine powder, with an iron rich residue being left behind. It is also thought that soft ferromagnetic iron present during the powder aligning process can cause stray fields that result in poor alignment. Iron is unlikely to persist through into the microstructure of the finished magnet, as any particles will be very fine and would react rapidly with the liquid phase during sintering to form the matrix phase. This material may form as non-aligned grains, thus reducing the final remanence.

Minor ferromagnetic phases , named Al and A2, have also been reported in the grain boundaries (Schneider et al., 1989). Both A1 and A2 phases were confirmed with the composition of the residual solidifying liquid in the sintered magnets, $FeNd_2B_3$. The phases are magnetically soft compared to $Nd_2Fe_{14}B$ and are deleterious to coercivity. They are thought to dissolve during the annealing process.

It has been reported that a high boron content can be used to suppress the formation of free α-Fe in the as-cast microstructure (Buschow et al., 1985), which subsequently reduces processing costs by negating the need for expensive high temperature, homogenising heat-treatments.

2.3.5.2 Nd₂Fe₁₇ Phase

The hexagonal Nd_2Fe_{17} phase can be formed in compositions that are low in B or Nd by the reaction:

$$L + \gamma\text{-Fe} \rightarrow Nd_2Fe_{14}B + Nd_2Fe_{17}$$

<div align="right">Equation 2-15</div>

A boron concentration greater than 5.8 at% is necessary to inhibit the formation of the soft magnetic Nd_2Fe_{17} phase at the grain boundary. This phase is ferromagnetic at room temperature, having a Curie temperature of 57°C (Croat et al., 1984, Bo-Ping and Coey, 1988). The presence of this phase in finished magnets is extremely detrimental to the coercivity.

2.4 Additions to Nd-Fe-B Magnets

Nowadays, NdFeB magnets are no longer ternary systems. By adding different small amounts of additives, the performance of magnets reproduced by magnetisation saturation, coercivity, temperature stability and Curie temperature, can be improved via microstructure change. Accordingly to Fidler (Fidler, 1992), additives can be classified into two types. Type I are represented by low melting metals such as Al, Ga, Cu, Si, while Type II are additives with high melting temperature such as Ti, V, Zr, Nb, Mo, Ta, W. Both dopant additive types influence microstructure in a different way.

Type I dopants improve the wetting of the liquid phase during sintering and therefore influence the magnetic decoupling of the grains. Normally, intergranular phases form in the Nd-rich area during the cooling. Since the better separation and decoupling of hard magnetic grains lead to the enhancement of coercivity of the magnets, the replacement of the intergranular phase in Nd-rich area by new dopant containing phases would improve the magnetic properties.

Type II dopants have low solubility within the hard magnetic phase. Most of these dopants form boride precipitates which can improve the corrosion resistance. For example, the advantage of the Nb and Zr additions is to avoid the formation of α-Fe in magnets.

Additions of heavy rare earths like Gd, Tb, Dy, Ho and Er can significantly increase the coercivity and reduce the remanence. The reason is the opposite magnetic moments occurred of Nd and Fe atoms (Narasimhan, 1981). For example, additions of Dy will result in higher magnetocrystalline anisotropy than $Nd_2Fe_{14}B$, with a lower magnetization and hence lower maximum energy product.

2.4.1 Dysprosium

Dysprosium substitutes partially for neodymium in the $Nd_2Fe_{14}B$ lattice, increasing the coercivity and magnetocrystalline anisotropy (Rodewald, 1985, Handstein et al., 1990). An increase in coercivity of 640 kA/m was observed when Dy was substituted into a magnet of composition $(Nd_{1-x}Dy_x)Fe_{77}B_8$ (Sagawa et al., 1984b). The antiparallel alignment of the large dysprosium moment in the $(Nd,Dy)_xFe_{14}B$ crystal, however, reduces the saturation magnetisation. It also found that dysprosium substitutions provide a desirable inhibition of grain growth during sintering (Ma and Krause, 1987).

2.4.2 Cobalt

In order to increase the Curie temperature in Nd-Fe-B magnets, cobalt is often added despite its high price. Since the exchange integrals for Co-Co and Fe-Co are greater than for Fe-Fe, and cobalt substitutes for Fe in the $Nd_2Fe_{14}B$ lattice, this causes a significant increase in the Curie temperature (i.e. 312°C to ~398°C). Fidler observed additional grain boundary phases, which are $Nd(Fe,Co)_2$, Nd_7Co_3, $NdCo_3$ and $Nd_3(Fe, Co)$, in Co-containing NdFeB alloys

(Fidler, 1985). These phases, which are soft ferromagnetic, reduce the coercivity. Combinations of Co and other elements are usually used to improve both Curie temperature and coercivity. Dysprosium and cobalt are often added in combination to improve both the coercivity and the Curie point (Gauder et al., 1988).

2.4.3 Aluminium

The coercivity of Nd-Fe-B magnets can be improved by up to 50% by appropriate aluminium addition (Kim, 1988). Al has been found to be present in both the $Nd_2Fe_{14}B$ and Nd-rich phases. It was suggested that the coercivity is improved by microstructural changes, in which the Nd-rich liquid is finely distributed and wets the grains during sintering. The wettability of $Nd_2Fe_{14}B$ grains is enhanced by an Al containing phase at the grain boundaries (Knoch et al., 1989). The improvement of coercivity in Nd-Fe-B-Al magnets also occurs in conjunction with dysprosium additions.

2.4.4 Niobium

The addition of niobium has been reported to increase the coercivity. This improvement may be associated with the precipitation of finely dispersed niobium-containing precipitates, which may serve as domain-wall pinning sites (Ishikawa et al., 1989). In the cast state, Kowalczyk reported that the addition of niobium to Nd-Fe-B leads to alloys having a high Curie temperature and anisotropy fields but decreases the saturation magnetization (Kowalczyk et al., 1989). Liu and Ahmed reported that the amount of precipitated Fe was reduced by 50% from the low Nd content alloys by the addition of 0.5 at% niobium (Liu et al., 1992, Ahmed et al., 1994). This considerably reduced the homogenisation time required for removing free iron from the microstructure.

2.4.5 Zirconium

Jurczyk suggested that Zr, which is not a rare earth element, could partially replace R in certain $R_2Fe_{14}B$ compounds (R=Y, Ce, Pr, Nd, Gd, Dy) (Jurczyk and Wallace, 1986). This partial substitution gave a slight decrease in lattice parameters (a and c), as the Zr atom is smaller than the R atoms. It has also been reported that the replacement of R (Nd) by 0.4at% Zr results in a decrease (~10°C) in the Curie temperature of $Nd_2Fe_{14}B$ (Leonowicz, 1990).

Nakamura summarised the effects of Zr, Co and Ga additions to HDDR processed NdFeB. 1.0 at% addition of Zr makes the disproportionation reaction sluggish during hydrogenation. Cobalt and gallium decrease the temperature of the recombination reaction and cobalt enhances the HDDR process (Nakamura et al., 1995).

Matzinger concluded that Zr forms agglomerated ZrB_2 platelets within large intergranular Nd-rich areas, thus inhibiting grain growth (Matzinger et al., 1996). It was observed that the presence of Zr suppressed the formation of free iron dendrites. During hydrogenation, the ZrB_2 platelets are not affected and no new Zr containing phases are formed. A memory effect occurs only in Zr-containing annealed specimens and becomes more pronounced with increasing Zr content. Thermomagnetic analysis and X-ray powder diffraction results imply that a few Zr atoms substitute into Nd sites, which makes the $Nd_2Fe_{14}B$ phase more stable against hydrogen disproportionation and partially preserves the crystallographic orientations of the initial grains and magnetically hard direction of the specimen. As a result of ZrB_2 formation, boron is removed from the hard magnetic matrix phase.

Gao demonstrated that Zr and Co additions to NdFeB alloys have significant effects on the microstructure and anisotropy (Gao et al., 1997). It was concluded that the HDDR-treated NdFeCoZrB alloy powder is anisotropic, whereas the NdFeZrB alloy powder is isotropic. The

Zr-rich phase exists during homogenising and remains unchanged during HDDR processing. However, Co addition suppresses the formation of the Zr-rich phase, resulting in a reduced volume fraction of this phase and also, a decreased Zr content of this phase. It was suggested that optimisation of the chemical composition of the starting NdFeB alloy to promote the entry of alloying elements into the $Nd_2Fe_{14}B$ phase is critical for HDDR processed powders.

McGuiness showed that Zr additions resulted in improved coercivity due to refinement of the microstructure during HDDR and the creation of a larger processing window at the critical phase of the HDDR process (McGuiness et al., 1998). Zr-containing NdFeB has improved corrosion resistance in dry conditions; however, the presence of ZrB_2 leads to the increased formation of local corrosion cells in humid conditions.

Pollard have studied Zr additions in a sintered magnet (Pollard et al., 1988). They found that a substantial amount of Zr was present in the $Nd_1Fe_4B_4$ phase, where some of the Fe atoms (~15 at%) were replaced by Zr. Some Zr precipitates within the $Nd_2Fe_{14}B$ grains were found, which might provide domain wall pinning sites to improve the coercivity. A combination of Zr with Al and Co in Nd-Fe-B magnets substantially increased the coercivity and the corrosion resistance (Kim and Camp, 1997).

Work by Yi on Zr-containing NdFeB alloys with a high boron content, demonstrated that Zr addition had no effect on the shape of the $Nd_2Fe_{14}B$ grains and that it did not change the magnetic anisotropy (Yi et al., 2000). It does however reduce the average grain size by ~1/3 and results in HDDR powders with a more uniform grain size.

De Rango showed that the addition of Zr resulted in an incomplete disproportionation reaction, with the production of nano-scaled $Nd_2Fe_{14}B$ precipitates in the disproportionated mixture (De Rango et al., 2003). The crystallographic orientation of these particles in relation

to the original $Nd_2Fe_{14}B$ grains induces an orientated grain growth during the recombination step. Liesert showed that this mechanism also occurs in Zr-free samples (Liesert et al., 1996).

Zirconium affects the magnetic properties of the HDDR treated powder. It has been found that a small substitution (0.15-0.7 at%) of Zr retards the disproportionation kinetics of the hydrogenated material (Kwon, 1997, De Rango et al., 2003). Zirconium, however, facilitates the recombination reaction of disproportionated material and suppresses the degradation of coercivity that would normally be due to the excessive grain growth of the recombined grains on prolonged recombination. Variation of the intrinsic coercivity as a function of recombination time for the alloys with different Zr content (between 0 and 2 at%) is presented in Figure 2.17.
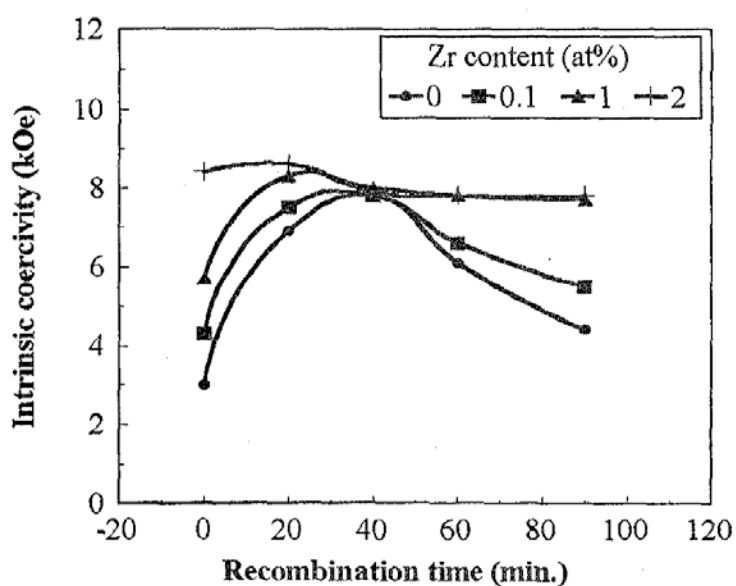
Figure 2.17 Variation of coercivity with zirconium content and recombination time in HDDR (Kwon, 1997).

In early studies, Zr was found to be important for anisotropy inducement in the HDDR treated powders. The anisotropic NdFeB magnetic powders offer the ability to produce high energy bonded and hot pressed magnets. The addition of Zr, which acts as a grain growth

inhibitor, and the integrated optimisation of HDDR, allow the HDDR treated powder to be processed into bonded magnets by the hot pressing and hot deformation route (Cannesan, 2003).

Chen et al. investigated the effect of Zr substitution for rare earth on the microstructure and hard magnetic properties of $(Nd_{0.75}Pr_{0.25})_{12.5-x}Zr_xFe_{82}B_{5.5}$ (x=0-3) (Chen et al., 2002). They found that the coercivity decreases monotonically with increasing Zr content, from 12.0 kOe at x=0 to 10.1 kOe with x=3. The remanence, however, first increased with Zr substitution, from 8.65 up to 8.93 kG at x=2, and then decreased with further Zr addition. The lattice constants and the Curie temperature of the 2-14-1 phases were found to decrease monotonically with increasing Zr content, suggesting that all the Zr is situated in the 2-14-1 matrix, occupying the rare earth sites. The observations suggested that the change in magnetic properties with Zr substitution resulted from grain size reduction.

Wu et al. studied the magnetic properties and microstructures of α-Fe/Nd_2Fe_{14}B nanocomposites produced from $Nd_8Fe_{87-x}B_5Zr_x$ (x=0-5) ribbons (Wu et al., 2002). Zr substitution were found to increase coercivity significantly from 356 kA/m for x=0 to 625.2 kA/m for x=5 alloys at the expense of remanence (as shown in Figure 2.18). Zr atoms are exclusively partitioned to the hard phase and are slightly enriched at the interface, resulting in refinement of the microstructure.

Xu et al. performed a systematic study on annealed ingots and melt-spun ribbons with different annealing conditions of $(Nd_{1-x},Zr_x)_2Fe_{14}$B with small Zr additions ($0 \leq x \leq 0.16$) (Xu et al., 2006). It was concluded that a very large amount of Zr substituting for Nd still results in primarily 2-14-1 in the as-quenched state. However, when small amounts of Zr (<0.06) are added to a cast ingot, the 2-14-1 is no longer the primary solidifying phase. While some Zr

does appear to substitute for Nd, it has only a minimal effect on the intrinsic magnetic properties and easily exsolves from the crystal structure on annealing. It is the formation of Zr compounds on the grain boundaries which improves the extrinsic magnetic properties of $Nd_2Fe_{14}B$ ribbons.
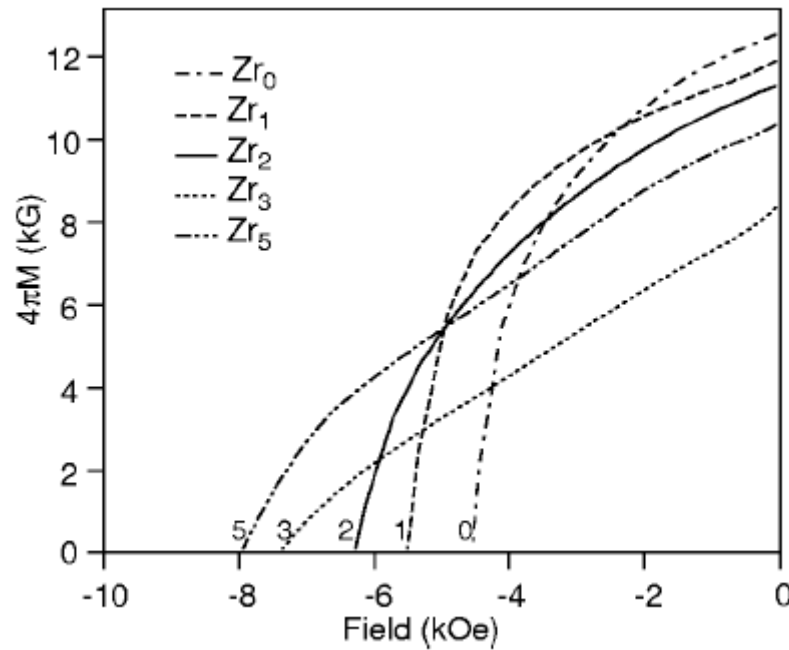
Figure 2.18 Demagnetisation curves for the $Nd_8Fe_{87-x}B_5Zr_x$ ribbons (x=0-5) (Wu et al., 2002).

Bao et al. showed the role of Zr in the microstructure, magnetic properties and thermal stability of nanocrystalline $Nd_{12.3}Fe_{81.7-x}Zr_xB_6$ (x=0-3) magnet (Bao et al., 2009). They found that the remanence polarization and maximum energy product increase initially and then slightly decrease with increasing Zr content (as shown in Figure 2.19). The microstructure was slightly refined by Zr addition, thus resulting in better magnetic properties in a fine and homogeneous grain structure.
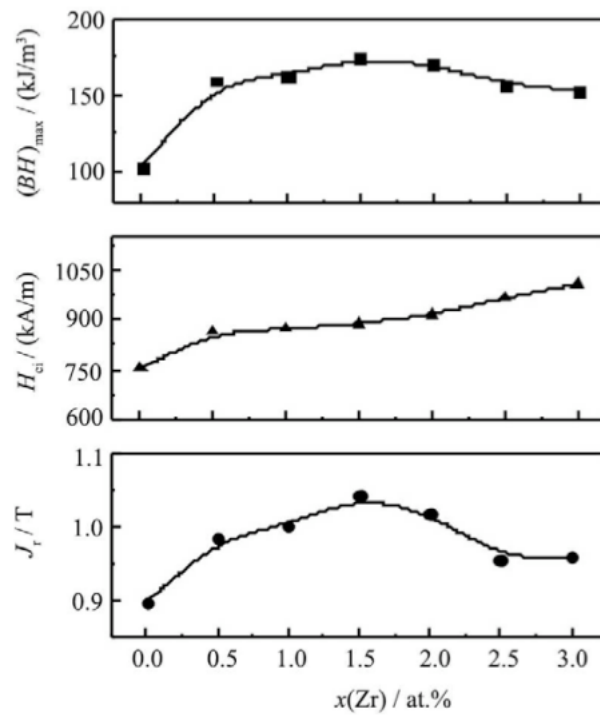
Figure 2.19 J_r, H_{ci} and $(BH)_{max}$ of $Nd_{12.3}Fe_{81.7-x}Zr_xB_6$ ribbons vs Zr content x (Bao et al., 2009).

Fujita carried out a detailed investigation of the effects of Zr addition on near stoichiometric Nd-Fe-B alloys (Fujita, 2000). Ingots of mass between 0.7 and 15g were prepared using an arc furnace. The ingots of different masses were produced with different thicknesses and therefore experienced different cooling rates. It was found that Zr suppresses the formation of α-Fe dendrites during solidification. The effect is more significant when the mass of the ingot is smaller.

Fujita investigated the addition of Zr at different percentages (between 0.1 and 2.0 at%) and concluded that 0.5 at% Zr eliminated dendrites completely in a sample of mass 0.7g. The existence of higher Nd or B was found in α-Fe dendrites. The ingots with less B and Nd content have more dendrites, and he thus concluded that the composition of the ingot influences the formation of the dendrites. Zr promotes the growth of a columnar structure during the

fabrication process. Fujita investigated the role of Zr during the homogenisation treatment and concluded that Zr inhibits grain growth and preserves the columnar structure.

Shaaban reported that the Fe dendrites observed in as-cast ingots are due to the presence of a peritectic reaction during cooling (Shaaban, 2005). The cooling rate influences the formation of the phases. At high cooling rate (i.e. near the mould interface), the number of Fe dendrites is small and the $Nd_2Fe_{14}B$ phase forms in a comparatively high proportion. In a conventionally cast ingot, the cooling rate reduces over the thickness of the ingot (i.e. from the mould interface to the central part of the ingot) as demonstrated by the distribution of phases. The addition of a small amount of Zr (0.1 and 0.3at.%) to a Nd-Fe-B composition with a low Nd-content results in a further reduction in Fe dendrites. The Nd-rich phase is distributed finely at the grain boundaries and smaller grains are produced, particularly in a region near the mould interface where the cooling rate is high.

Addition of ZrB_2 according to the formula: $(Nd_{0.123}Fe_{0.819}B_{0.058})_{100-3x}(ZrB_2)_x$ decreases the formation of dendrites in small ingots (~lg in weight) prepared using an arc furnace (Shaaban, 2005). At concentrations of ~1.0 at.% the formation of α-Fe dendrites is suppressed and the single $Nd_2Fe_{14}B$ phase is formed, together with a new NdFeBZr phase at the grain boundary. The appearance of this phase reduces the proportion of Nd-rich grain boundary phase, but does not affect the proportion of the hard magnetic $Nd_2Fe_{14}B$ phase.

The formation of Fe dendrites is inhibited when pure Zr is added into the alloy of composition $(Nd_{0.123}Fe_{0.819}B_{0.058})_{100-3x}(ZrB_2)_x$. However, a significant proportion of Fe dendrites still form at x=0.8 at.%. Comparing Zr with ZrB_2 additions, the ZrB_2-additions are much more effective in suppressing the formation of Fe dendrites.

Kirby examined the role of casting conditions and heat treatment on the magnetic

properties of selected NdFeB alloys with Zr additions. Within a range between 0.2 to 2.0 at%, he revealed that additions of 1 at% of ZrB_2 resulted in free iron levels of less than 1 volume% in the as-cast microstructure. The addition of the ZrB_2 modifies the phase diagram in such a manner that the pertectic reaction L$\rightarrow$L+Fe is avoided (Kirby, 2007).

2.5 The Objectives of This Project

It has been reported that NdFeB-type magnets have a very high $(BH)_{max}$ value and a stoichiometric composition of $Nd_2Fe_{14}B$. This phase forms by a peritectic reaction from liquid and Fe and the magnets can be produced from the cast alloy. Thus with conventional casting methods, a large amount of free α iron is formed in the cast condition. In order to remove α-Fe dendrites from the $Nd_2Fe_{14}B$ alloy, the alloy has to be either homogenised by a prolonged high temperature anneal or fabricated by a strip casting process. Both extra treatments to the cast material have not only increase the price of the final magnet but also consume a large amount of energy.

Previous work from Fujita (Fujita, 2000), Shaaban (Shaaban, 2005) and Kirby (Kirby, 2007) has shown that the amount of free α iron can be reduced by small additions of Zr (0.6 at%) and ZrB_2 (1 at%) to the NdFeB alloy; the influences of ZrB_2 needles on the NdFeB magnet and the mechanism whereby magnetic properties are influenced have not yet been studied. Hence, the objective of this project is to elucidate the effect of ZrB_2 needles on both free α-Fe content and subsequently on the magnetic properties of sintered NdFeB magnets. This project will begin by establishing the location of the zirconium boride compound in the near stoichiometric NdFeB alloy, followed by a determination of the mechanism involved in removing the free α-Fe by ZrB_2 in the Nd-Fe-B alloys using a combination of EPMA and Transmission Electron and Secondary Electron Microscopy.

References for Chapter 2

Ahmed F. M., Edgley D. S. & Harris I. R. 1994. *Proceedings of the 13th International Workshop on Rare-Earth Magnets and their Applications, Birmingham, UK*.

Bao X., Zhu J., Li W., Gao X. & Zhou S. 2009. Influence of zirconium addition on microstructure, magnetic properties and thermal stability of nanocrystalline $Nd_{12.3}Fe_{81.7}B_{6.0}$ alloy. *Journal of Rare Earths,* 27**,** 843-847.

Barkhausen H. 1919. Zwei mit Hilfe der neuen Verstärker entdeckte Erscheinungen (Two phenomena uncovered with help of the new amplifiers). *Zeitschrift für Physik,* 20**,** 401.

Bernardi J. & Fidler J. 1998. Microstructural analysis of strip cast Nd-Fe-B alloys for high $(BH)_{max}$ magnets. *Journal of Applied Physics,* 83**,** 3.

Bezinge A., Braun H. F., Muller J. & Yvon K. 1985. Tetragonal rare earth (R) Iron borides, $R_{1+\varepsilon}Fe_4B_4$ (ε =0.1), with incommensurate rare earth and iron substructures. *Solid State Communications,* 55**,** 131-135.

Bloch F. 1932. Zur Theorie des Austauschproblems und der Remanenzerscheinung der Ferromagnetika (On the theory of the exchange problem and the remanence phenomenon of ferromagnets). *Zeitschrift für Physik,* 74**,** 295-335.

Bo-Ping H. & Coey J. M. D. 1988. Effect of hydrogen on the curie temperature of $Nd_2(Fe_{15}M_2)$; M = Al, Si, Co. *Journal of the Less Common Metals,* 142**,** 295-300.

Boller H. & Oesterreicher H. 1984. On the structure of $Nd_2Fe_{14}B$. *Journal of the Less Common Metals,* 103**,** L5-L7.

Buschow K. H. J., de Mooij D. B. & van Noort H. M. 1985. Fe-rich Isothermal section of Nd-Fe-B at 900 degree C. *Philips Journal of Research,* 40.

Campbell P. 1994. *Permanent magnet materials and their application*, Cambridge University Press.

Cannesan N. 2003. *The production and characterisation of anisotropic HDDR (Pr,Nd) FeB-based powders.* Ph. D., The University of Birmingham.

Chaban N. F., Kuzma Y. B., Bolinizhko N. S., Kachmar O. & Petrov N. U. 1979. Ternary (Nd,Sm,Gd) Fe-B Systems. *DOPOVIDI AKADEMII NAUK UKRAINSKOI RSR SERIYA A-FIZIKO-MATEMATICHNI TA TECHNICHNI NAUKI.*

Chen Z., Smith B. R., Brown D. N. & Ma B. M. Year. Effect of Zr substitution for rare earth on microstructure and magnetic properties of melt-spun $(Nd_{0.75}Pr_{0.25})_{12.5-x}Zr_xFe_{82}B_{5.5}$ (x = 0-3) ribbons. *In*, 2002. AIP, 8168-8170.

Coey J. M. D. 1996. *Rare-earth iron permanent magnets*, Oxford : Clarendon Press

Croat J. J., Herbst J. F., Lee R. W. & Pinkerton F. E. 1984. Pr-Fe and Nd-Fe-based materials: A new class of high-performance permanent magnets (invited). *Journal of Applied Physics,* 55**,** 2078-2082.

De Rango P., Rivoirard S., Traverse A., Fruchart D. & Genin F. N. 2003. Role of Zr and Ga additions on the hydrogen process of Nd-Fe-B magnets. *Journal of Alloys and Compounds,* 356-357**,** 579-583.

Durst K. D., Kronmüller H. & Schneider G. 1987. Proceedings of the 5th International Symposium on Magnetic Anisotropy and Coercivity in RE Transition Metal Alloys, Bad Soden.

Fidler J. 1985. Analytical microscope studies of sintered Nd-Fe-B magnets. *IEEE Transactions on Magnetics,* 21**,** 1955-1957.

Fidler J. 1987. On the role of the Nd-rich phases in sintered Nd-Fe-B magnets. *IEEE Transactions on Magnetics,* 23**,** 2106-2108.

Fidler J. 1992. Two types of dopant with different microstructural effects leading to an improvement of rare earth-iron based magnets. *7th Int. Symp. on Magnetic Anisotropy and Coercivity in RE-TM Alloys*.

Fidler J. & Knoch K. G. 1989. Electron microscopy of Nd-Fe-B based magnets. *Journal of Magnetism and Magnetic Materials,* 80**,** 48-56.

Fujita A. 2000. *A study on magnetic anisotropy induced in the HDDR process.* Ph.D., University of Birmingham.

Gao J. R., Song X. P. & Wang X. T. 1997. Effects of Co and Zr additions on microstructure and anisotropy of HDDR-treated NdFeB alloy powders. *Journal of Alloys and Compounds,* 248**,** 176-179.

Gauder D. R., Froning M. H., White R. J. & Ray A. E. 1988. Elevated temperature study of Nd-Fe-B-based magnets with cobalt and dysprosium additions. *Journal of Applied Physics,* 63**,** 3522-3524.

Gelato L. M. & Parthe E. 1987. Structure Tidy - a computer program to standardize crystal structure data. *Journal of Applied Crystallography,* 20**,** 139-143.

Givord D., Li H. S. & Moreau J. M. 1984. Magnetic properties and crystal structure of $Nd_2Fe_{14}B$. *Solid State Communications,* 50**,** 497-499.

Gutfleisch O., Matzinger M., Fidler J. & Harris I. R. 1995. Characterisation of solid-HDDR processed $Nd_{16}Fe_{76}B_8$ alloys by means of electron microscopy. *Journal of Magnetism and Magnetic Materials,* 147**,** 320-330.

Hallemans B., Wollants P. & Roos J. 1995. Thermodynamic assessment of the Fe-Nd-B phase diagram. *Journal of Phase Equilibria,* 16**,** 137-149.

Handstein A., Schneider J., Müller K. H., Krewenka R., Grössinger R. & Kirchmayr H. R. 1990. Temperature dependence of magnetic properties of sintered Nd-Fe-B magnets modified with Dy. *Journal of Magnetism and Magnetic Materials,* 83**,** 199-200.

Harris I. R. & McGuiness P. J. 1991. Hydrogen: its use in the processing of NdFeB-type magnets. *Journal of the Less Common Metals,* 172-174**,** 1273-1284.

Harris I. R., Noble C. & Bailey T. 1985. The hydrogen decrepitation of an $Nd_{15}Fe_{77}B_8$ magnetic alloy. *Journal of the Less Common Metals,* 106**,** L1-L4.

Herbst J. F., Croat J. J., Pinkerton F. E. & Yelon W. B. 1984. Relationships between crystal structure and magnetic properties in $Nd_2Fe_{14}B$. *Physical Review B,* 29**,** 4176.

Herbst J. F., Lee R. W. & Pinkerton F. E. 1986. Rare earth-iron-boron materials - A new era in permanent magnets. *Annual review of materials science.,* 16.

Hiraga K., Hirabayashi M., Sagawa M. & Matsuura Y. 1985. High Resolution Electron Microscopy of Grain Boundaries in Sintered $Fe_{77}Nd_{15}B_8$ Permanent Magnets. *Japanese Journal of Applied Physics,* 24**,** L30.

Hirosawa S. & Tsubokawa Y. 1990. The Nd-Fe-B materials for permanent magnets. *Journal of Magnetism and Magnetic Materials,* 84**,** 309-316.

Holc J., Beseničar S. & Kolar D. 1990. A study of $Nd_2Fe_{14}B$ and a neodymium-rich phase in sintered NdFeB magnets. *Journal of Materials Science,* 25**,** 215-219.

Ishikawa T., Hamada Y. & Ohmori K. 1989. Domain wall pinning by fine precipitates. *IEEE Transactions on Magnetics,* 25**,** 3434-3436.

Jiles D. C. 1998. *Introduction to Magnetism and Magnetic Materials*, Routledge Chapman & Hall.

Jurczyk M. & Wallace W. E. 1986. Magnetic behavior of $R_{1.9}Zr_{0.1}Fe_{14}B$ and $R_{1.9}Zr_{0.1}Fe_{12}Co_2B$ compounds. *Journal of Magnetism and Magnetic Materials,* 59**,** L182-L184.

Kaneko Y. 2000. *Proceedings of the 16th International Workshop on Rare-Earth Magnets and Their Applications, Sendai, Japan,*.

Kawai T., Ma B. M., Sankar S. G. & Wallace W. E. 1990. Effect of crystal alignment on the remanence of sintered NdFeB magnets. *Journal of Applied Physics,* 67**,** 4610-4612.

Kim A. S. 1988. Effect of oxygen on magnetic properties of Nd-Fe-B magnets. *Journal of Applied Physics,* 64**,** 5571-5573.

Kim A. S. & Camp F. E. 1997. Microstructure of Zr containing NdFeB. *IEEE Transactions on Magnetics,* 33**,** 3823-3825.

Kirby K. A. 2007. *The role of casting conditions and heat treatment on the permanent magnetic properties of selected $Sm_2(Co, Fe, Cu, Zr)_{17}$ and NdFeB-Type magnets.* PhD., University of Birmingham.

Knoch K. G., Schneider G., Fidler J., Henig E. T. & Kronmuller H. 1989. Al-doped Nd-Fe-B permanent magnets: wetting and microstructural investigations. *IEEE Transactions on Magnetics,* 25**,** 3426-3428.

Kowalczyk A., Stefanski P. & Wrzeciono A. 1989. Effect of Niobium Substitution on the Magnetic Properties of $Nd_2Fe_{14}B$ and $Nd_2Fe_{12}Co_2B$ Alloys *Journal of Magnetism and Magnetic Materials,* 79.

Kumar K. 1988. $RETM_5$ and RE_2TM_{17} Permanent Magnets Development. *Journal of Applied Physics,* 63**,** R13-R57.

Kwon H. W. 1997. Study of the effect of Zr-substitution on the HDDR characteristics of Nd-Fe-B-type alloys. *IEEE Transactions on Magnetics,* 33**,** 3826-3828.

Leonowicz M. 1990. Magnetic properties and microstructure of $Nd_{16}Fe_{76-x}M_xB_8$ magnets (M = Ga, Cr, Nb, Bi, Sn, Zr, W, V, Mo, Mn). *Journal of Magnetism and Magnetic Materials,* 83**,** 211-213.

Liesert S., de Rango P., Soubeyroux J. L., Fruchart D. & Perrier de la B,thie R. 1996. Anisotropic and coercive HDDR Nd-Fe-B powders prepared under magnetic field. *Journal of Magnetism and Magnetic Materials,* 157-158**,** 57-58.

Liu W. L., Liang Y. L., Ma B. M. & Bounds C. O. 1992. Effects of Nb addition and/or casting method on the amount of precipitated Fe in NdFeB alloys. *IEEE Transactions on Magnetics,* 28**,** 2154-2156.

Ma B. M. & Bounds C. O. Year. The impact of the directional solidification on the magnetic properties of NdFeB magnets. *In*, 1991. AIP, 6471-6473.

Ma B. M. & Krause R. F. 1987. *Proc. 5th Intern. Symp. on Magn. Anisotropy and Coercivity in RE-Transition Metal Alloys, Bad Soden***,** 141.

Makita K. & Yamashita O. 1999. Phase boundary structure in Nd-Fe-B sintered magnets. *Applied Physics Letters,* 74**,** 2056-2058.

Matsuura Y., Hirosawa S., Yamamoto H., Fujimura S. & Sagawa M. 1985. Magnetic properties of the $Nd_2(Fe_{(1-x)}Co_x)_{14}B$ system. *Applied Physics Letters,* 46**,** 308-310.

Matzinger M., Fidler J., Fujita A. & Harris I. R. 1996. Microstructure of solid-HDDR Nd-Fe-B:Zr magnets. *Journal of Magnetism and Magnetic Materials,* 157-158**,** 54-56.

McGuiness P. J., Devlin E., Harris I. R., Rozendaal E. & Ormerod J. 1989. A study of Nd-Fe-B magnets produced using a combination of hydrogen decrepitation and jet milling. *Journal of Materials Science,* 24**,** 2541-2548.

McGuiness P. J., Skulj I., Porenta A. & Kobe S. 1998. Magnetic properties and microstructure in NdDyFeBZr-HDDR. *Journal of Magnetism and Magnetic Materials,* 188**,** 119-124.

Mishra R. K., Chen J. K. & Thomas G. 1986. Effect of annealing on the microstructure of sintered Nd-Fe-B magnets. *Journal of Applied Physics,* 59**,** 2244-2246.

Nakamura H., Sugimoto S., Tanaka T., Okada M. & Homma M. 1995. Effects of additives on hydrogenation, disproportionation, desorption and recombination phenomena in $Nd_2Fe_{14}B$ compounds. *Journal of Alloys and Compounds,* 222**,** 136-140.

Narasimhan K. S. V. L. 1981. Higher Energy Product Rare Earth-Cobalt Permanent Magnets. *Fifth International Workshop on Rare Earth-Cobalt Permanent Magnets and Their Application.*

Ogilvy A. J. W., Gregan G. P. & Davies H. A. Year. The Effect of Solidification Rate on the Structure and Magnetic Properties of Iron-Neodymium-Boron Alloys *In:* MITCHELL, I. V., ed. Proc. of a Workshop meeting on Nd-Fe Permanent Magnets, 1984 Brussels 5.

Otsuki E., Otsuka T. & I. I. 1990. *Proc. 11th Int. Workshop on Rare Earth Magnets and Their Applications, Pittsburgh, ,* 1.

Parker R. J. 1990. *Advances in permanent magnetism*, Wiley-interscience publications.

Pollard R. J., Grundy P. J., Parker S. F. H. & Lord D. G. 1988. Effect of Zr additions on the microstructural and magnetic properties of NdFeB based magnets. *IEEE Transactions on Magnetics,* 24**,** 1626-1628.

Rodewald W. 1985. *Proceedings of the Fourth International Symposium on Magnetic Anisotropy and Coercivity in Rare Earth-Transition Metal Alloys*.

Sagawa M., Fujimura S., Togawa N., Yamamoto H. & Matsuura Y. 1984a. New material for permanent magnets on a base of Nd and Fe (invited). *Journal of Applied Physics,* 55**,** 2083-2087.

Sagawa M., Fujimura S., Yamamoto H., Matsuura Y. & Hiraga K. 1984b. Permanent magnet materials based on the rare earth-iron-boron tetragonal compounds. *IEEE Transactions on Magnetics,* 20**,** 1584-1589.

Schneider G., Landgraf F. J. G. & Missell F. P. 1989. Additional ferromagnetic phases in the Fe-Nd-B system and the effect of a 600℃ annealing. *Journal of the Less Common Metals,* 153**,** 169-180.

Schultz L., Schnitzke K., Wecker J., Katter M. & Kuhrt C. 1991. Permanent magnets by mechanical alloying (invited). *Journal of Applied Physics,* 70**,** 6339-6344.

Shaaban A. 2005. *A study of near stoichiometric Nd-Fe-B alloys and magnets.* PhD., University of Birmingham.

Shoemaker C. B., Shoemaker D. P. & Fruchart R. 1984. The structure of a new magnetic phase related to the sigma phase: iron neodymium boride $Nd_2Fe_{14}B$. *Acta Crystallographica Section C,* 40**,** 1665-1668.

Skomski R. & Coey J. M. D. 1999. *Permanent Magnetism*, Institute of Physics Publishing Ltd.

Stadelmaier H. H., Elmasry N. A., Liu N. C. & Cheng S. F. 1984. The metallurgy of the iron-neodymium-boron permanent magnet system. *Materials Letters,* 2**,** 411-415.

Takeshita T. & Nakayama R. 1989. *Proc. 10th Int. Workshop on Rare-Earth Magnets and Applications***,** 551.

Tang W., Zhou S. & Wang R. 1988. On the neodymium-rich phases in Nd-Fe-B magnets. *Journal of the Less Common Metals,* 141**,** 217-223.

Tomida T., Sano N., Hanafusa K., Tomizawa H. & Hirosawa S. 1999. Intermediate hydrogenation phase in the hydrogenation-disproportionation-desorption-recombination process of $Nd_2Fe_{14}B$-based anisotropic magnets. *Acta Materialia,* 47**,** 875-885.

Vial F., Joly F., Nevalainen E., Sagawa M., Hiraga K. & Park K. T. 2002. Improvement of coercivity of sintered NdFeB permanent magnets by heat treatment. *Journal of Magnetism and Magnetic Materials,* 242-245**,** 1329-1334.

Wang S. C. & Li Y. 2005. In situ TEM study of Nd-rich phase in NdFeB magnet. *Journal of Magnetism and Magnetic Materials,* 285**,** 177-182.

Weiss P. 1907. L'hypothèse du champ moléculaire et la propriété ferromagnétique (The hypothesis of the molecular field and the property of ferromagnetism). *J. Phys. (Paris),* 6**,** 661.

Williams A. J., McGuiness P. J. & Harris I. R. 1991. Mass spectrometer hydrogen desorption studies on some hydrided NdFeB-type alloys. *Journal of the Less Common Metals,* 171**,** 149-155.

Wu Y. Q., Ping D. H., Xiong X. Y. & Hono K. 2002. Magnetic properties and microstructures of alpha-Fe/$Nd_2Fe_{14}B$ nanocomposite microalloyed with Zr. 91**,** 8176.

Wyatt O. H. & Dew-Hughes D. 1974. *Metals, Ceramics and Polymers*, Cambridge University Press, London.

Xu Y., Kramer M. J., Wu Y. Q., Dennis K. W. & McCallum R. W. 2006. The mechanism of magnetic properties improvement and microstructure refinement of Zr in $Nd_2Fe_{14}B$. *Journal of Applied Physics,* 99**,** 08B511-3.

Yi G., Chapman J. N., Brown D. N. & Harris I. R. 2000. TEM studies of the effects of Zr additions on some HDDR-processed, high boron, NdFeB-type powders and hot-pressed magnets. *Journal of Magnetism and Magnetic Materials,* 220**,** 115-123.

3   The Electron Microprobe and Microscope

3.0   Introduction

Over the years, scanning electron microscope and electron microprobe designs have tended to converge. A scanning electron microscope provides topographic information by collecting the secondary electrons while electron microprobes are designed to analyse the X-rays emitted from a specimen. Since secondary electrons and X-rays are excited by a focussed electron beam, most SEMs are now equipped with analytical capability. Typically, the spatial resolution of a high resolution SEM is less than 5 nm, but for X-ray analysis the resolution is about 0.5 µm (Lee, 1993).

3.1   Electron Microscopy

Electron microscopes are designed to produce high-resolution topological images of a material. When a focused beam of electrons interacts with the surface of a sample, there are many interactions and many signals are generated, as illustrated in Figure 3.1. Secondary and backscattered electrons are used in SEM imaging, while transmitted electrons are used in transmission electron microscopy. X-rays and Auger electrons can both be used for quantitative chemical analysis in different ways (Lee, 1993).

The information produced from the specimen is generated from different depths of the interaction volume within the specimen, (see Figure 3.2).
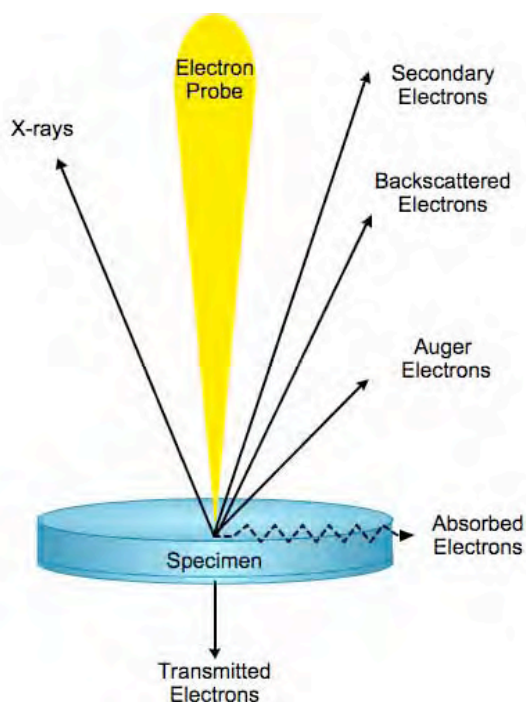
Figure 3.1 Information of the generated signals when a focused beam of electrons interacts with the specimen.
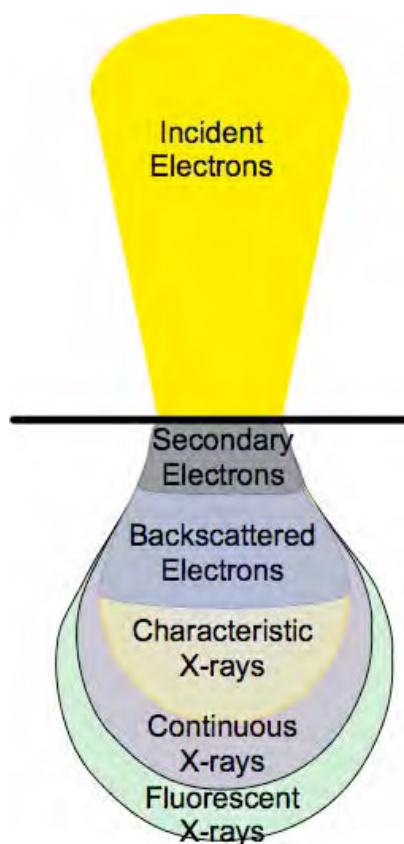
Figure 3.2 Escape depths of different types of signals from a specimen.

3.1.1   Scanning Electron Microscopy

There are two principal types of image formed in a scanning electron microscope: Secondary Electron Images (SEI) and Backscattered Electron Images (BEI) (Reimer, 1988). Secondary electrons have no more then 50 eV of energy and can only escape from a very thin surface layer less than 10 nm in thickness. High energy backscattered electrons can escape from a much greater depth (as shown in Figure 3.2).

The secondary electron signals are produced from the atoms on the top of the sample. The surface morphology of the sample will affect the surface topography contrast.

The backscattered electrons from the surface of the sample are useful for the qualitative identification of phases. Light contrast indicates elements of higher average atomic number; elements with low atomic number appear darker. By using the variation of contrast on the surface of the sample, we can easily determine the distribution of the elemental composition.

3.1.2   Transmission Electron Microscopy

The first TEM was built by Max Knoll and Ernst Ruska in 1932, with this group developing the first TEM with resolving power greater than that of light microscope in 1933; the first commercial TEM was built in 1939. Within the past few decades, TEM has become a very powerful technique for the metallurgist (Williams and Carter, 1996). Transmission electron microscopy (TEM) is a microscopy technique whereby a beam of electrons is transmitted through an ultra-thin specimen, interacting with the specimen as it passes through it. An image formed from the electrons transmitted through the specimen is magnified and focused by an objective lens and appears on an imaging screen, (1) a fluorescent screen in most TEMs, plus a monitor, (2) a layer of photographic film, or (3) is detected by a sensor such as a

CCD camera. Figure 3.3 shows a schematic diagram of a TEM system.

Theoretically, the maximum resolution, d, that one can obtain with a light microscope is limited by the wavelength of the photons used, λ and the numerical aperture of the system, NA.

$$d = \frac{\lambda}{2n\sin\alpha} \approx \frac{\lambda}{2NA}$$ Equation 3-1

Early twentieth century scientists theorized ways of getting around the limitations of the relatively large wavelength of visible light (wavelengths of 400~700nm) by using electrons. Like all matter, electrons have both wave and particle properties (as suggested by Louis-Victor de Broglie) and their wave-like properties mean that a beam of electrons can be made to behave like a beam of electromagnetic radiation (Williams and Carter, 1996). The wavelength of the electrons is given by the de Broglie equation. An additional correction must be made to account for relativistic effects, as in a TEM an electron's velocity approaches the speed of light, c.

$$\lambda_e = \frac{h}{\sqrt{2m_0 E(1 + \frac{E}{2m_0 c^2})}}$$ Equation 3-2

Electrons are usually generated in an electron microscope by thermionic emission from a filament, usually tungsten, in the same manner as in a light bulb, or by field emission. The electrons are then accelerated by an electric potential (measured in volts) and focused by electrostatic and electromagnetic lenses onto the sample. The transmitted beam contains information about electron density, phase and periodicity; this is used to form an image.
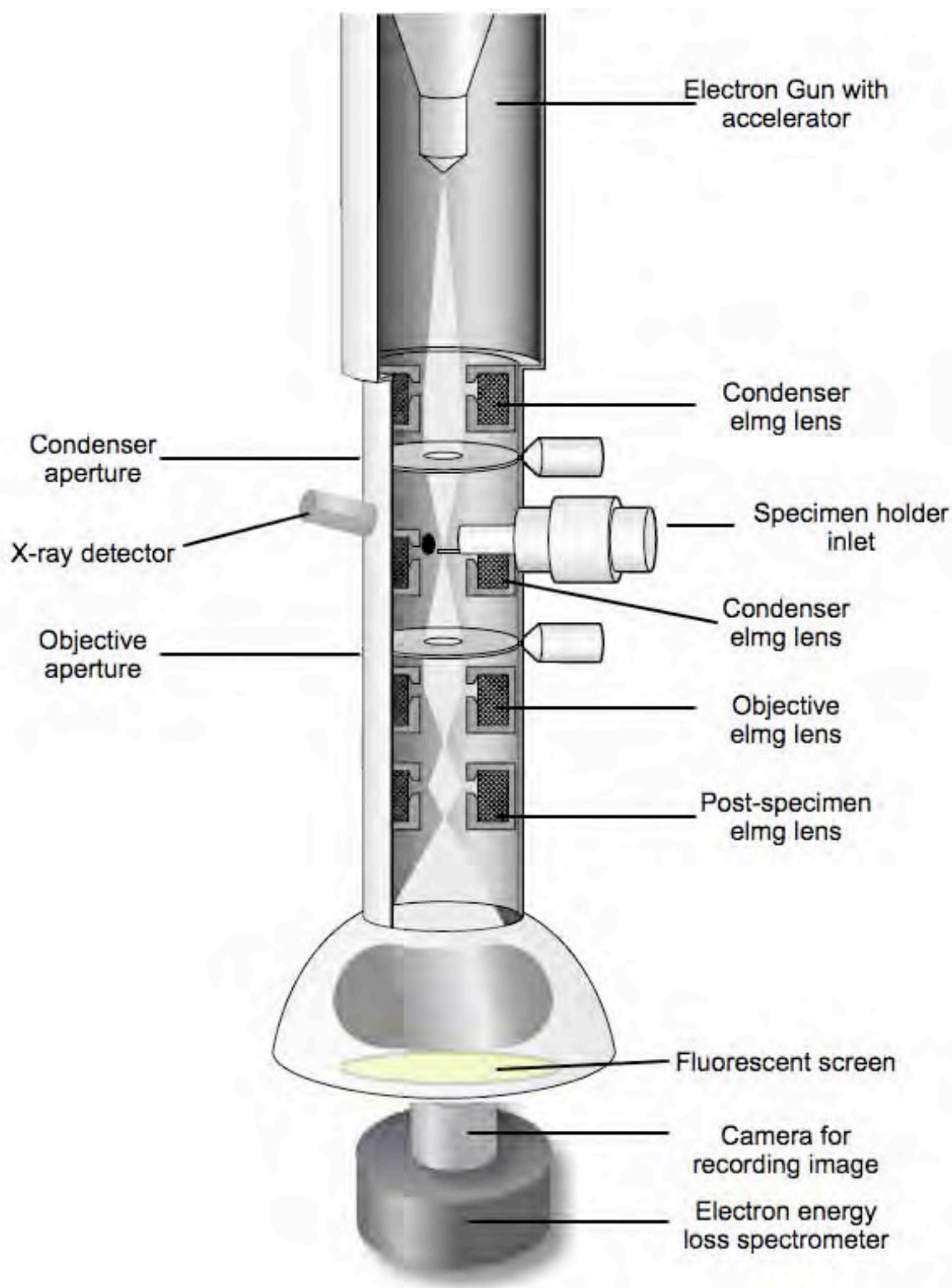
Figure 3.3 A schematic diagram of a TEM. (elmg lens: Electromagnetic lens)

3.1.2.1   Beam Formation

From the top down, the TEM consists of an emission source, which may be a tungsten filament, or a lanthanum hexaboride (LaB_6) source. For tungsten, this will be in the form of either a hairpin-style filament, or a small spike-shaped filament. LaB_6 sources utilize small single crystals. By connecting this gun to an HV source (typically ~120kV for many applications) the gun will, given sufficient current, begin to emit electrons into a vacuum (Williams and Carter, 1996). This extraction is usually aided by the use of a Wehnelt cylinder. The upper lenses of the TEM allow for the formation of the electron probe of the desired size and location for later interaction with the sample.

Manipulation of the electron beam is performed using two physical effects. The interaction of electrons with a magnetic field will cause electrons to move according to the right hand rule, thus allowing electromagnets to manipulate the electron beam. The use of magnetic fields allows for the formation of a magnetic lens of variable focusing power, and hence the lens shape is due to the distribution of magnetic flux. Additionally, electrostatic fields can cause the electrons to be deflected through a constant angle. Coupling two deflections allows for the formation of a shift in the beam path, which is used in TEM for beam shifting: this is extremely important to STEM. From these two effects, as well as the use of an imaging system (such as a phosphor screen), sufficient control over the beam path is possible for TEM operation.

The lenses of a TEM allow for beam convergence, the angle of which can be varied, giving the TEM the ability to change magnification simply by modifying the amount of current that flows. Typically a TEM consists of three stages of lensing, with many possible variations on lens configurations. The stages are the condenser lenses, the objective lenses and the

projector lenses. The condenser lenses are responsible for primary beam formation, whilst the objective lenses focusses the beam down onto the sample itself. The projector lenses are used to expand the beam onto the phosphor screen or other imaging device, such as film. The magnification of the TEM is due to the ratio of the distances between the specimen and the objective lens image plane.

3.1.2.2 Contrast Formation

Contrast formation in the TEM depends greatly on the mode of operation. Complex imaging techniques that utilize the ability to change lens strength or to deactivate a lens allow for many operating modes. These modes may be used to determine the information that is of particular interest to the investigator.

-Bright field image

Bright field imaging is a common imaging mode in TEM operation. In this mode, the contrast formation is formed directly by occlusion and absorption of electrons in the sample when considered classically. The image will appear dark in a thicker area or a region with a higher atomic number; meanwhile regions with no sample in the beam path will appear bright - hence the term "bright field".

-Diffraction contrast

The reason for diffraction contrast is that the electron beam undergoes Bragg scattering, which in the case of a crystalline sample disperses electrons into discrete locations in the back focal plane. By the placement of apertures in the back focal plane, i.e. the objective aperture, the desired Bragg reflections can be selected (or excluded) and the parts of the sample that are causing the electrons to scatter to the selected reflections will show contrast.

If the reflections that are selected do not include the unscattered beam (which will appear at the focal point of the lens), then the image will appear dark wherever no sample scattering to the selected peak is present; as such a region without a specimen will appear dark, this is known as a dark-field image.

TEMs are often equipped with a goniometer stage that allows the user to tilt the specimen to a range of angles in order to obtain specific diffraction conditions. Moreover, a set of selection apertures, placed above the specimen, allows the user to acquire a diffraction pattern from a specific area.

3.1.2.3 Diffraction

In a TEM, a thin crystalline specimen is subjected to a parallel beam of high-energy electrons. As TEM specimens are typically ~100nm thick, and the electrons typically have an energy of 100-400 keV, the electrons pass through the sample easily. In this case, electrons are treated as wave-like, rather than particle-like. Because the wavelength of high-energy electrons is a fraction of a nanometre, and the spacing between atoms in a solid are only slightly larger, the atoms act as a diffraction grating for the electrons, which are thus diffracted. That is, some fraction of them will be scattered to particular angles, as determined by the crystal structure of the sample, while others continue to pass through the sample without deflection.

For thin crystalline samples, these scattered electrons produce an image that consists of a series of dots (diffraction pattern) in the case of a single crystal, or a series of rings in the case of a polycrystalline material. For the single crystal case, the diffraction pattern is dependent upon the orientation of the specimen. The information of the space group symmetries in the crystal and crystal's orientation can be carried out from the Kikuchi line. This is typically done without utilizing any information other than the position at which the diffraction spots appear

and the observed image symmetries.

Diffraction patterns in the crystalline sample may have a large dynamic range with great intensities. By using a CCD camera or film cartridge, an image of the diffraction patterns can be obtained.

Analysis of diffraction patterns beyond simple point positions can be complex, as the image is sensitive to a number of factors such as specimen thickness and orientation, objective lens defocus and spherical and chromatic aberration. Although quantitative interpretation of the contrast shown in lattice images is possible, it is inherently complicated and can require extensive computer simulation and analysis. More complex diffraction behaviour is also possible, with phenomena such as Kikuchi lines or convergent beam electron diffraction (CBED) providing additional information, beyond structural data, such as sample thickness (Williams and Carter, 1996).

3.1.2.4　HAADF Imaging or Z-Contrast Microscopy

The diffraction effects in annular dark field (ADF) images of crystalline materials can be greatly suppressed by increasing the inner collection angle of the ADF detector beyond the Bragg reflections so that only high-angle scattered electrons contribute to the collected signal (see Figure 3.4). This imaging mode is called HAADF or Z-contrast microscopy. The inner collection angle, $\beta 1$, is the most critical parameter in determining the nature of the HAADF images; the outer collection angle, $\beta 2$, is generally made large enough to collect more high-angle scattered signals.

In HAADF imaging, diffraction and phase contrast are significantly suppressed and the compositional sensitivity is improved; but, the signal strength is greatly reduced. The

development of HAADF imaging has proved very successful for characterizing small particles and supported metal catalysts with sub-nanometre or atomic resolution and high compositional sensitivity (Liu, 2005). Thus, small metal or alloy nanoparticles in high surface-area supports can always be easily revealed by its contrast difference resulting from composition difference through HAADF images.
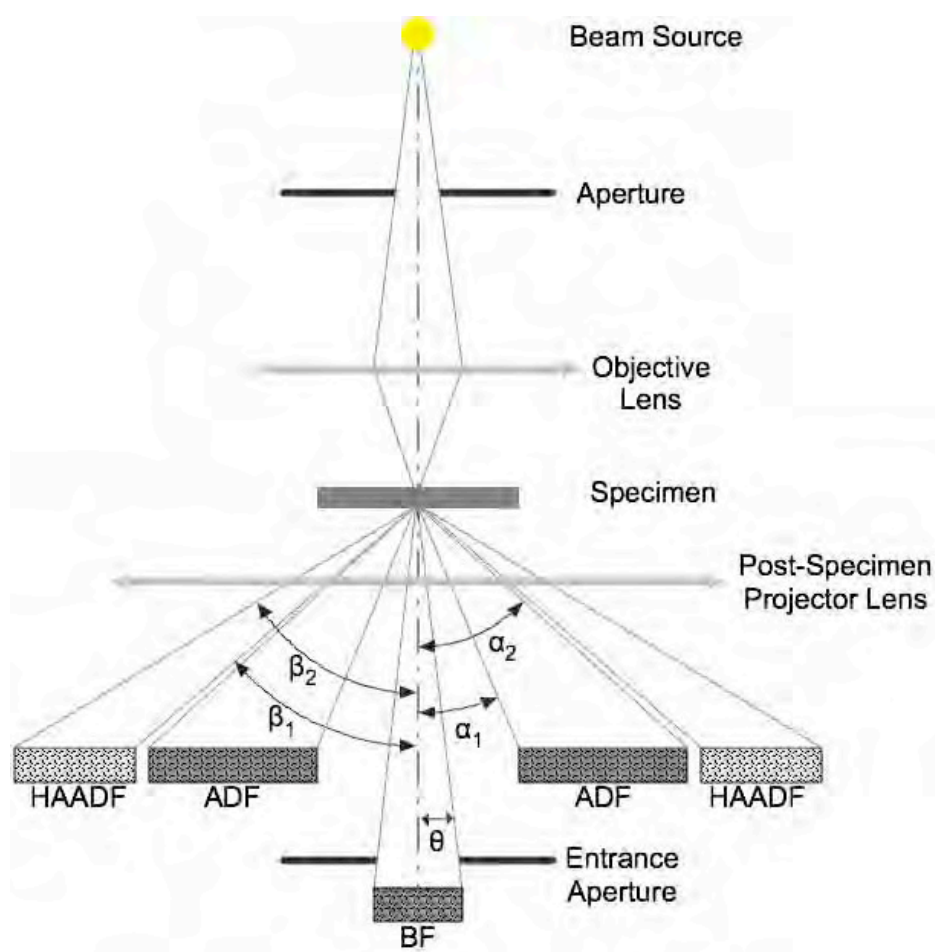
Figure 3.4 Schematic diagram of the geometric arrangement of BF, ADF and HAADF detectors.

3.2 Electron Probe Micro Analysis

The information produced from the specimen is generated from different depths within the specimen (see Figure 3.2). The X-rays produced, within an excited volume of several

microns on and below the surface, are used for electron probe microanalysis (Jones, 1992).

X-ray emission lines are produced by transitions between inner atomic energy levels. For such a transition to be possible, a vacancy must be produced by the ejection of an inner electron. In electron probe micro analysis, an inner level ionization of an inner level electron is required as result of bombardment by the incident electrons (see Figure 3.5). For instance, if the initial ionisation was in the innermost atomic shell (the K shell), the resulting X-ray emission is identified as K radiation. The K spectrum contains several lines due to transitions from different levels in the L, M etc. shells, which contain electron orbits of increasing mean radius and decreasing binding energy. The L shell consists of three subshells (L_{1-3}), while the M shell includes five (M_{1-5}). The principal K line, designated $K_{\alpha 1,}$ is produced by an L_3-K transition (Lee, 1993, Reed, 2005).

The quantum energy of the emitted radiation is equal to the difference between the potential energy of the state of the atom in its initial and final states. Many emissions of this type create a line upon the X-ray spectrum. These X-ray line emissions are known as "Characteristic radiation" because the wavelengths of lines are specific to the emitting elements. Hence, from the wavelength and intensity of the lines in the X-ray spectrum, the elements present may be identified and their concentrations determined.

Besides characteristic radiation, a continuous X-ray spectrum or 'bremsstrahlung' (braking radiation) is also emitted during electron bombardment. Continuous radiation consists of photons emitted by electrons decelerated by nuclei collisions.
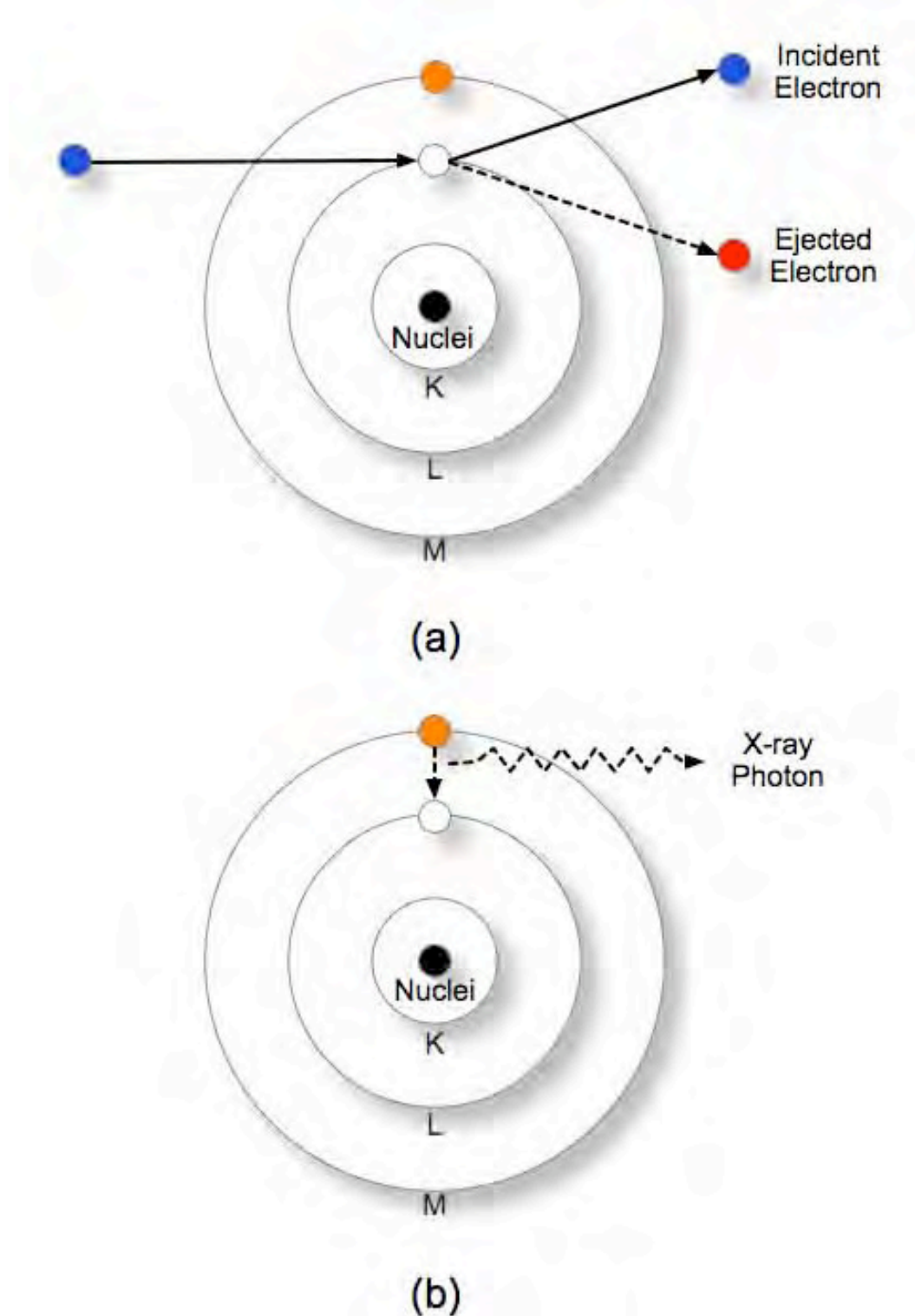
Figure 3.5 An illustration of the Characteristic X-ray production. (a) Removal the inner electron by X-ray bombardment, (b) Emission of X-ray Photon due to electron transition between shells.

3.2.1 Energy Dispersive X-ray (EDX) Analysis

In Energy Dispersive Spectroscopy, the energy of the X-rays is used to produce electron-hole pairs in a semiconductor crystal and the signal is used to produce a spectrum.

An EDS system consists of three basic components (X-ray detector, Pulse Processor and Analyzer) that must be designed to work together to achieve optimum results. The X-ray detector detects and converts the x-rays into electronic signals. The Pulse Processor measures the electronic signals to determine the energy of each X-ray detected. The analyser displays and interprets the X-ray data (Lee, 1993).
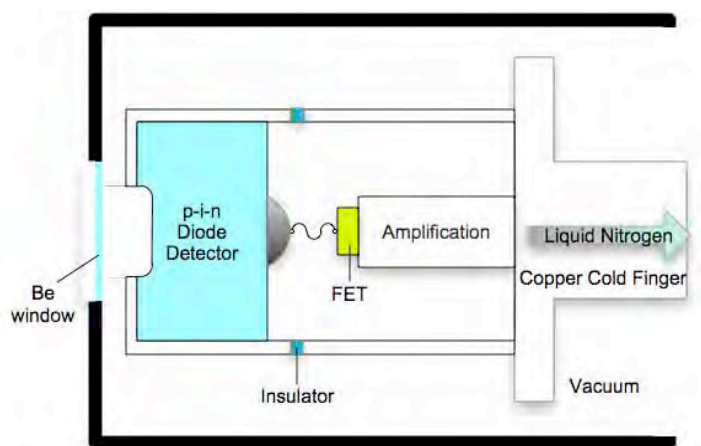
Figure 3.6 Schematic diagram of an EDX detector

In an EDX detector (as shown in Figure 3.6), the incoming X-ray passes through a window that provides a barrier to maintain the vacuum and stop light within the detector whilst being as transparent as possible to low energy X-rays. There are two main types of window materials, Beryllium and polymer-based thin windows. Beryllium (~8μm thick) is highly robust and has a relatively low absorption coefficient. However, light element radiation (< 1keV) will be absorbed [Reed, 1993]. Polymer-based thin windows can be made much thinner than Be windows and are therefore transparent to much lower energy X-rays down to 100eV (Oxford Instruments-technical briefing, 2008a, Oxford Instruments, 2008a).
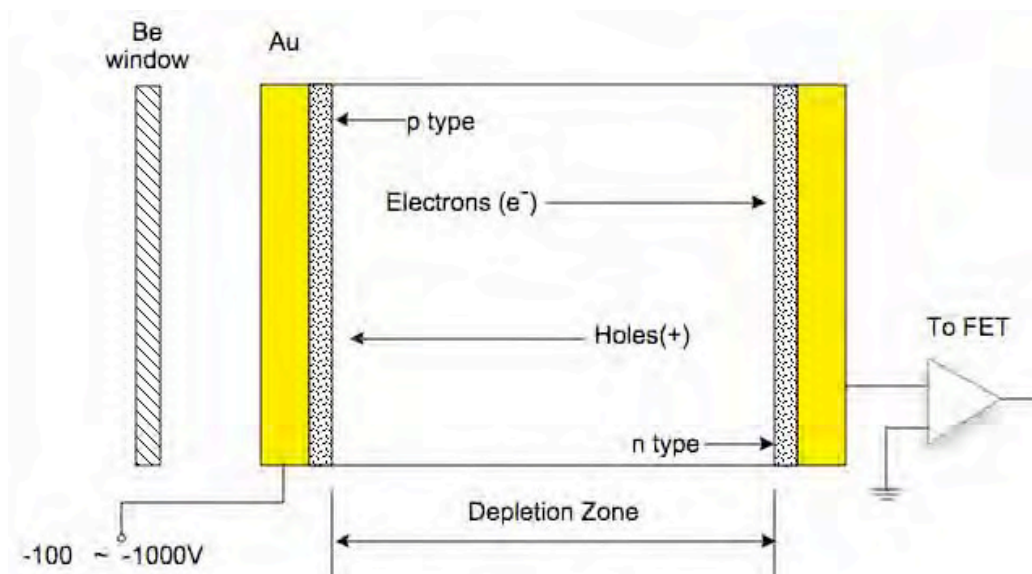
Figure 3.7 Schematic diagram of a p-i-n detector

The EDS detector converts the energy of each individual X-ray into a voltage signal of proportional size via a semiconductor. The X-ray detection medium is a p-i-n detector (Figure 3.7) (either silicon or germanium) in which the valence band is normally fully occupied by electrons. The valence and conduction bands are separated by an energy gap (1.1eV for Si; 0.7eV for Ge). When an X-ray photon is absorbed, it generates Auger electrons and photoelectrons, which dissipate their energy partly by raising valence electrons to the conduction band. The arrival of each photon thus creates a brief pulse of current caused by electrons in the latter and holes in the former, moving in opposite directions under the influence of the bias voltage applied to the detector.

At the operating temperature of the detector, the mean energy used in generating an electron-hole pair is 3.8eV for Si (2.9eV for Ge). The size of the output pulse is based on the number of such pairs, which is given by the X-ray energy divided by the mean energy (Reed, 2005). Hence, a 6.3996 keV Zr K_α photon, for example, produce an average of 1668 electron-hole pairs in a Si detector (the actual numbers are subject to some statistical fluctuation).

Two main materials are used for the p-i-n diode detectors, Silicon and Germanium. In order to reduce the undesirable effects caused by the impurities contained even in highly refined silicon, lithium is introduced to compensate for small levels of impurities by using a process known as 'drifting'. Hence, the name 'lithium–drifted silicon' or 'Si(Li)' detector. High purity germanium (HpGe), which does not require the addition of Li, is also used. Si(Li) was the first material used in EDS detectors and remains the most common choice today. HpGe offers performance advantages when measuring higher energy X-rays.

The charge pulses generated by the p-i-n detector are then passed through a field effect transistor (FET) for amplification. This charge is converted into a voltage signal by the FET preamplifier. The FET is positioned just behind the detecting crystal. It is the first stage of the amplification process that measures the charge liberated in the crystal by an incident X-ray and converts it to a voltage output. Finally, the voltage signal is input into the pulse processor for measurement. The output from the preamplifier is a voltage 'ramp' where each X-ray appears as a voltage step on the ramp. The height of an amplified, shaped pulse is then a measure of the energy of the incident X-ray photon. A multi-channel analyser processes the pulses to produce a distribution chart of wavelength against the number of counts. Since the amplification and pulse shaping takes about 10μs, if a second pulse arrives too soon either a sum peak will be generated or both pulses will be rejected by the 'pulse pile-up rejection' system (Williams, 1968). This results in a significant dead time for most count rates.

Both the p-i-n diode detector and FET are kept cold by liquid nitrogen. The reason for this is to protect the detector from damage resulting from warming up while the bias voltage is on.

EDX is only suitable for the quantitative analysis of non-light elements (down to Z=4),

which produce higher energy X-rays. Unlike wavelength dispersive X-ray (WDX) analysis, the total spectrum of interest (0-30 keV) is recorded simultaneously.
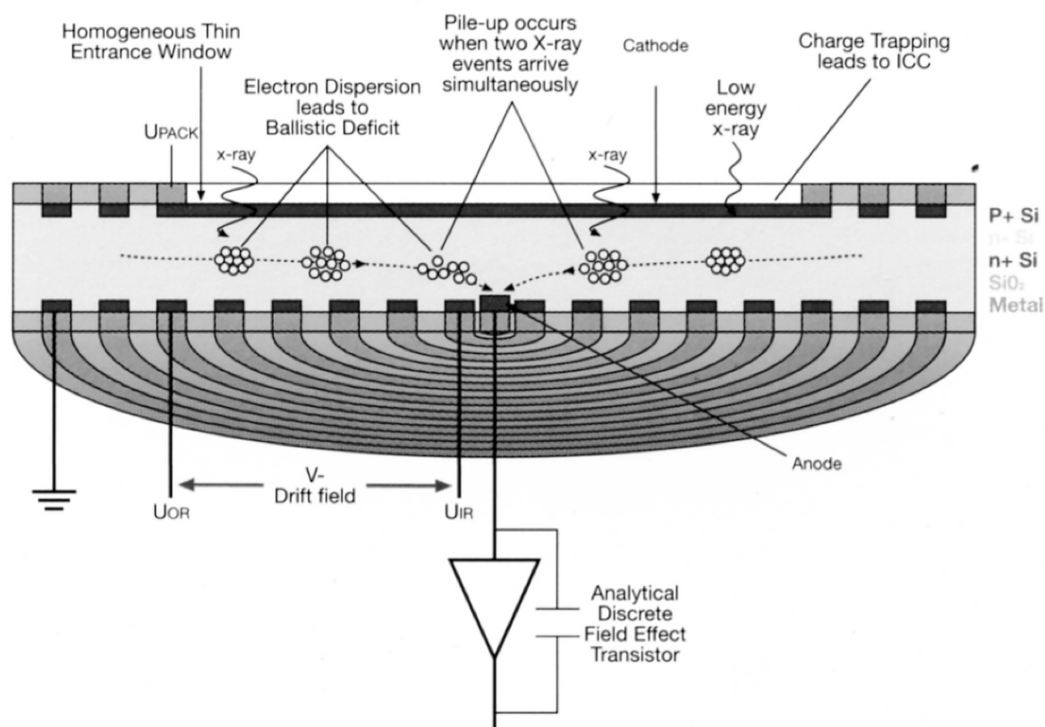
Figure 3.8 Schematic diagram of cross-section of a radial SDD detector.

The more well-developed detector is the silicon drift detector (SDD). The basic physical principle of operation of this detector is exactly the same as the standard detector. The difference is in the structure of the detector crystal itself, which was proposed by Gatti (Gatti and Rehak, 1984) . Instead of a very carefully maintained uniform electric field generated by the front and back electrodes, the SDD has a series of concentric electrodes designed to generate a controlled field shape in the crystal, steering the charge towards a very small collector electrode in the centre (Figure 3.8). Because the collector electrode is very small, its capacitance is far lower than that of the standard detector, which means that the system noise is much lower (thus, the energy resolution is good for soft X-rays), and the amplifier time constant can be reduced. In turn, this means that the detector is capable of much higher count

rates than the standard detectors. It also means that the detector need not be run at a low temperature as the Si (Li) detector.

Nowadays, the largest active area of a SDD detector can be up to 80 mm^2 (Oxford Instruments-technical briefing, 2009), which means the detector can acquire more counts in a short time with less beam damage, contamination and better spatial resolution.

3.2.2   Wavelength Dispersive X-ray (WDX) Analysis

In wavelength dispersive spectroscopy, the wavelength of the X-rays is measured. The wavelength of X-ray photons is related to the energy according to Planck's Law:

$$E = \frac{hc}{\lambda}$$

Equation 3-3

where E = energy of the X-ray Photon

h = Planck's constant = $6.6262 * 10^{-34}$ J $*$ s

λ = wavelength of the X-ray photon

c = speed of light = $3.0 * 10^8$ m/s

According to Planck's Law, there is an inverse relationship between energy and wavelength; the greater the energy, the shorter the wavelength. X-ray wavelengths commonly measured using wavelength dispersive spectroscopy vary from 0.1 to 10.0 nm (Reed, 2005).

3.2.2.1 Diffraction

In wavelength dispersive spectroscopy, the wavelengths of the X-rays are commonly separated with a crystal that diffracts certain specific wavelengths onto a detector. The crystal

has a basic pattern of atoms that is repeated in three dimensions, which means that the crystal has the same distance between parallel lattice planes (same d-spacing).

3.2.2.2   Crystals

When the X-rays emitted from each element enter the lattice of a crystal, they are scattered by the electrons in the crystal. In Figure 3.9, two incoming monochromatic X-rays striking the same plane of a crystal in two different places will result in diffraction. No matter whether the incoming monochromatic X-rays strike the same lattice plane or not, if two X-rays are diffracted at the same angle, this will cause the reinforcement of the waves (Figure 3.10). General reinforcement will occur when Bragg's law is satisfied.

$$n\lambda = 2d\sin\theta \qquad\qquad\qquad \text{Equation 3-4}$$

where λ = wavelength of the diffracted X-rays

d = interplanar spacing of the crystal

θ = the angle between the crystal surface and the incident and diffracted X-rays

n = integer (whole number)

The smaller the spacing of the atomic planes in the crystal (d), the higher is the angle of diffraction of the X-rays. A wavelength dispersive spectrometer cannot measure all the X-rays from 0.1 to 1.0 nm with one kind of crystal. Therefore, wavelength dispersive spectrometers in SEM usually have more than one crystal spectrometer so that a more complete spectrum of wavelengths can be obtained (Lee, 1993, Garratt-Reed and Bell, 2003).
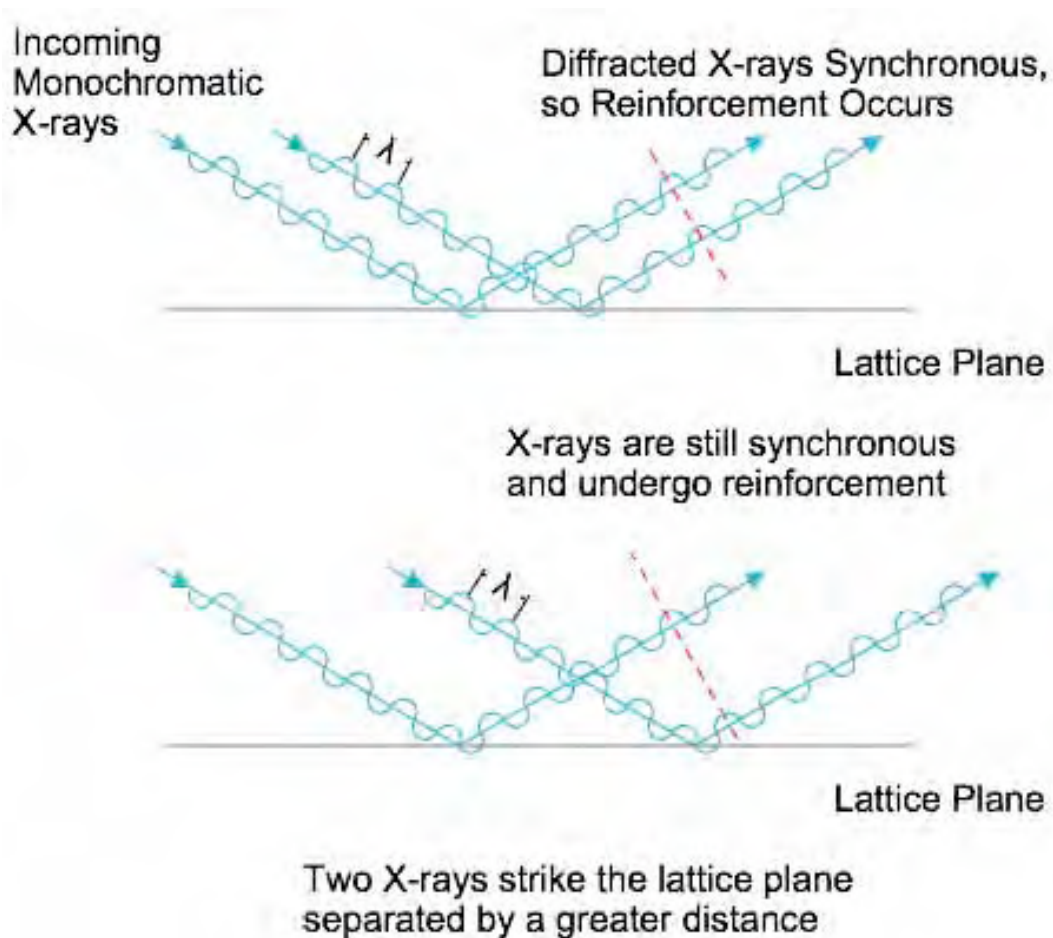
Figure 3.9 The diffraction of X-rays and reinforcement
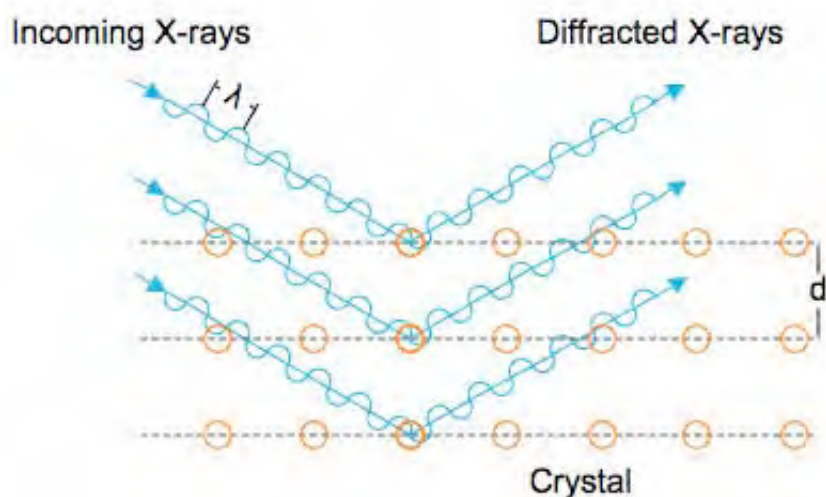
Figure 3.10 X-rays striking a crystal interact with a number of successive lattice planes. The X-rays will be diffracted only if they strike the crystal at the correct angle.

Table 3.1 The crystals commonly used in a WDX system (Oxford Instruments-technical briefing, 2008b, Oxford Instruments, 2008b).

Crystal Designation	Crystal Type	2d Spacing, Å	Analyzing Range, Å	Analyzing Range, eV	Element Range Kα
LIF(220)	Lithium Fluoride	2.8473	0.8087 - 2.6306	15,330 - 4,712	V to Y
LIF(200)	Lithium Fluoride	4.0267	1.1436 - 3.7202	10,841 - 3,332	Ca to Ge
PET	Pentaerythritol	8.74	2.4827 - 8.0765	4,994 - 1,535	Si to Ti
TAP	Thallium acid phthalate	25.75	7.3130 - 23.79	1,695 - 521.2	O to Si
LSM-060	W-Si	~61	~17 - ~56	~729 - ~221	C to F
LSM-080	Ni-C	~78	~22 - ~72	~564 - ~172	B to O
LSM-200	Mo-B_4C	~204	~58 - ~190	~214 - ~65	Be and B

Table 3.1 lists some of the crystals used in a WDX system. Basically, there are four kinds of analysing crystals commonly used, which are layered synthetic microstructures (LSM), thallium acid phthalate (TAP), pentaerythritol (PET) and lithium fluoride (LiF). Each crystal is designed for a different range of wavelengths. LSM crystals are constructed from alternating layers of low atomic number (B, C) and high atomic number (Hf, W, Re, Os) atoms, only a few nanometres thick, deposited on a rigid substrate which is usually silicon. The use of these crystals improves the count rate and peak to background ratios that can be attained and suppresses any higher order reflections.

No matter that the crystal spectrometers satisfy the Bragg condition across the entire surface of the crystal, the sample, crystal and the X-ray detector must be located in a specific curve called the Focusing circle or Rowland circle as shown in Figure 3.11 (Won, 1998).
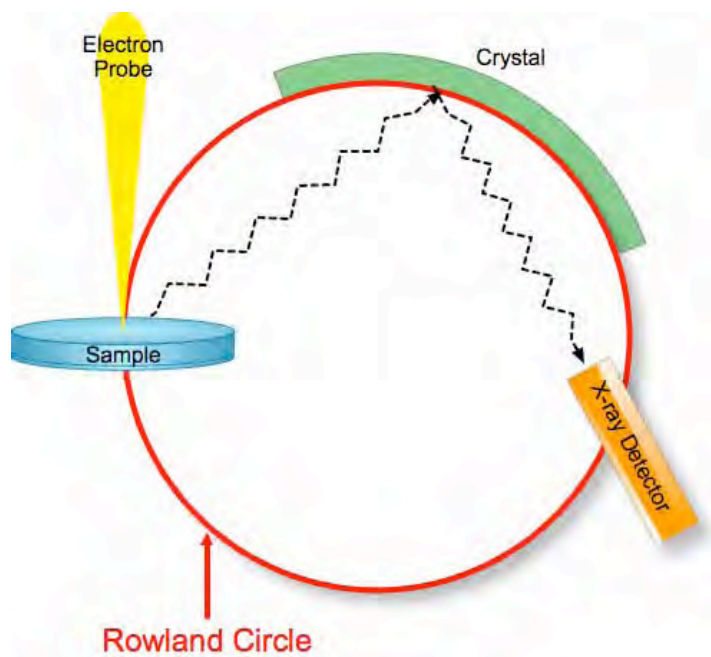
Figure 3.11 Schematic diagram of the Focussing circle or Rowland circle

There are two types of crystal geometry in use today. In the first, called the Johann geometry, the diffracting crystal is bent to a radius of 2R, where R is the radius of the Rowland circle (Figure 3.12) (Johann, 1931). The second, called the Johansson geometry, is more precise. It has the crystal bent to radius 2R and then ground to radius R, so that all of the points of reflection lie on the Rowland circle (Figure 3.13) (Johansson, 1933). Due to the difficulty in grinding the crystal for both PET and TAP, the Johann geometry (where the entire surface of the crystal does not lie on the Rowland circle) is generally used in practice (Reed, 1996).
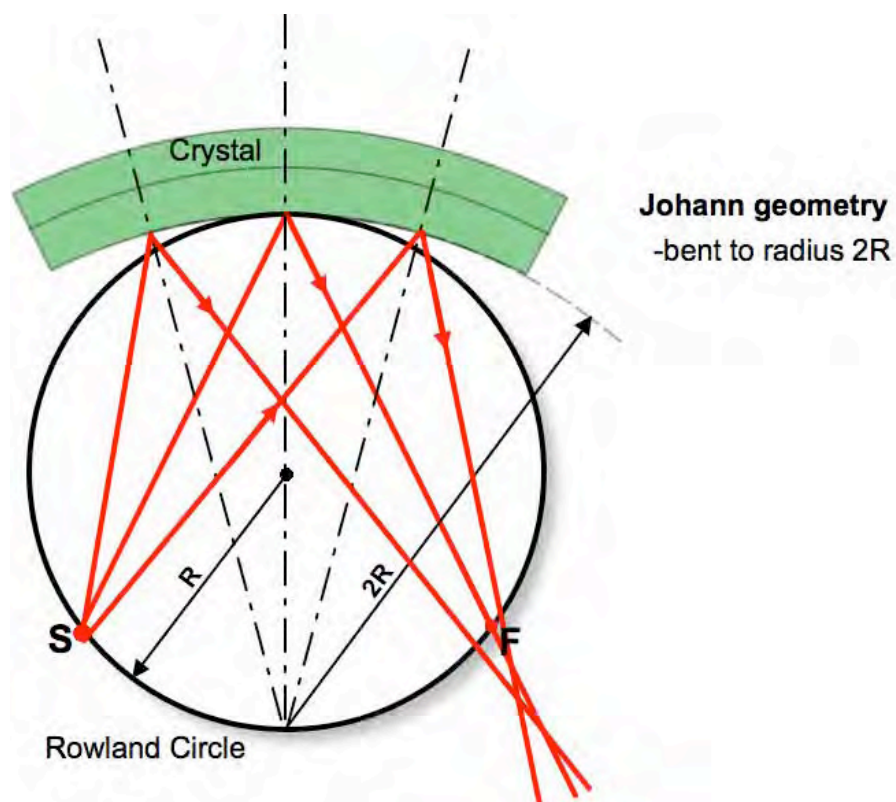
Figure 3.12 Schematic diagram of the Johann geometry (S: source; F: focus).
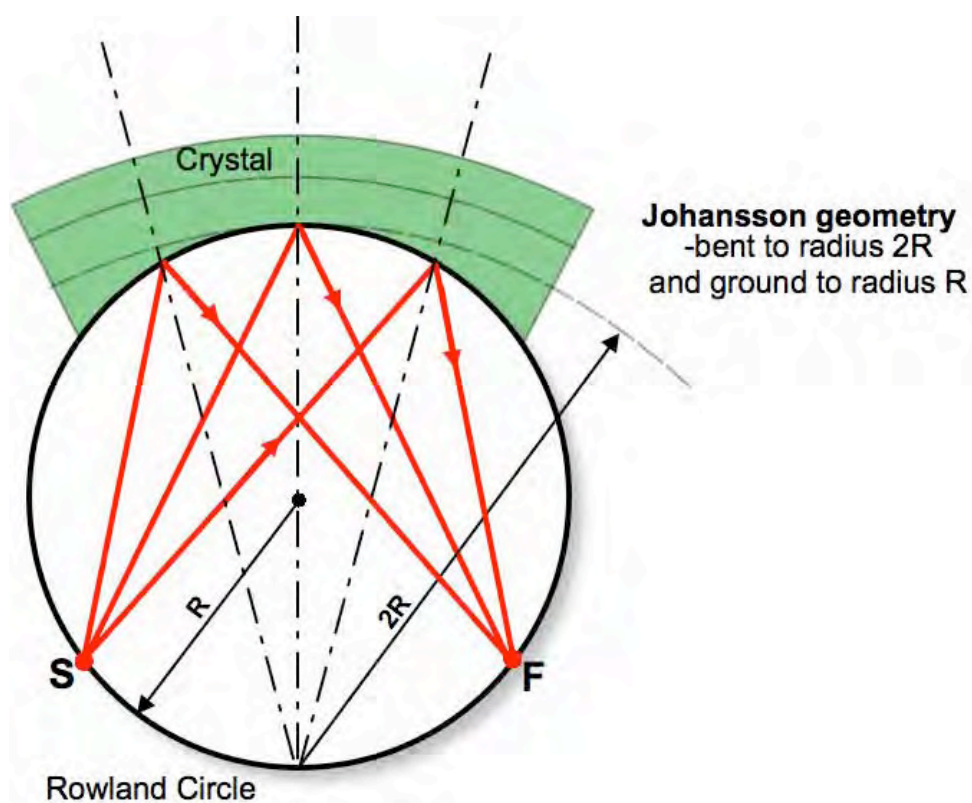
Figure 3.13 Schematic diagram of the Johansson geometry (S: source; F: focus).

3.2.2.3　Detector

For WDX analysis the detector is usually a gas-flow proportional counter, as shown in Figure 3.14. Generally, X-ray photons are diffracted into the detector through a collimator (receiving slit), entering the counter through a thin window. They are then absorbed by atoms of the counter gas. A photoelectron is ejected from each atom absorbing an X-ray. The photoelectrons are accelerated to the central wire causing further ionization events in the gas, so that an "avalanche" of electrons drawn to the wire produces an electrical pulse. The detector potential is set so that the amplitude of this pulse is proportional to the energy of the X-ray photon that started the process.
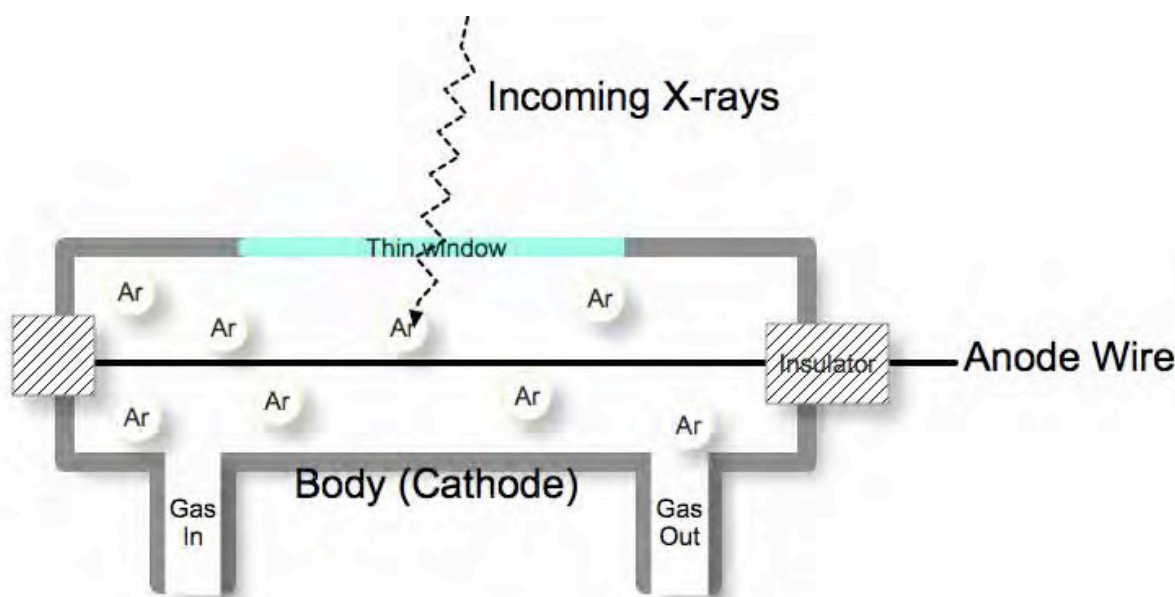
Figure 3.14 Schematic diagram of the gas-flow proportional counter used as an X-ray detector in a WDX system.

Electronic pulse height analysis is subsequently performed on the pulses to filter out noise. There are two types of gas proportional counters: sealed (SPC) and gas flow (FPC). Generally, SPCs are used for high-energy X-ray lines, while FPCs are used for low energy lines (Oxford Instruments, 2008b, Oxford Instruments-technical briefing, 2008b).

Sealed proportional counters have a relatively thick window (e.g. beryllium, ~50μm thick), in order to prevent leakage of the gas (usually xenon or a xenon-CO_2 mixture) which is sealed into the detector. Gas flow proportional counters commonly use ultrathin (0.5-1μm thick) mylar or polypropylene windows, and the counter gas (known as P-10: argon with 10% methane) flows through the detector at a constant rate.

WDX spectrometers determine the intensity of X-rays for a given wavelength. Compared with EDX analysis, WDX analysis has better resolution but has the considerable disadvantage of monochromatic spectrometry and so EDX counting is more efficient. EDX analysis is generally used in preference except when there are resolution problems. For light element analysis, however, due to the absorption problems caused by the window in the EDX detector and the superior resolution of WDX analysis, WDX analysis is better.

3.2.3 Conditions for Electron Probe Microanalysis

3.2.3.1 Electron Beam Operating or Acceleration Voltage

The main considerations in selecting an optimum acceleration voltage are the X-ray excitation efficiency and the penetration of the incident electrons into the specimen. The accelerating voltage must be greater than the critical excitation energy for an X-ray line to be emitted and the intensity of X-rays emitted depends upon how much greater it is.

However, electron penetration increases rapidly with increasing acceleration voltage, causing deterioration of the spatial resolution. Therefore, an optimum acceleration voltage for all the elements in the detecting sample is required. The typical range of operating voltages used for EPMA is 5-25 keV (Reed, 2005).

3.2.3.2 Probe Current and Probe Current Drift

Increasing the probe current increases the detected count rate, but this also increases the probe diameter. Thus a compromise must be found to provide a high-count rate without causing unsatisfactory spatial resolution.

Probe current drift is usually caused by variations in the lens or gun supply voltages, electrostatic charging of the insulating material in the column, aperture contamination and inadequate conduction by the specimen. As the count rate is dependent upon the probe current, probe current drift will cause the analysis to be unreliable. Therefore, during quantitative analysis, the probe current should be measured frequently and, periodically, adjusted to a constant value.

3.2.3.3 Specimen Condition

Optimum specimen preparation is extremely important for quantitative analysis. Any irregularities due to polishing defects will cause unwanted scattering and diffraction, changing the x-rays travel distance through the specimen and thus changing the magnitude of the absorption.

Besides, any non-recently polished specimens may have a degree of surface oxidation. It has been reported that surface adsorption of oxygen is unavoidable for all the materials although an approach for correcting the oxygen analysis has been proposed (Goldstein et al., 1993). Therefore, a recently polished (fresh) specimen is always required for WDX.

3.2.3.4 Standards

Elemental or compound standards are used to calibrate the electron microprobe. By comparing the intensity of an element peak from the specimen with that of a standard of known

composition, an intensity fraction (K-ratio) is obtained. A ZAF correction is then used to convert the measurement into quantitative data (Philibert and Tixier, 1968).

For convenience, elemental peaks in EDX analysis are commonly characterised by a pre-calibration procedure using standards. For WDX analysis, however, it is necessary to calibrate the elemental peak under consideration, on an appropriate standard, for each set of results.

Standards should be chosen for their stoichiometry, homogeneity, resistance to electron bombardment and similarity in composition to the compound being analysed. Similar considerations for the surface of the standard as for the specimen are also required. All these requirement can reduce the magnitude of errors caused by the corrections of the ZAF process and the peak shape change (Garratt-Reed and Bell, 2003, Reed, 2005).

WDX analysis is suitable for analysing the light elements. The difference from Energy dispersive X-ray (EDX) analysis is that in WDX each individual spectrum of interest is recorded using different crystals in the WDX system. Moreover, a standard database that came from the similar texture with the detecting sample is required in the WDX analyses. Otherwise, WDX analysis may exhibit differences in the peak wavelength between standards and specimen, owing to chemical bonding effects, thus causing significant errors (Reed, 2005).

3.2.4 ZAF Corrections

ZAF correction (atomic number-absorption-fluorescence) is the most widely used correction scheme for EPMA. In an ideal condition, the basic scheme for the composition of element i in the sample, C_i, which is applicable to polished, flat, homogeneous samples can be expressed as follows:

$$C_i = \frac{I_i}{I_{(i)}}$$ Equation 3-5

where I_i: the measured characterstic X-ray intensity from element i, (from sample)

   $I_{(i)}$: the intensity from a pure sample of the element under ideal conditions

In order to obtain the "true" concentration from the uncorrected concentration, Castaing (1951) suggested that three main factors, ZAF, should be applied to the Equation 3-5 (Garratt-Reed and Bell, 2003). Starting from the composition so derived, a correction is applied to compensate for the different X-ray generation (influenced by the electron penetration and backscattering) because the mean atomic number, Z, of the sample is different from the pure element; from the depth distribution is computed an absorption correction, A; and a fluorescence correction, F, is applied, so that

$$C_i = [Z.A.F.]\frac{I_i}{I_{(i)}}$$ Equation 3-6

3.2.4.1 Z: Atomic Number Corrections

The efficiency of excitation of characteristic X-rays depends on the mean atomic number of the specimen, which is related to two distinct phenomena - electron penetration and backscattering. The penetration depth of incident electrons is determined by the rate of energy loss, known as " stopping power", which is defined as $-dE/d(\rho s)$, where E is the exciting energy for the X-ray photon, ρ is the density of the specimen and s is the distance the electrons travel, which decreases with increasing Z (Reed, 2005). The generated X-ray intensity (per unit concentration) is dependent on the mass penetrated and therefore increases with Z. The correction for the loss of X-ray intensity due to electron backscattering is related to the electron backscattering factor η (the fraction of incident electrons that leave the specimen), which

increases rapidly with Z. In the combined "atomic number correction", these two factors effectively counterbalance each other but overall are dominated by the backscattering term. Therefore, when the sample has a higher mean atomic number than the standard, the concentration must be corrected upward.

3.2.4.2   A: Absorption Corrections

Absorption corrections are used to adjust for the difference in the absorption of X-rays by the specimen. When characteristic X-rays are generated throughout the volume of penetration of the electron beam in the specimen, a significant number of the X-rays are re-absorbed by the specimen atoms and do not exit the specimen. The amount of reabsorption of X-rays is determined largely by the accelerating voltage of the electron beam and by the density of the specimen. These determine the shape and the size of the volume in the specimen where X-rays are generated (Lee, 1993). The X-rays produced over a range of depths can be expressed by the depth distribution function, $\varphi(\rho z)$, where ρ is the density of the specimen and z is the depth where the X-rays are produced. In the classical ZAF correction method, $\varphi(\rho z)$ is represented by a simple approximate expression, which gives satisfactory results provided that the absorption is not less than about 0.5. Nowadays, the complicated interactions between electron beam and sample can be acquired from the CASINO simulation program, which is based on a single-scattering algorithm and Monte Carlo simulation (Drouin et al., 2007).

3.2.4.3   F: Fluorescence Corrections

The characteristic X-rays of a given element can be excited by other X-rays when the energy of the latter exceeds the critical excitation energy of the former. Fluorescence is excited by characteristic lines that satisfy this energy criterion. For example, Fe K_α X-rays (6.40 keV) excite Cr (critical excitation energy 5.99 keV), but Cr K_α X-rays (5.41 keV) do not excite Fe

(critical excitation energy 7.11 keV). A fluorescence correction is therefore required for the former but not for the latter case. In principle, a fluorescence correction should be applied but it is neglected in most correction programs since it occurs in both specimen and standard and so tends to cancel out (Reed, 2005).

3.3 X-ray Microanalysis in EM

Accuracy is defined as how close to the correct answer is the mean result, and precision is how much scatter there is about the mean result. In reality, the sources of error in EPMA (Electron Probe Microanalysis) are numerous and diverse. Assuming that the specimen used is in a perfect condition (conductive, suitably mounted, reasonably flat, freshly polished and thick enough…etc), there are still many possible sources of error caused during the examination (Heinrich, 2002).

Quantitative EPMA results can be produced from the k-ratios, which are the intensities of specific principal lines in a specimen divided by the intensities of the same line from the pure elemental standard. Although the method of measuring intensities is different between SEM-WDX and TEM-EDX analysis, matrix or 'ZAF'(atomic number–absorption-fluorescence) corrections are always required in order to allow for the effect of the difference in composition between standards and specimen on the emitted intensities. Using this information and a set of physical constants and mathematical models of the physics involved, the data are corrected ('ZAF correction') into quantitative measurements in the MCA system (Multi-channel analyser) (Reed, 2005).

Although recent improvements in the measurement of physical constants and models have led quantitative EPMA results to a considerable improvement in accuracy and precision of results produced, quantitative analysis of light elements such as B in the $Nd_2Fe_{14}B$ phase is still

challenging because of the small amount of B (5.88 at%) in the $Nd_2Fe_{14}B$. The x-ray signal emitted from this small amount of B is believed to suffer different inevitable degradations and therefore cause significant errors in quantitative results (Birajdar et al., 2007, Eibl, 1993). Hence, an iterative procedure involving modeling the electron microprobe analysis has been introduced to improve the quality of the EPMA results in SEM-WDX and to explain the unexpected EPMA results from B in the $Nd_2Fe_{14}B$ phase in the subsequent sections.

3.3.1 Absorption Effect in SEM

Although most of the light element analysis errors result from the x-ray absorption caused by the specimen, it is possible to improve it by choosing an appropriate set-up in the electron microscope. The modeling program CASINO (based on Monte Carlo simulation of electron trajectories in solids) is able to model both the electron scattering and the X-ray production by those electrons and to provide useful information to determine the best accelerating voltage (Drouin et al., 2007). It was used to decide the proper accelerating voltage to analyse both $Nd_2Fe_{14}B$ and the ZrB_2-type needles in this project.

A higher accelerating voltage will always provide a higher beam current and thus corresponding x-ray intensities. However, contrary factors will sometimes lead to worse chemical analysis results. For example, increasing the electron range in the sample may result in worsened spatial resolution and increased absorption corrections. Since a lower accelerating voltage will minimise the absorption corrections, an accelerating voltage of 10kV or less has an advantage (i.e. obtaining a better spatial resolution, owing to decrease in electron range, reducing the beam diameter) for light element analysis (Reed, 2005). In soft X-ray analysis, such as B in $Nd_2Fe_{14}B$, it is therefore desirable to use a low accelerating voltage in the interest of minimising absorption corrections. Meanwhile, for quantitative analysis in the SEM, the
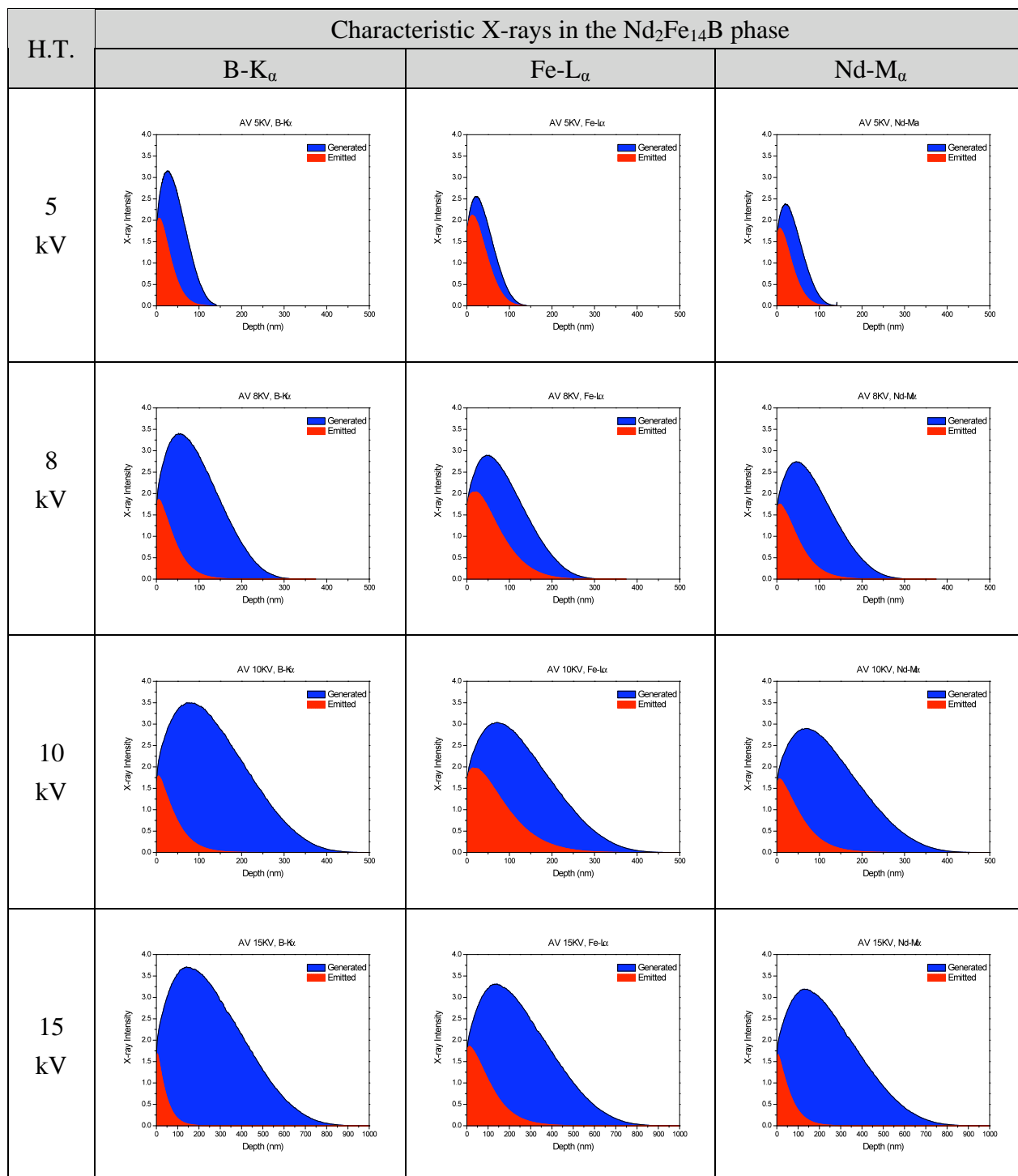
accelerating voltage should always preferably be at least twice (or optimum 3 times) the highest

relevant excitation potential, in order to obtain enough ionization (Jones, 1992). Hence, based

on the possible range of the accelerating voltage (5-15 kV), the correct shell for each element

was decided before the experiment (as shown in Table 4.3).

Figure 3.15 shows the $\Phi(\rho Z)$ curves - X-ray generation and emission versus depth -

calculated from the CASINO simulation programme for B-K_α, Fe-L_α and Nd-L_α X-rays in the

$Nd_2Fe_{14}B$ phase at different accelerating voltages in an SEM. In these figures, the blue area

shows the X-rays generated but absorbed within the sample and the red area shows the X-rays

actually emitted (escaped) from the sample.

Simulated results show that B x-rays are emitted exclusively from the uppermost 150

nm of the $Nd_2Fe_{14}B$ at 15kV as well as at 10kV, 8kV and 5kV accelerating voltage. Meanwhile,

the B-K_α, Fe-L_α and Nd-L_α X-rays in the $Nd_2Fe_{14}B$ phase are also generated within a similar

interaction volume at each corresponding accelerating voltage, indicating that the interaction

volume for each of the elements mentioned above are the same in the $Nd_2Fe_{14}B$ solid. It is also

found that the emitting volumes of each element at the same accelerating voltage are

significantly different when the accelerating voltage is larger than 8kV.

Based on the characteristic x-ray intensities calculated from the area below the $\Phi(\rho Z)$

curves, the best accelerating voltage for exciting enough x-ray intensity could be obtained by

picking the smallest absorption rate in the samples. The fraction absorbed by each element in

the sample is defined as the intensity of generated x-rays divided by the total amount of x-ray

intensities, as shown in the following formula:

$$Fraction \ \ Absorbed \ \ (i) = \frac{Int._{generated}}{Int._{generated} + Int._{Emitted}} \times 100\% \qquad \text{Equation 3-7}$$

H.T.	Characteristic X-rays in the Nd$_2$Fe$_{14}$B phase		
	B-K$_\alpha$	Fe-L$_\alpha$	Nd-M$_\alpha$
5 kV			
8 kV			
10 kV			
15 kV			

Figure 3.15 The depth distribution function for generated (blue) and emitted (Monteverde et al.) x-rays, Φ(ρZ), simulated at 5, 8, 10 and 15 kV in SEM-EDX respectively, with 20,000 electron trajectories for the B-K$_\alpha$, Fe-L$_\alpha$ and Nd-M$_\alpha$ characteristic X-rays in the Nd$_2$Fe$_{14}$B phase. (H.T.: High Tension)

Figure 3.16 shows the X-ray absorption rate for the B-K_α, Fe-L_α and Nd-L_α lines in the $Nd_2Fe_{14}B$ phase. It is found that approximately 95% of the generated B-K_α x-rays are absorbed by the $Nd_2Fe_{14}B$ matrix at 15kV. The absorption rate will then decreases to 70% at the lower acceleration voltage of 5kV. However, working at this lower voltage may not produce sufficient ionisation for other element x-rays in the same phase (i.e. Fe-L_α and Nd-L_α).

Consequently, a suggested appropriate accelerating voltage in the SEM is thus 8kV for analysing the $Nd_2Fe_{14}B$ phase, as a compromise between the interaction volume and the X-ray absorption of each element.
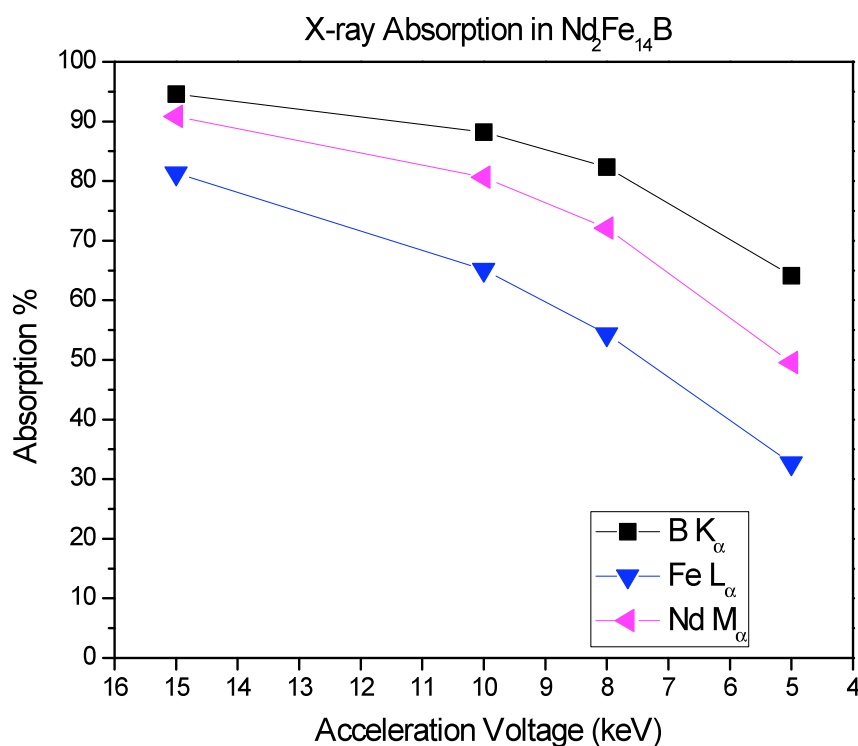
Figure 3.16 The absorption for B-K_α, Fe-L_α and Nd-M_α X-rays in $Nd_2Fe_{14}B$ (simulated for SEM-EDX).

3.3.2   Absorption Effect in TEM

It has been reported by Birajdar that the possible reasons that make quantitative analysis of the boron using EDX in TEM challenging can be summarised as follow (Birajdar et al., 2007):

1. Carbon and oxygen contamination artefacts during sample preparation and under the electron beam in the microscope

2. Overlap of EDX x-ray peaks (eg. B-K$_\alpha$ and C-K$_\alpha$)

3. Preferential absorption of soft x-rays in the sample

4. Low fluorescence yield

Obviously the X-ray intensity of the light elements, such as B-K$_\alpha$ in the TEM-EDX, is highly dependent on the thickness of the sample (Liao et al., 2003) and the fraction absorbed of B-K$_\alpha$ in the sample (Wenzel et al., 2003). Despite the thickness and fraction absorbed, it is found that the fraction of emitted X-ray intensity also has a massive influence on the EPMA results. The fraction of emitted X-ray intensity can be expressed as follows:

$$\text{Fraction of Emitted X-ray intensinsity } (i) = \frac{Int_{\cdot Emitted,i}}{\sum\limits_{i=1}^{n} Int_{\cdot Emitted,i}} \times 100\% \qquad \text{Equation 3-8}$$

Figure 3.17   show the simulated TEM-EDX results for the fraction absorbed and the fraction of emitted X-ray intensity for B-K$_\alpha$ from the Nd$_2$Fe$_{14}$B and the ZrB$_2$-type needles. The fraction absorbed of the B-K$_\alpha$ is increased by ~30% when the sample thickness increased (50 nm ~ 250 nm), whereas the emitted X-ray intensity ratio of B-K$_\alpha$ decreases as the sample

thickness is increased. Compared with the fraction of emitted x-ray intensity of B-K_α in both $Nd_2Fe_{14}B$ and ZrB_2-type needles, it is found that the fraction of emitted x-rays of B-K_α from ZrB_2-type needles is ~30 times larger than in the corresponding thickness of $Nd_2Fe_{14}B$. This difference may originate from the different fraction of B contents in these two phases (5.88 at% of B in $Nd_2Fe_{14}B$, 66.66 at% of B in ZrB_2) and thereby explain the low intensity of the B-K_α in TEM-EDX which was found only when analysing the $Nd_2Fe_{14}B$ phase, whereas not in the ZrB_2-type needles (Table 5.9, Table 5.10 and Table 5.13).
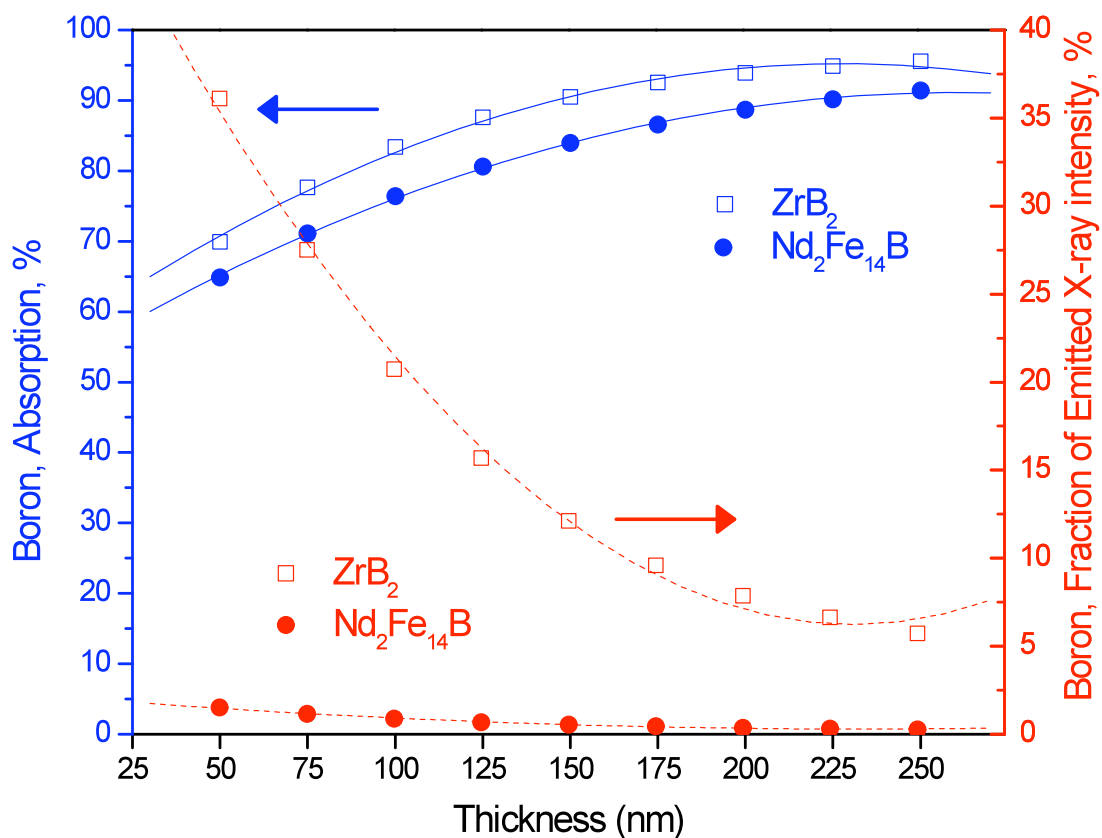
Figure 3.17 X-ray absorption and fraction of emitted x-ray intensity of B-Kα from both $Nd_2Fe_{14}B$ and ZrB_2 (Simulated for TEM-EDX).

References for Chapter 3

Birajdar B., Peranio N. & Eibl O. Year. Quantitative boron-analysis using EDX in SEM and TEM. *In:* Microscopy Conference, 2-7 Sept. 2007 Germany. 290-1.

Drouin D., Couture A. R., Joly D., Tastet X., Aimez V. & Gauvin R. 2007. CASINO V2.42-A Fast and Easy-to-use Modeling Tool for Scanning Electron Microscopy and Microanalysis Users. *Scanning,* 29**,** 92-101.

Eibl O. 1993. Improved, parameterless, constant-current method for absorption correction in quantitative EDX microanalysis in the TEM. *Ultramicroscopy,* 50**,** 203-205.

Garratt-Reed A. J. & Bell D. C. 2003. *Energy Dispersive X-ray Analysis in the Electron Microscope* BIOS Scientific Publisher Ltd.

Gatti E. & Rehak P. 1984. Semiconductor drift chamber - An application of a novel charge transport scheme. *Nuclear Instruments and Methods in Physics Research,* 225**,** 608-614.

Goldstein J. I., Choi S. K., Loo v. F. J. J., Heijligers H. J. M., Bastin G. J. & Sloof W. G. 1993. The influence of oxide surface layers on bulk electron probe microanalysis of oxygen : application to Ti-Si-O compounds. *Scanning,* 15**,** 165.

Heinrich K. F. J. 2002. Uncertainty in Quantitative Electron Probe Microanalysis. *Journal of Research of the National Institute of Standards and Technology,* 107.

Johann H. H. 1931. Die Erzeugung lichtstarker Röntgenspektren mit Hilfe von Konkavkristallen. *Z. Phys.,* 69.

Johansson T. 1933. Über ein neuartiges, genau fokussierendes Röntgenspektrometer. *Zeitschrift für Physik A Hadrons and Nuclei,* 82**,** 507-528.

Jones I. P. 1992. *Chemical microanalysis using electron beams*, London : Institute of Materials.

Lee R. E. 1993. *Scanning Electron Microscopy and X-ray Microanalysis*, PTR Prentice-Hall, Englewood Cliffs, NJ.

Liao X. Z., Serquis A., Zhu Y. T., Huang J. Y., Civale L., Peterson D. E., Mueller F. M. & Xu H. F. 2003. $Mg(B,O)_2$ precipitation in MgB_2. *Journal of Applied Physics,* 93**,** 6208-6215.

Liu J. 2005. Scanning transmission electron microscopy and its application to the study of nanoparticles and nanoparticle systems. *J Electron Microsc (Tokyo),* 54**,** 25.

Monteverde F., Guicciardi S. & Bellosi A. 2003. Advances in microstructure and mechanical properties of zirconium diboride based ceramics. *Materials Science and Engineering A,* 346**,** 310-319.

Oxford Instruments-technical briefing 2008a. Energy Dispersive X-ray Microanalysis Hardware. Oxford Instruments Analytical Ltd.

Oxford Instruments-technical briefing 2008b. Wavelength Dispersive X-ray Microanalysis Hardware. Oxford Instruments Analytical Ltd.

Oxford Instruments-technical briefing 2009. X-Max TEM Large Area SDD. Oxford Instruments Analytical Ltd.

Oxford Instruments 2008a. Technical briefing-"Energy Dispersive X-ray Microanalysis Hardware". *Oxford Instruments Analytical Ltd.*: Oxford Instruments Analytical Ltd.

Oxford Instruments 2008b. Technical briefing-"Wavelength Dispersive X-ray Microanalysis Hardware". Oxford Instruments Analytical Ltd.

Philibert J. & Tixier R. 1968. *Quantitative Electron Probe Microanalysis,* , National Bureau of Standards Special Publication. .

Reed S. J. B. 1996. *Electron Microprobe Analysis and scanning electron microscopy in geology*, Cambridge University Press.

Reed S. J. B. 2005. *Electron Microprobe Analysis and Scanning Electron Microscopy in Geology* Cambridge University Press.

Reimer L. 1988. *Scanning Electron Microscope: Physics of Image Formation and Microanalysis,* , Springer-Volay.

Wenzel T., Nickel K. G., Glaser J., Meyer H.-J., Eyidi D. & Eibl O. 2003. Electron probe microanalysis of Mg-B compounds: stoichiometry and heterogeneity of superconductors. *physica status solidi (a),* 198**,** 374-386.

Williams C. W. 1968. Reducing Pulse Height Spectral Distortion by Means of DC Restoration and Pile-Up Rejection. *IEEE Transactions on Nuclear Science,* 15.

Williams D. B. & Carter C. B. 1996. *Transmission Electron Microscopy*, Plenum Press.

Won C. M. 1998. *Material Anlysis*, CSMS Press.

4   Experimental Procedure and Techniques

4.0   Introduction

The aim of this research project is to study the effects of zirconium additions on as cast, homogenized and sintered Nd-Fe-B alloys. Arc melted ingots (as-cast alloy) were prepared with the objective of suppressing formation of free iron by different additions of zirconium and zirconium diboride. A flow chart of the experimental procedure is presented in Figure 4.1. The chemical compositions of the alloys used in this work are presented in Table 4.1. All the samples were characterized with respect to their microstructure and chemistry. Table 4.2 lists the process states and identifiers for the alloys used in this project. This chapter will present the details of the processing routes and the characterisation tools employed.
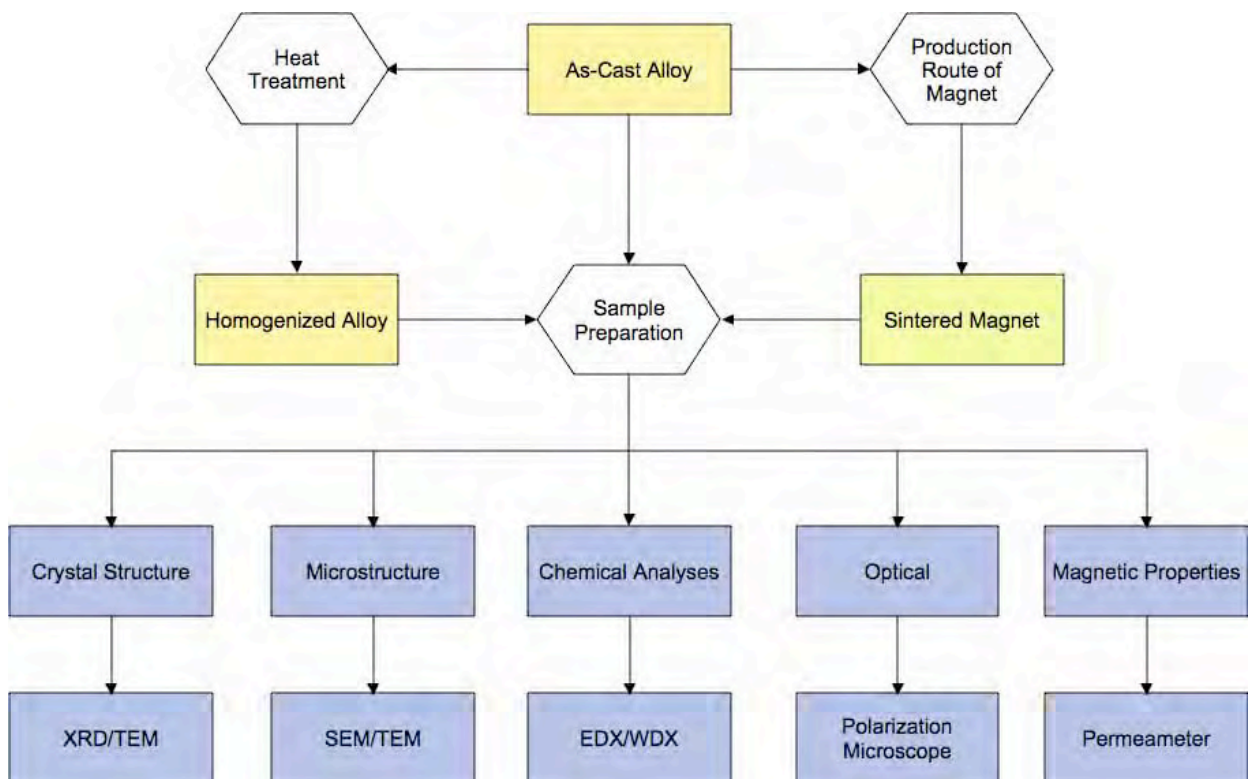
Figure 4.1 A flow diagram of the experimental procedure.

Table 4.1 Alloy compositions used in this work (identified by ICP-OES results from Less Common Metals, UK)

Sample Identifier	Starting Components	Composition	
		ICP-OES results (wt%)	**Converted from ICP-OES Result (at%)**
A1 (Nil-Zr alloy)	$Nd+Fe+Fe_2B$	$Nd_{28.5}Fe_{70.42}B_{1.08}$	$Nd_{12.68}Fe_{80.91}B_{6.41}$
A4 (0.6 at% Zr-addition)	$Nd+Fe+Fe_2B + 0.6$ at% Zr	$Nd_{28.41}Fe_{69.67}B_{1.08}Zr_{0.85}$	$Nd_{12.68}Fe_{80.31}B_{6.41}Zr_{0.6}$
A12 (1.0 at% ZrB_2 addition)	$Nd+Fe+Fe_2B+ 1.0$ at% ZrB_2	$Nd_{28.75}Fe_{68.39}B_{1.43}Zr_{1.43}$	$Nd_{12.68}Fe_{77.91}B_{8.41}Zr_{1.0}$

Table 4.2 The process states and identifiers for the alloys used in this project.

Sample State	Sample identifier	Stoichiometric composition (at%)	Alloy addition
As-cast	**A1**	$Nd_{12.68}Fe_{80.91}B_{6.41}$	Nil-Zr alloy
	A4	$Nd_{12.68}Fe_{80.31}B_{6.41}Zr_{0.6}$	0.6 at% Zr addition
	A12	$Nd_{12.68}Fe_{77.91}B_{8.41}Zr_{1.0}$	1.0 at% ZrB_2 addition
Homogenized	**A1H**	$Nd_{12.68}Fe_{80.91}B_{6.41}$	Nil-Zr alloy
	A4H	$Nd_{12.68}Fe_{80.31}B_{6.41}Zr_{0.6}$	0.6 at% Zr addition
	A12H	$Nd_{12.68}Fe_{77.91}B_{8.41}Zr_{1.0}$	1.0 at% ZrB_2 addition
Sintered	**MA1**	$Nd_{12.68}Fe_{80.91}B_{6.41}$	Nil-Zr alloy
	MA4	$Nd_{12.68}Fe_{80.31}B_{6.41}Zr_{0.6}$	0.6 at% Zr addition
	MA12	$Nd_{12.68}Fe_{77.91}B_{8.41}Zr_{1.0}$	1.0 at% ZrB_2 addition

4.1 Production of the Cast Alloy

The as-cast alloy used in this work was supplied by Less Common Metals, UK. The method of preparing the alloy is as follows: the starting materials, including Fe, ferroboron and Nd-metal were placed in an alumina crucible with Fe and ferroboron at the bottom. In the case of the zirconium additions, the Zr-metal was also mixed together with the same amount of non-zirconium starting materials. The melting of the alloy started at 650ºC. An excess of Nd between 1% to 4% is added into the crucible to replace any subsequent Nd loss by evaporation or oxidation (Kirby, 2007).

The crucible was then placed in an induction coil of a high vacuum induction furnace. The furnace chamber was evacuated to a pressure of $\sim 10^{-6}$ bar and back filled with argon to a pressure of ~0.3 bar before melting. The alloy was held at 1600ºC for ~15 minutes. After heating, the melt was poured into a water-cooled copper mould. The ingot was then allowed to cool under vacuum for approximately 1 hour before being removed from the mould. The block shape ingot has dimension of 25 cm*15 cm* 2.5 cm. Table 4.1list the alloy composition used in this work.

As shown in Table 4.1, in order to avoid the formation of both Nd_2Fe_{17} and Nd_5Fe_{17} phases in the cast alloy, provide sufficient boron as a source for the formation of both ZrB_2 and $Nd_2Fe_{14}B$ in A4 and A12 sample, the purpose of the different additions in the A4 and A12 samples (Zr or ZrB_2 addition to NdFeB) is to provide sufficient boron to form the ZrB_2 phase during casting. Without this step, the Zr would consume B from the $Nd_2Fe_{14}B$ phase and the resulting insufficient B would cause Nd_2Fe_{17} or Nd_5Fe_{17} to form (Shaaban, 2005).

4.2 Production of the Homogenized Alloy

The as-cast sample (~100g) was wrapped in stainless steel foil before being loaded into a furnace tube. This was done to avoid any contamination or any possible reaction between the sample and the Nimonic tube at elevated temperature. The tube was first evacuated by rotary pump and then by diffusion pump to achieve a vacuum of ~10^5 mbar as measured by a Penning gauge. The furnace was then heated at a rate of 15°C/min to 1100°C. The samples were homogenized for 20 hours. After homogenization, the furnace was allowed to cool to room temperature by switching the power off.

4.3 Production of the Sintered Magnet

Figure 4.2 shows a flow diagram for the sintered magnet production in this study. The HD-process and sintering have been employed. The HD-process was patented by Harris (Harris et al., 1979) for producing rare-earth transition metal (R/TM) magnetic alloys. The as-received NdFeB alloys were first converted to a powder by the HD-process (see section 2.3.1).
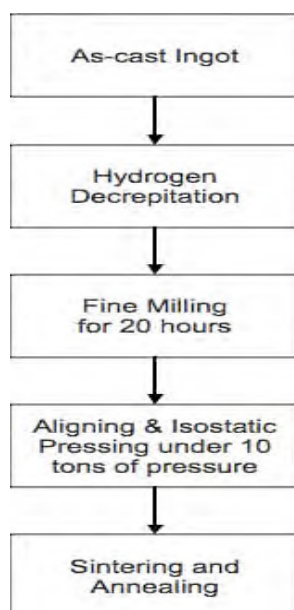

Figure 4.2 Flow diagram for sintered magnet production.

An average of 40-50g of NdFeB alloy was placed into a hydrogenation chamber and attached to a hydrogen delivery system as shown in Figure 4.3 (hydrogen rig). A rotary pump evacuated the chamber until a vacuum of better than 10^{-1} bar was achieved. Hydrogen was then admitted to the chamber at 10 bar. When the alloy had absorbed the supplied hydrogen, it resulted in a simultaneous rise in temperature and a corresponding drop of pressure in the chamber. The reaction was complete when the pressure gauge remained stable, which indicated that no more H_2 was being absorbed. The chamber was then evacuated again to $\leq 10^{-1}$ bar and the sample removed from the chamber within an argon atmosphere glove box, containing less than 75 ppm of oxygen (Harris and McGuiness, 1991).
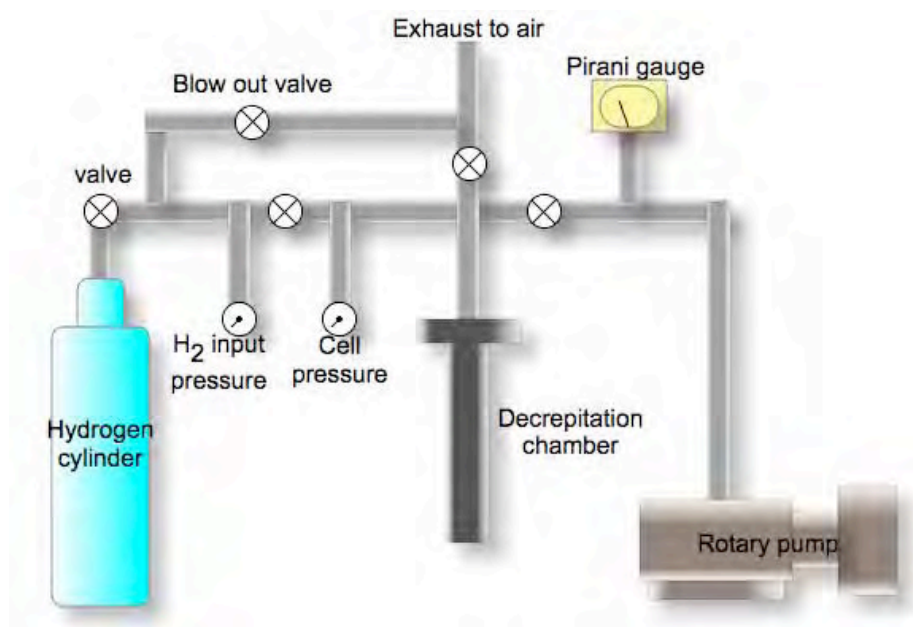
Figure 4.3 A schematic representation of the hydrogen rig.

To produce appropriate powder sizes for sintering, the hydrogen decrepitated material was mechanically milled using a roller mill. About 35 g of the material was tumbled with the cyclohexane in a stainless steel milling pot containing 300 g of tungsten-carbide milling balls (as shown in Figure 4.4 (a)). The pot was then sealed in the glove box and rotated at 100 rpm for 20 hours on a roller mill (Figure 4.4 (b)).

(a)   (b)
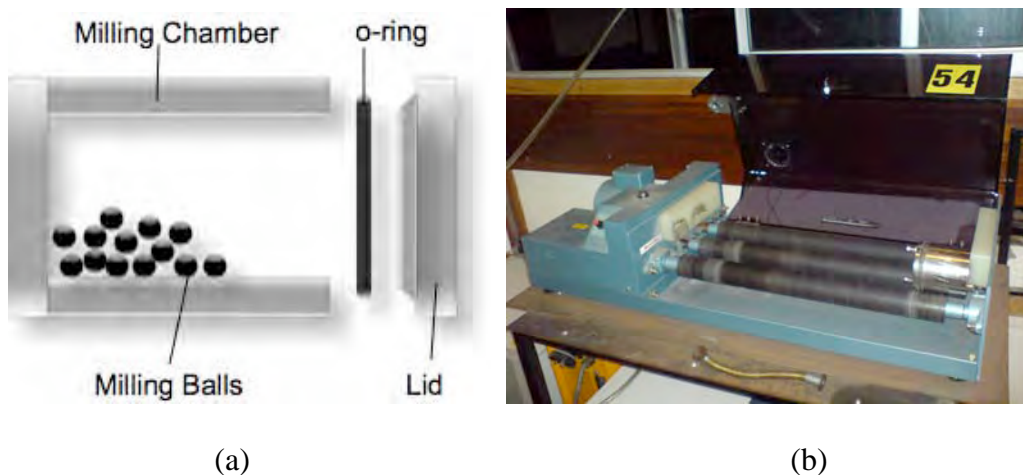
Figure 4.4 (a) Illustration of milling pot (b) Roller mill

At the end of the milling process, the remaining powder was then dried under vacuum in the port of the glove box to ensure all the cyclohexane had evaporated prior to further processing. After the dried powder was taken out from the milling pot, 20g of powder was then packed into a Neoprene isostatic press bag (as shown in Figure 4.5 (a)) within the glove box. To ensure even density, the press bag was tapped regularly during filling. The powder was then aligned in a pulse field of 6 Tesla using a pulse magnetiser with the coil (as shown in Figure 4.5 (b)). The pulse magnetiser is shown in Figure 4.6 (a).
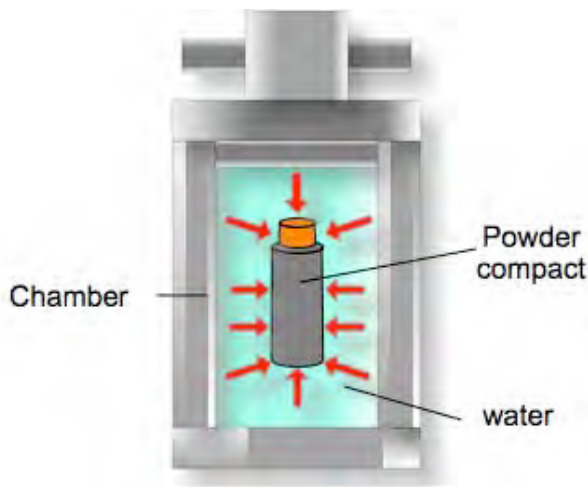

(a)   (b)
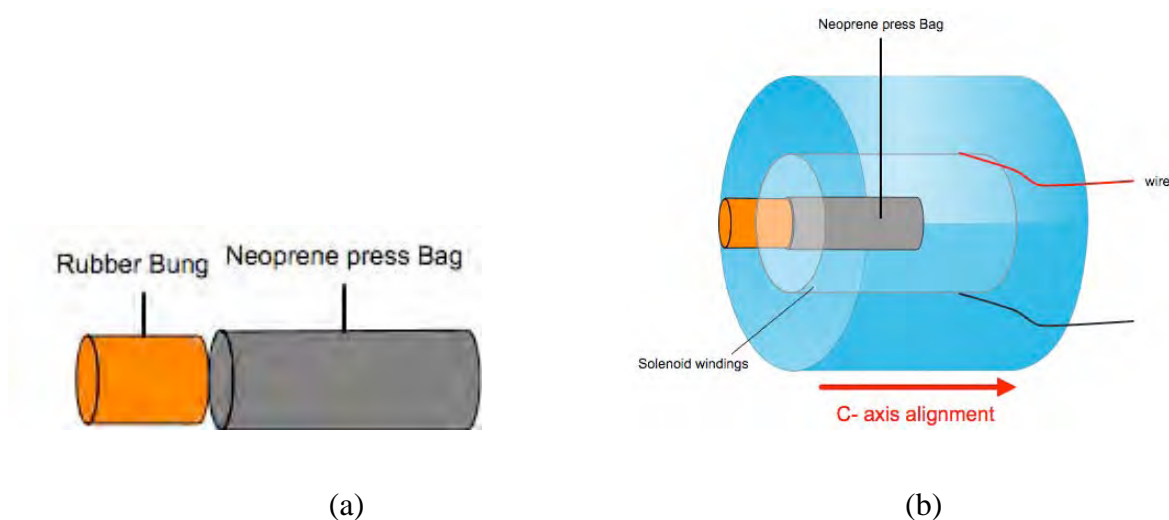
Figure 4.5 Illustration of (a) Neoprene isostatic press bag (b) pulse aligning coil

(a)

(b)

(c)

(d)

Figure 4.6 (a) Pulse magnetiser (b) isostatic press (c) illustration of isostatic stainless chamber (d) isostatic stainless chamber

After pulsing, the press bag was carefully transferred to an isostatic press chamber (shown in Figure 4.6(b)) produce a green compact prior to sintering. The chamber was then filled with water and a pressurized to 5 MPa in order to compact the powder.

The aligned and pressed green compacts were immediately transferred from the press bag to a stainless steel boat and then to a vacuum sintering furnace (as shown in Figure 4.7). The system was evacuated to lower than 4×10^{-1} bar and the heating profile shown in Figure 4.8 was initiated for all alloys. As shown in Figure 4.8, the green compacts were heated at a heating

rate of 5 °C/min and sintered at 1070 °C for 12 hours followed by a 1 hour anneal at 630 °C. This sintering temperature and time profile are based on previous work on MA12 at the University of Birmingham [Kirby, 2007]. A Eurotherm multi ramp temperature controller was used in conjunction with the vacuum furnace. The thermocouples attached to the temperature controller gave a temperature reading from the furnace and this was checked regularly using a voltmeter linked to a K-type thermocouple. Degassing was monitored by observing the pressure change during out-gassing. A decrease in the vacuum indicates that desorption was occurring. Desorption of sintered magnets was complete once the vacuum had recovered. After sintering, the furnace tube was then slowly cooled to room temperature. The sample was removed from the chamber, sliced into discs and prepared for examination.

Figure 4.7 Vacuum furnace system
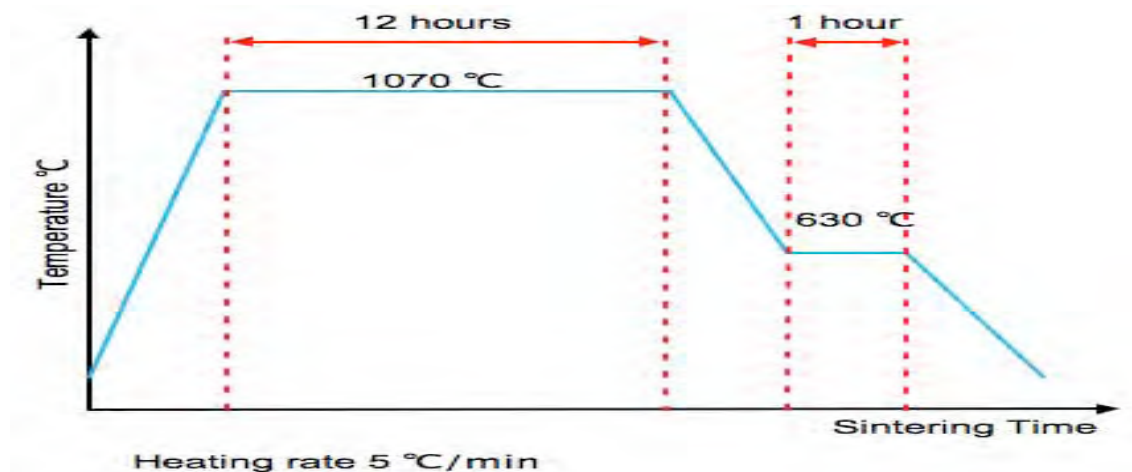
Figure 4.8 Schematic of the sintering process conditions for all NdFeB alloys in this study.

4.4 Specimen Preparation

4.4.1 SEM Specimens

In order to examine the effect of the additions to the NdFeB alloys, all the SEM samples were taken from the top surface of each ingot. All samples were mounted in conductive bakelite using a hot mounting press. The mounting process took around 20 minutes at a temperature of 160°C.

The mounted samples were ground successively on four grades of silicon carbide paper (#240, 400, 800, 1200). In order to prevent oxidation damage on the sample, a non-water based lubricant (Lapping fluid, Marcon) was used. After grinding, samples were polished on a wheel with 0.25 μm of diamond paste and non-water based laping fluid. After each polishing stage, the specimens were washed with ethanol and dried. In order to reveal the grain structure more clearly, the polished specimens were lightly etched for 15-40 seconds. The chemical etchants used in this project were 2% nital and Viella's regent (1gm picric acid in 5ml hydrochloric acid and 100 ml of methanol).

4.4.2   TEM Specimens

Specimen preparation for TEM investigation is more complicated and takes a longer time than for SEM. Various specimen preparation techniques have been developed and a few of them have been used in the present study. Two main methods, mechanical polishing and ion beam milling by focussed ion beam (FIB) were used for the preparation of TEM specimens from the bulk sample.

4.4.2.1   Mechanical Polishing

Samples of the as-cast, homogenized and sintered alloys, were first sliced (1-2 mm) using a precision diamond saw (Leco, VC-50). Discs were then produced using Electrical Discharge Machining (EDM) with a 3-mm diameter brass tube using different types of discharge.

The 3-mm disc specimens were then stuck to a grinding holder and ground on two grades of silicon carbide paper (#1200, 2400) until 70-90 μm in thickness. Figure 4.9   shows the grinder used in this study. In order to reduce oxidation during sample preparation, a non-water based lubricant (Lapping fluid, Marcon) was used.

In the pre-thinning stage, the specimen was dimpled at the centre of the disc to 30-40 μm using a dimpling apparatus (Testbourne, Model 515) at a wheel speed of 3.5. A non-water based lapping fluid mixed with 0.25 μm diamond paste was used as a lubricant during the dimpling process. Figure 4.10 shows the dimple holder used in this study.

In the final thinning stage, a small hole was made using a Gatan Model 691 Precision Ion Polisher System (PIPS) at an incident angle of 8° and beam energy of 5 keV, followed by a final thinning at an incident angle of 6° and then 3° at 3 keV till perforation. Figure 4.11 shows
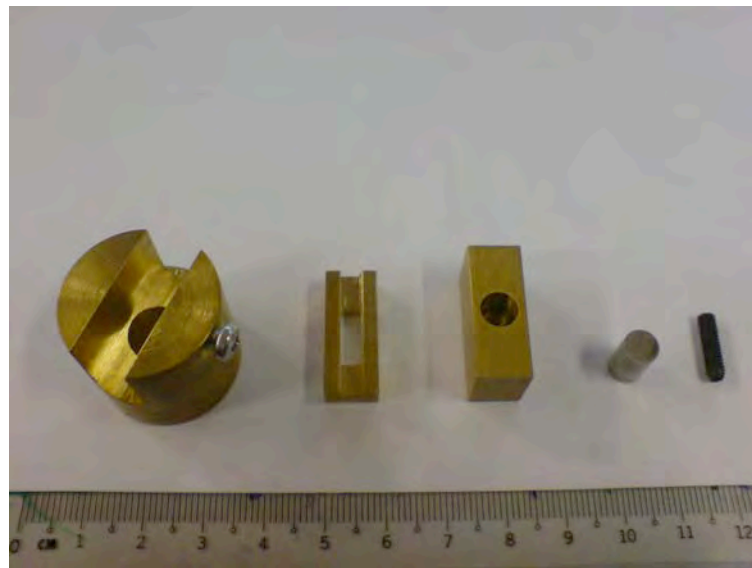
the TEM sample preparation process for NdFeB specimens.
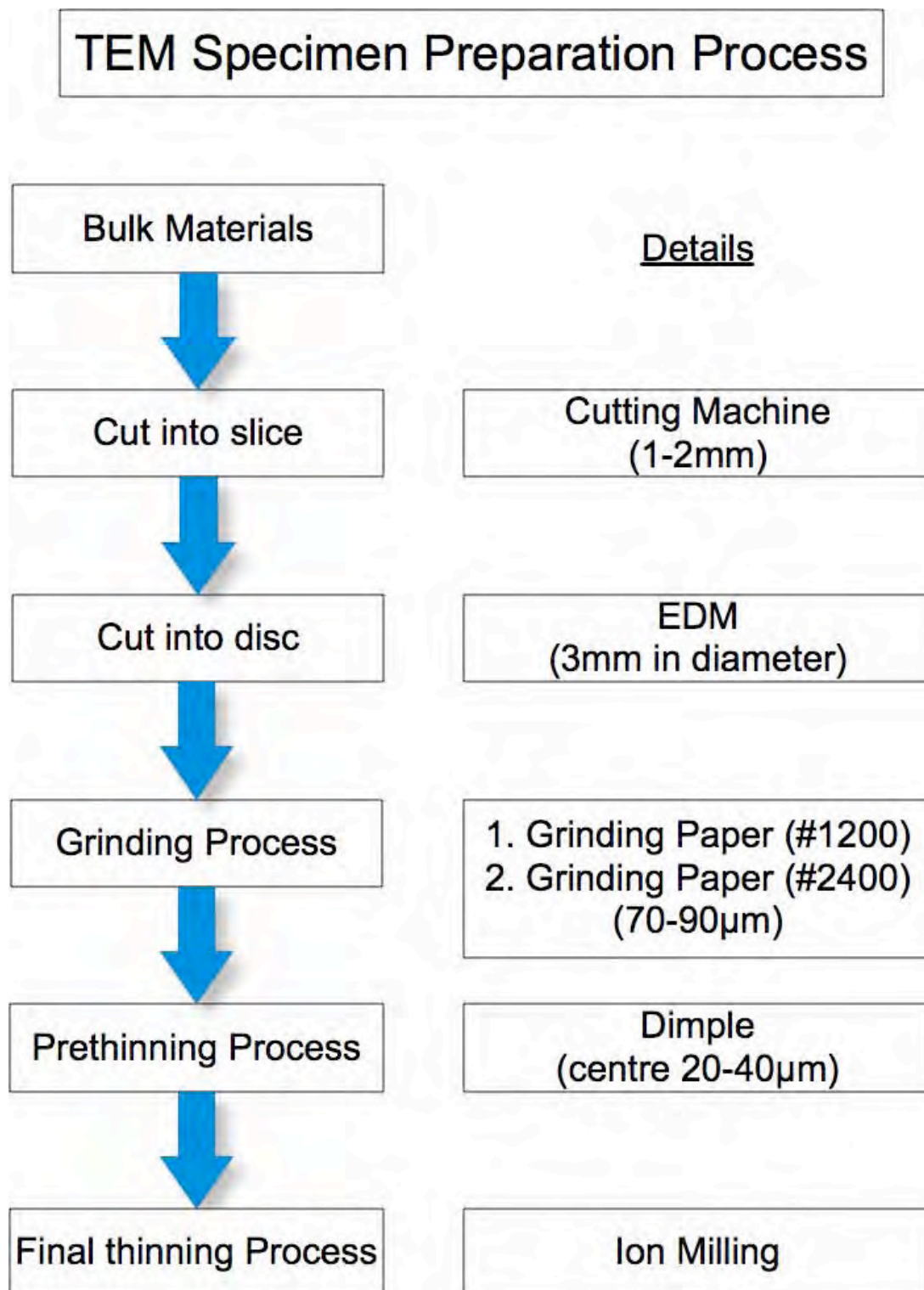

(a)
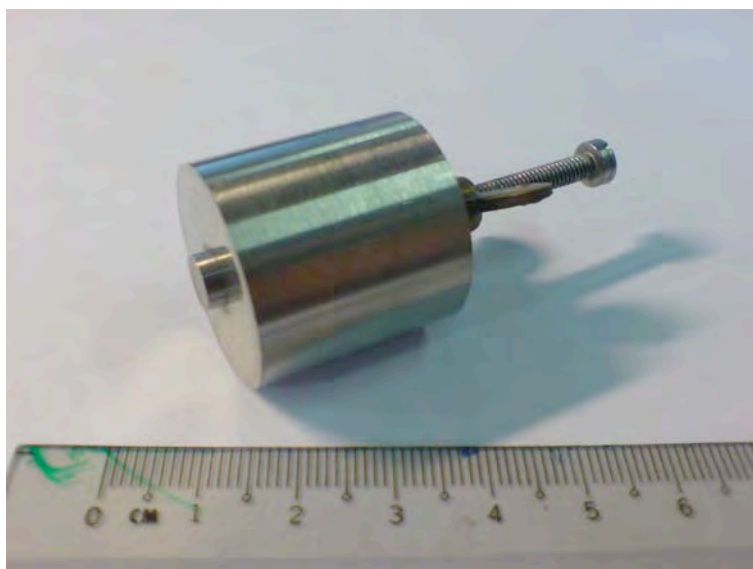
(b)

Figure 4.9 The grinder used in this study.

(a)

(b)

Figure 4.10 The dimple holder used in this study.

TEM Specimen Preparation Process

	Details
Bulk Materials	
↓	
Cut into slice	Cutting Machine (1-2mm)
↓	
Cut into disc	EDM (3mm in diameter)
↓	
Grinding Process	1. Grinding Paper (#1200) 2. Grinding Paper (#2400) (70-90µm)
↓	
Prethinning Process	Dimple (centre 20-40µm)
↓	
Final thinning Process	Ion Milling

All processes were done in non-water based lapping fluid .

Figure 4.11 TEM specimen preparation process via mechanical polishing.

4.4.2.2   Focussed Ion Beam (FIB)

Originally, the FIB was used for the final thinning step and to adhere mechanically prepared ribbons of semiconductor material to a modified TEM grid. It is only when the use of a chamber mounted nanomanipulator (omniprobe) and beam-induced material deposition were introduced that FIB came to be so useful for TEM sample preparation.

A dual beam FIB system operates in a similar way to a SEM, except that FIB uses in addition a finely focussed beam of gallium ions which can operate either at low beam current for imaging or at high beam current for site-specific milling. Figure 4.12 shows a schematic diagram of a dual beam FIB.
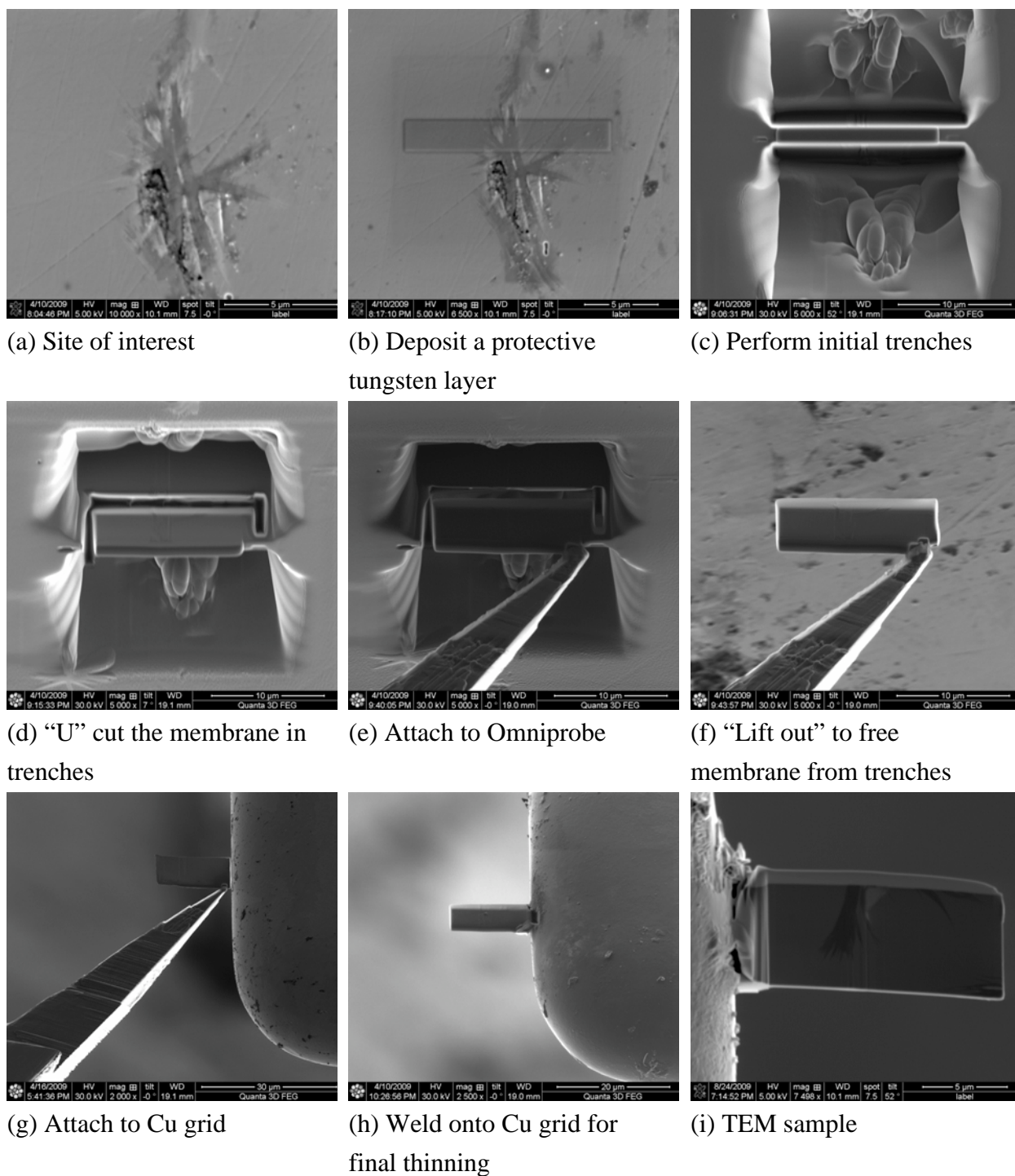
In this study, the cross-sectional method was used to prepare TEM samples by focused ion beam milling in a FEI Quanta 3D FIB, which consists of both a focussed gallium ion beam and a conventional field-emission scanning electron (FEGSEM) column. The dual-beam FIB offers the ability to locate the lift-out site with SEM resolution. The area of interest, identified in BEI mode, was firstly coated with 1.5μm thick tungsten as a protective layer at the site of interest (as shown in Figure 4.13 (a) and (b)) against the subsequent ion milling process.

This was followed by the use of an ion beam to excise the membrane without sacrificing the original bulk sample. Two initial trenches were made (as shown in Figure 4.13 (c) and (d)) by carrying out two rapid ion milling steps or "cuts". The first was a "U"-shaped cut which partially surrounded the site of interest. This was followed by a straight cut which intersected the first cut beneath the target and produced a wedge-shaped sample. The probe was then fixed to the released membrane by ion-beam metal deposition. The membrane containing the site of interest was later removed from the bulk sample by the nanomanipulator.

The membrane was then translated via the probe tip to a custom Omniprobe TEM sample holder, called a "lift-out grid" where it was again attached to the grid by ion beam-induced metal deposition (Figure 4.13 (e), (f) and (g)). The membrane was later detached from the probe tip using FIB milling (Figure 4.13(h)). The extracted sample was then thinned to the required thickness for TEM inspection. The ion (Ga^+) beam operated at 30 kV with a beam current ranging from 50,000 down to 3000 pA was used to thin the membrane down to ~1 μm. The sample was further polished to 150 nm using successive currents of 1000, 300, and 100 pA (Figure 4.13 (i)). The sample was finally cleaned at 48 pA and 5 kV.
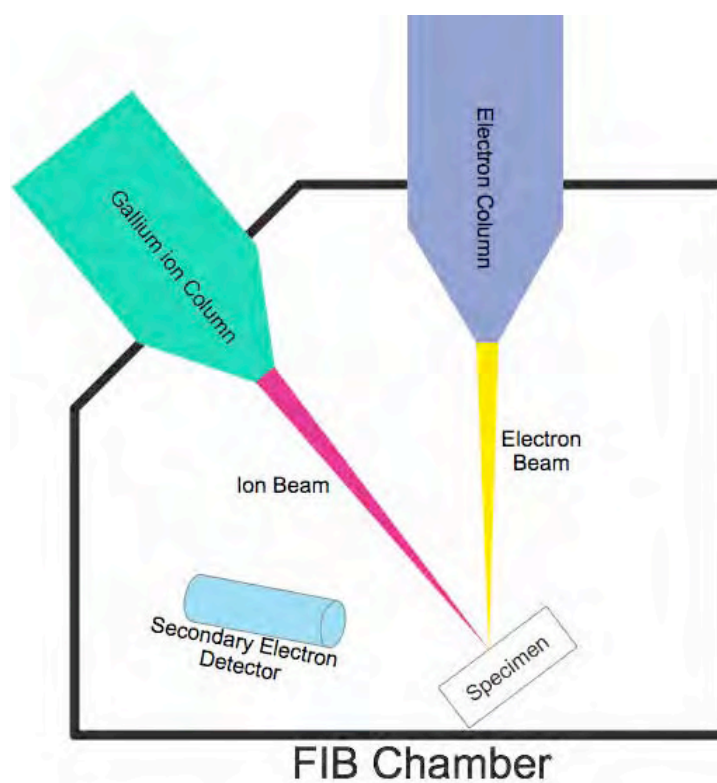
Figure 4.12 A FIB instrument showing the Ion and Electron columns and the specimen inside the vacuum chamber.

(a) Site of interest

(b) Deposit a protective tungsten layer

(c) Perform initial trenches

(d) "U" cut the membrane in trenches

(e) Attach to Omniprobe

(f) "Lift out" to free membrane from trenches

(g) Attach to Cu grid

(h) Weld onto Cu grid for final thinning

(i) TEM sample

Figure 4.13 TEM specimen preparation via FIB.

4.5 Microstructural and Chemical Characterization

The following equipment and methods were employed to characterize all the aspects of the NdFeB specimens.

4.5.1 Optical Microscope - Polarization Microscope

An optical microscope (Carl Zeiss, Jenavert) with a polarizer was used to observe grains and domain patterns. The images were acquired using a Nikon Coolpix digital camera at its maximum magnification of 125x. Reflected polarized light will be slightly rotated by the magnetic domain on the samples. The degree of rotation of the polarization plane is dependent on the direction of magnetization. Therefore, we can determine whether the domain is parallel or perpendicular to the observed plane by observing the reflected polarized light. The magnetic Kerr effect is more clearly observed on grains having a uniaxial magnetocrystalline anisotropy, such as $Nd_2Fe_{14}B$. Grains with the c-axis parallel to the observed surface show typical 'cigar'-shaped domains, whereas grains with the c-axis perpendicular to the observed plane show a 'cog-wheel'-like shape. These two types of domain orientation are shown in Figure 4.14 (Jones, 2001).
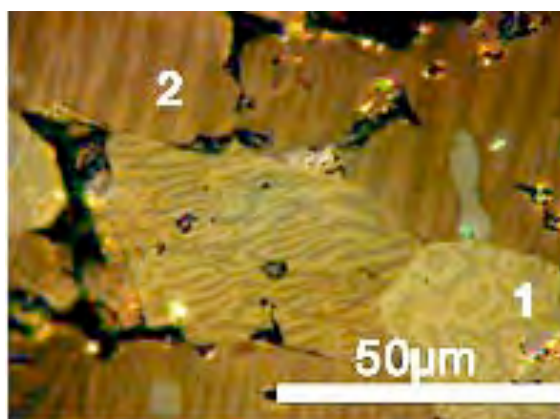
Figure 4.14 A Kerr effect image of the magnetic domains in $Nd_2Fe_{14}B$, (1) cog wheel pattern and (2) cigar or striped domain pattern

4.5.2 Electron Microscopy

4.5.2.1 Scanning Electron Microscopy

The microstructure of the specimens in this project were examined using a field-emission SEM (JEOL JSM 7000F) equipped with an energy dispersive x-ray detector (INCA x-sight model 7558, Oxford Instruments Ltd.) and wavelength dispersive x-ray detector (INCA Wave model 700, Oxford Instruments Ltd.). For both imaging and microanalysis a fixed working distance of 10 mm was used with an acceleration voltage between 5-25 kV.

There are two principal types of image formed in a scanning electron microscope: Secondary Electron Image (SEI) and Backscattered Electron Image (BEI). In this project, SEI images are used for the calculation of grain size and BEI images are used to check the distribution of phases via differences in contrast.

4.5.2.2 Transmission Electron Microscopy

TEM investigation was carried out using both a Philips CM20 (LaB_6 filament) and FEI Tecnai F20 FEG (S)TEM in the Electron Microscopy Centre at the University of Birmingham. Both have double tilt goniometer stages so that crystallographic analysis can be performed. Various TEM techniques were used, such as SAD (Selected Area Diffraction) and imaging, CBED (Convergent Beam Electron Diffraction), HAADF (High Angle Angular Dark Field) and EDX composition line scan and mapping.

The CM20 was operated at a HT of 200 kV, with the largest C2 aperture size (200 µm) and Spot Size (Cl intensity) 6, giving a probe size ~100 nm. For EDX analysis, the specimen was tilted to 30° in order to achieve the best X-ray count rate. An Oxford Ultra-thin window Si(Li) X-ray detector was used with an elevation of 20° and collection Live Time of 100

seconds.

A FEI Tecnai F20 FEG (S)TEM equipped with Oxford EDX and Gatan digiPEELS was operated at 200 kV, with an extraction voltage of 3800 V and a gun lens voltage of 0.75 kV. The biggest Cl aperture size (2000 µm) was always selected in order to achieve the highest electron intensity.

The operating pressure in the microscope column was less than 10^{-5} Pa (10^{-10} bar). In EDX analysis, a silicon drift detector (Oxford X-Max large area SDD) detector was used at an elevation of 20°, and the collection Live Times were 10, 30, 50 and 100s, depending on the situation and the experiment, but for each round of experiments it was not changed. All energy-dispersive X-ray (EDX) spectra were processed using the Oxford Instruments commercial software 'The Microanalysis Suite Issue 18b+SP1' using the default peak shapes provided in the package.

4.5.3   Electron Probe Micro Analysis (EPMA)

The electron probe micoanalysis was carried out using both EDX and WDX on a JEOL 7000F. The HT (High Tension) was set at 20, 15, 10 and 8 kV, depending on the situation and the experimental need, but it was fixed for each round of experiments. For example, it is easy to obtain a clear secondary image but poor chemical analysis under a higher HT. In order to have the best resolution for EPMA detectors, the working distance was always fixed at 10 mm and the magnification at 4000x.

4.5.3.1   Energy Dispersive X-ray (EDX) Analysis

EDX analysis in this project was obtained by an Oxford INCA x-sight EDX detector and processed using the Oxford Instruments commercial software package 'The Microanalysis

Suite Issue 17a+SP1'. Before each round of experiments, iron was selected as an optimization element for the EDX Quant analysis.

During the EDX analysis, an optimal high tension (HT) for the experiment was required for acquiring the x-ray signals from both heavy elements (ie. Nd, Zr and Fe) and light elements (ie. B) at the same time. The collection live time was 90 seconds with 20-25% of dead time. The process time was fixed at 5 and the number of acquisition channels was set to 2000.

4.5.3.2　Wavelength Dispersive X-ray (WDX) Analysis

In this study, the accelerating voltage, beam current, background acquisition and acquisition time were fixed at 8kV and 20kV, 10nA, 10 seconds and 20 seconds, respectively. Table 4.3 present the details of the set-up on the electron microscope.

Table 4.3 The normal settings for performing WDX analysis on SEM JEOL 7000F

Acquisition Time:	**Acquire background**	10 seconds
	Acquire spectrum	20 seconds
Magnification		4000x
Beam current		10 nA
Objective lens Aperture size		3
Working distance		10 mm
Accelerating Voltage		8 kV / 20kV

Compared with EDX, where any X-ray that reaches the detector is included, and the entire X-ray spectrum is measured continuously; WDX must be mechanically scanned over different ranges (and angles) with several crystal changes. Therefore, each element spectrum in WDX was produced by slowly scanning over a certain range with a specific crystal. Table 4.4 lists all the analysis settings of the crystals in the WDX spectrometer (Wave 700, Oxford Instruments) used in this project.

Table 4.4 Analysing crystals and standards for WDX

Accelerating Voltage 8kV, Magnification 4kX, Beam Current 10 nA, Peak Acquisition: 20 sec from peak / 10 sec from background						
	WDX settings		**Phase and standards**			
Element	**Principal Lines (keV)**	**Analysing Crystal**	$Nd_2Fe_{14}B$	$Nd_1Fe_4B_4$	**Nd-rich**	ZrB_2
B	K_α (0.1834)	LSM200	Matrix*	Element		Element
Fe	L_α (0.7048)	TAP	Matrix*	Element		
Nd	M_α (0.9778)	TAP	Matrix*	Element	Element	
Zr	L_α (2.0424)	PET				Element
O	K_α (0.5249)	LSM80			Al_2O_3	

*The standards for the $Nd_2Fe_{14}B$ phase were collected from the matrix of the homogenised NdFeB alloy (A1H).

In WDX analysis, standard databases for each element for different Avs (Accelerating voltages) need to be created first. The WDX standards should be chosen based on their similarity in composition to the compound being analysed. In order to reduce the excessive difference in peak wavelength between standards and specimen caused by chemical bonding and matrix (or ZAF) corrections, various standards were gradually assembled from the alloys with different stoichiometric concentrations for different phase analysis. For example, the standard for analyzing the boron content in the $Nd_2Fe_{14}B$ phase might not be suitable for the boron content of the ZrB_2 phase. This is to reduce the matrix (or ZAF) corrections for the different compositions of standards compared with the phases under investigation. Table 4.5 summarises the WDX standards used in this study.

After the computer recorded the standard spectra, the characteristic X-ray peaks from the examined alloys were analysed and acquired under the same conditions.

Table 4.5 WDX standards used in this study

Element	WDX Standard Source	at% of element
Nd	Pure	100.00
	$Nd_2Fe_{14}B$	11.76
Fe	Pure	100.00
	$Nd_2Fe_{14}B$	82.35
	Fe_2B	66.66
	FeS_2	33.33
B	Pure	100.00
	BN	50.00
	Fe_2B	33.33
	$Nd_2Fe_{14}B$	5.88
O	Al_2O_3	60.00
Zr	Pure	100.00

4.5.4 Inductively Coupled Plasma (ICP-OES)

Inductively coupled plasma optical emission spectrometry (ICP-OES), also referred to as inductively coupled plasma atomic emission spectroscopy (ICP-AES), is an analytical technique used for the detection of trace metals. It is a type of emission spectroscopy that uses inductively coupled plasma to produce excited atoms and ions that emit electromagnetic radiation at wavelengths characteristic of a particular element. The intensity of this emission is indicative of the concentration of the element within the sample. The composition of all the starting materials was determined using ICP-OES at Less Common Metals Ltd., which showed the composition of the starting material to be $Nd_{12.68}Fe_{77.91-80.91}B_{6.41-8.41}Zr_{0-1}$ (at%) with a small amount of Pr, Al, and Si (< 0.08 wt%).

4.5.5   X-ray Diffraction

X-ray diffraction has been employed to obtain diffraction patterns for analysis of phases, lattice spacings and phase constitution. Solid samples with a smooth surface are required to produce diffraction peaks with minimum noise. The sample was mounted on a sample holder and illuminated with X-rays of a fixed wavelength. The data was then analysed as a function of the reflection angle to calculate the inter-atomic spacings. The measurement was set-up in a way that, when the incoming beam forms an angle θ with a certain lattice plane, the reflected beam which later produces the X-ray diffraction pattern is recorded at an angle of 2θ. The intensity of the diffraction peaks is related to the content of the unit cell, which is the atomic position or the electron density distribution. The distances (d- spacing) between lattice planes are calculated using Bragg's Law:

$$n\lambda = 2\mathrm{d}\sin\theta \qquad\qquad\qquad \text{Equation 4-1}$$

where n is an integer, and λ is the X-ray wavelength. The accuracy of the lattice spacing is ± 0.002Å.

Analysis of all samples was performed on a Philips X-pert diffractometer (SIEMENS D500) using monochromatic CuKα radiation ($\lambda=1.50462$Å) at 40 keV and 300 mA. It employed a 2θ range from $20°$ to $90°$ with a step size of $0.02°$/sec.

4.6   Magnetic Property Measurement

The magnetic properties of the bulk magnets were examined using a permeameter. A permeameter is a device for testing the magnetic properties of the bulk magnets in a closed magnetic circuit. The permeameter consists of an electromagnet with the gap completed by the specimen. Using the system it is possible to measure the values of remanence (B_r), intrinsic

(iH_c) and inductive (bH_c) coercivity and maximum energy product $(BH)_{max}$. These terms were defined in Chapter 2.

Permeameter specimens require a known cross-sectional area. When a magnetic field is applied and increased gradually, the coils measure the fractional change of the total magnetic flux by measuring the variation of induced voltage with time. Integration of the voltage yields the total magnetic induction and therefore the magnetization of the specimen.

The flux density can be measured since the cross sectional areas of the coil and sample are known. The specimen is first pulse magnetized and then placed in the centre between the tips of the coils. The upper pole is wound down until in contact with the sample and locked into position. This produces a closed loop of magnetic field; thus the self-demagnetization fields from the sample are eliminated. The field is then increased until the sample is fully magnetized and then applied in the reverse direction finally to reduce the magnetization to zero in the second quadrant of the demagnetisation curve.

A computer was used to control the power supply and the measuring sequence. The computer program takes values from the second quadrant of the demagnetization curve to calculate the magnetic properties of the specimens. The permeameter is water cooled to keep itself and the specimen at a constant temperature during the measurements and calibrated regularly with a Ni standard sample. A schematic of the permeameter is shown in Figure 4.14.
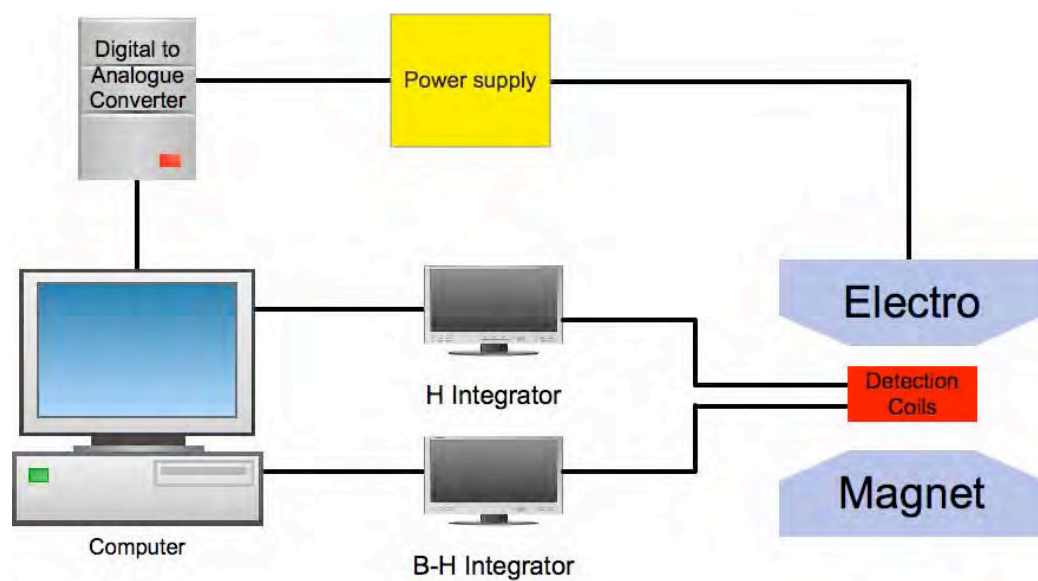
Figure 4.15 A schematic of the permeameter used in this study.

Reference for Chapter 4

Harris I. R., Evans J. & Nyholm P. 1979. UK patent application.

Harris I. R. & McGuiness P. J. 1991. Hydrogen: its use in the processing of NdFeB-type magnets. *Journal of the Less Common Metals,* 172-174**,** 1273-1284.

Jones I. P. 2001. *Materials Science for Electrical and Electronic Engineers*, Oxford University Press.

Kirby K. A. 2007. *The role of casting conditions and heat treatment on the permanent magnetic properties of selected $Sm_2(Co, Fe, Cu, Zr)_{17}$ and NdFeB-Type magnets.* PhD., University of Birmingham.

Shaaban A. 2005. *A study of near stoichiometric Nd-Fe-B alloys and magnets.* PhD., University of Birmingham.

5 Results

5.0 Introduction

The volume fraction of α-Fe dendrites in the cast state is highly dependent on the alloy composition and solidification rate. A near stoichiometric, conventionally cast NdFeB alloy contains a substantial amount of α-Fe dendrites resulting from inhomogeneity in the liquid and from non-equilibrium cooling of the melt. The α-Fe dendrites are magnetically soft and highly undesirable. It has been reported that it is possible to reduce the proportion of dendrites by the addition of zirconium. This chapter reports an investigation of the effect of Zr and ZrB_2 on the constitution of cast NdFeB alloys (both in the as-cast and homogenized states) and on the properties of the resulting magnets.

5.1   Analysis of NdFeB-Zr Cast Alloys

5.1.1   X-ray Diffraction

X-ray diffraction patterns from the cast NdFeB-Zr alloys were obtained to identify the phases formed before and after Zr or ZrB_2 had been added. The XRD profiles are shown in Figure 5.1 (a).

Evidently, both α-Fe and $Nd_2Fe_{14}B$ exist in A1 and A4 (As shown in Figure 5.1 (b) and (c)). However, α-Fe did not appear in the A12 sample, which indicates that the ZrB_2 rather than the Zr has eliminated the α-Fe (within the limit of XRD).

According to the literature review, the cast A1 alloy should consist of four basic phases: a $Nd_2Fe_{14}B$ matrix grain phase, a Nd-rich grain boundary phase, an α-Fe phase and a minor $NdFe_4B_4$ phase. However, the peaks from the Nd-rich and $NdFe_4B_4$ phases are difficult to identify since they not only overlap with those from the $Nd_2Fe_{14}B$ phase but also correspond to only a small fraction of the microstructure. The same reason might also explain the non-existence of ZrB_2 needle phases in the A4 and A12 alloys.
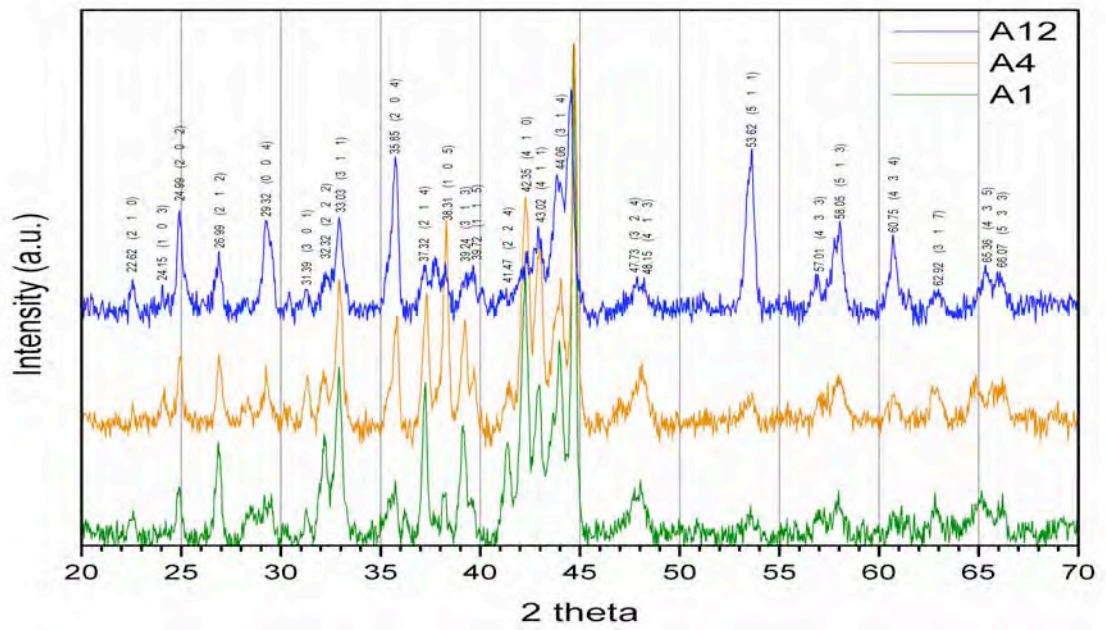
(a)
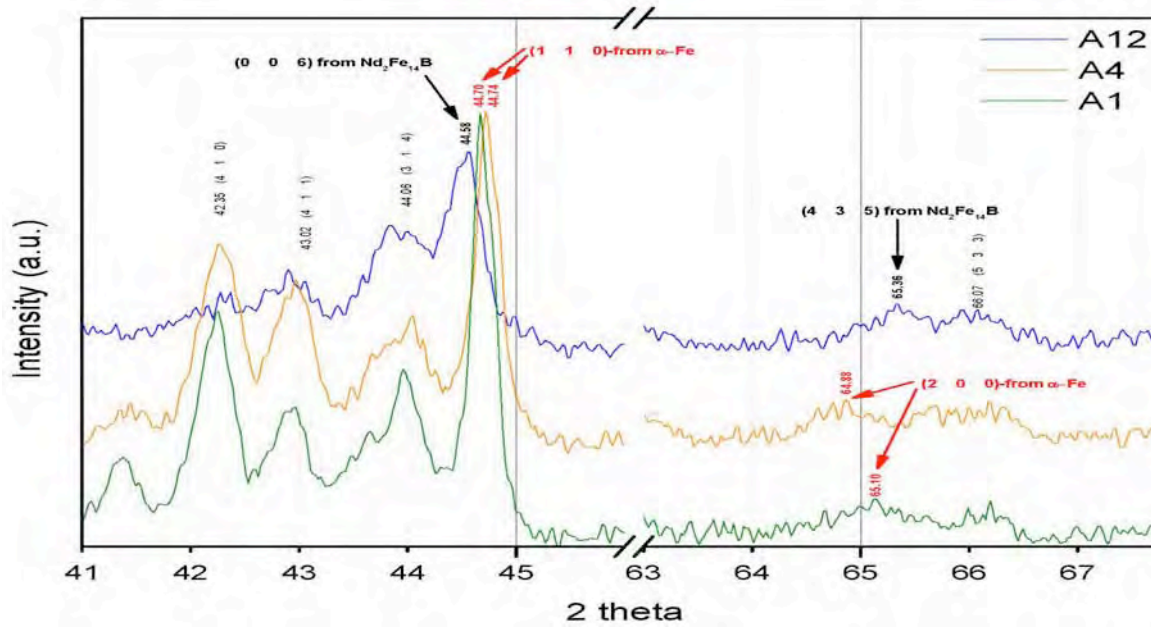
(b)

Figure 5.1 X-ray diffraction patterns from NdFeB and NdFeB-Zr cast alloys. (Peaks from Nd₂Fe₁₄B are labeled in black and α-Fe are labeled in red)
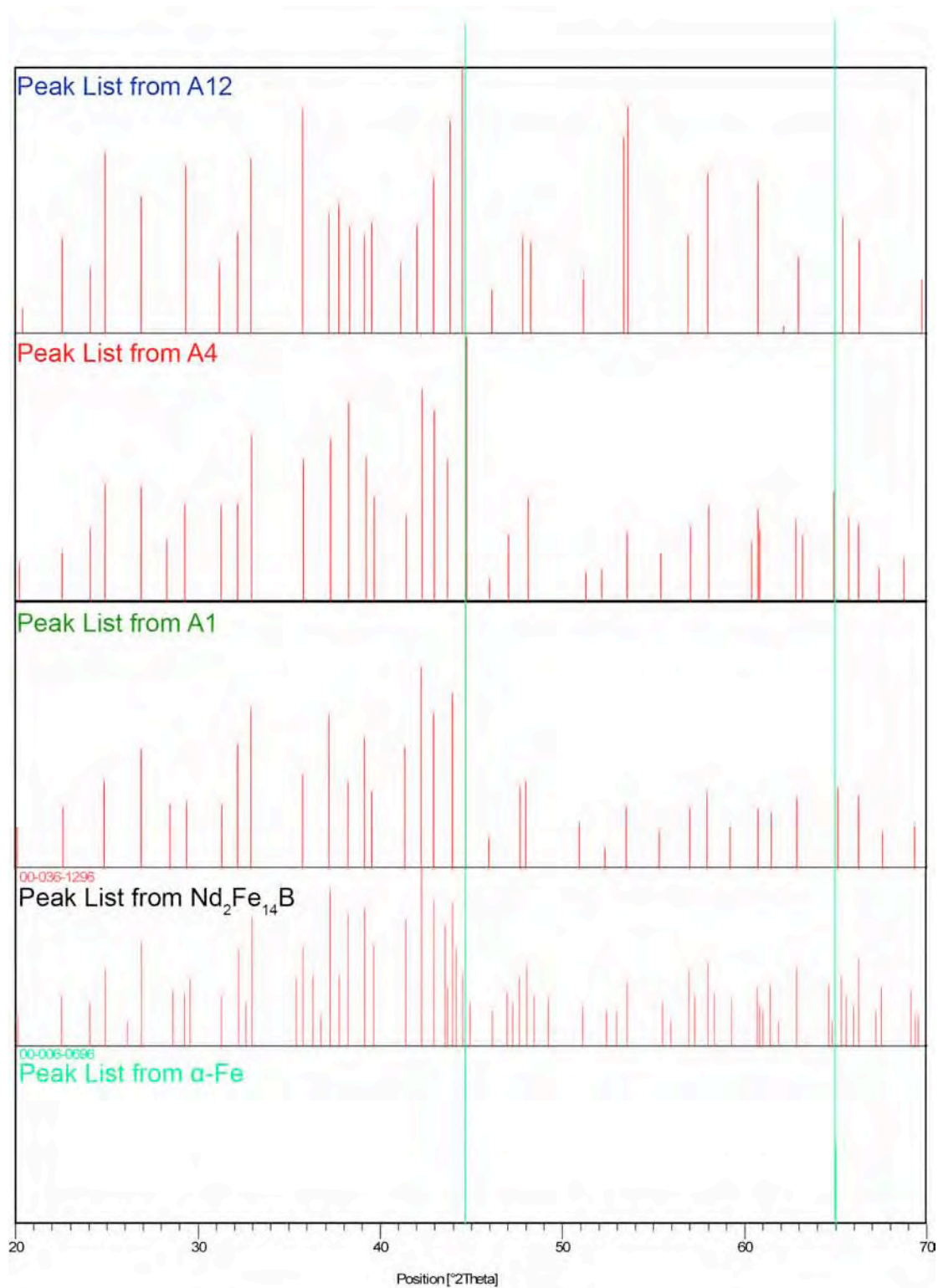
(c)

Figure 5.1 (Continued)

5.1.2 Overall Microstructure

Figure 5.2 (a), (b) and (c) show BSE micrographs of the A1, A4 and A12 alloys. $Nd_2Fe_{14}B$ phase is the matrix phase in NdFeB alloys. The matrix phase in the cast alloys is surrounded mainly by Nd-rich phase. Additional phases, for instance $Nd_1Fe_4B_4$, α-Fe or ZrB_2 can also be observed within the $Nd_2Fe_{14}B$ phase for different alloys, which will be discussed in detail in section 5.1.3.1.

In order to correlate the phase distributions with both the solidification rate and the zirconium additions, low magnification micrographs were used. Note that neither the $Nd_1Fe_4B_4$ nor the ZrB_2 can be observed very clearly at lower magnification. These figures reveal that the proportion of the α-Fe phase (labelled C) was reduced by the addition of ZrB_2 (A12) but not perceptibly by Zr additions alone. Backscattered images were used to measure the volume fraction of α-Fe using image analysis software (ImageJ). Table 5.1 presents the area percentages of the different phases.

The iron contents (~8.1-8.7 vol. %) observed in the present study are lower than those observed by Chang et al (1989) on stoichiometric $Nd_{11.76}Fe_{82.35}B_{5.88}$ (21 vol.% of Fe) and similar to those of Shaaban (2005) on $Nd_{12.7}Fe_{81.3}B_{6.0}$ alloy (7.8 vol.% of Fe). The difference with Chang et al can be attributed to several factors, including mould properties, casting technique, solidification rate and the part of the sample examined.

Table 5.1 The area fractions of the phases in the central regions of the ingots in the NdFeB and NdFeB-Zr cast alloys. (Each result was deduced from 5 BSE micrographs.)

Sample	Area Fraction (%)				
	$Nd_2Fe_{14}B$	$Nd_1Fe_4B_4$	Nd-rich	α-Fe	ZrB_2
A1	80.85±0.64	3.50±0.98	6.95±0.03	8.70±0.17	
A4	78.45±3.04	1.35±0.07	6.80±0.99	8.20±0.29	(5.20±0.42*)
A12	93.60±1.54		4.60±1.25		1.80±0.40

*The ZrB_2 area fraction in A4 appears larger than that in A12: this is because the software mistakenly lumps together all the needles.

Table 5.2 shows the average grain sizes and the phase area in the cast NdFeB-Zr alloys. The grain size of the NdFeB-Zr alloy is defined as the size of the matrix phase ($Nd_2Fe_{14}B$), which was calculated from the SEI micrographs on the etched sample. Phase area is defined as the size of the remaining phases (i.e. Nd-rich, α-Fe, ZrB_2…etc) identified by BEI micrographs. The measured area of both grain size and phase area was first calculated in ImageJ and then converted to the grain/phase size by assuming the grain/phase is spherical in shape. As can be seen, the size of the iron dendrites in the cast alloy also decreases with the amount of zirconium. Since ZrB_2 is a well-known grain refiner, it also affects the size of the $Nd_2Fe_{14}B$, Nd-rich and the $Nd_1Fe_4B_4$ phases.

Table 5.2 The average size (µm) of the grain and phase area in the central region of the ingots in NdFeB and NdFeB-Zr cast alloys. (Each result was deduced from 5 different SEI micrographs.)

Sample	Average Size (µm)			
	Grain	Phases		
	$Nd_2Fe_{14}B$	$Nd_1Fe_4B_4$	Nd-rich	α-Fe
A1	8.12±3.05	0.23±0.16	1.64±0.13	1.49±0.59
A4	3.29±1.55	0.17±0.08	0.92±0.43	0.99±0.42
A12	5.04±3.45		0.43±0.36	
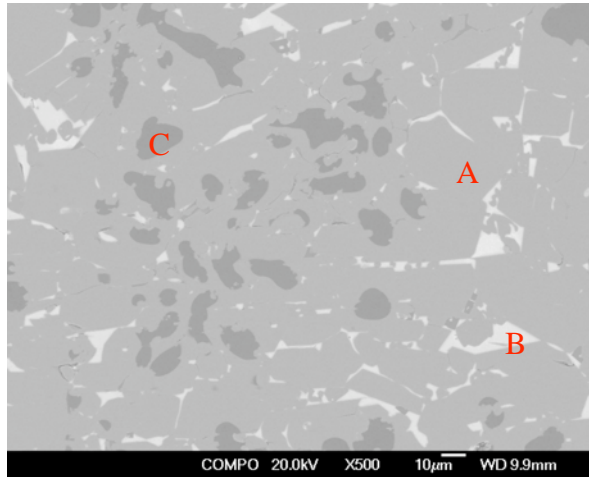
(a) A1 BSE micrograph (lower mag.).
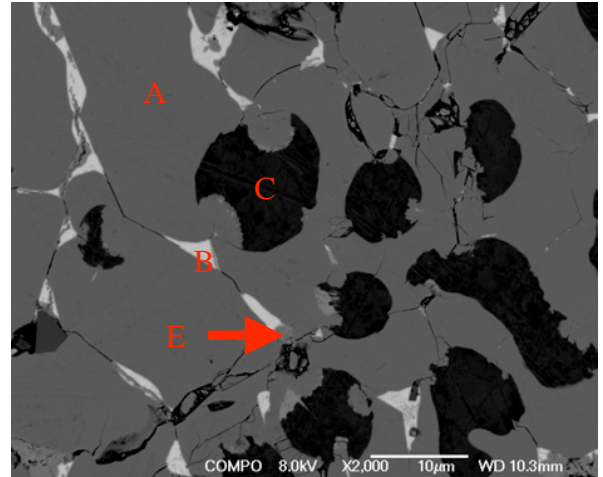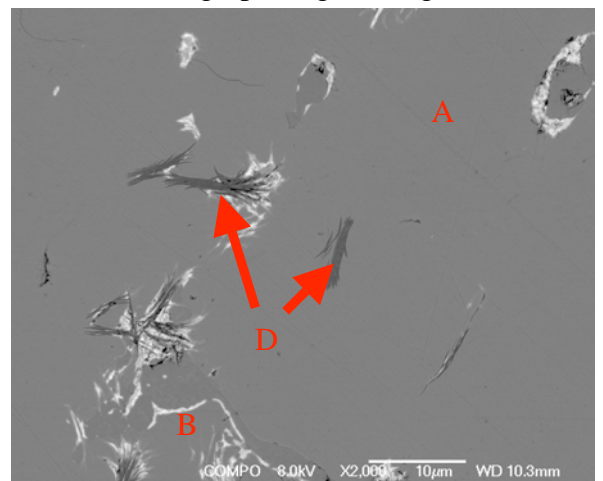
A1 BSE micrograph (higher mag.).
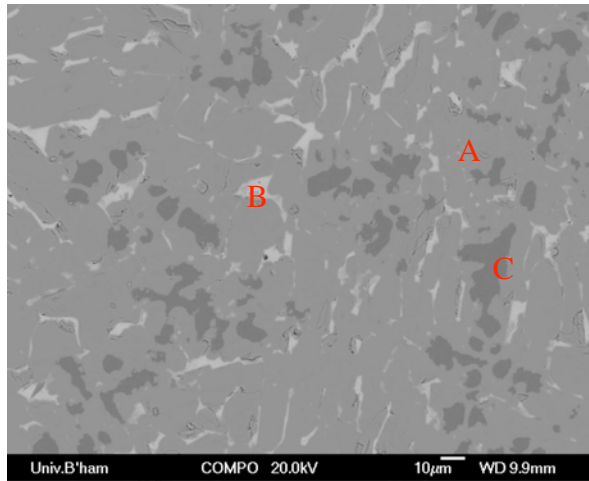
(b) A4 BSE micrograph (lower mag.).
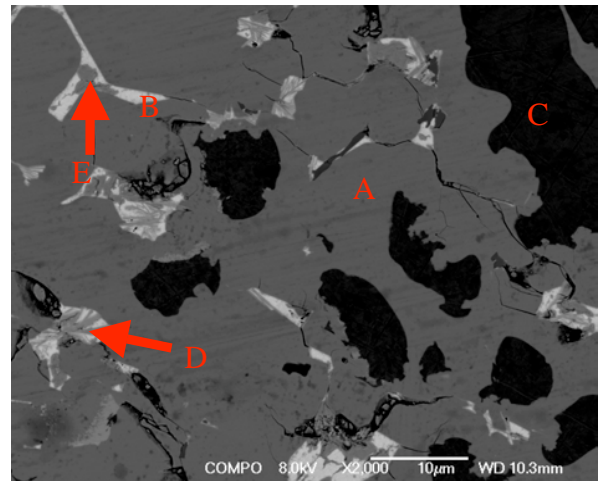
A4 BSE micrograph (higher mag.).
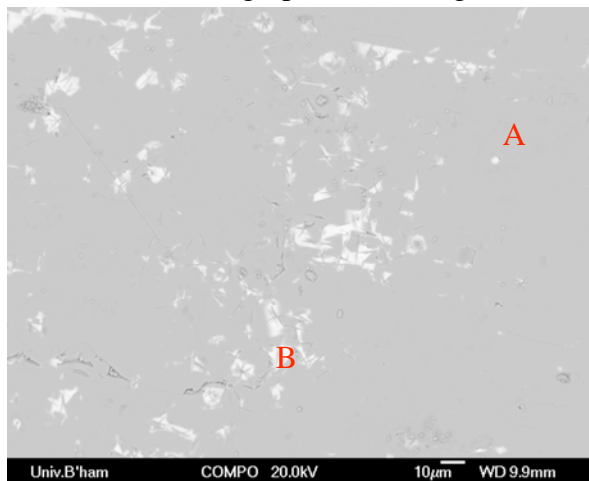
(c) A12 BSE micrograph (lower mag.).

A12 BSE micrograph (higher mag.).

Note: A: $Nd_2Fe_{14}B$, B: Nd-rich phase, C: α-Fe, D: ZrB_2 needle, E: $Nd_1Fe_4B_4$ phase

Figure 5.2 BSE micrographs of cast NdFeB and NdFeB-Zr alloys at lower and higher magnification. (a) A1 (b) A4 (c) A12

5.1.3 Microstructure and Chemical Analysis of Individual Phases in Cast Alloys

5.1.3.1 $Nd_2Fe_{14}B$ phase

Figure 5.3 shows the microstructures of the $Nd_2Fe_{14}B$ matrix phase for three different alloys at 2000X magnification. $NdFe_4B_4$ and α-Fe can be observed inside both A1 and A4; ZrB_2 needles can be observed inside the matrix in A12.

Table 5.3 shows WDX analyses of the matrix phase in the A1, A4 and A12 alloys. The theoretical composition derived from the chemical formula is also provided. The WDX analyses confirm the line compound nature of the matrix phase. It has been confirmed that there is no other detectable element (e.g. Zr or oxygen) in the matrix phase.

**Table 5.3 The composition of the matrix $Nd_2Fe_{14}B$ phase in the cast NdFeB and NdFeB-Zr alloy. (The phase has been analysed 5 times in different places. The highlighted row is the composition derived from the chemical formula.)**

Sample	B (at%)	Fe (at%)	Nd (at%)
$Nd_2Fe_{14}B$	5.88	82.35	11.76
A1	5.87±0.12	82.18±0.58	11.95±0.62
A4	5.93±0.23	82.72±0.63	11.35±0.47
A12	6.02±0.21	82.39±0.53	11.59±0.49

(a)

(b)

(c)
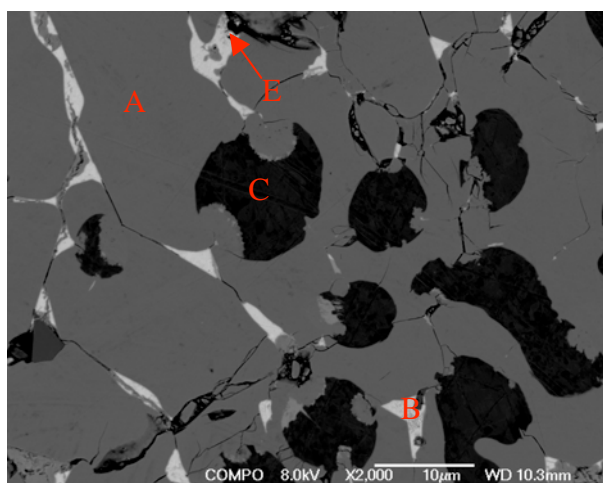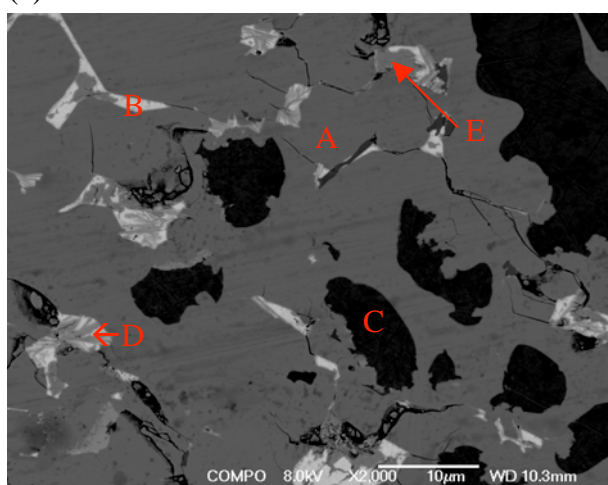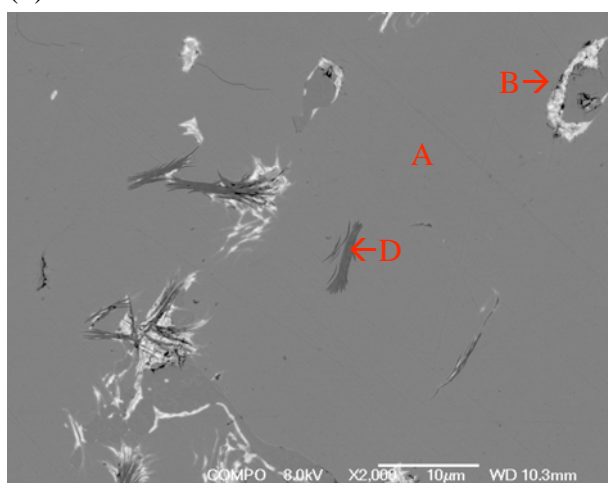
Note: A: $Nd_2Fe_{14}B$, B: Nd-rich phase, C: α-Fe, D: ZrB_2 needles, E: $Nd_1Fe_4B_4$

Figure 5.3 BSE micrographs of the cast NdFeB and NdFeB-Zr alloys (a) A1 (b) A4 (c) A12

5.1.3.2   Nd-rich phase

Figure 5.4 (a), (b) and (c) show high magnification BSE micrographs highlighting the Nd-rich phase in the as-cast NdFeB-Zr alloys. The Nd-rich phase can always be found at the grain boundaries of the $Nd_2Fe_{14}B$ matrix phase. The $Nd_1Fe_4B_4$ phase (labelled E) is always inside the Nd-rich phase (labelled B) in the A1 and A4 alloys.

Table 5.4 shows the WDX results from the Nd-rich phase. The Nd-rich phase in the cast alloys always contains a small amount of oxygen. The oxygen might result from both the casting and the sample preparation processes, because the neodymium is known to be very reactive with oxygen. A small amount of oxygen in the Nd-rich phase is believed to come from the grinding process in water during sample preparation. In addition, a small amount of Fe (~5 at%) has also been detected.

Table 5.4 The composition of the Nd-rich phase in the cast NdFeB and NdFeB-Zr alloys. (The phase has been analysed 5 times in different places.)

Sample	O (at%)	Fe (at%)	Nd (at%)	Zr (at%)
A1	9.72±0.40	4.97±0.62	85.31±0.46	0
A4	9.61±1.66	4.81±0.82	85.50±1.60	0.09±0.03
A12	11.22±1.86	3.46±1.38	84.61±3.16	0.71±0.52

(a)

(b)

(c)
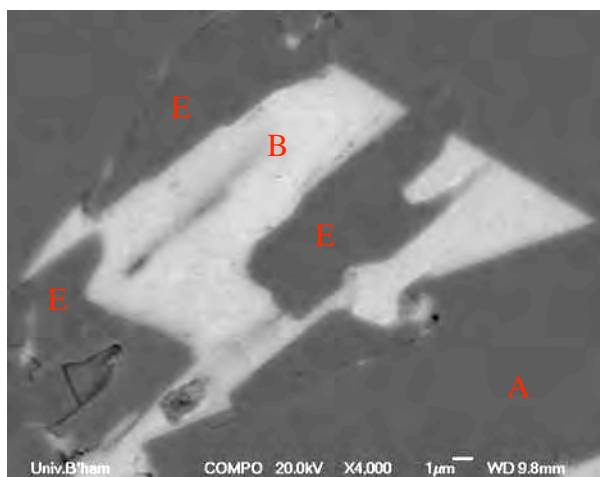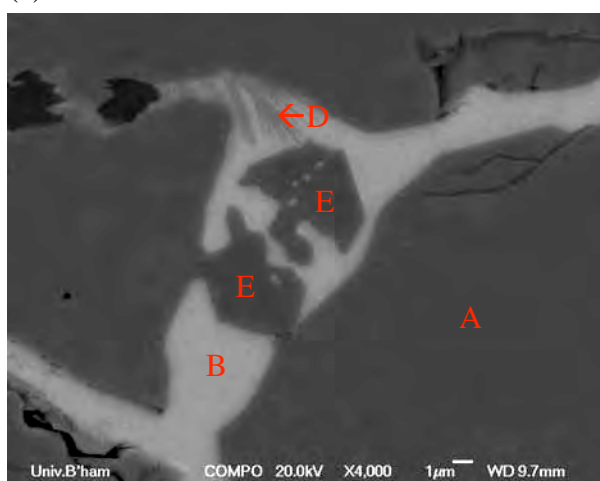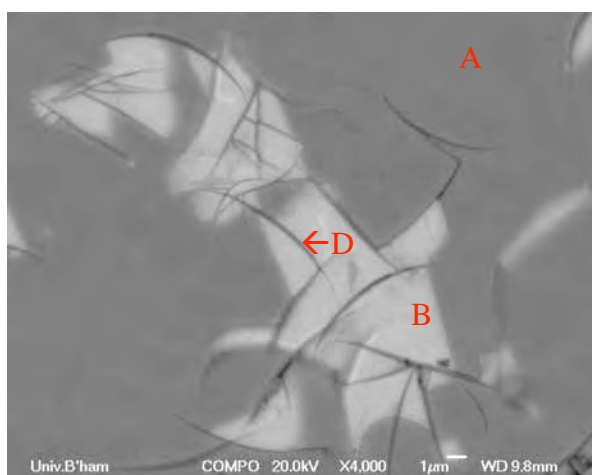
Note: A: $Nd_2Fe_{14}B$, B: Nd-rich phase, D: ZrB_2 needles, E: $Nd_1Fe_4B_4$

Figure 5.4 BSE micrographs of the Nd-rich phase in the cast NdFeB and NdFeB-Zr alloys (a) A1 (b) A4 (c) A12

5.1.3.3   ZrB$_2$ phase

Figure 5.5 (a), (b) and (c) show needles of ZrB$_2$ in the cast alloys. The ZrB$_2$ needles are linked mainly to the Nd-rich phase in the NdFeB-Zr alloys. The difference between A4 and A12 is that the ZrB$_2$ needles in A4 only appear in the Nd-rich phase but appear in both the Nd-rich and the Nd$_2$Fe$_{14}$B phases in A12.

The ZrB$_2$ phase forms mainly as needles in both Zr-containing alloys. However, the shape of the ZrB$_2$ needles is slightly different in A4 and A12. In A4, the needles form as a loose cluster (Figure 5.5 (a)). In A12, however, it forms as a tightly-knit sheaf of needles not only in the Nd-rich phase but as a tight-bundle of needles in the matrix phase (Figure 5.5 (b) and (c)) as well. The ZrB$_2$ needles are both sharper and more curved in the latter case.

Table 5.5 shows the WDX chemical analyses of the ZrB$_2$ needles. Due to beam spreading (~1 μm) in the SEM, X-rays from other phases will be acquired during the WDX analysis of the ZrB$_2$ needles in the A4 and A12 alloys. Thus the WDX results in Table 5.5 can only suggest that there is a large amount of boron and there may be a small amount of iron in the ZrB$_2$ needles. Therefore, the chemical formula of the ZrB$_2$ needles phase is roughly $(Zr_x, Fe_{(1-x)})B_2$ (where x~0.7). Quantitative chemical analysis will also be presented in the TEM-EDX results (section 5.4).

Table 5.5 The composition of the ZrB$_2$-type needles in the A4 and A12 alloys. (The phase has been analysed 5 times in different places. The highlighted row is the composition derived from the chemical formula.)

Sample	B (at%)	Zr (at%)	Fe (at%)
ZrB$_2$	**66.66**	**33.33**	
A4-in NdR	69.40±0.45	21.75±0.33	8.85±0.68
A12-within NdR	66.36±2.39	20.01±1.83	13.63±2.16
A12-in Matrix	69.39±0.52	12.96±0.63	*17.66±0.87

* More likely to overlap with Fe from matrix phase than small amount in Nd-rich area. Hence enhanced value for Fe in $(Zr_x,Fe_{(1-x)})B_2$ phase.
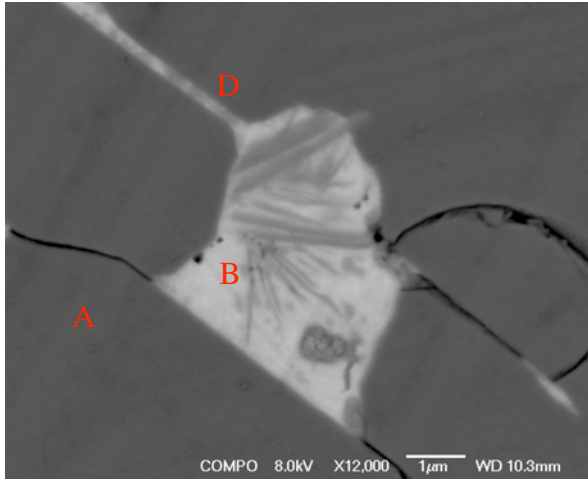
(a) BSE image of ZrB_2 in the Nd-rich phase in A4
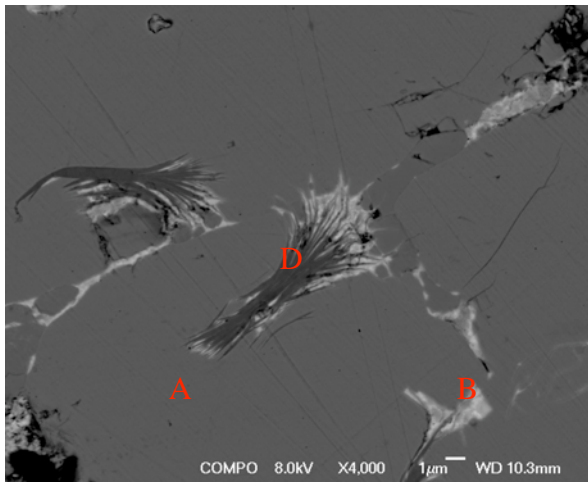
(b) BSE image of ZrB_2 in the Nd-rich phase in A12
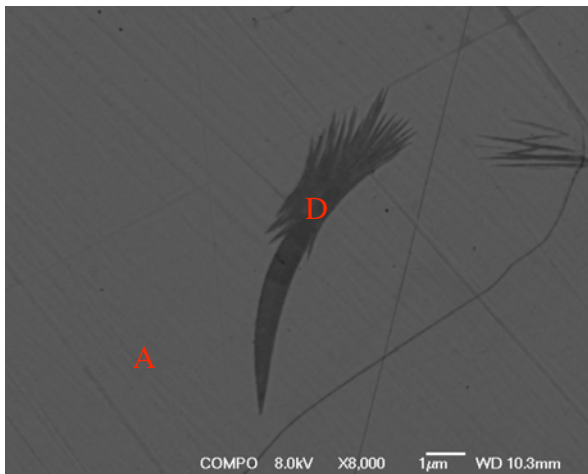
(c) BSE image of ZrB_2 in the matrix phase in A12

Note: A: $Nd_2Fe_{14}B$, B: Nd-rich phase, D: ZrB_2 needles

Figure 5.5 BSE images of ZrB_2 needles in the cast NdFeB-Zr alloys. (a) Within the Nd-rich phase in A4, (b) within the Nd-rich phase in A12 and (c) from the A12 matrix - $Nd_2Fe_{14}B$ - phase.

5.1.3.4 $Nd_{1+\varepsilon}Fe_4B_4$ (ε=0.1)

Figure 5.6 shows the $Nd_{1+\varepsilon}Fe_4B_4$ phase (ε=0.1). $Nd_{1+\varepsilon}Fe_4B_4$ can be observed inside both the $Nd_2Fe_{14}B$ and the Nd-rich phases in A1 and A4, but it only appears within the Nd-rich phase in A12. The theoretical and WDX analyses of $Nd_{1+\varepsilon}Fe_4B_4$ (ε=0.1) are shown in Table 5.6.

Table 5.6 The chemical composition of $Nd_1Fe_4B_4$ in the cast NdFeB and NdFeB-Zr alloys. (The phase has been analysed 5 times in different places. The highlighted row is the composition derived from the chemical formula.)

Sample	B (at%)	Fe (at%)	Nd (at%)
$Nd_{1+\varepsilon}Fe_4B_4$ (ε=0.1)	43.96	43.96	12.09
A1	43.95±0.74	45.34±0.91	10.71±0.73
A4	44.92±0.92	44.01±0.91	11.07±0.87
A12	46.71±0.94	43.29±0.57	10.00±1.08
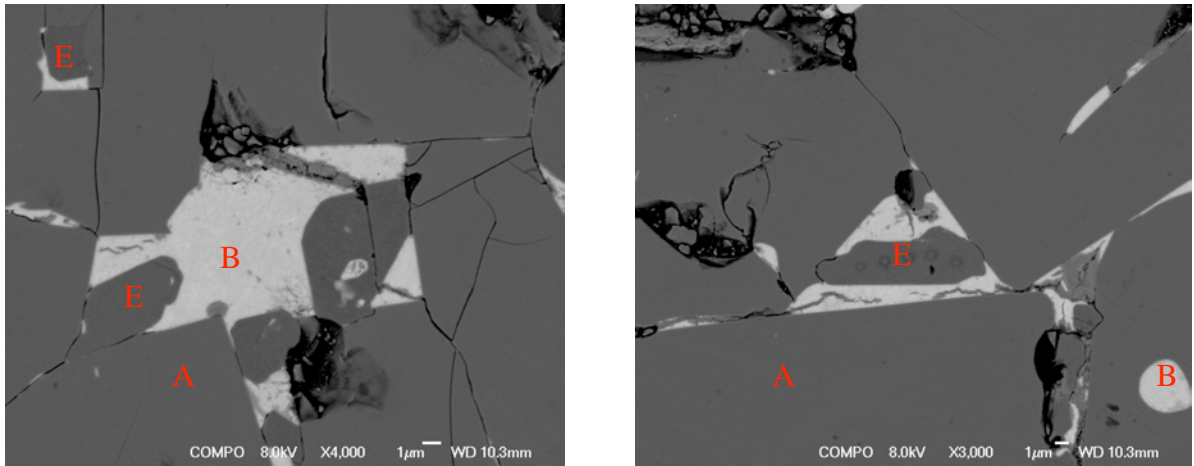
(a) BSE image of $Nd_1Fe_4B_4$ in the matrix and inside the Nd-rich phase in A1.
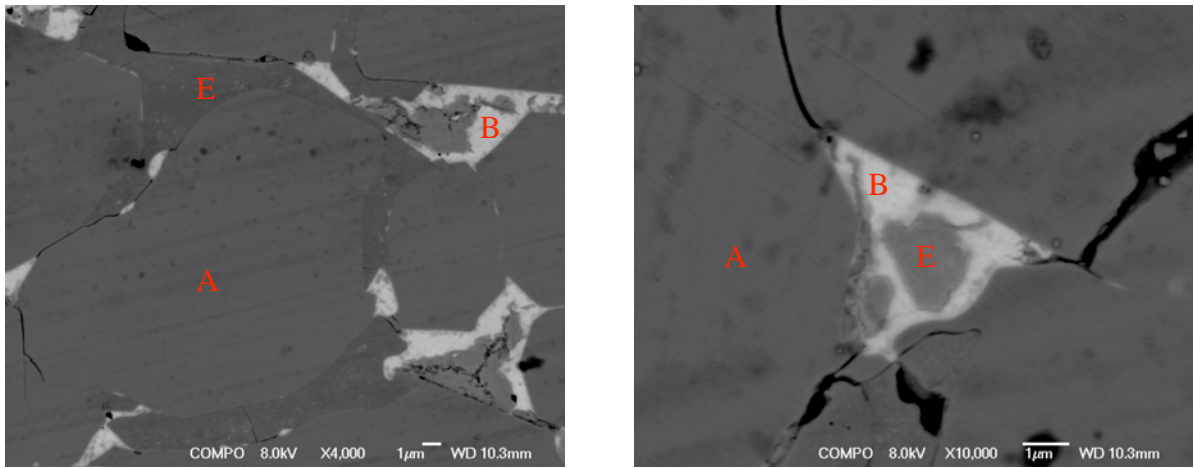
(b) BSE image of $Nd_1Fe_4B_4$ in the matrix and inside the Nd-rich phase in A4.
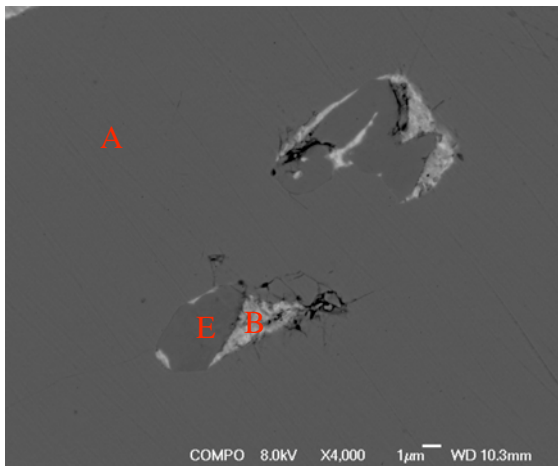
(c) BSE image of $Nd_1Fe_4B_4$ inside the Nd-rich phase in A12.
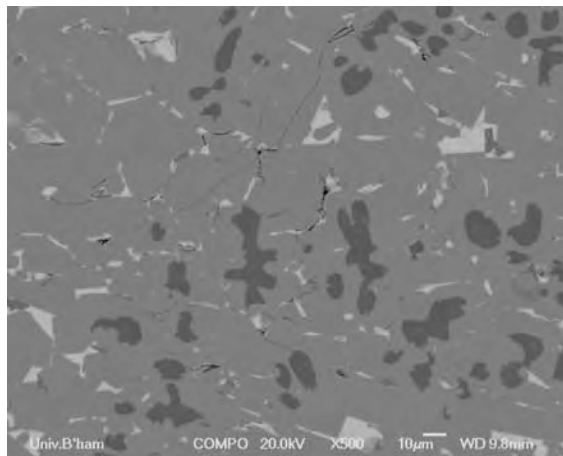
Note: A: $Nd_2Fe_{14}B$, B: Nd-rich phase, E: $Nd_1Fe_4B_4$ phase

Figure 5.6 BSE images of $Nd_1Fe_4B_4$ phase in (a) the matrix phase in A1, (b) the Nd-rich phase in A4 and (c) the Nd-rich phase in A12

5.1.3.5   Fe-rich phase

Figure 5.7 shows BSE micrographs of the α-Fe phase in A1 and A4. α-Fe is always in the matrix grains of A1 and A4 only. There was no significant difference between its chemical composition, as shown in Table 5.7. Note that the small amount of oxygen in α-Fe is probably on the surface as a result of the sample preparations.

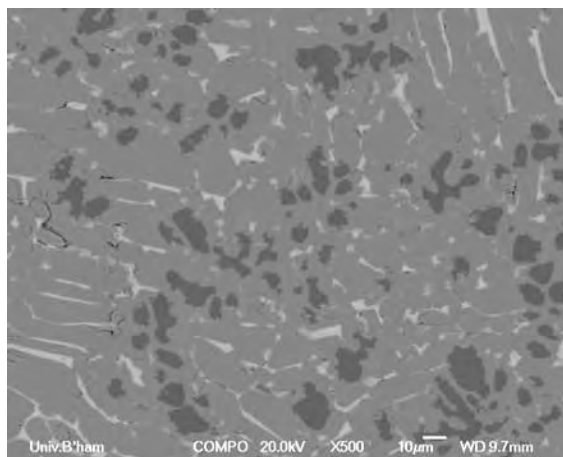**Table 5.7 The chemical composition of α-Fe in the cast NdFeB and NdFeB-Zr alloys.**

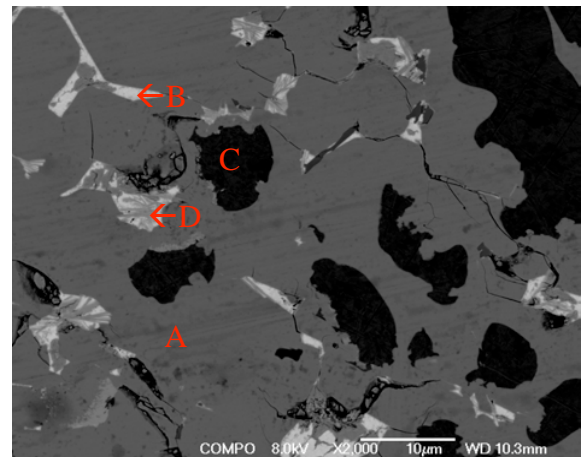| Sample	O (at%)	Fe (at%)
A1	3.14±0.15	96.86±0.15
A4	1.68±0.08	98.32±0.08

(a) A1 BSE micrograph (lower mag.).   A1 BSE micrograph (higher mag.).
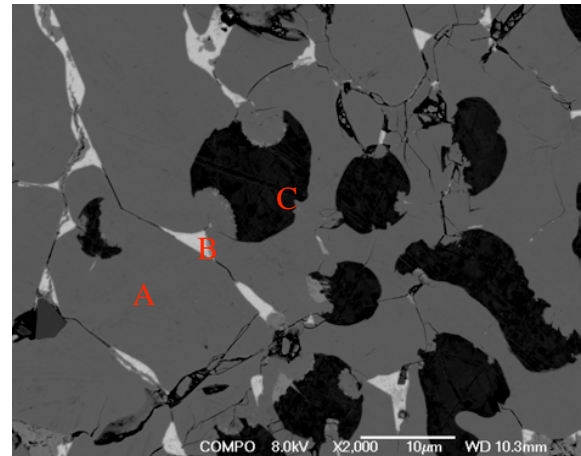
(b) A4 BSE micrograph (lower mag.).   A4 BSE micrograph (higher mag.).

Note: A: $Nd_2Fe_{14}B$, B: Nd-rich phase, C: α-Fe, D: ZrB_2 needles

Figure 5.7 The BSE micrographs of the α-Fe phase in (a) A1 and (b) A4 cast alloys. Low magnification micrographs are on the left.

5.1.4   TEM Characterisation

The composition of the ZrB_2-type needles in alloys A4 and A12 cannot be accurately assessed by SEM equipped with WDX due to the beam spreading and the interaction volume problem significantly affect the EPMA results. TEM was therefore used to investigate the chemical composition and the microstructure of the ZrB_2-type needles. The TEM work was performed on A1, A4 and A12 cast samples respectively.

5.1.4.1   Microstructure and Chemistry of A1

Figure 5.8 shows an overall HAADF image from A1, which consists mainly of three phases: $Nd_2Fe_{14}B$, α-Fe and Nd-rich phase. Nd oxides can also be observed in some parts of the Nd-rich phase. The tungsten layer was deposited as protection against the subsequent ion milling.

Table 5.8 lists the EDX results from a silicon drift detector in TEM for each phase in A1. EDX spectra of these phases are displayed in Figure 5.9 (a)(b)(c)(d). It should be noted that a small amount of Fe (~2.5 at%) exists in the Nd-rich area, confirming the WDX observations.

Figure 5.10(a) is an HAADF image illustrating the Nd-rich and $Nd_2Fe_{14}B$ phases. EDX linescanning along the arrow, as shown in Figure 5.10(b), indicates that the Nd-rich phase contains ~ 3 at% of Fe.
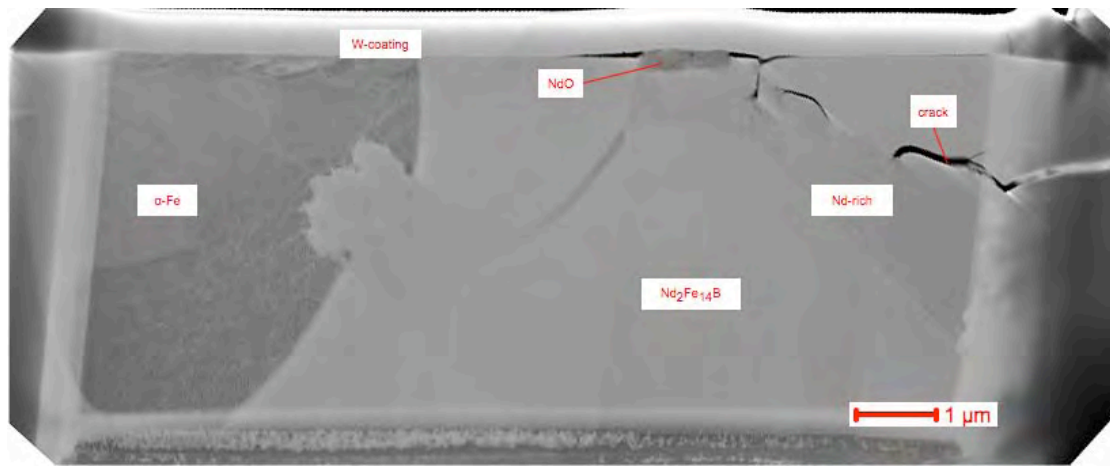
Figure 5.8 HAADF images of cast A1.

Table 5.8 The chemical composition of the phases in A1. (The phases have been analysed 5 times in different places.)

	B (at%)	O (at%)	Fe (at%)	Nd (at%)
$Nd_2Fe_{14}B$	*	2.75±0.28	82.58±0.28	14.66±0.11
Nd-rich		23.82±3.60	2.31±0.31	73.87±3.31
NdO_x		79.19±2.80	0.21±0.30	20.60±2.45
α-Fe		4.84±0.23	95.02±0.25	0.13±0.03

A rough calculation suggests that 90% of the B signal is absorbed by the $Nd_2Fe_{14}B$ making the analyses very inaccurate.
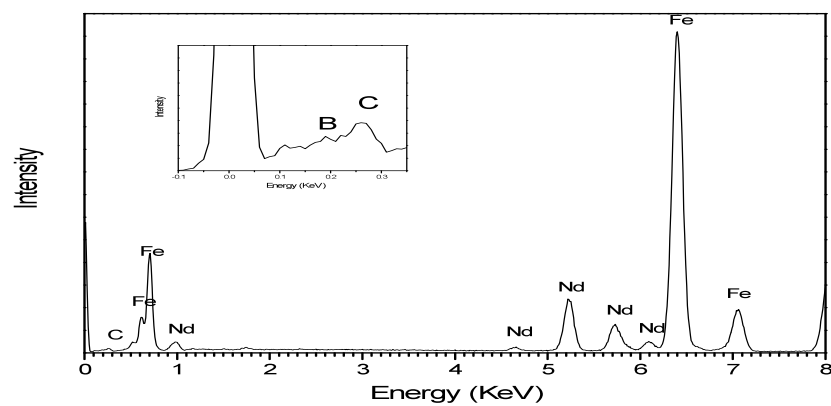
(a) EDX spectrum from the $Nd_2Fe_{14}B$ phase in A1
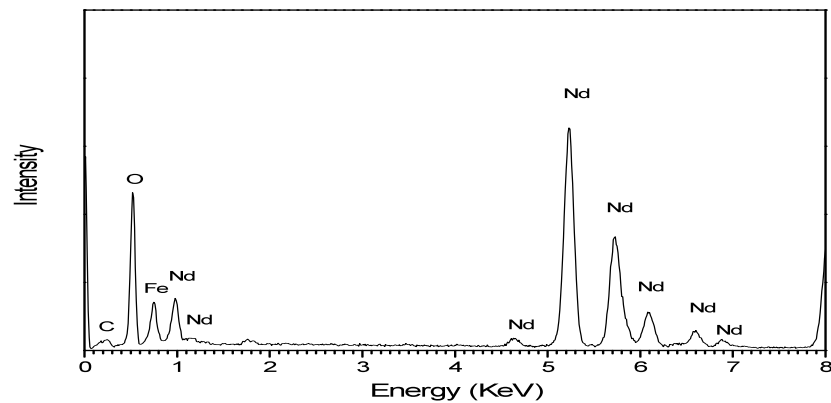
(b) EDX spectrum from the NdO_x phase in A1
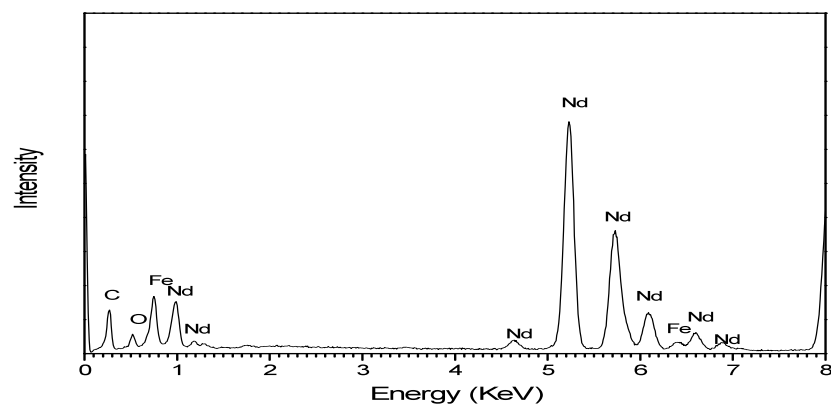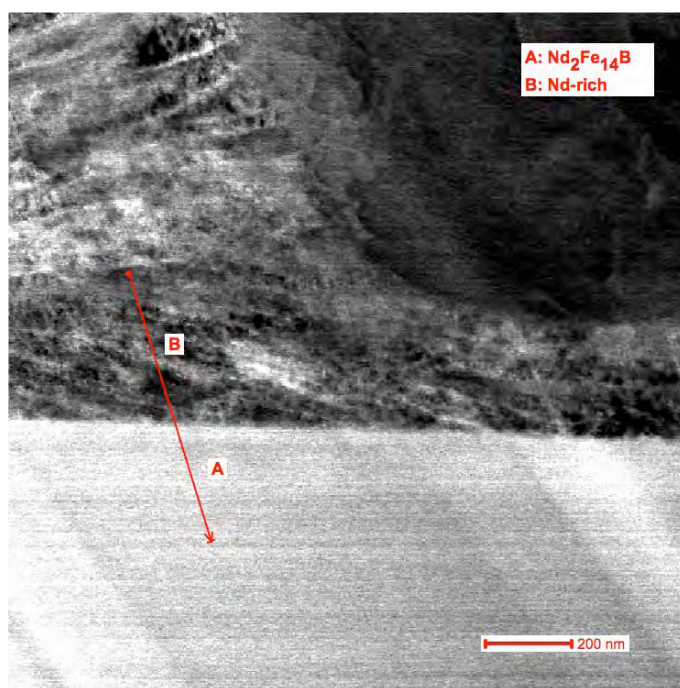

(c) EDX spectrum from the Nd-rich phase in A1
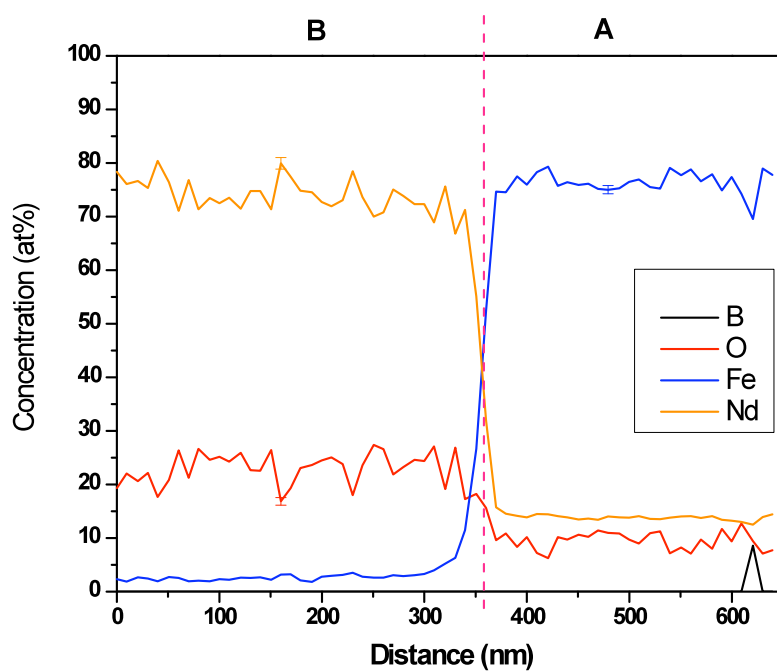
Figure 5.9 TEM/EDX spectra from A1.
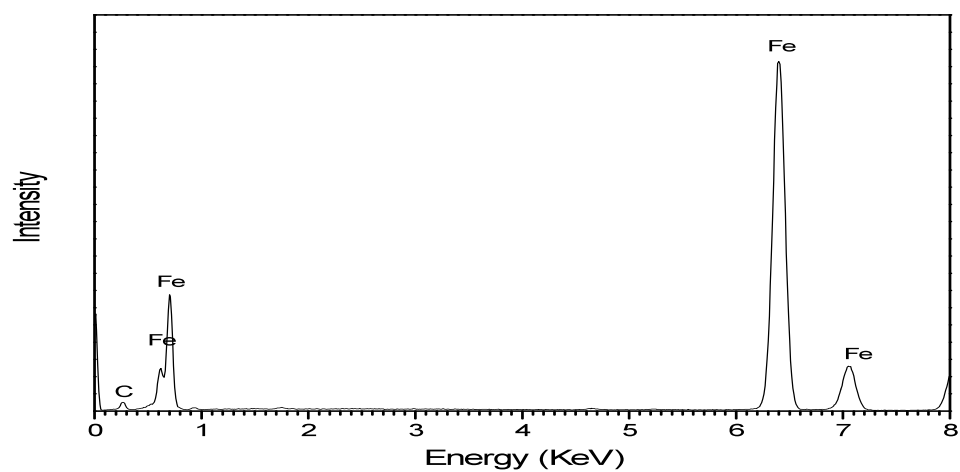
(d) EDX spectrum from the α-Fe phase in A1

Figure 5.9 (continued)

(a)

(b)

Figure 5.10 (a) HAADF image of interface between Nd-rich and Nd$_2$Fe$_{14}$B phases in A1 (b) EDX linescan results along the arrow.

5.1.4.2 Microstructure and Chemistry of A4

Figure 5.11 is an overall HAADF image from an A4 sample. It mainly contains three phases: $Nd_2Fe_{14}B$, Nd-rich and ZrB_2-type needles. Two kinds of ZrB_2-type needles can be observed, small needles (~ 200nm) and normal one (~ 5 μm). Neodymium oxide is also found in some parts of the Nd-rich phase.

The EDX results from a silicon drift detector in TEM for each phase in A4 are listed in Table 5.9. The EDX spectra of these phases are also shown in Figure 5.12(a)(b)(c).

Figure 5.13 is a high magnification HAADF image from a Nd-rich area in A4. A dark acicular extra phase is found to exist in the Nd-rich area. Comparing the chemical analysis results of these small needles with that of the NdO and Nd-rich phases, which are listed in Table 5.10, it is found that these small needle phase contains high Zr (~8.56 at%) and B (~52.19 at%). (See Figure 5.14).

A higher magnification HAADF image showing small needles in the Nd-rich area is shown in Figure 5.15(a) with the EDX linescan results across the needles in Figure 5.15(b). The small needles are composed mainly of B (~60 at%), Nd (~25 at%) and a small amount of Zr (~8 at%), O (~6 at%) and Fe (~3 at%). Therefore, it can be assumed that these small needles are the precursor of the ZrB_2-type needles in A4.

Figure 5.16 is an HAADF image from the Nd-rich phase between the ZrB_2-type needles. The chemical analysis of this area is shown in Table 5.11. A comparison of the chemical analysis results from the Nd-rich phase and that from the Nd-rich phase between the ZrB_2-type needles, revealed that the latter contains a higher oxygen content, which implies the ZrB_2-type needles could act as a barrier layer against the oxidation of the Nd-rich phase.

The ZrB$_2$-type needles in A4 were also examined under HAADF, as shown in Figure 5.17(a). The DP achieved from the ZrB$_2$-type needles in A4 (as shown in Figure 5.17(b)) is consistent with an HCP structure with lattice parameters a= 3.26±0.04 Å and c= 3.53±0.08 Å, respectively.

EDX linescanning (Figure 5.17(c)) was carried out along the arrow shown in Figure 5.17(a). Region B is found to be a Nd-rich phase with around 65 at% of Nd and ~ 20 at% of oxygen plus a small amount of Zr (~5 at%) and Fe (~3 at%).

In region C, with higher B content, it is found that ZrB$_2$-type needles are composed mainly of B (65 at%) and Zr (15 at%) with around 5 at% of Nd, Fe and O.
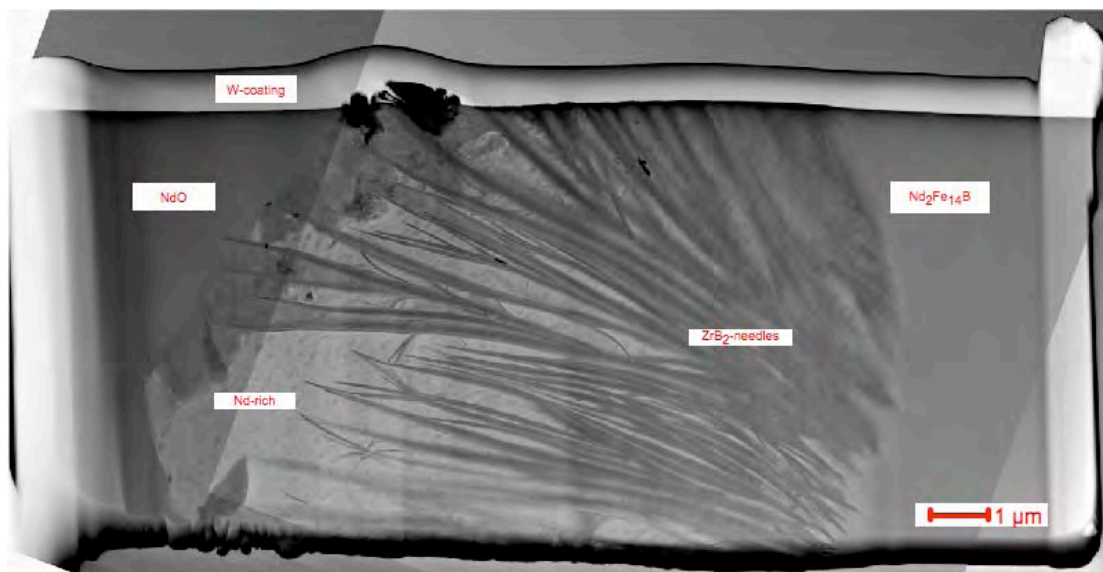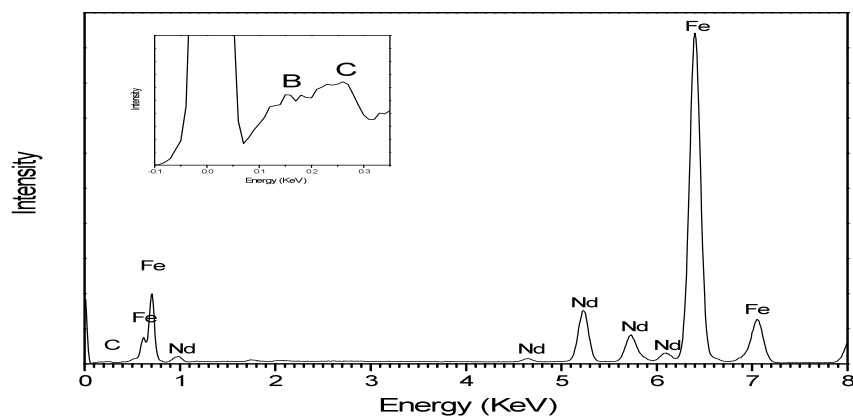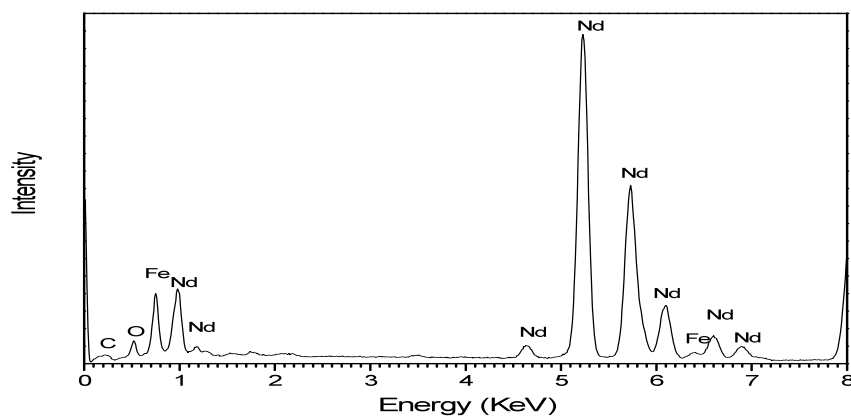
Figure 5.11 HAADF images of cast A4.

Table 5.9 The chemical composition of the phases in A4. (The phases have been analysed 5 times in different places.)

	B (at%)	**O (at%)**	**Fe (at%)**	**Zr (at%)**	**Nd (at%)**
Nd₂Fe₁₄B	*	3.70±0.43	81.73±0.37	0.37±0.07	14.20±0.08
Nd-rich		22.78±1.62	2.16±0.08	0.59±0.19	74.48±1.68
NdOₓ		78.20±1.80	0.31±0.30	0.79±0.21	20.60±2.45
ZrB₂-type needles	66.92±2.64	3.81±1.27	8.30±0.53	19.68±0.87	1.28±0.03

* A rough calculation suggests that 90% of the B signal is absorbed by the $Nd_2Fe_{14}B$ making the analyses very inaccurate.

(a) EDX spectrum from the $Nd_2Fe_{14}B$ phase in A4
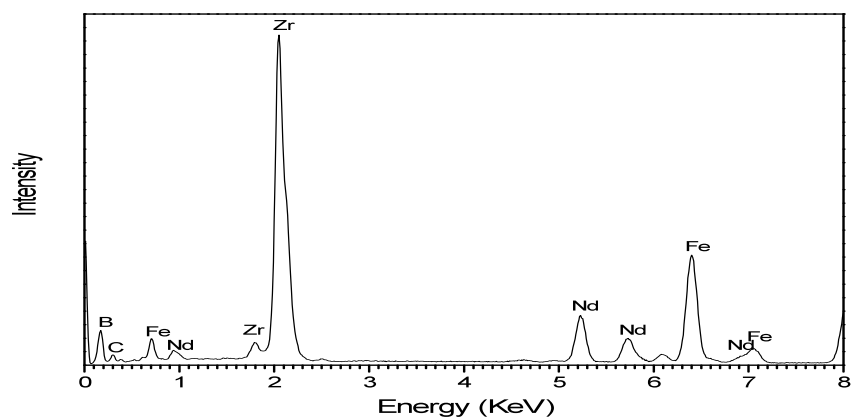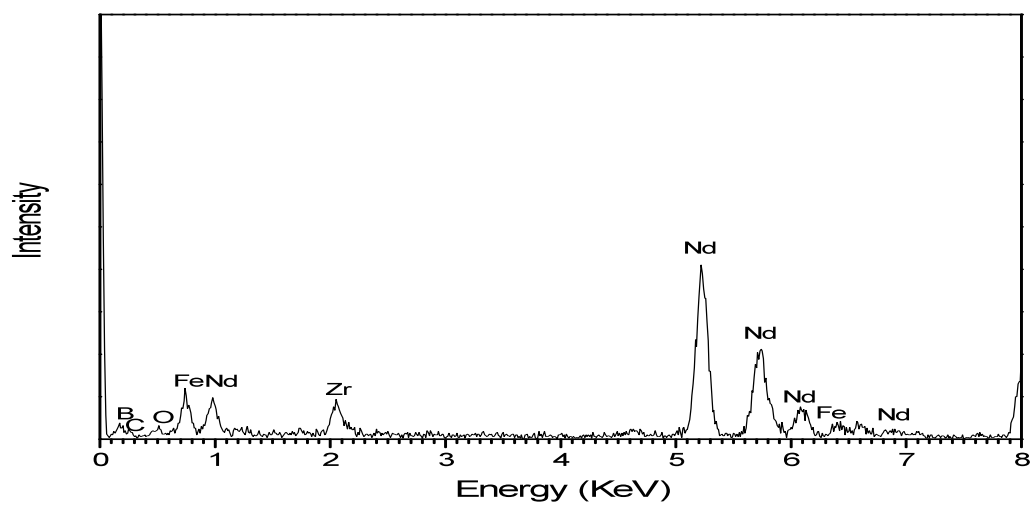

(b) EDX spectrum from the Nd-rich phase in A4

(c) EDX spectrum from the ZrB_2-type needles in A4

Figure 5.12 TEM/EDX spectra from A4.

Figure 5.13 HAADF image from the Nd-rich area in A4.

Table 5.10 The chemical compositions of the phases shown in Figure 5.13. (The phases have been analysed 5 times in different places.)

	B (at%)	O (at%)	Fe (at%)	Zr (at%)	Nd (at%)
Nd-rich		19.76±0.21	0.46±0.01	1.37±0.15	78.44±0.06
Small needles	52.19±1.72	6.49±1.85	2.07±0.19	8.56±0.01	30.69±1.97
NdO$_x$		31.45±2.45	3.75±0.52	1.07±0.83	63.73±1.10

(a) EDX spectrum from the small needles in the Nd-rich phase in A4
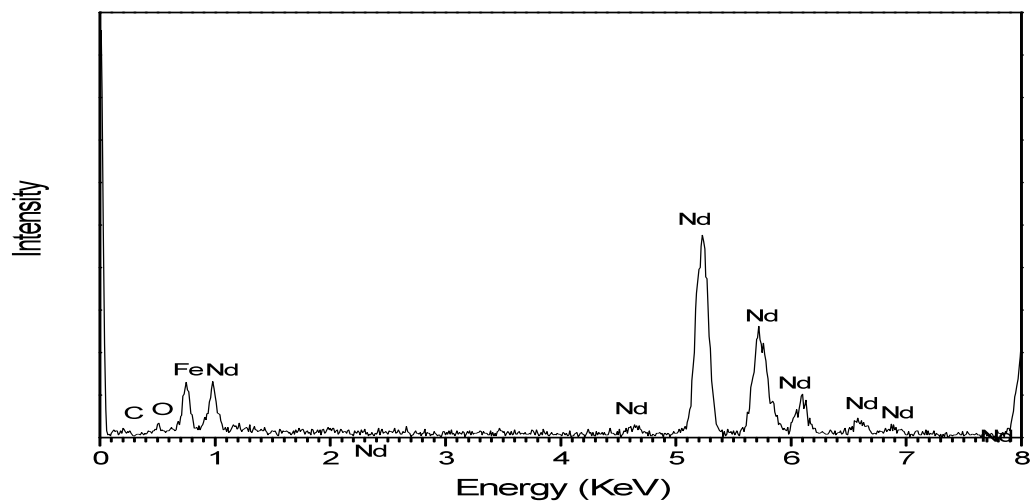
(b) EDX spectrum from the Nd-rich phase beside the small needles in A4
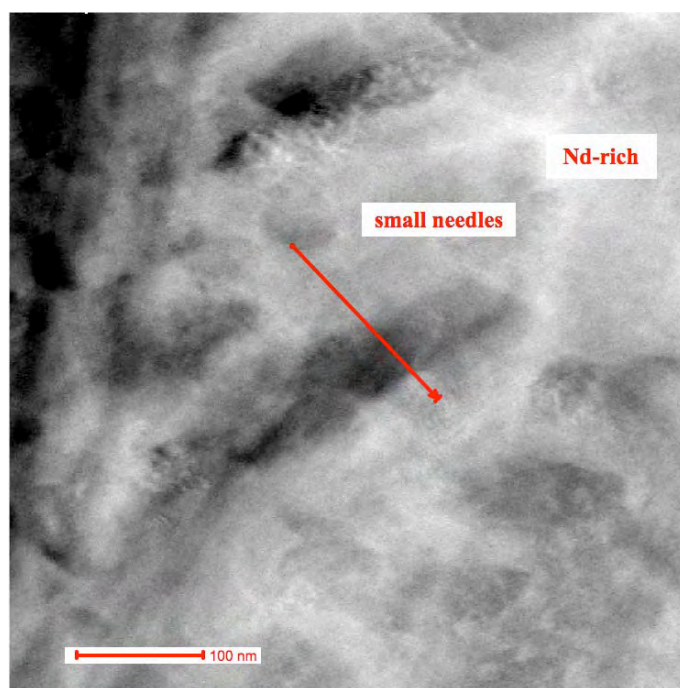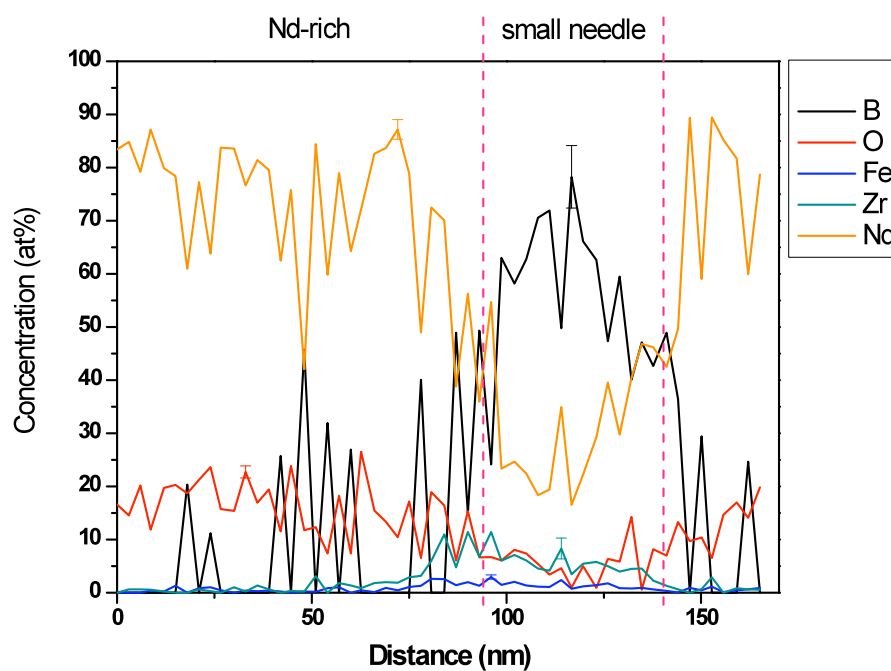
Figure 5.14 TEM/EDX spectra from the Nd-rich area in A4.

(a)

(b)

Figure 5.15 (a) HAADF image of the small needles in the Nd-rich phase of A4. (b) EDX linescan results along the arrow.
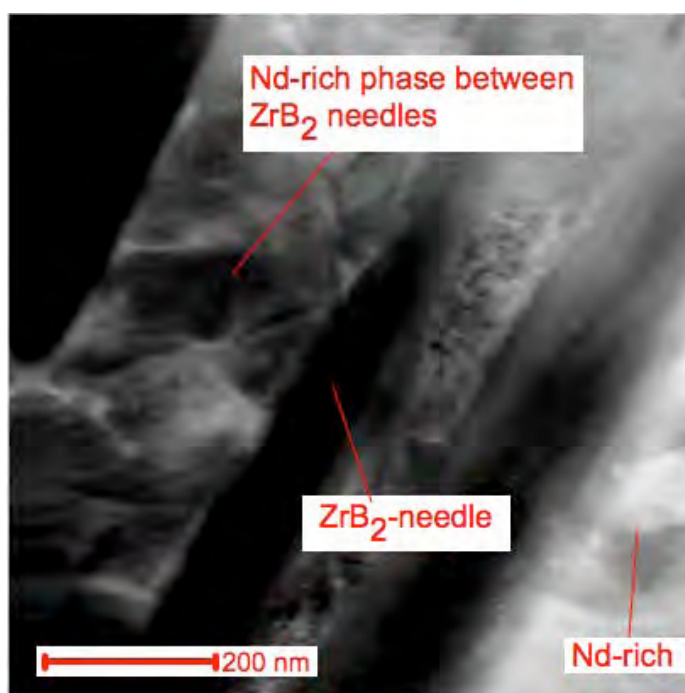
Figure 5.16 HAADF image from the Nd-rich between the ZrB$_2$ needles in A4.

Table 5.11 The chemical composition of the Nd-rich between the ZrB$_2$ needles. (The phases have been analysed 5 times in different places.)

	O (at%)	Fe (at%)	Zr (at%)	Nd (at%)
Nd-rich phase between ZrB$_2$-type needles	45.30±3.13	0.40±0.07	0.47±0.21	53.83±3.37
Nd-rich	25.54±3.56	0.38±0.12	0.27±0.14	73.80±3.39
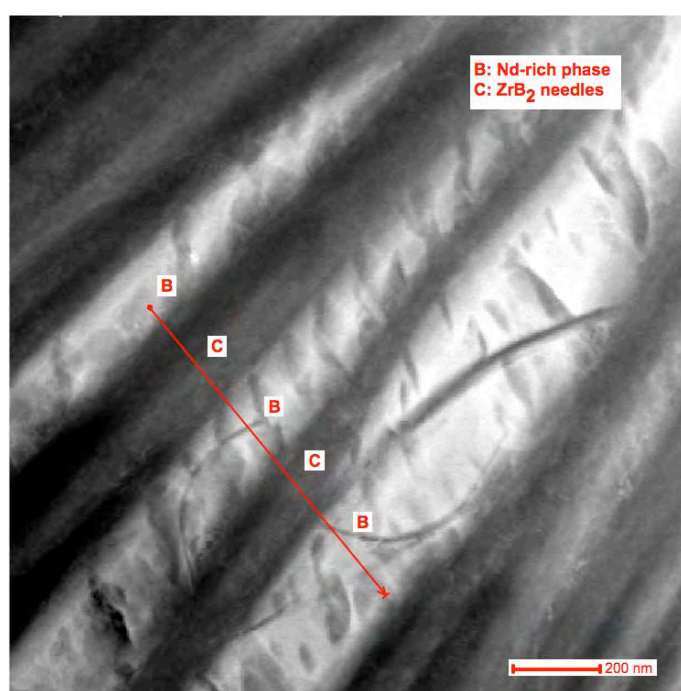
(a)

$[0\bar{1}12]$

(b)

(c)

Figure 5.17 (a) ZrB$_2$-type needles in a Nd-rich grain of A4 and (b) DP from the ZrB$_2$-type needles. (c) EDX linescan results along the arrow.

5.1.4.3 Microstructure and Chemistry of A12

Sample A12 was examined under HAADF, as shown in Figure 5.18. Three phases were found: $Nd_2Fe_{14}B$, Nd-rich and ZrB_2-type needles.

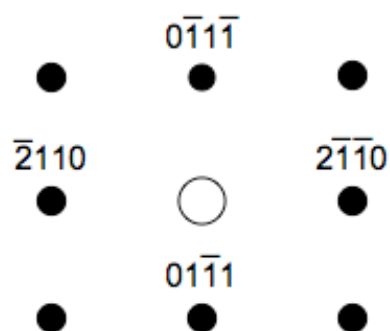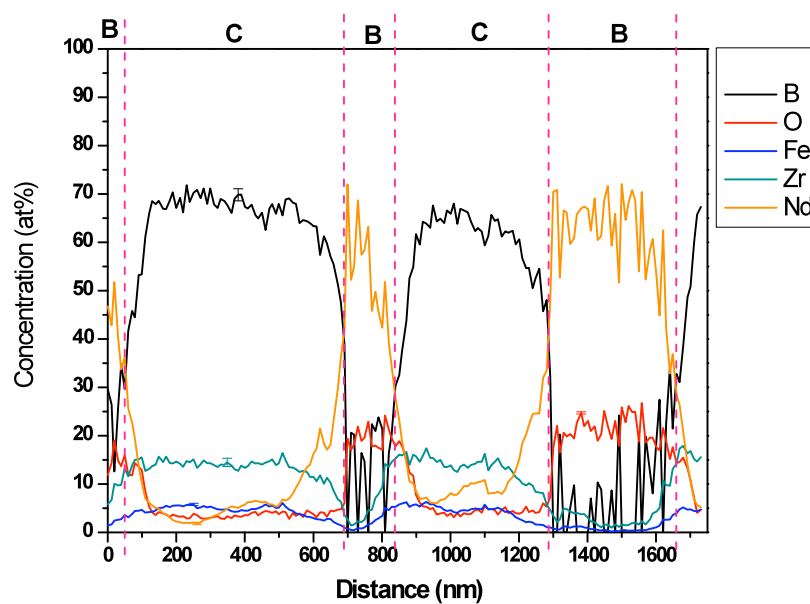The EDX results from a silicon drift detector in TEM for each phase in A12 are shown in Table 5.12. The EDX spectra of these phases are also shown in Figure 5.19(a)(b)(c).

An HAADF image of the needle phase in A12 is shown in Figure 5.20(a) with an EDX linescan along the arrow, as may be seen in Figure 5.20(b). Region A is the $Nd_2Fe_{14}B$ phase: it shows a high Fe concentration (~70 at%) with ~15 at% of Nd but no Zr. The linescan results from region B, the higher Nd content region, demonstrate that region B is composed mainly of around 60 at% of Nd with ~35 at% of oxygen and ~3 at% of Fe. In region C, the high Zr content region, the ZrB_2-type needles are mainly composed of around 15 at% of Zr and 75 at% of B with a small, but significant amount of Fe (~5 at%).

The DPs from the ZrB_2-type needles in A12 are displayed in Figure 5.21(a) and (b), which demonstrate an HCP structure for the needles with lattice parameters of a=3.29±0.02 Å and c=3.52±0.07 Å. Compared with the DPs from the ZrB_2-needles in A4, both ZrB_2-needles in A4 and A12 has the same crystal structure.

In order to understand the elemental distributions, a TEM quantitative map from the needles in A12 is also shown in Figure 5.22. The quantitative map was first collected in the TEM and then analysed via INCA software. The quantitative map of Fe also provides evidence that Fe exists in the ZrB_2-type needles. The dark line in the boron map is probably caused by beam damage during the EDX linescan.
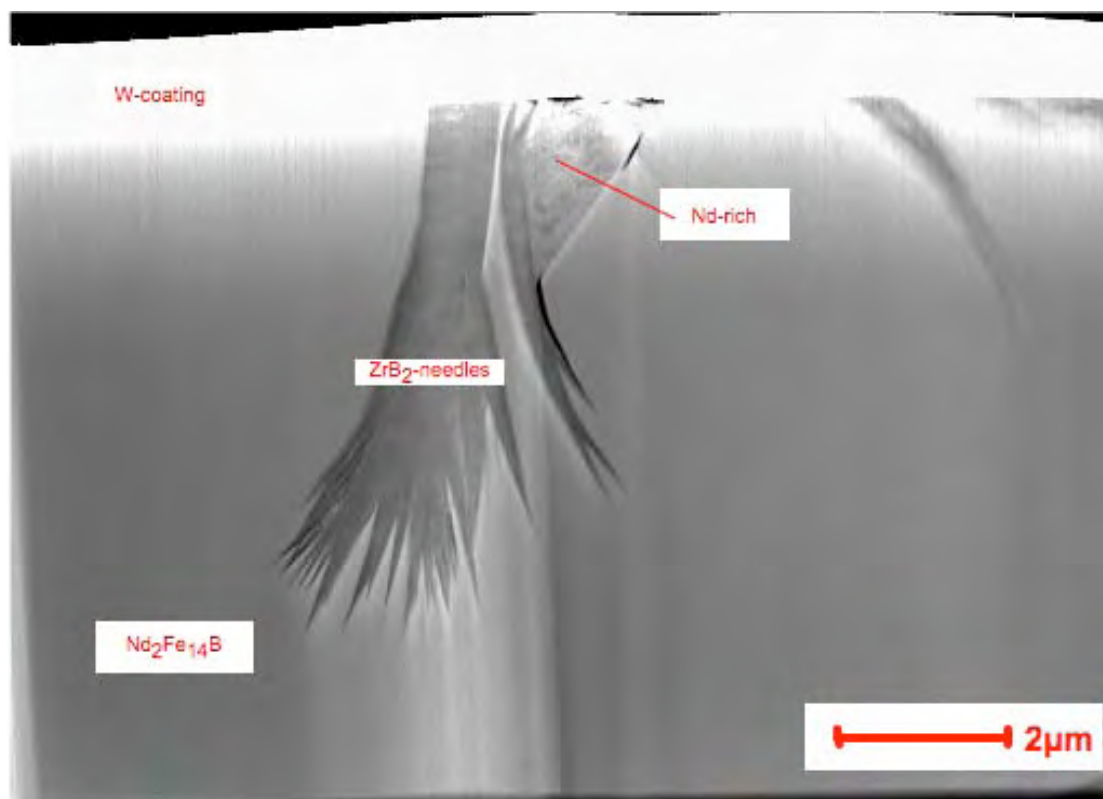
Figure 5.18 HAADF images of cast A12

Table 5.12 The chemical composition of the phases in A12. (The phase has been analysed 5 times in different places.)

	B (at%)	O (at%)	Fe (at%)	Zr (at%)	Nd (at%)
$Nd_2Fe_{14}B$	(1.56±0.85*)	2.29±0.39	81.03±0.58	0.62±0.12	14.50±0.15
Nd-rich		5.28±0.98	3.24±0.25	1.60±0.24	89.89±0.73
ZrB_2-type needles	75.03±1.48	2.60±0.29	4.37±0.31	17.61±1.19	0.40±0.05

* A rough calculation suggests that 90% of the B signal is absorbed by the $Nd_2Fe_{14}B$ making the analyses very inaccurate.
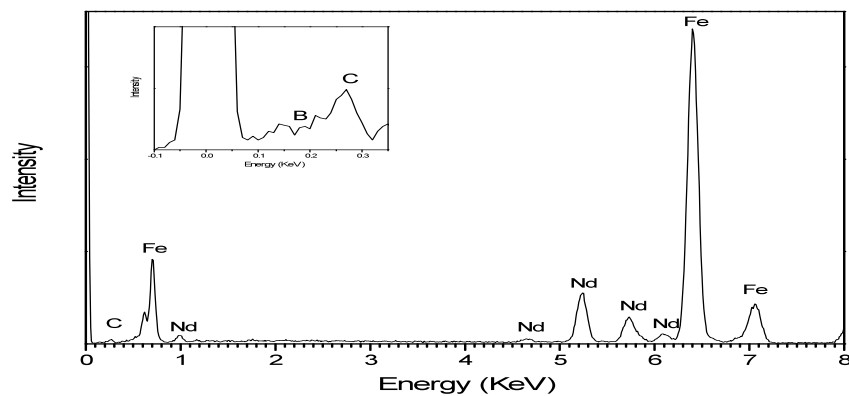
(a) EDX spectrum from $Nd_2Fe_{14}B$ in A12
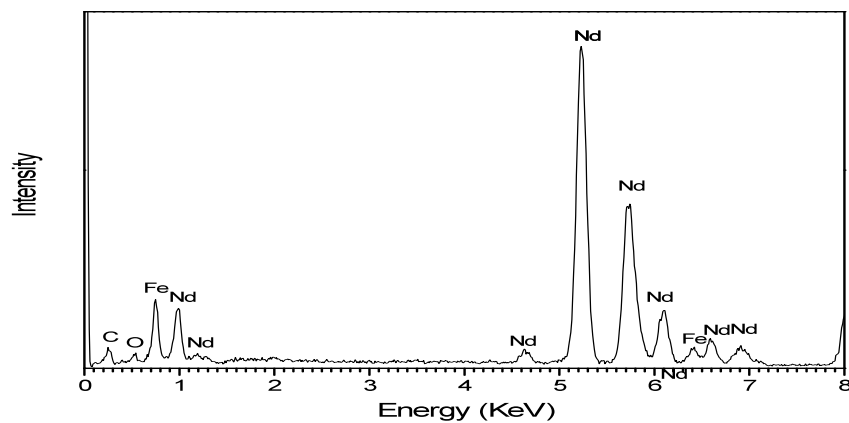
(b) EDX spectrum from the Nd-rich phase in A12
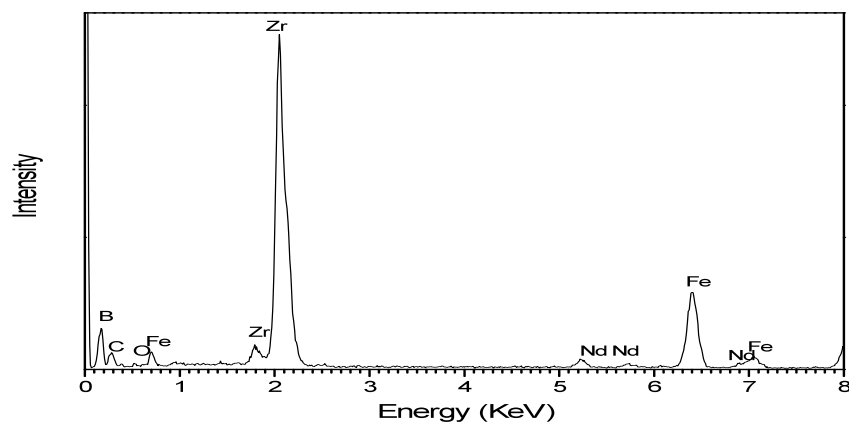
(c) EDX spectrum from the ZrB_2-type needles in A12

Figure 5.19 TEM/EDX spectra from A12.
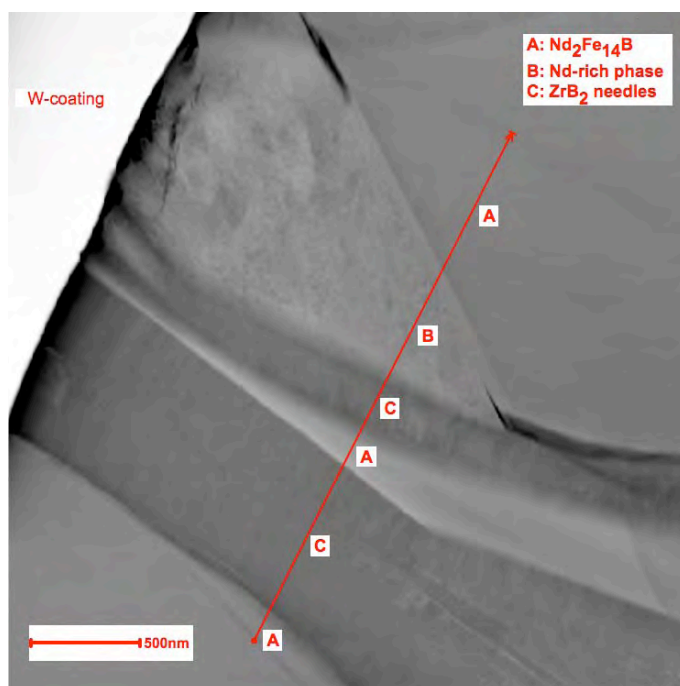
(a) HAADF image of the phases in A12
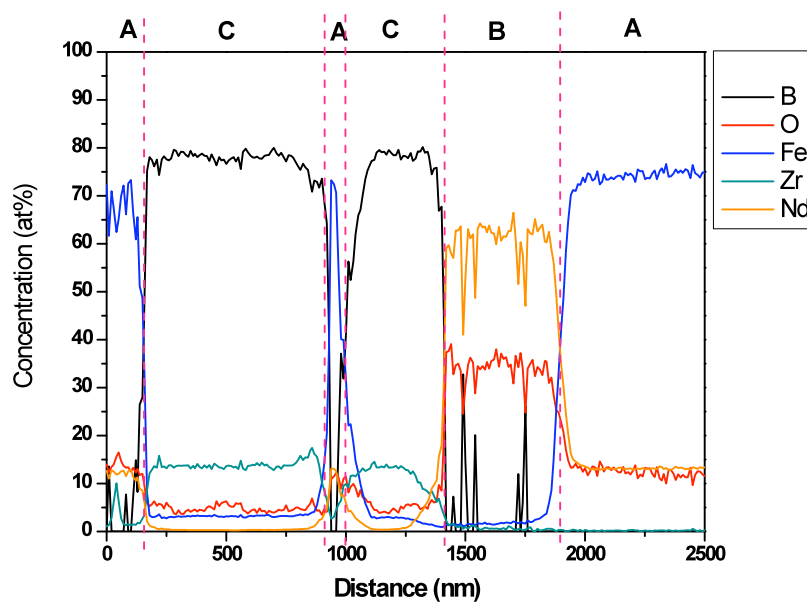
(b) EDX linescan results across three different phases in A12

Figure 5.20 (a) HAADF image from ZrB$_2$-type needles in A12. (b) EDX linescan results along the arrow.

[10$\bar{1}$0]

(a)

[$\bar{1}$1$\bar{2}$0]

(b)
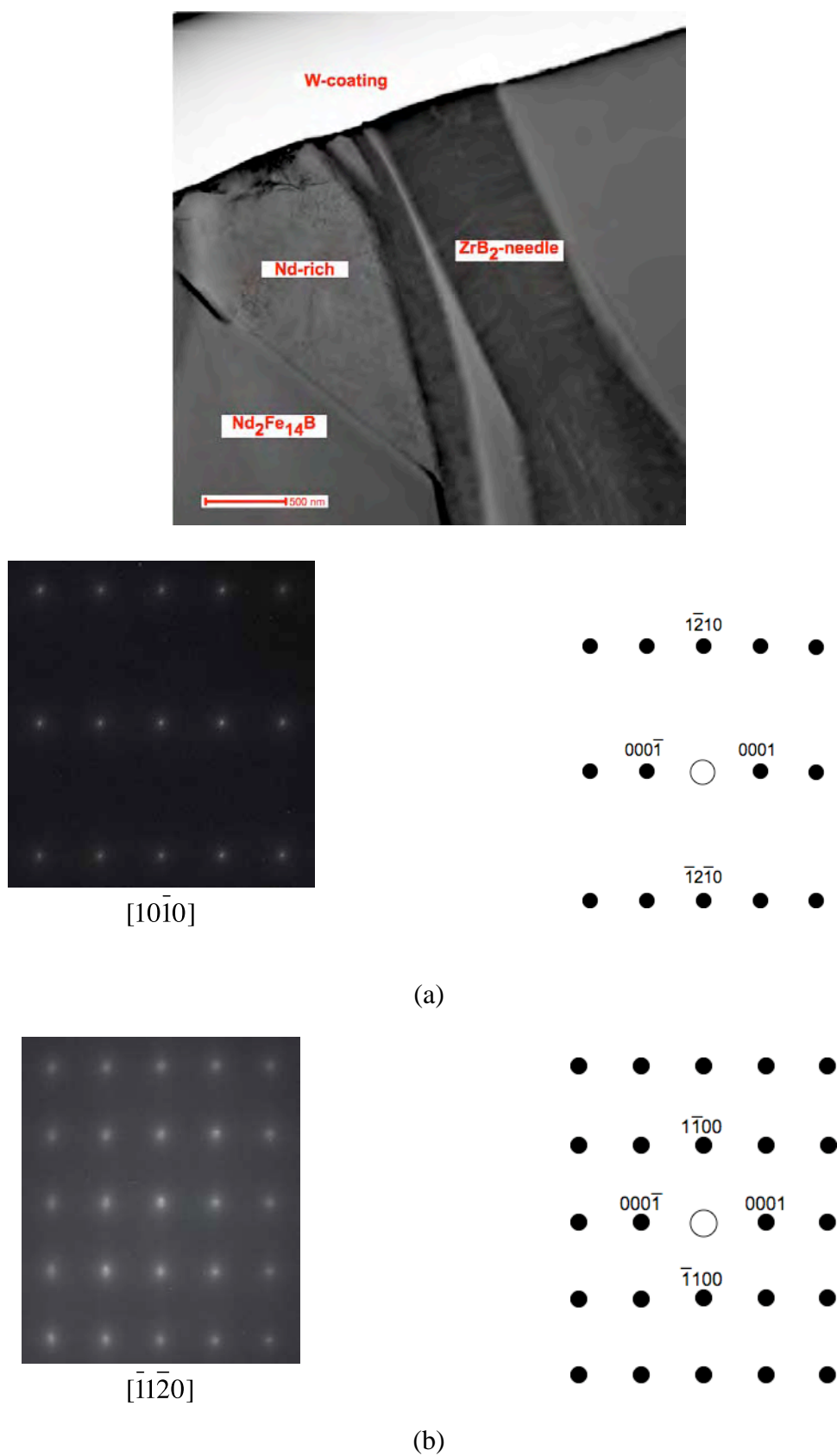
Figure 5.21 DPs from the ZrB$_2$-type needles in A12.
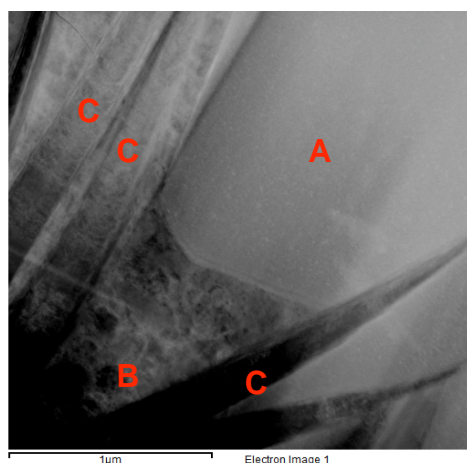
(a) HAADF image
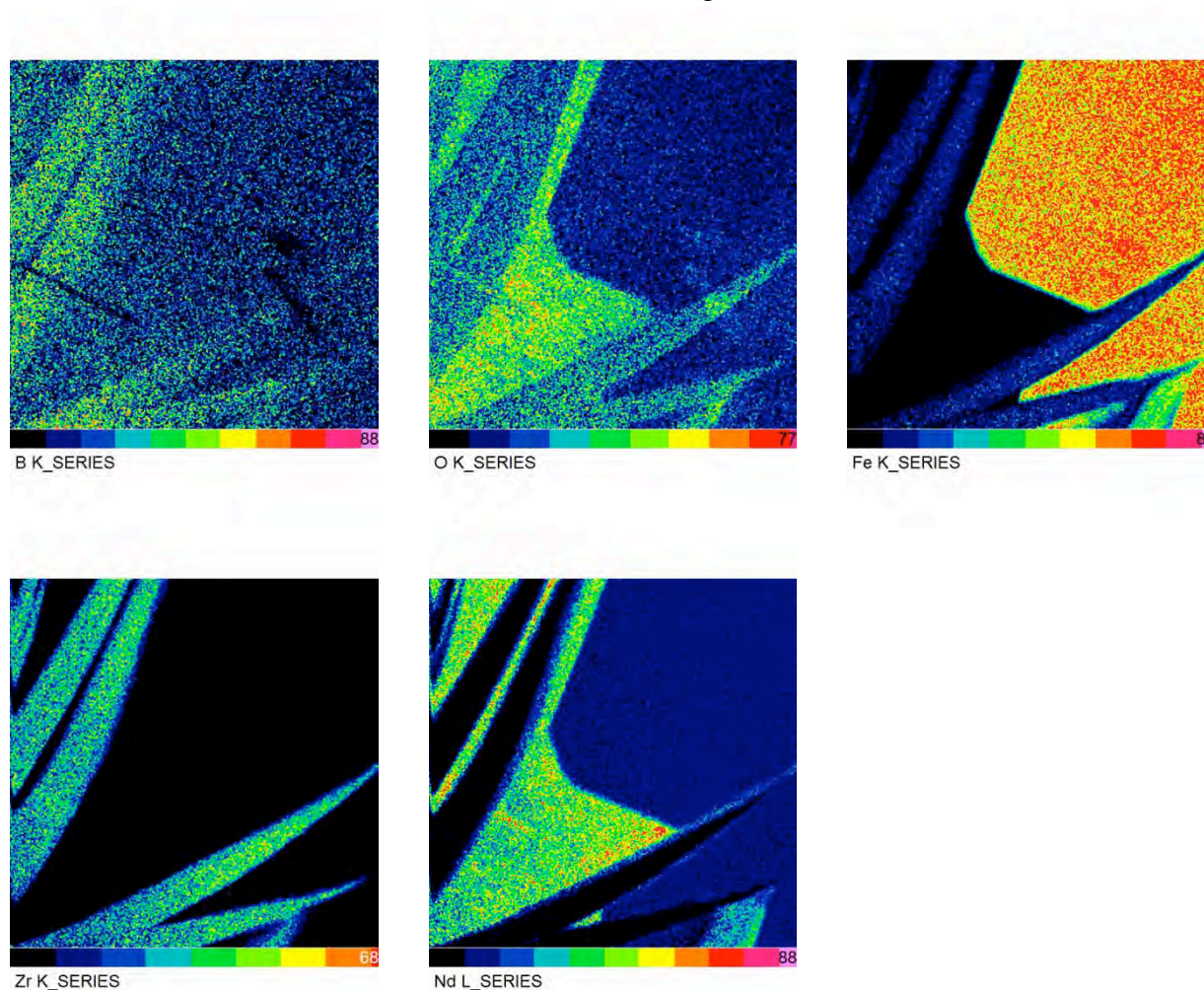
Note: A: $Nd_2Fe_{14}B$, B: Nd-rich phase, C: ZrB_2-type needles

Figure 5.22 Quant maps from ZrB₂-type needles in A12 via silicon drift EDX detector in TEM.

5.1.5   Summary of Results from Cast Alloys

1. The α-Fe dendrites are eliminated by the addition of 1 at% ZrB_2 to the cast $Nd_2Fe_{14}B$ alloy. **[Figure 5.1, Table 5.1]**

2. The volume fraction of the $Nd_2Fe_{14}B$ phase increases significantly in the A12 alloy (NdFeB with 1 at% of ZrB_2 addition). **[Table 5.1]**

3. The grain size of all the phases is reduced by the addition of Zr *or* ZrB_2. **[Table 5.2]**

4. The non-magnetic phase, $Nd_1Fe_4B_4$, can be found both in the matrix and the Nd-rich phase in A1 and A4, but it only appears within the Nd-rich phase of A12. **[Figure 5.4, Figure 5.6]**

5. The chemical analysis results from WDX are consistent with the formulae $Nd_2Fe_{14}B$ and $Nd_1Fe_4B_4$ in the NdFeB-Zr cast alloy. **[Table 5.3, Table 5.6]**

6. The Nd-rich phase can be found at the triple points of the $Nd_2Fe_{14}B$ grains. Chemical analyses from SEM-WDX and TEM-EDX show that there is a small amount of Fe (WDX: ~5 at%; EDX: ~3 at%) in the Nd-rich phase of all cast NdFeB-Zr alloys. **[Table 5.4, Table 5.8, Figure 5.9(c), Figure 5.10(b), Table 5.9, Figure 5.12(b), Figure 5.14(b), Table 5.12, Figure 5.19(b)]**

7. ZrB_2-type needles occupy mainly the Nd-rich phases of both A4 and A12. However, ZrB_2 needles can also be found in both the $Nd_2Fe_{14}B$ and Nd-rich phase of A12 with same composition. The shape of the ZrB_2 needles is slightly different in A4 and A12. In A4, the ZrB_2-type needles form as a loose cluster. In A12, however, they form as a tightly-knit sheaf in the Nd-rich phase but as a tight bundle in the matrix phase. The ZrB_2-type needles are both sharper and more curved in the latter case. **[Figure 5.5]**

8. Chemical analyses from SEM-WDX and TEM-EDX suggest that the ZrB_2-type needles in both NdFeB-Zr alloys are composed mainly of B and Zr with a small, but significant

amount of Fe (WDX: A4: ~10 at%, A12: ~15 at%; EDX: A4: ~8 at%, A12: ~ 4 at%). **[Table 5.5, Table 5.9, Table 5.12, Figure 5.12(c), Figure 5.14(a), Figure 5.15(b), Figure 5.17(c), Figure 5.19(c), Figure 5.20(b), Figure 5.22]**

9. DPs indicate that ZrB_2 needles have an HCP structure with parameters of (A4) a= 3.26±0.04 Å and c= 3.53±0.08 Å and (A12) a=3.29±0.02 Å and c=3.52±0.07 Å. **[Figure 5.17(b), Figure 5.21]**

10. The small needles in the Nd-rich phase of A4 are suggested to be a precursor of the ZrB_2. The small needles are mainly composed of B (~60 at%), Nd (~25 at%) and a small amount of Zr (~8 at%), O (~6 at%) and Fe (~3 at%). **[Figure 5.13, Figure 5.14, Figure 5.15]**

11. A comparison of the chemical analysis results from the Nd-rich phase and the Nd-rich phase between the ZrB_2 needles revealed that the latter contains higher levels of oxygen. **[Figure 5.13, Figure 5.16, Table 5.11]**

5.2   Analysis of NdFeB-Zr Homogenised Alloys

Heat treatment is the conventional way of removing α-Fe dendrites from the $Nd_2Fe_{14}B$ alloys. The effect of heat treatment on the NdFeB alloys after Zr *or* ZrB_2 additions will be presented in this section.

Since the high temperature heat treatment is expected to speed up the reactions between the α-Fe dendrites and the Nd- and B- rich phases to form new $Nd_2Fe_{14}B$ grains and this is significantly dependent upon the temperature and time profiles. Samples in this study were homogenized under a partial vacuum of 10^{-3} mbar at 1070°C for 20 hours based on previous work at the University of Birmingham [K. A. Kirby, 2007].

5.2.1   X-ray Diffraction

Figure 5.23 (a) shows X-ray diffraction patterns from the homogenised NdFeB-Zr alloys. The profiles confirmed that the α -Fe phase has been eliminated from all the homogenised NdFeB-Zr alloys after the heat treatment (Figure 5.23 (b) and (c)).

The peaks from the Nd-rich and ZrB_2 phases are difficult to identify since they overlap with those from $Nd_2Fe_{14}B$ and they also constitute only a small fraction of the overall microstructure.
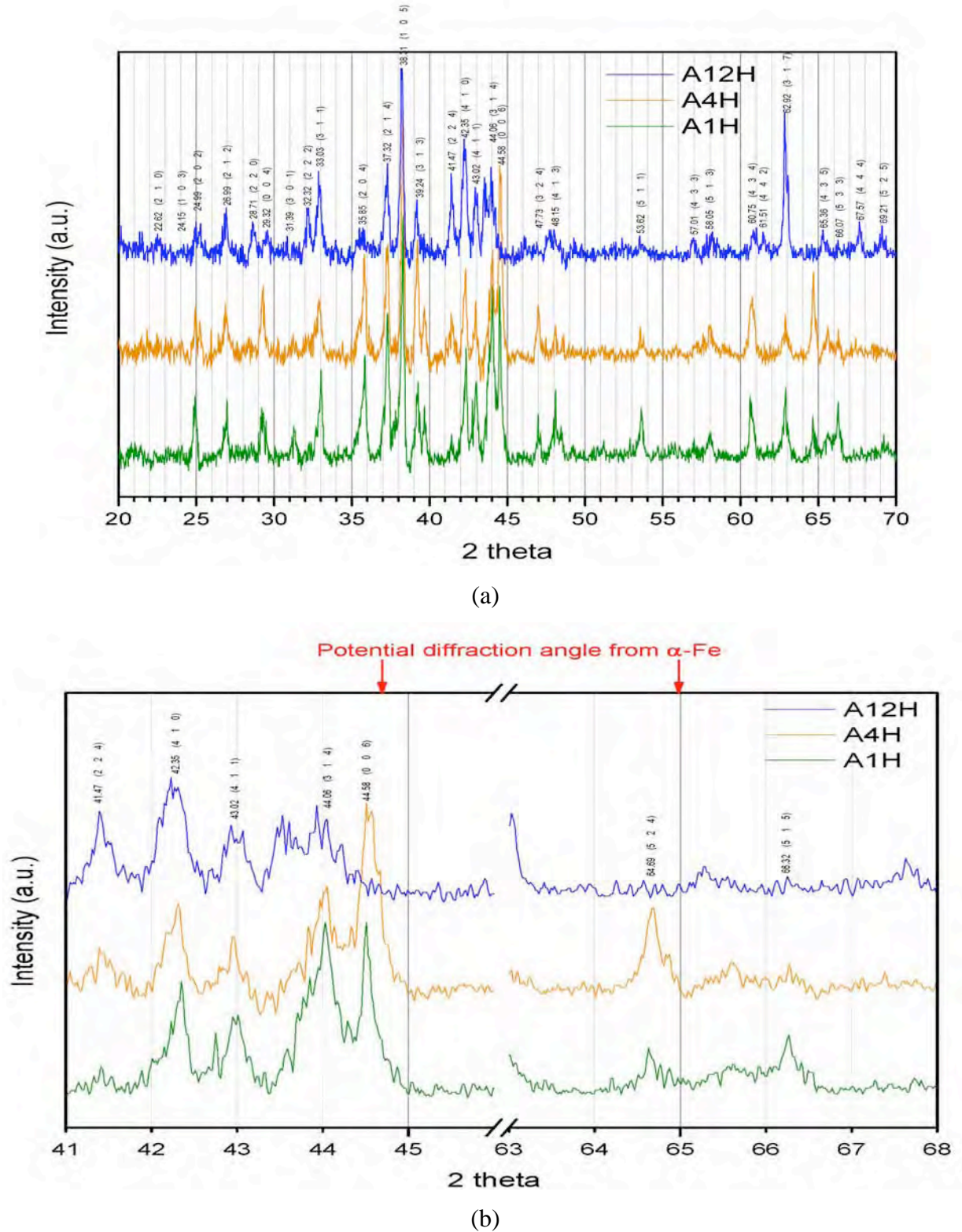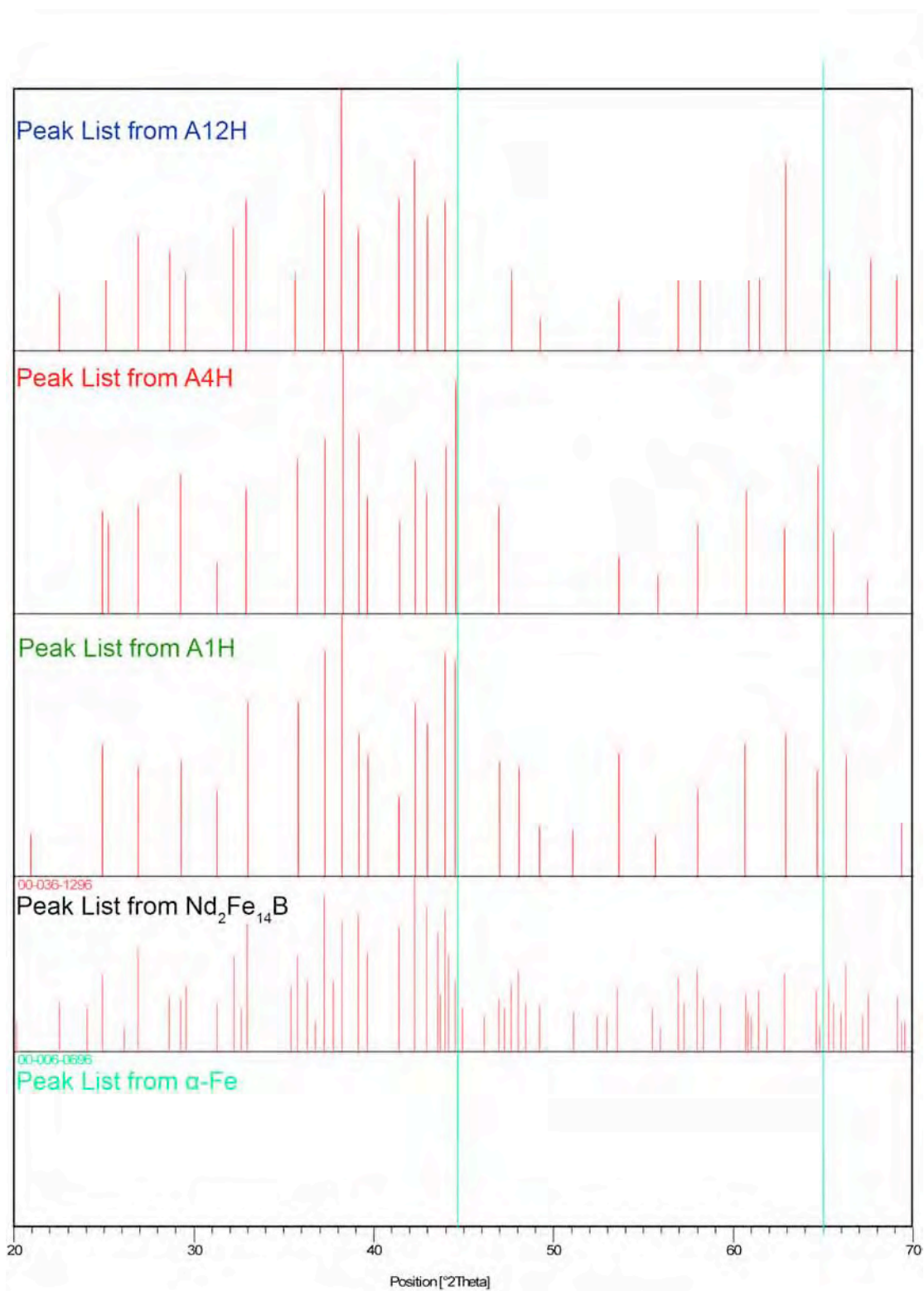
(a)

(b)

Figure 5.23 X-ray diffraction patterns from NdFeB and NdFeB-Zr homogenised alloys. (Peaks from Nd$_2$Fe$_{14}$B are labeled in black and α-Fe are labeled in red)

(c)

Figure 5.23 (Continued)

5.2.2 Overall Microstructure

The phase distributions in A1H, A4H and A12H are shown in Figure 5.24 (a), (b) and (c). Three main phases are found in all three samples, namely $Nd_2Fe_{14}B$, Nd-rich and ZrB_2 needles. It is also found that, after the heat treatment, the proportion of α-Fe dendrites is eliminated in the homogenized samples.

All the figures indicate the general effect of the heat treatment in A1H, A4H and A12H. The Nd-rich phase is redistributed along the grain boundaries, with a proportion forming large pockets at the triple points between the $Nd_2Fe_{14}B$ grains. The shape of the Nd-rich grain is also changed from elongated to more spherical-type shapes.

Table 5.13 lists the area percentages of the different phases in the samples. The proportion of the $Nd_2Fe_{14}B$ matrix phase increases significantly after the heat treatment. Meanwhile, while the proportion of the Nd-rich phase stays the same after the heat treatment in A1H, the proportions of the Nd-rich phase in both A4H and A12H are found to decrease. The area fraction of ZrB_2 in A4H appears to be larger than that in A12H, because the ZrB_2 exists as a mixture of phases in the Nd-rich phase of A4H and causes the software to mistakenly lump together all the needles.

Table 5.14 shows the grain sizes in the NdFeB-Zr homogenised alloys. Comparing the cast alloy in Table 5.2, there is grain growth of the matrix phase, the Nd-rich phase and ZrB_2 needles, which is attributed to the effect of the heat treatment. However, grain growth of both major phases is limited by additions of Zr or ZrB_2.

Table 5.13 The area fractions of the phases in the central regions of NdFeB and NdFeB-Zr homogenised alloys. (Each result was deduced from 5 BSE micrographs.)

Sample	Area Fraction (%)		
	$Nd_2Fe_{14}B$	Nd-rich	ZrB_2
A1H	94.05±0.14	5.95±0.14	
A4H	93.23±0.36	2.35±0.86	(4.42±0.47*)
A12H	95.72±0.75	2.22±0.92	2.06±0.53

*The ZrB_2 area fraction in A4H appears larger than in A12H because the software mistakenly lumps together all the needles.

Table 5.14 The average size (µm) of the grain and phase area in the central region of NdFeB and NdFeB-Zr homogenised alloys. (Each result was deduced from 5 SEI micrographs.)

Sample	Average Size (µm)	
	Grain	Phases
	$Nd_2Fe_{14}B$	Nd-rich
A1H	28.60±3.30	3.25±1.45
A4H	10.50±4.94	1.29±0.68
A12H	24.20±5.88	1.32±0.37
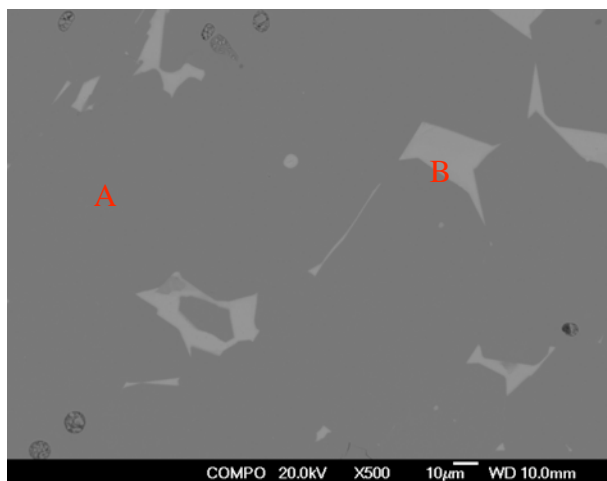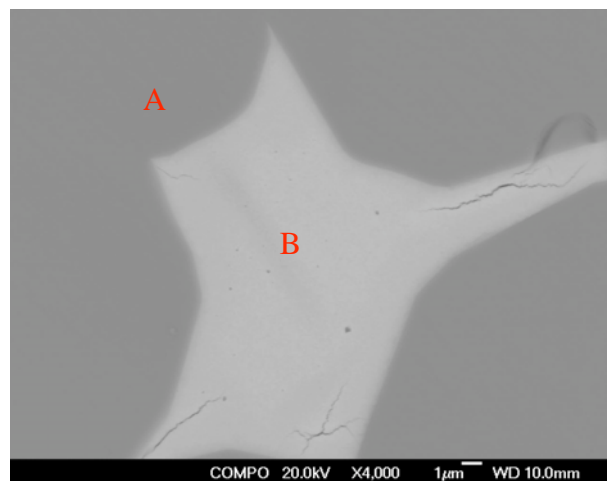
(a) A1H (lower mag.)   A1H (higher mag.)
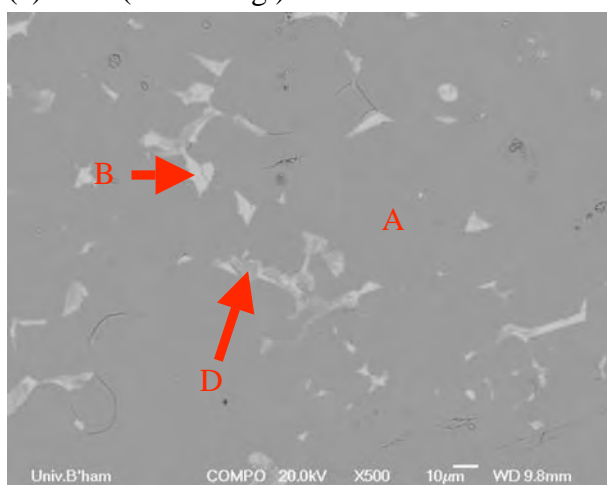
(b) A4H (lower mag.)   A4H (higher mag.)
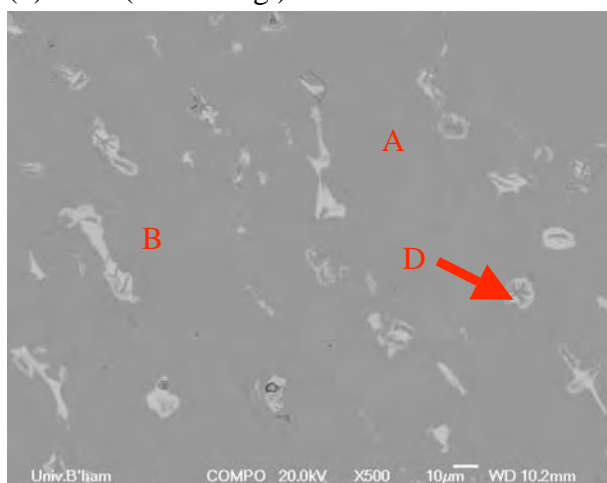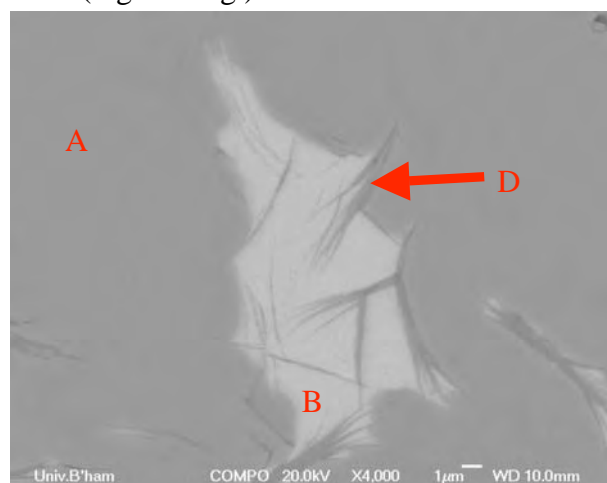
(c) A12H (lower mag.)   A12H (higher mag.)

Note: A: $Nd_2Fe_{14}B$, B: Nd-rich phase, D: ZrB_2 needles

Figure 5.24 BSE micrographs of homogenised NdFeB and NdFeB-Zr alloys at lower and higher magnification. (a) A1H (b) A4H (c) A12H

5.2.3 Microstructure and Chemical Analysis of Individual Phases in Homogenised Alloys

5.2.3.1 $Nd_2Fe_{14}B$ matrix phase

Table 5.15 shows the composition of the matrix phase in the homogenised NdFeB-Zr alloys. The theoretical composition derived from the chemical formula is also provided. The WDX analysis confirmed that neither heat treatment nor the additions of Zr *or* ZrB_2 change the chemical composition of $Nd_2Fe_{14}B$.

Table 5.15 The composition of the matrix phase in homogenised NdFeB and NdFeB-Zr alloys. (The phase has been analysed 5 times in different places. The highlighted row is the composition derived from the chemical formula.)

Homogenised matrix	B (at%)	Fe (at%)	Nd (at%)
$Nd_2Fe_{14}B$	5.88	82.35	11.76
A1H	5.83±0.14	82.51±0.37	11.66±0.30
A4H	5.96±0.17	82.31±0.54	11.73±0.51
A12H	6.13±0.15	82.22±0.81	11.65±0.67

5.2.3.2 Nd-rich phase

Figure 5.25(a), (b) and (c) are BSE micrographs of the Nd-rich phases in the homogenised NdFeB-Zr alloys. As mentioned before, the Nd-rich phase is distributed along the grain boundaries of the $Nd_2Fe_{14}B$ phase with some forming a large pocket at the intersections of the $Nd_2Fe_{14}B$ grains.

Table 5.16 shows the WDX results from the Nd-rich phase in the homogenised

NdFeB-Zr Alloys. A small amount of oxygen (~8 at%) is detected in this area, which is believed to come from the heat treatment and/or grinding processes during sample preparation.

Meanwhile, a small amount of iron (~3-4 at%) was also detected in the Nd-rich phase of the homogenised NdFeB-Zr alloys. A comparison between the cast and homogenised alloys of the Fe contents in the Nd-rich phase show that the Fe in the Nd-rich phase of the nil-Zr containing NdFeB alloy is eliminated by the heat treatment. However, the Fe in the Nd-rich phase of both A4 and A12 remains there in both A4H (~ 2.5 at% of Fe) and A12H (~4 at% of Fe) after the heat treatment.

Table 5.16 The composition of the Nd-rich phase in homogenised NdFeB and NdFeB-Zr alloys. (The phase has been analysed 5 times in different places.)

Sample	O (at%)	Fe (at%)	Nd (at%)	Zr (at%)
A1H	8.64±0.73	0.89±0.17	90.47±0.19	
A4H	8.91±0.63	3.43±0.42	87.52±1.90	0.14±0.02
A12H	8.96±0.20	4.03±0.94	86.55±1.34	0.46±0.19
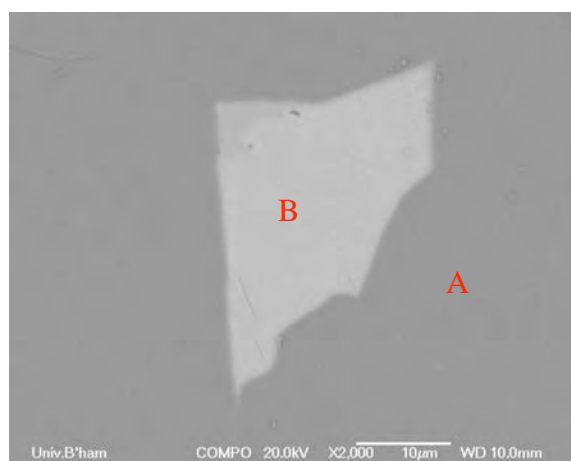
(a) A1H
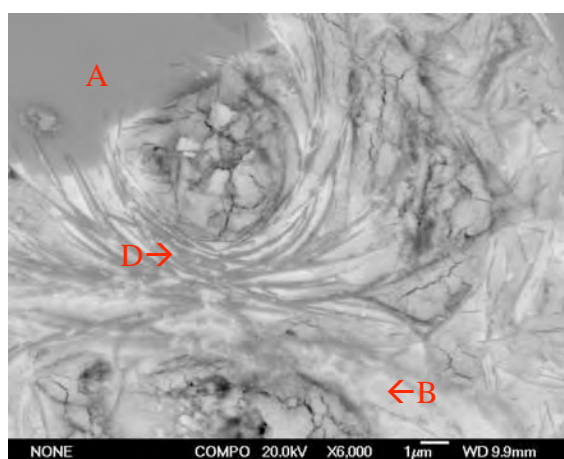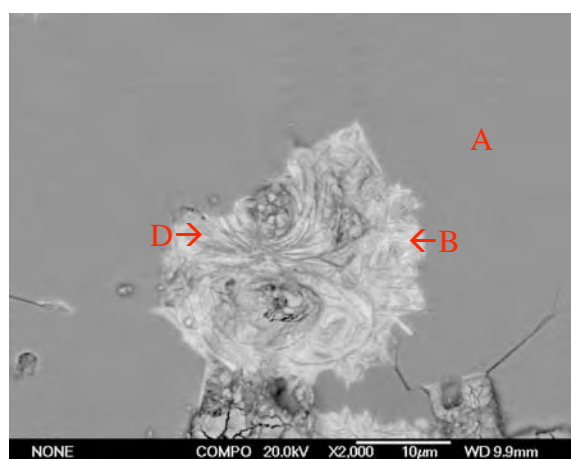
(b) A4H
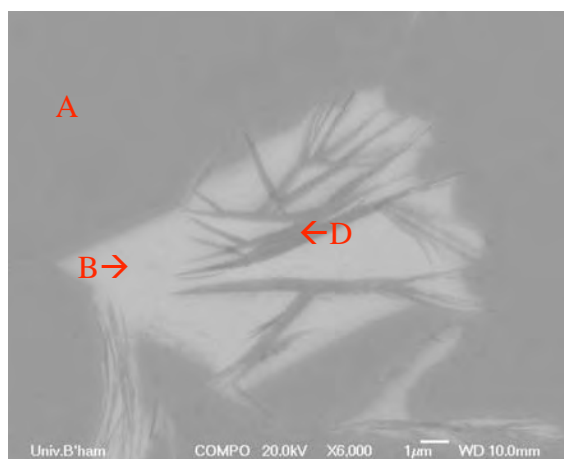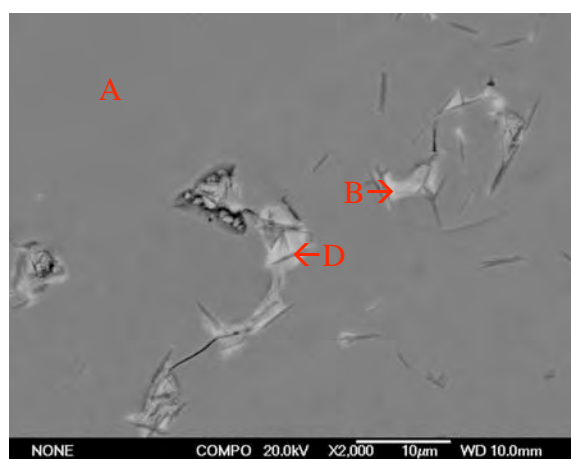
(c) A12H

Note: A: $Nd_2Fe_{14}B$, B: Nd-rich phase, D: ZrB_2 needles

Figure 5.25 BSE micrographs of Nd-rich phase in homogenised NdFeB and NdFeB-Zr alloys (a) A1H (b) A4H (c) A12H

5.2.3.3 ZrB$_2$ phase

Figure 5.26(a), (b) and (c) show ZrB$_2$-type needles in the homogenised NdFeB-Zr alloys. ZrB$_2$-type needles are always found in the Nd-rich phase of A4H.

The ZrB$_2$-type needles are feather-like and more regularly arranged in the Nd-rich phase of A4H than in the Nd-rich phase of A12H, where they are much sharper and less regular in arrangement. The difference is attributed to a ZrB$_2$-Nd eutectic product in the Nd-rich phase of A4H, resulting from insufficient boron in its starting composition: the ZrB$_2$-type needles in A4H formed using boron from the matrix phases (Nd$_2$Fe$_{14}$B). However, the ZrB$_2$-type needles in A12H are formed using boron from the initial addition (1 at% of ZrB$_2$). Meanwhile, it is observed that the ZrB$_2$-type needles in the Nd-rich phase penetrated into the matrix of A12H but not into that of A4H.

Table 5.17 gives the chemical compositions of the ZrB$_2$-type needles in A4H and A12H. Due to the beam spreading (~1um) in the SEM, X-rays from other phases were acquired during the WDX analysis on this phase. Thus, the WDX in Table 5.17 can only indicate the existence of a small amount of Fe (~2-5 at%), which is less than in the cast alloys (Table 5.5).

Table 5.17 The composition of ZrB$_2$-type needles in A4H and A12H alloys. (The phase has been analysed 5 times in different places. The highlighted row is the composition derived from the chemical formula.)

Sample	B (at%)	Zr (at%)	Fe (at%)
ZrB$_2$	66.66	33.33	
A4H-in NdR	67.31±1.04	30.68±1.34	2.01±0.38
A12H-within NdR	66.99±1.02	30.37±0.35	3.06±0.72
A12H-in Matrix	66.49±1.03	27.52±0.47	*5.99±0.63

* enhanced value due to overlap with matrix
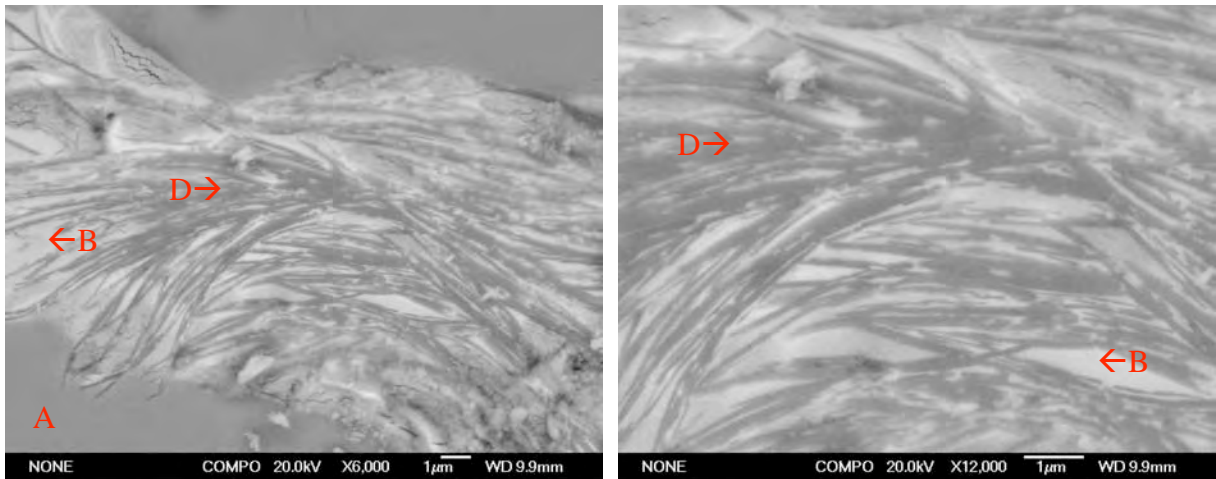
(a) BSE image of ZrB_2 in the Nd-rich phase in A4H
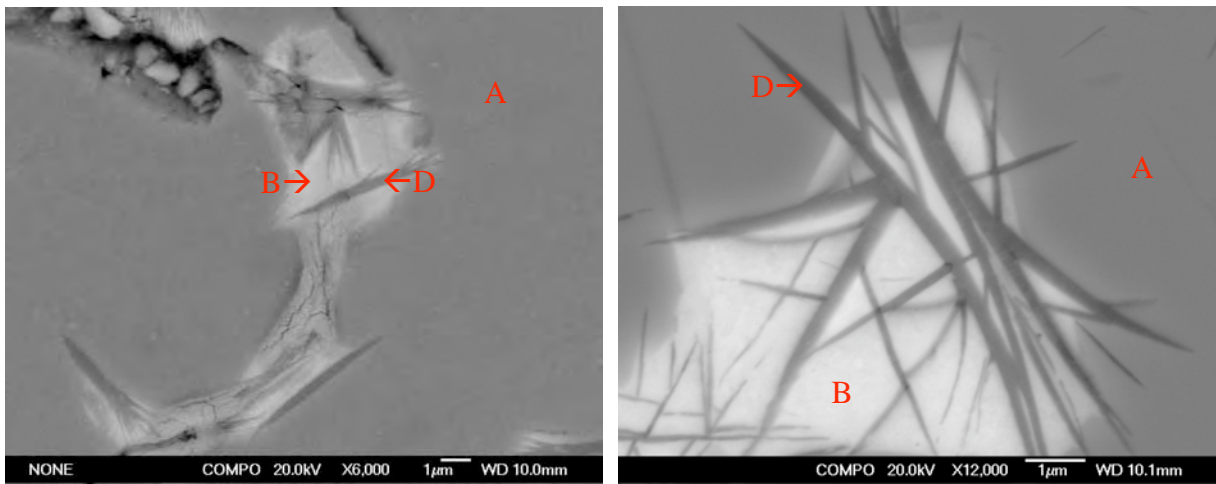
(b) BSE image of ZrB_2 in the Nd-rich phase in A12H
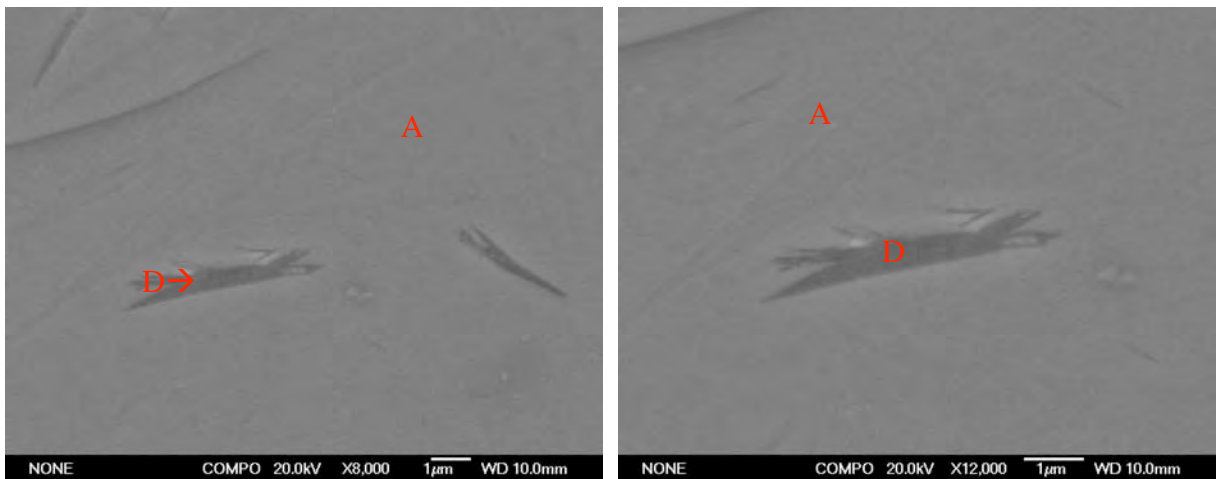
(c) BSE image of ZrB_2 in the matrix of A12H

Note: A: $Nd_2Fe_{14}B$, B: Nd-rich phase, D: ZrB_2 needles

Figure 5.26 BSE images of ZrB_2 in NdFeB-Zr homogenised alloys. (a) from the Nd-rich phase in A4H, (b) from the Nd-rich phase in A12H and (c) from the A12H matrix.

5.2.4 Summary of Results from Homogenised Alloys

1. The α-Fe dendrites in all the NdFeB-Zr homogenised alloys are eliminated by the heat treatment. **[Figure 5.23, Figure 5.24, Table 5.13]**

2. The proportion of $Nd_2Fe_{14}B$ in all homogenised alloys significantly increases after the heat treatment. **[Table 5.1, Table 5.13]**

3. The proportion of the Nd-rich phase stays the same as in the cast alloy after annealing of A1H. However, the proportion of the Nd-rich phase in A4H and A12H is found to decrease. **[Table 5.1, Table 5.13]**

4. Grain growth is observed for all the phases. However, grain growth of both the major phases, $Nd_2Fe_{14}B$ and the Nd-rich phase, is limited by additions of Zr *or* ZrB_2. **[Table 5.13, Table 5.14]**

5. Neither heat treatment nor the addition of Zr *or* ZrB_2 changes the chemical composition of the $Nd_2Fe_{14}B$ phase. **[Table 5.15]**

6. The Nd-rich phases in the homogenised alloys are found redistributed along the grain boundaries of the $Nd_2Fe_{14}B$ phase with some forming large pockets at the triple points. **[Figure 5.2, Figure 5.24]**

7. The Fe in the Nd-rich phase of the Zr-free alloy (A1) is removed by the heat treatment. The Fe in the Nd-rich phase of both A4 and A12 remains present in both A4H (~1.5 at%) and A12H (~4 at%) after annealing. **[Table 5.4, Table 5.16]**

8. ZrB_2-type needles are always found in the Nd-rich phases. The ZrB_2 needles are feather-like and more regularly arranged in the Nd-rich phase of A4H compare to A12H. Those in the same phase of A12H are much sharper and more irregular in arrangement. It was found that the ZrB_2 needles in the Nd-rich phase penetrate into the matrix of A12H whereas not in A4H. **[Figure 5.26]**

9. WDX from the ZrB_2-type needles in homogenised NdFeB-Zr alloys suggests the existence of a small amount of Fe (~2-6 at%), but less than that in the cast alloys. **[Table 5.5, Table 5.17]**

5.3 Analysis of NdFeB-Zr Sintered Magnets

As described in Ch 4.3, the NdFeB-Zr alloys were produced and decrepitated in hydrogen and milled for 20 hours. All powders (A1, A4 and A12) were then aligned, isostatically pressed under 10 tons before sintering at 1070°C for 1 hour followed by annealing at 630°C for 1 hour. The sintering temperature and time profile for all the magnets in this study are based on previous work on MA12 at the University of Birmingham [K. A. Kirby, 2007]. The densities of the NdFeB and NdFeB-Zr sintered magnets are list in Table 5.18 and all the sintered magnets have ~ 97% of its full density.

Table 5.18 The densities of NdFeB and NdFeB-Zr sintered magnets.

Sample	Density (g/cm^3)		
	Measured	**Theoretical**	**Ratio**
MA1	7.33±0.15	7.42	98.7%
MA4	7.21±0.18	7.41	97.3%
MA12	7.17±0.12	7.34	97.7%

In order to investigate the influence of the Zr *or* ZrB$_2$ additions to the NdFeB sintered magnets, extra Nd was not added before sintering to remedy the exhaustion of Nd during the sintering process. The reason is that extra Nd would shift the overall composition of the starting alloys from the Nd$_{12.68}$Fe$_{77.91-80.91}$B$_{6.41-8.41}$Zr$_{0-1}$ (at%) composition. It should be noted that 12.68 at% of Nd would not be sufficient to make a sintered magnet with a good coercivity of more than 1000 kA/m^3 due to the lack of boundary phase in the magnets. Meanwhile, although α-Fe can be eliminated by modifying the heat treatment process (as shown in section 5.2), the potential influence resulting from the formation of ZrB$_2$ needles in the NdFeB magnets has not yet been elucidated. Therefore, the investigation in this section is focused on the effects of Zr *or* ZrB$_2$ additions in order to understand the mechanism of how these additions lead to

optimum microstructure and magnetic properties of sintered magnets produced from the

$Nd_{12.68}Fe_{77.91-80.91}B_{6.41-8.41}Zr_{0-1}$ (at%) alloys.

5.3.1   X-ray Diffraction

X-ray diffraction patterns from sintered NdFeB-Zr magnets were obtained to identify

the phases before and after Zr or ZrB_2 had been added, as shown in Figure 5.27. Since a pulse

field of 6 Tesla has aligned the powder during the sample preparation process and the sintered

magnets were cut perpendicular to the aligned direction, c-axis, the XRD profiles for all

sintered magnets were then presented from the same crystal orientation, c-axis. The XRD

profiles suggest that there is no α-Fe in any of NdFeB-Zr sintered magnets. Although α-Fe is

removed by sintering, NdFeB with ZrB_2 addition is believed to be economically feasible since

all the α-Fe was removed during the casting stage without a need for the homogenising and

sintering stage. Meanwhile, comparing the FWHM (Full Width at Half Maximum) at (006) of

the $Nd_2Fe_{14}B$ phase (as shown in Figure 5.27(b)), it is found that the size of the $Nd_2Fe_{14}B$

grains in the NDFeB-Zr sintered magnets decreases with additions of Zr and ZrB_2.
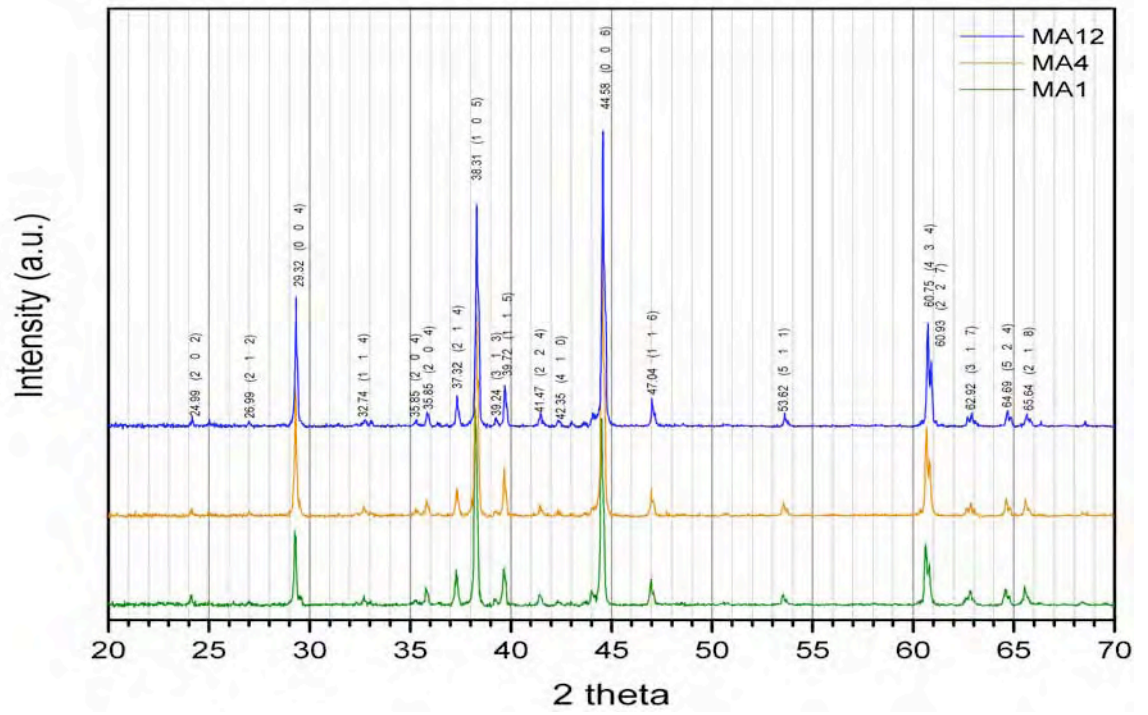
(a)
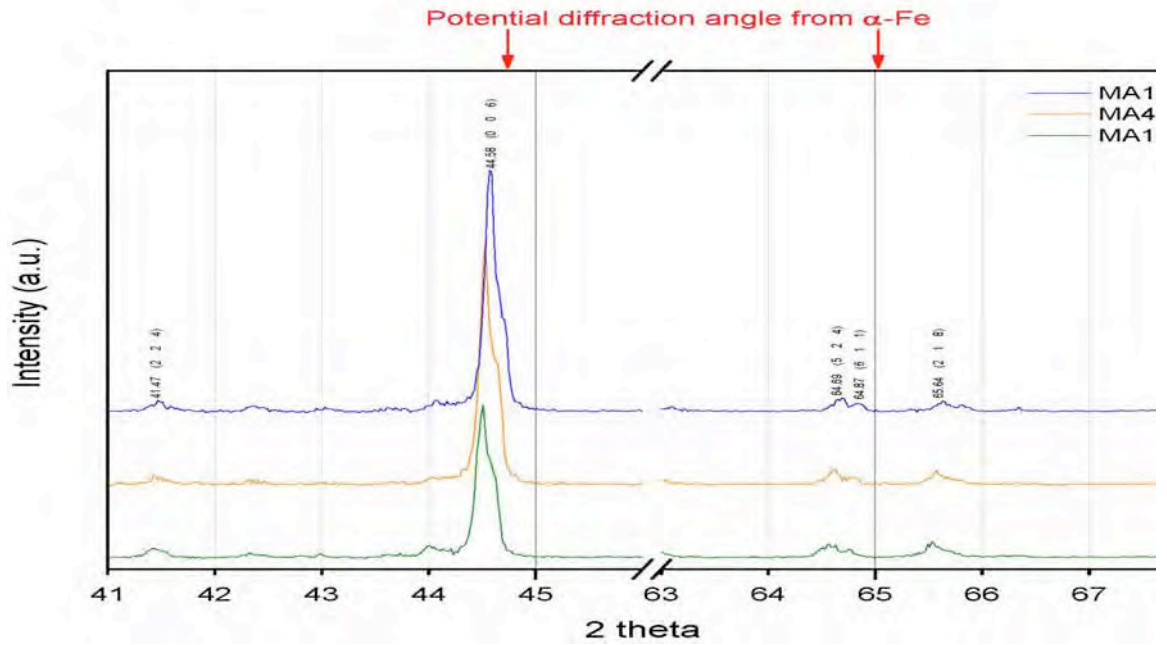
(b)

Figure 5.27 X-ray diffraction patterns of NdFeB and NdFeB-Zr sintered magnets. (Peaks from $Nd_2Fe_{14}B$ are labeled in black and α-Fe are labeled in red)
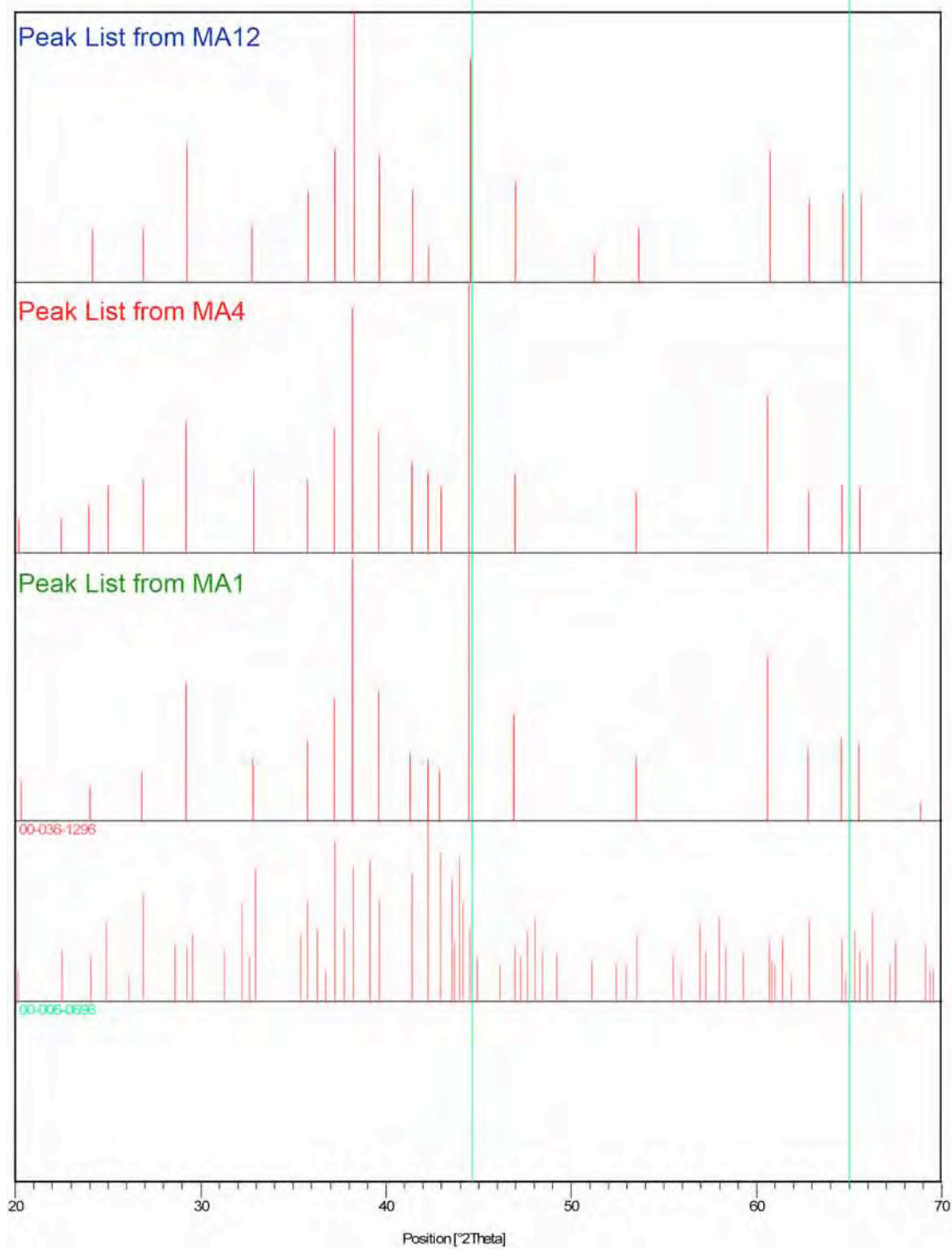
(c)

Figure 5.27 (Continued)

5.3.2 Overall Microstructure

Figure 5.28(a), (b) and (c) show the phase distributions in MA1, MA4 and MA12. Three main phases were observed for all three samples: $Nd_2Fe_{14}B$, Nd-rich and ZrB_2. It is clear that α-Fe dendrites are entirely eliminated by the sintering process.

It is also found that the phases in the sintered magnets are smaller than those in both the cast and homogenised alloys. The Nd-rich phase consist mainly of small pockets at the triple points of the $Nd_2Fe_{14}B$ grains. The shape of the Nd-rich grains became much rounder than in either the cast or the homogenised alloys. Some of the porosity in MA4 and MA12 is believed to be due to the Nd-rich phase, which has been pulled out during the grinding and polishing process.

Table 5.19 lists the area percentages of the three phases in the sintered magnets. The Nd-rich phase has almost the same area fraction in both the non-Zr and Zr-containing sintered alloys.

Table 5.20 shows the average grain sizes in the NdFeB-Zr sintered alloys. As can be observed, the size of the $Nd_2Fe_{14}B$ grains decreases with increasing Zr *or* ZrB_2. Since the amount of the Nd would be exhausted (evaporated) during sintering, it is very difficult to distinguish whether the Zr *or* ZrB_2 additions or the sintering process affects the size of the Nd-rich grains in the sintered alloys.

Table 5.19 The area fractions of the phases in the central regions of the NdFeB and NdFeB-Zr sintered magnets. (Each result was deduced from 5 BSE micrographs.)

Sample	Area Fraction (%)		
	$Nd_2Fe_{14}B$	Nd-rich	ZrB_2
MA1	96.48±0.51	3.52±0.59	
MA4	94.15±0.79	3.30±0.94	2.55±0.35
MA12	92.76±1.15	3.78±1.05	3.46±0.54

Table 5.20 The average size (μm) of the grains and phase area in the central region of the NdFeB and NdFeB-Zr sintered magnets. (Each result was deduced from 5 SEI micrographs.)

Sample	Average Size (μm)	
	Grain	Phases
	$Nd_2Fe_{14}B$	Nd-rich
MA1	10.50±4.26	3.52±0.58
MA4	7.37±3.36	3.17±1.46
MA12	6.67±3.20	4.48±1.95
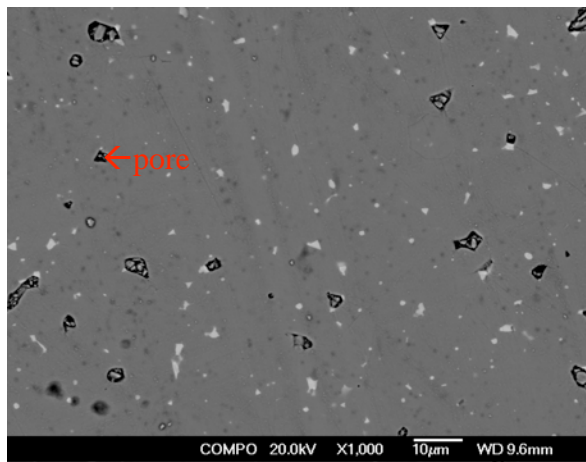
(a) MA1 (lower mag.)   MA1 (higher mag.)
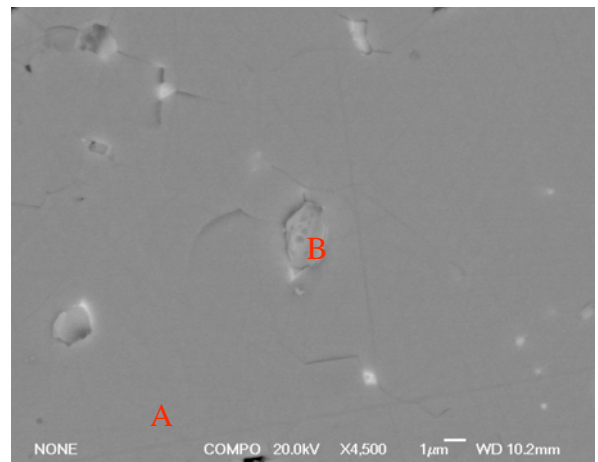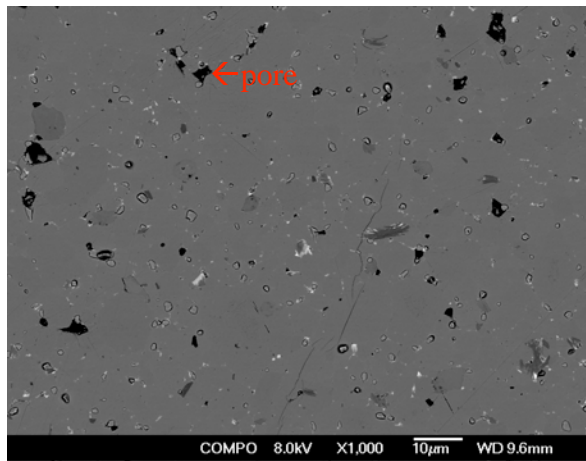
(b) MA4 (lower mag.)   MA4 (higher mag.)

(c) MA12 (lower mag.)   MA12 (higher mag.)

Note: A: $Nd_2Fe_{14}B$, B: Nd-rich phase, D: ZrB_2 needles

Figure 5.28 BSE micrographs of sintered NdFeB-Zr magnets (a) MA1 (b) MA4 and (c) MA12

5.3.3 Microstructure and Chemical Analysis of Individual Phases in Sintered Magnets

5.3.3.1 $Nd_2Fe_{14}B$ phase

Table 5.21 shows the compositions of the matrix phase in MA1, MA4 and MA12. The theoretical composition derived from the chemical formula is also provided. The WDX analysis confirmed that the chemical composition of $Nd_2Fe_{14}B$ remained unchanged as a result of the sintering or of the Zr or ZrB_2 additions.

Table 5.21 The composition of the matrix phase in the NdFeB and NdFeB-Zr sintered magnets. (The phase has been analysed 5 times in different places. The highlighted row is the composition derived from the chemical formula.)

Sintered matrix	B (at%)	Fe (at%)	Nd (at%)
$Nd_2Fe_{14}B$	5.88	82.35	11.76
MA1	5.79±0.35	82.44±0.58	11.78±0.65
MA4	5.88±0.39	82.33±0.71	11.80±0.37
MA12	5.75±0.32	82.35±0.67	11.90±0.94

5.3.3.2 Nd-rich phase

Figure 5.29(a), (b) and (c) show BSE micrographs of the Nd-rich phase in the sintered NdFeB-Zr magnets. A comparison with the morphology of the Nd-rich phase in the cast alloy revealed that the Nd-rich phases in the sintered magnets are much smaller and rounder in shape. This may be caused by the milling process, which enables the fine powder to react fully and exhaust (evaporate) during the sintering process. As can be seen, ZrB_2 needles occupy most of the Nd-rich phase in the Zr-containing sintered magnets.

Table 5.22 shows the WDX results from the Nd-rich phase in the sintered magnets. A

comparison of the oxygen contained in the Nd-rich phase of the NdFeB-Zr as-cast alloys (~10 at%), the Nd-rich phases in the sintered magnets contain much higher oxygen (~55 at%). It can be identified as Nd_2O_3, which may be introduced during the sintering in the furnace chamber. Meanwhile, a small amount of Fe has been detected in the Nd-rich phase of both MA4 (~2.3 at%) and MA12 (~4.5 at%).

Table 5.22 The composition of the Nd-rich phase in NdFeB and NdFeB-Zr sintered magnets. (The phase has been analysed 5 times in different places.)

Sample	O (at%)	Fe (at%)	Nd (at%)	Zr (at%)
MA1	57.08±1.52	0.35±0.14	42.92±1.52	
MA4	54.41±3.12	2.32±0.87	42.93±3.12	0.34±0.14
MA12	52.59±2.30	4.84±0.49	41.90±2.30	0.67±0.34
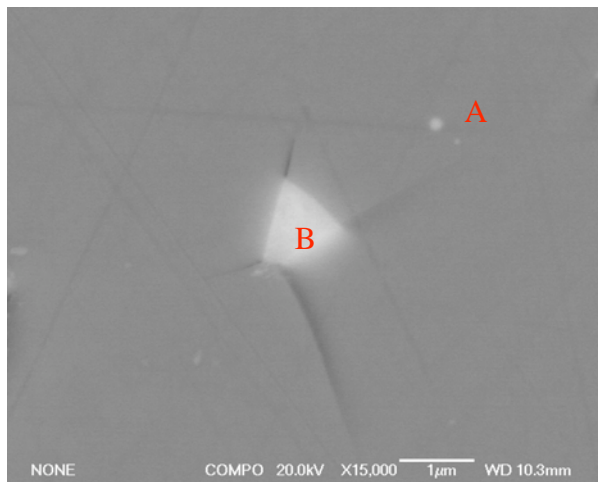
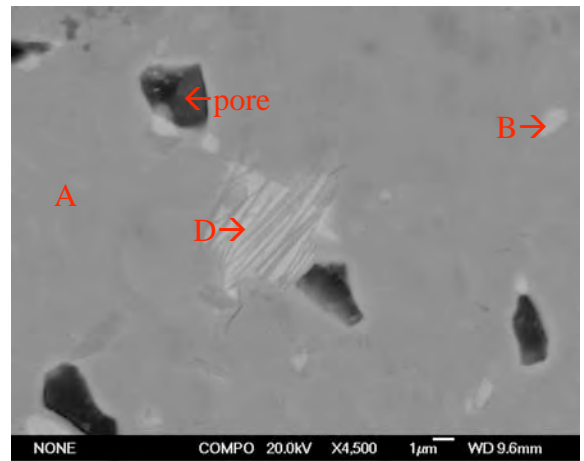(a) MA1 (lower mag.)   MA1 (higher mag.)
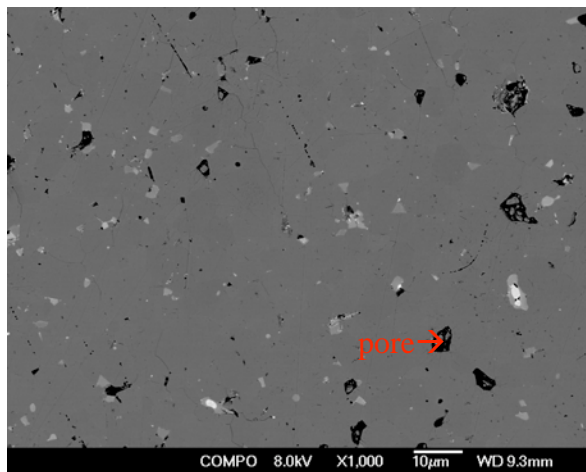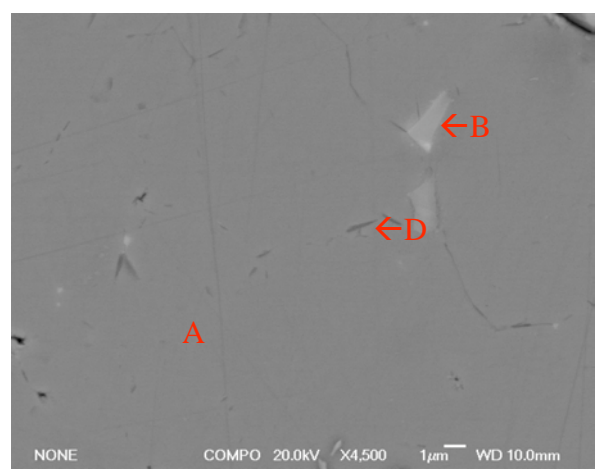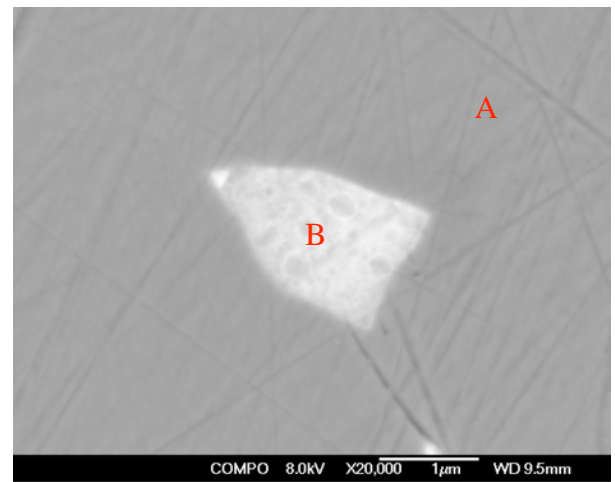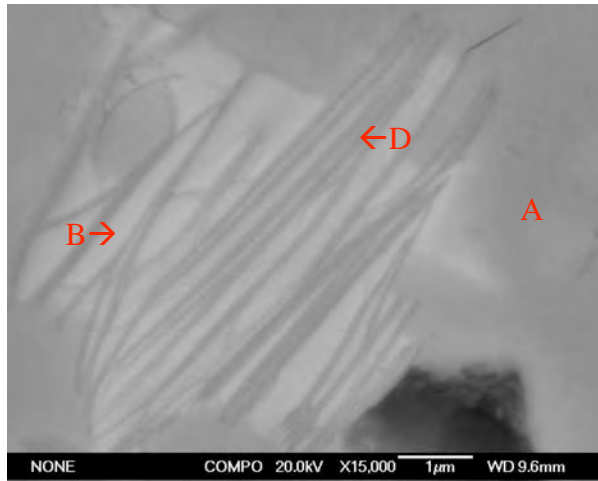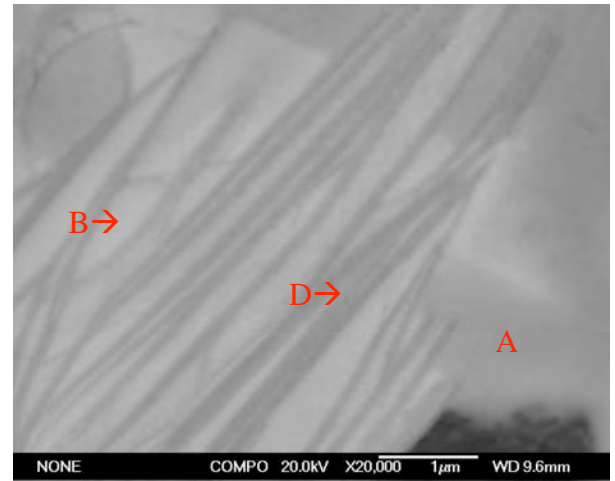
(b) MA4 (lower mag.)   MA4 (higher mag)
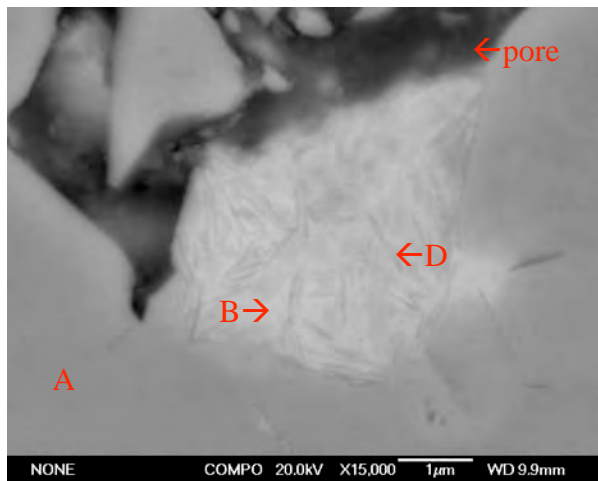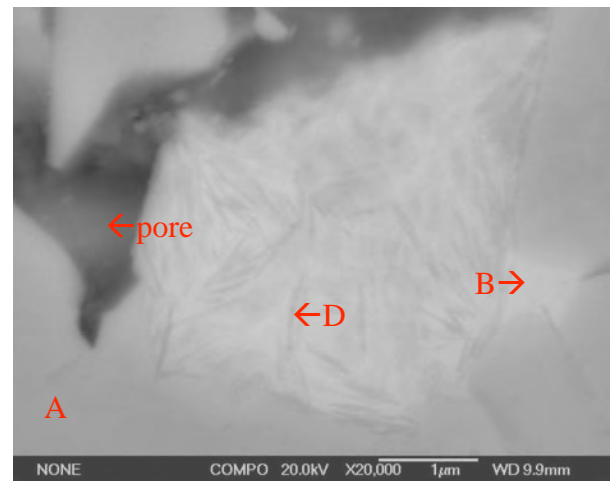
(c) MA12 (lower mag.)   MA12 (higher mag.)

Note: A: $Nd_2Fe_{14}B$, B: Nd-rich phase, D: ZrB_2 needles

Figure 5.29 BSE micrographs of the Nd-rich phase in NdFeB and NdFeB-Zr sintered magnets (a) MA1 (b) MA4 and (c) MA12

5.3.3.3 ZrB$_2$ phase

Figure 5.30 shows the ZrB$_2$ needles in the sintered magnets. In sintered magnets, it is observed that the ZrB$_2$ needles form mainly in the Nd-rich phase although some of them can also be found in the centre of, or between, the matrix (Nd$_2$Fe$_{14}$B) grains.

The shape of the ZrB$_2$ needles is different in MA4 and MA12. In MA4, ZrB$_2$ forms an eutectic-like phase (~3-4 µm) in the Nd-rich phase penetrating into matrix and some individual needles (~2 µm) in the matrix. In MA12, however, ZrB$_2$ needles form as small segments (~0.5-1 µm) in the Nd-rich phase and distribute randomly inside the Nd$_2$Fe$_{14}$B grains or at the grain boundaries.

Table 5.23 gives the WDX chemical analyses of the ZrB$_2$ needles in MA4 and MA12. Due to beam spreading (~1 µm) in the SEM, x-rays from other phases will be acquired during the WDX analysis of the ZrB$_2$ needles. Thus, the WDX data in Table 5.23 can only suggest the existence of a large amount of B and a small amount of Fe (~5 at%) in the ZrB$_2$ needles.

Table 5.23 The composition of ZrB$_2$-type needles in MA4 and MA12 sintered magnets. (The phase has been analysed 5 times in different places. The highlighted row is the composition derived from the chemical formula.)

Sample	B (at%)	Zr (at%)	Fe (at%)
ZrB$_2$	66.66	33.33	
MA4-in NdR	66.26±0.81	28.38±0.93	5.36±0.55
MA4-in Matrix	66.46±0.35	26.45±0.48	*7.09±0.40
MA12-in NdR	68.06±1.15	28.53±2.93	4.41±2.10
MA12-in Matrix	66.46±0.41	26.87±0.53	*6.67±0.49

 * enhanced value due to overlap with matrix
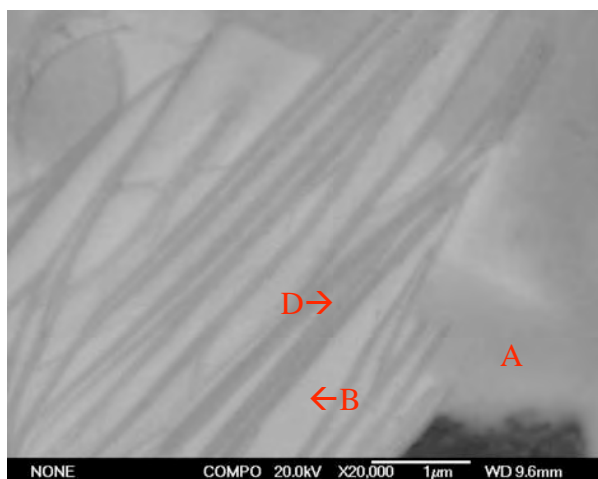
(a) MA4
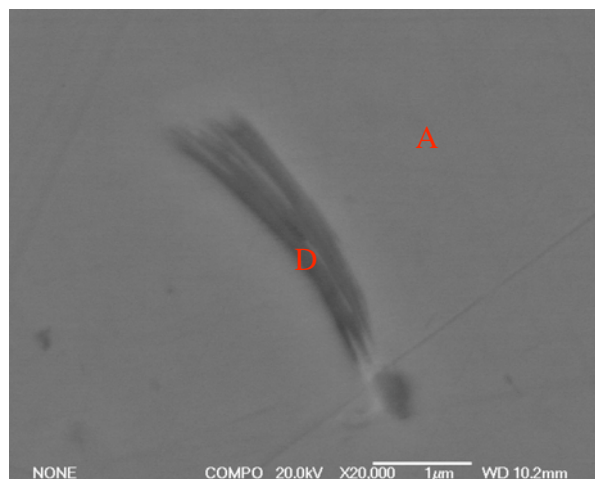
(b) MA4
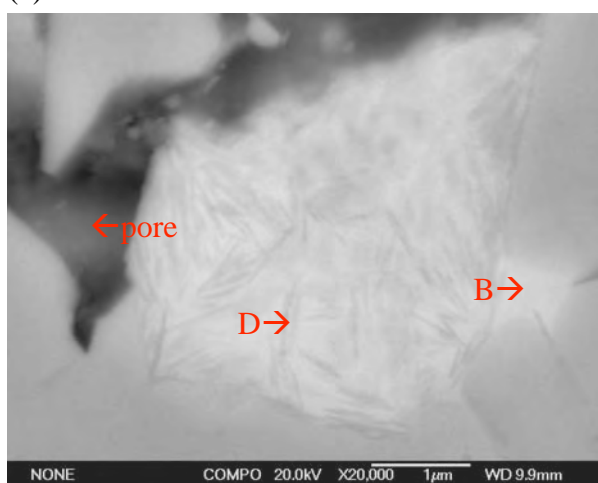
(c) MA12
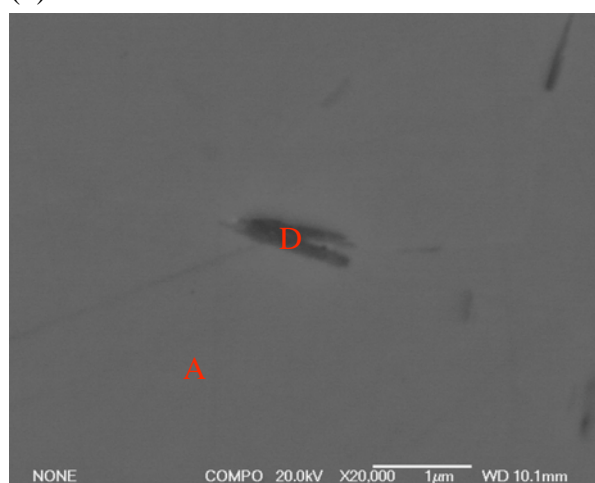
(d) MA12

Note: A: $Nd_2Fe_{14}B$, B: Nd-rich phase, D: ZrB_2 needles

Figure 5.30 BSE images of ZrB_2 in sintered NdFeB-Zr magnets (a) from the Nd-rich phase in MA4, (b) from the matrix phase in MA4.(c) from the Nd-rich phase in MA12 (d) from the matrix in MA12

5.3.4 Magnetic Properties of NdFeB and NdFeB-Zr Sintered Magnets

The magnetic properties of NdFeB and NdFeB-Zr magnets are listed and shown in Table 5.24, Figure 5.31 and Figure 5.32.

Figure 5.31 shows the magnetisation curves for both the NdFeB and NdFeB-Zr sintered magnets. This is not the initial magnetisation curve but the first quadrant after pulse magnetisation. It shows that the magnetisation of MA1 is greater than that of MA12 and MA4, indicating a greater proportion of $Nd_2Fe_{14}B$ phase. MA4 has the lowest magnetisation and therefore the least $Nd_2Fe_{14}B$ phase.

Figure 5.32 shows the coercivity of NdFeB and NdFeB-Zr sintered magnets. The results show that MA12 has the best magnetic properties, both coercivity and remanence, of all the three sintered magnets. The results also suggest that the coercivity of the NdFeB magnet is dependent on the number of ZrB_2 needles in the sintered magnets. Although the location where the ZrB_2-type needles formed and the sharp tips of the needles may lead to reverse domain nucleation, the results from the second quadrant (Figure 5.32) indicate that the presence of the ZrB_2-type needles in the $Nd_{12.68}Fe_{77.91-80.91}B_{6.41-8.41}Zr_{0-1}$ (at%) improves the coercivity of the sintered NdFeB magnet. However, the impact of the ZrB_2-type needles on the grain size and phases in the sintered magnet is likely to have a greater influence on the coercivity.

Table 5.24 Hc, Br, Squareness Factor and BH_{max} of both NdFeB and NdFeB-Zr sintered magnets.

	-Hc	Br	Squareness Factor %	BH_{max} (kJm^{-3})
MA1	27	1122	30	13
MA4	46	1090	65	30
MA12	72	1155	48	87
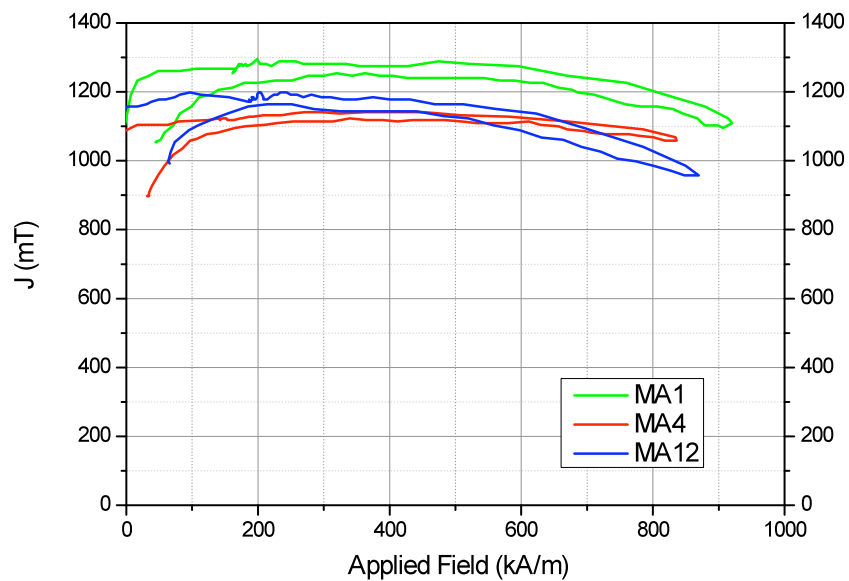
Figure 5.31 Magnetisation curves of NdFeB and NdFeB-Zr sintered magnets.
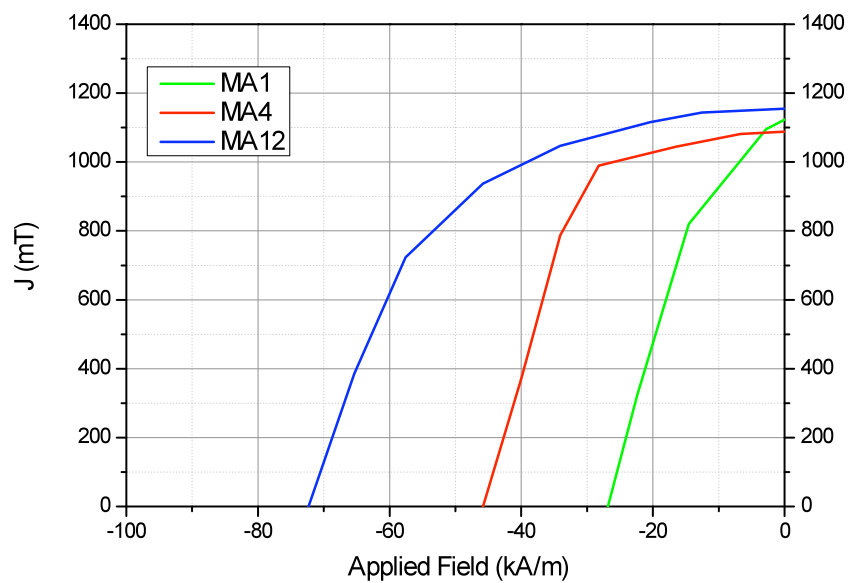
Figure 5.32 Demagnetisation curves of NdFeB and NdFeB-Zr sintered magnets.

5.3.5 Summary of Results from Sintered Magnets

1. There is no α-Fe in any of NdFeB-Zr sintered magnets. **[Figure 5.27, Figure 5.28, Table 5.19]**

2. Compared with the cast alloys, the grains of both the $Nd_2Fe_{14}B$ and Nd-rich phases have grown. However, this is limited by the addition of Zr *or* ZrB_2. **[Table 5.1, Table 5.2, Table 5.19, Table 5.20]**

3. The Nd-rich area in part of sintered magnets was identified as Nd_2O_3 and forms with a round shape as small pockets at the triple points of the $Nd_2Fe_{14}B$ grains. **[Figure 5.28, Figure 5.29, Table 5.22]**

4. A small amount of Fe has been detected in the Nd-rich phase of both MA4 (~2.3 at%) and MA12 (~4.5 at%). **[Table 5.22]**

5. The shape of the ZrB_2 needles is different in MA4 and MA12. In MA4, ZrB_2 forms an Nd-ZrB_2 eutectic-like mixture (~3-4 µm) in the Nd-rich phase but individual needles (~2 µm) in the matrix. In MA12, however, ZrB_2 forms small segments (~0.5 µm) in the Nd-rich phase and distribute randomly in the matrix or between the grain boundaries. **[Figure 5.30]**

6. WDX results on the ZrB_2 needles indicated the presence of a small amount of Fe (~6 at%). **[Table 5.23]**

7. Magnetic measurement results from the first quadrant (magnetisation curves) indicate that magnetisation of MA1 is greater than MA12 and MA4, indicating a greater proportion of $Nd_2Fe_{14}B$ phase. MA4 has the lowest magnetisation and therefore the least $Nd_2Fe_{14}B$ phase. **[Figure 5.31]**

8. Magnetic measurement results from second quadrant (demagnetisation curves) suggest that the presence of the ZrB_2-type needles in the composition of $Nd_{12.68}Fe_{77.91-80.91}B_{6.41-8.41}Zr_{0-1}$ (at%) is believed to improve coercivity in sintered NdFeB magnets. **[Figure 5.32]**

6 Discussion

6.1 NdFeB-Zr Cast Alloys

According to the pseudobinary phase diagram shown in Figure 6.1, the solidification path for a conventionally cast NdFeB alloy with a composition consisting of more than ~76 at% Fe would pass through an Fe-liquid region causing the nucleation of Fe crystals in the liquid (L→L+γ-Fe). For the cast NdFeB-Zr alloys ($Nd_{12.68}Fe_{77.91-80.91}B_{6.41-8.41}Zr_{0-1}$, at%) employed in this study, the nucleation of Fe (~77-80 at%) starts at ~1180°C. The nucleation of the Fe-crystals continues until the peritectic point, where the $Nd_2Fe_{14}B$ starts to form. The peritectic transformation is always incomplete since a solid shell of $Nd_2Fe_{14}B$ separates the reactants. Thus, it has been reported by Liu (Liu et al., 1992) that the γ-Fe crystals, which form during the cooling of the NdFeB liquid, prevent the Fe from reacting any further with the liquid. During the following stage, the γ-Fe (f.c.c.) undergoes a structural transition to α-Fe (b.c.c) at ~930°C. Hence, potential ways to avoid the nucleation of α-Fe dendrites in the NdFeB cast alloys could be by increasing the cooling rate of the NdFeB liquid passing through the "γ-Fe + L" region or via changing the solidification path by appropriate additions to the NdFeB alloy.

It was found, in the as-cast state, that the proportion of α-Fe dendrites was reduced remarkably by the addition of ZrB_2 (A12), as shown in Table 5.2. Comparing the grain sizes of the three alloys in Table 5.3, in the Zr-containing alloys (A4 and A12) the grains are finer for both the Nd-rich areas and the $Nd_2Fe_{14}B$ phases than that in the Zr-free alloy (A1). This result is in agreement with the statement that ZrB_2 is a grain refiner (Jones and Pearson, 1976, Branagan et al., 1996). Since most ZrB_2-type needles in the NdFeB alloys are observed to be in the Nd-rich areas, the grain growth of the $Nd_2Fe_{14}B$ phase may therefore be inhibited by the addition (A12) or the formation (A4) of ZrB_2-type needles in the liquid. The ZrB_2-type needles

are trapped in the Nd-rich areas at the $Nd_2Fe_{14}B$ grain boundaries, pinning them and thus resulting in finer grains in both the Zr-containing NdFeB alloys.

BSE images from the Zr-containing NdFeB alloys (Figure 5.2(b)(c)) show that the microstructure of the NdFeB cast alloy is dominated by two interrelated processes: ZrB_2-type needle formation and the nucleation of $Nd_2Fe_{14}B$ grains. These two processes are controlled by the solidification conditions, which influence the phase transformations and in turn control the nucleation of the phases. The distinct physical properties of ZrB_2, namely, its high heat of formation (-293 kJ/mole) and melting point (3040 °C), suggest that it will form more readily than any other additional phase in the NdFeB alloy and is likely to last until the end of the reaction. Since, in the present study, the composition (as shown in Table 5.1) is shifted slightly towards that of the Neomax composition ($Nd_{15}Fe_{77}B_8$) and away from that of the stoichiometric composition ($Nd_{11.76}Fe_{82.35}B_{5.88}$), (shown by the dashed line in Figure 6.1), this would contribute to changing the solidification behaviour of the Zr-containing NdFeB alloys. It could then be inferred that the "temperature window" for the nucleation of γ-Fe in the liquid during the solidification of the Zr-free NdFeB alloy (A1) is larger than those of the Zr-containing NdFeB alloys (A4 and A12). Moreover, it is believed that the different sequences of forming ZrB_2 needles corresponding to the addition of Zr (A4) or of ZrB_2 (A12) may also result in the changing of the solidification path for the NdFeB cast alloys.

In A12, since the ZrB_2-type needles exists in the liquid, the composition of the liquid ($Nd_{12.68}Fe_{77.91}B_{8.41}Zr_{1.0}$) is shifted closer to that the Neomax composition (as shown in Figure 6.1). During the cooling, the melt will pass through a smaller "γ-Fe + L" region (compared with that of the stoichiometric composition) and therefore this will reduce the possibility of forming γ-Fe dendrites in the early stages of solidification. It has also been reported by Elsner (Elsner and Norman, 1998) that the thermal conductivity of the liquid alloy can be improved somewhat

by the ZrB_2 addition. Thus, it can be assumed that a faster solidification rate of the NdFeB melt, thanks to the effect of the ZrB_2 addition may also lead to the cooling melt following the liquidus line down to the eutectic point instead of passing through the "γ-Fe + L" region. Hence, on cooling, either the nucleation of γ-Fe from the melt has been compressed into a very small "γ-Fe + L" region or $Nd_2Fe_{14}B$ has nucleated directly from the melt by passing through the eutectic point, which avoids the possibility of forming α -Fe dendrites in the A12 alloy. Meanwhile, ZrB_2-type needles also play a role as nuclei for the $Nd_2Fe_{14}B$ during the cooling and therefore were also observed in the centres of the matrix grains. Most of the ZrB_2-type needles will then last in the liquid until the ε phase (Nd-rich phase) solidifies and the other $Nd_2Fe_{14}B$ grains form. This could be the reason why most of the Nd-rich phase at the grain boundaries has disappeared (as compared with A1) to be replaced by the ZrB_2-type needles, with some of them penetrating to the edge of the $Nd_2Fe_{14}B$ grains in A12. Moreover, since the metastable phase, $Nd_{1.1}Fe_4B_4$, is always found in the Nd-rich area in the NdFeB alloy (A1), the absence of $Nd_{1.1}Fe_4B_4$ in A12 may also be due to the improvement of thermal conductivity in the Nd-rich area caused by ZrB_2-type needles during the solidification.

The composition of A4 ($Nd_{12.68}Fe_{80.31}B_{6.41}Zr_{0.6}$) is also shifted toward a smaller "γ-Fe + L" region (as shown in Figure 6.1). The Zr will initially consume the B in the liquid in order to form ZrB_2-type needles in the early stage of cooling from the melt. The reaction, forming ZrB_2-type needles in the A4 liquid, may however result in a considerably lower solidification rate improvement than in A12. Since the thermal conductivity of the melting alloy has not yet been fully improved by the formation of ZrB_2-type needles and the overall composition is far away from that of the Neomax composition, the solidification path of A4 may then pass through a smaller "γ-Fe + L" region and result in the formation of α-Fe dendrites in A4 in the later cooling stages. Meanwhile, since the ZrB_2-type needles form in the liquid, the total B

content in the liquid will not be enough to form the B-rich phase ($Nd_{1+\varepsilon}Fe_4B_4$, $\varepsilon=0.1$) (as shown in Table 5.2 and Table 5.3) and therefore result in no B-rich phase formation in A4 (compare with A1). On the other hand, the formation of the ZrB_2-type needles in A4 also raises the ratio of Fe in the liquid, which will also increase the possibility of forming α-Fe dendrites in the later cooling stage. The ZrB_2-type needles then flow with and grow in the intergranular liquid during the formation and grain growth of the $Nd_2Fe_{14}B$. Since the growth of ZrB_2-type needles occurs at the same time as the grain growth of the $Nd_2Fe_{14}B$ grains and the inevitable direct contacts between $Nd_2Fe_{14}B$ particles during the casting (because the volume fraction of liquid Nd-rich phase is not high enough), the ZrB_2-type needles in A4 form as thin fragments and look much more curved than in A12. The small ZrB_2-type needles existing in the Nd-rich phase of A4 (Figure 5.13 and 5.14) may be evidence for the earlier nucleation of ZrB_2-type needles and the reaction of Zr with B throughout the liquid phase until the solidification reaction is completed. This could also be the reason why the ZrB_2-type needles in A4 look blurred and are always found in the grain boundary region.
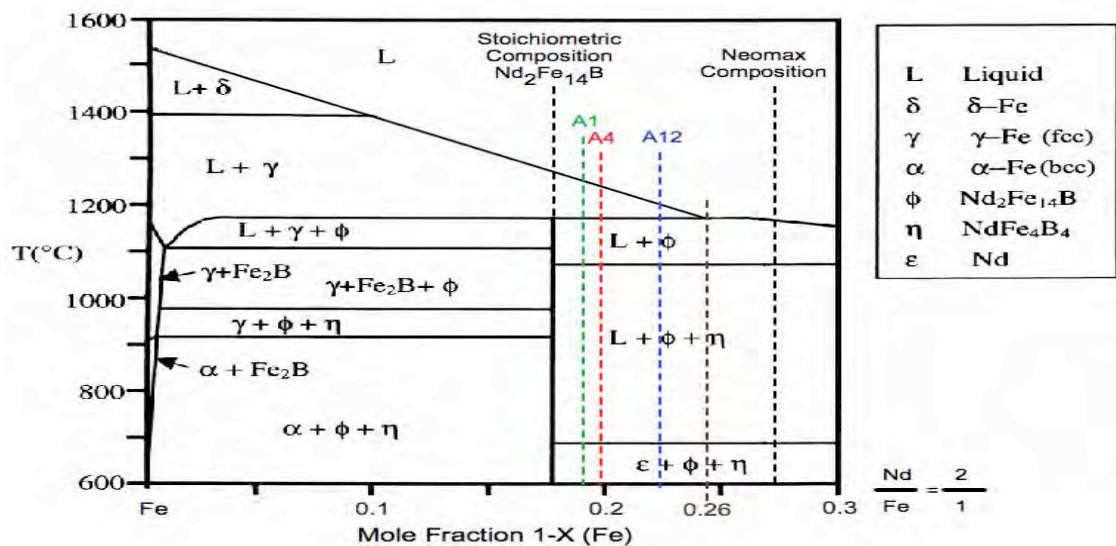
Figure 6.1 The possible solidification paths for A4 and A12 NdFeB-Zr alloys.
      (Earlier presented as Figure 2.15)

As regards the chemical analysis of the Zr-containing NdFeB alloys, there was no trace of other Zr-containing phases either in the matrix or within the α-Fe dendrites or the Nd-rich phase. It was found that, in both Zr-containing NdFeB alloys, the ZrB_2-type needles in the NdFeB alloys are composed mainly of B (~70 at%) and Zr (~20 at%) with a small but significant amount of Fe (~7 at%) (as shown in Tables 5.10 and 5.13).

Since there are no experimental data available for the system $Fe-ZrB_2$ on the ZrB_2 rich side, the explanation of the solubility of the small amount of Fe (~5-7 at%) in ZrB_2-type needles is still unclear (Funke and Iudkovskii, 1962, Kuz'ma et al., 1965, Shurin and Panarin, 1974). However, similar observations are reported for the IVA group of transition metals, $Fe-TiB_2$ (Ottavi et al., 1992), which could explain the presence of Fe in the ZrB_2 needles. They observed the presence of three phases - TiB_2, TiB_2 containing up to 8-9 at % of Fe and Fe_2Ti (28 at% Ti) on the Ti-rich sides, - and stated that this small amount of Fe in TiB_2 resulted from non-equilibrium solidification.

Since the formation enthalpy of the TiB_2 (-294.5 kJ/mole) is very close to that of ZrB_2 (-293 kJ/mole) (Bram et al., 1999), the existence of $(Zr_{1-x}, Fe_x)B_2$ (x=0.3) in the NdFeB alloy can also be evidence for solubility of Fe in ZrB_2 when ZrB_2-type needles form at high temperature with a high Fe content liquid.

The ZrB_2-type needles in NdFeB alloys may act as barrier layers to prevent oxidation of the Nd-rich phase (as shown in Figure 5.11, Figure 5.13 and Table 5.12). A comparison of the chemical analyses of the Nd-rich area and the Nd-rich area between the ZrB_2 needles revealed that the latter is richer in oxygen, implying that ZrB_2-type needles may to some extent suppress the oxidation occurring in the Nd-rich phase. The result is in good agreement with similar results by Kwon (Kwon, 1997) and Gutfleisch (Gutfleisch et al., 2002) that the addition of Zr in

NdFeB alloy made the disproportion reaction sluggish.

The solidification condition of the NdFeB alloys is changed after the formation of the ZrB$_2$-type needles formed thereby suppressing the formation of the α-Fe dendrites in NdFeB cast alloys. Meanwhile, it is confirmed that, in the cast NdFeB alloy, the addition of 1 at% ZrB$_2$ has a bigger effect in removing the α-Fe dendrites than the addition of 0.6 at% Zr.

6.2 NdFeB-Zr Homogenised Alloys

Heat treatment is a conventional way of removing the α-Fe dendrites in the $Nd_2Fe_{14}B$ alloys. However, the effect of heat treatment on the Zr-containing NdFeB alloy has not yet been studied. Investigating the homogenised NdFeB-Zr alloy should provide an insight into the role/efficiency of ZrB_2-type needles in the NdFeB alloy on the annealing. Moreover, the investigation of homogenised Zr-containing alloys would be extended to explain the influence of heat treatment in the final product of a sintered magnet. It has been reported that the homogenising temperature chosen for NdFeB alloys is usually in the range 1050-1100°C (Liu and Zhou, 2007). Therefore, a high temperature treatment (partial vacuum of 10^{-3} atm at 1100°C for 20 hours in this work) would then be expected to enhance the kinetics of the reaction between metastable phases such as α-Fe dendrites, Nd-rich and B-rich-$Nd_{1.1}Fe_4B_4$ to form new $Nd_2Fe_{14}B$ grains.

BSE images of A1H and A4H (Figure 5.24 (a),(b)) show that α-Fe dendrites in both A1 (Zr-free) and A4 (0.6 at% of Zr addition) could be eliminated in this annealing regime, which means that those α-Fe dendrites which remain in A1 and A4 can readily be removed by isothermal homogenisation. X-ray diffraction profiles (Figure 5.23) also confirmed the elimination of the α-Fe dendrites in these NdFeB-Zr homogenised alloys.

The BSE images from homogenised NdFeB alloys also reveal that there is much more direct contact between the $Nd_2Fe_{14}B$ grains deriving from the lack or loss of Nd-rich phases from all the homogenised NdFeB-Zr alloys. Comparing the grain size of $Nd_2Fe_{14}B$ in the homogenised alloys (Table 5.15), with the grain growth resulting from the existence of ZrB_2 in both A4H and A12H is to some extent limited.

The grain growth of $Nd_2Fe_{14}B$ during the homogenisation treatment follows the

solution/precipitation mechanism (Davies et al., 2001). In the initial stage of heat treatment, a great number of fine $Nd_2Fe_{14}B$ grains and irregular protrusive parts of large $Nd_2Fe_{14}B$ grains with irregular shapes dissolve into the Nd-rich liquid phase and then the $Nd_2Fe_{14}B$ phase selectively precipitates onto some larger $Nd_2Fe_{14}B$ grains, which results in grain growth. Thus, an appreciable increase in $Nd_2Fe_{14}B$ grain size is observed in the Zr-Free NdFeB alloy (A1H). After the initial stage of grain growth, the $Nd_2Fe_{14}B$ grains during the heat treatment mainly follows a coalescence mechanism when the aging time is more than 0.5 hours (Liu and Zhou, 2007). As the sintering time extends, the number of fine grains and irregular obtrusive parts of large grains reduced. This led to a slower solution and reprecipitation process due to the smaller solubility difference between the grains. In this case, $Nd_2Fe_{14}B$ grains grow mainly by coalescence and the grain growth rate of $Nd_2Fe_{14}B$ in the NdFeB alloys decreases significantly.

The grain growth of both homogenised Zr-containing NdFeB alloys is limited by the existence of the ZrB_2-type needles (as shown in Table 5.15). The smaller grain size of $Nd_2Fe_{14}B$ as observed in the A4H, might possibly due to the insufficient amount of B source within the liquid for the nucleation. Additionally, since the formation sequence of the ZrB_2 needles is different between A4 (0.6 at% of Zr) and A12 (1.0 at% of ZrB_2), this may then result in a difference in the limitations of grain growth.

In A12H, ZrB_2-type needles are found in the Nd-rich area parallel to the grain boundaries of $Nd_2Fe_{14}B$, with some of the needles penetrating into the $Nd_2Fe_{14}B$ grains. During the period of grain growth in the homogenisation process, ZrB_2-type needles flow with Nd-rich liquid in between the $Nd_2Fe_{14}B$ grains (Figures 5.25(c), 5.26(c)). While the $Nd_2Fe_{14}B$ grains grow, due to the lack of Nd-rich phase in the NdFeB alloy, there will inevitably be contact between the new grains of $Nd_2Fe_{14}B$ (Figure 5.26(b)). The needles would have more potential to suppress grain growth when parallel to the grain boundaries (Figure 5.24(c)) and could act as

an obstruction. With the reduction in the proportion of the Nd-rich phase during the process, some of the needles in the Nd-rich phase will then be squeezed by the grain growth and forms into a curved shape with some of them penetrating the $Nd_2Fe_{14}B$ grains (Figure 5.26(b)).

In A4H, however, it is believed that most contribution to suppressing the grain growth of $Nd_2Fe_{14}B$ is its homogeneous grain size distribution rather than the existence of the feathery ZrB_2-type needles. Comparing the grain size of $Nd_2Fe_{14}B$ in the cast NdFeB-Zr (Table 5.3) shows that the grains of $Nd_2Fe_{14}B$ in A4 (with a grain size variation of ±1.5 µm) are much more homogeneous than that in A12 (with a grain size variation of ±3.5 µm). It has been reported that finer $Nd_2Fe_{14}B$ grains in NdFeB alloys result from a narrow grain size distribution of $Nd_2Fe_{14}B$ before heat treatment (Liu and Zhou, 2007). Hence, the reason for smaller $Nd_2Fe_{14}B$ grains being present in A4H can be attributed to the initial narrow grain size distribution.

Comparing the volume fractions of the phases in homogenised alloys (Table 5.14) with those of the cast alloys (Table 5.2), the proportion of $Nd_2Fe_{14}B$ in A1H, A4H and A12H are found to increase by about 14 %, 16 % and 2.5 %, respectively. It is believed that, in both A1H and A4H, the appreciably increased proportion of $Nd_2Fe_{14}B$ is due to the mass transformation reactions during the homogenisation process and such smaller change in A12H are due to the much smaller proportion of Nd-rich area. The reaction would then result in the elimination of the α-Fe dendrites, $Nd_{1.1}Fe_4B_4$ phase and also in a reduction in proportions of the Nd-rich area in the homogenised NdFeB alloy.

The Nd-rich areas in the homogenised samples do not perfectly isolate each grain due to the lack of Nd in the initial alloy. It is found that the Nd-rich material redistributes along the grain boundaries of $Nd_2Fe_{14}B$ and forms larger pockets at the triple points (Figure 5.24). Meanwhile, it is found that the Fe which used to exist in the Nd-rich phase of A1 (~5 at%) was

completely removed after the heat treatment, whereas, the Fe in the Nd-rich phase of both Zr-containing alloys still remains after annealing, as shown in Table 5.5 and Table 5.17. This could result from the ZrB_2-type needles in the Nd-rich areas, which act as a barrier between the Nd-rich liquid and the $Nd_2Fe_{14}B$ grains. ZrB_2-type needles will then prevent/reduce the Fe in the Nd liquid from diffusing to form new $Nd_2Fe_{14}B$ grains during the heat treatment.

As shown in Figures 5.25 and 5.26, ZrB_2-type needles existed mainly in the Nd-rich areas. In A4H, the needles are feathery and more regularly arranged exclusively in the Nd-rich phase only. However, in A12H, they are much sharper, more curved and more randomly distributed in the Nd-rich areas and occasionally in the matrix. Meanwhile, ZrB_2-type needles in the Nd-rich areas of A12H were observed to penetrate into the matrix with some of them found occasionally completely within the matrix. The different appearance of the ZrB_2-type needles in A4H and A12H may result from the grain growth of $Nd_2Fe_{14}B$ and also a low interfacial energy between the needles and the Nd-rich phase. Therefore, the ZrB_2-type needles were stable and remained in their original state but separated after the heat treatment. Despite the beam spreading in the SEM-WDX, the WDX from the ZrB_2-type needles in the homogenised NdFeB-Zr alloys still suggests the existence of a small amount of Fe (~2-5 at%), but less than in the cast alloys (Table 5.6 and Table 5.18).

Consideration of the results leads to the conclusion that ZrB_2-type needles have limited the grain growth of the $Nd_2Fe_{14}B$ grains during the heat treatment. The existence of the needles degrades the efficiency of the Fe diffusion in the Nd-rich phase during the heat treatment and may then obstruct the grain growth of $Nd_2Fe_{14}B$ during subsequent sintering.

6.3 NdFeB-Zr Sintered Magnets

Sintering is temperature and time dependent. Normally, a small amount of extra B and Nd is added to the green compacts after milling. The reason is to remedy any depletion of Nd, and avoid the formation of the soft magnetic phase Nd_2Fe_{17}. In this study, however, no extra B and Nd were added before sintering so that the influence of the additions of Zr or ZrB_2 to sintered magnets could be investigated.

BSE images in Figure 5.28 (a), (b) and (c) show that α-Fe dendrites were not observed in either the Zr-free or Zr-containing NdFeB magnets. X-ray diffraction profiles (Figure 5.27) also confirmed that the α-Fe dendrites can be removed from the sintered magnet with the composition $Nd_{12.68}Fe_{77.91-80.91}B_{6.41-8.41}Zr_{0-1}$ (at%) under this sintering regime, which is in good agreement with the results reported by Kirby (Kirby, 2007).

Table 5.19 summarises the grain size of the $Nd_2Fe_{14}B$ phase. $Nd_2Fe_{14}B$ grains are observed to be in direct contact without a separating layer of Nd-rich material between them in the sintered NdFeB magnets. Comparing the shape of the $Nd_2Fe_{14}B$ grains with that in the cast alloys (Figure 5.2), the grains in the sintered magnets are much more rounded (Figure 5.28). The rounded shape of the $Nd_2Fe_{14}B$ grains is evidence of the uniform fine powder after milling, which results in uniform grain boundary migration during sintering. As the sintering proceeds, fine $Nd_2Fe_{14}B$ grains dissolve into the liquid Nd-rich material followed by selective precipitation of $Nd_2Fe_{14}B$ onto some larger grains, resulting in the shrinkage and even disappearance of the fine grains and the growth of larger grains until the inevitable contact with another $Nd_2Fe_{14}B$ grain. The volume fraction of the $Nd_2Fe_{14}B$ phase in the sintered magnet (Table 5.20) also indicated that more $Nd_2Fe_{14}B$ formed after the sintering than in the cast alloys.

In the general production route for NdFeB sintered magnets, the grain size of the $Nd_2Fe_{14}B$ in the sintered magnets is dependent on the amount of Nd in the green compact, the sintering temperature and the ageing time. As mentioned earlier, no extra Nd was added to the green compacts before sintering and all the green compacts were subjected to the same sintering profile, making it easy to distinguish the influence of the ZrB_2-type needles on the grain size of the $Nd_2Fe_{14}B$.

As can be seen in Figure 5.28, from the lack of boundary phase (Nd-rich) in the NdFeB-Zr magnets, and also the place where ZrB_2-type needles form (at the $Nd_2Fe_{14}B$ grain boundaries, as shown in Figures 5.29 and 5.30), it can be assumed that the grain growth of the NdFeB-Zr magnets during sintering is limited by the ZrB_2-type needles (as shown in Tables 5.19 and 5.20). The grain refinement by the needles in the NdFeB sintered magnets might be due to blocking of diffusion pathway at the grain boundaries by the ZrB_2-type needles, which restricts the grain growth by solution-reprecipitation of $Nd_2Fe_{14}B$ grains during sintering (German, 1985).

The Nd-rich material in all the sintered magnets oxidises partially to Nd_2O_3 (as shown in Table 5.22) during the sintering treatment. The rounded Nd-rich areas (>1 μm) locate at the triple points of the $Nd_2Fe_{14}B$ grains (Figure 5.28, Figure 5.29) instead of wetting the grain boundaries. Moreover, it is found that most of the oxidised Nd-rich phase in the Zr-containing sintered magnet is dominated by ZrB_2-type needles (as shown in Figure 5.30) along with a small amount of Fe (MA4: ~2.3 at%; MA12: ~4.5 at%). This small amount of Fe in the Nd-rich phase of the Zr-containing NdFeB sintered magnets might result from the ZrB_2-type needles, which act as a barrier and to some extent reduce atomic diffusion during sintering. The results are in good agreement with the reports by Xiao (Xiao et al., 1988) and Fidler (Fidler, 1992) that the formation of second phases at the grain boundary obstructs atomic diffusion between the

Nd-rich area and the $Nd_2Fe_{14}B$ grains.

ZrB_2-type needles in the sintered magnet are found both in the $Nd_2Fe_{14}B$ and the Nd-rich phases but are different in shape. It is apparent that, in MA4, ZrB_2 forms a Nd-ZrB_2 eutectic-like mixture (~3-4 µm in length) in the Nd-rich area but individual needles (~2 µm in length) in the matrix. It is believed that the individual ZrB_2-type needles in the matrix are formed initially at the casting stage, are broken during the milling and act as nuclei for the $Nd_2Fe_{14}B$ during the sintering. Those ZrB_2-type needles forming a Nd-ZrB_2 eutectic mixture in the Nd-rich area are newly formed during the sintering.

In MA12, however, ZrB_2-type needles form segmented and separate structures (~0.5-1 µm in length) in the Nd-rich area while small segments distribute randomly in the matrix or at the grain boundaries. It is thought that most of the ZrB_2-type needles in MA12 formed initially at the casting stage and were broken into several smaller segments during the milling and therefore the ZrB_2-type needles in MA12 are smaller than those in MA4. Some of these smaller ZrB_2-type needles in MA12 will act as nuclei for the $Nd_2Fe_{14}B$ during the sintering and thus appear randomly in the solid $Nd_2Fe_{14}B$ phase. Those left in the liquid will then stay in the liquid until the ε phase (Nd-rich phases) solidifies; some of them will settle in between the $Nd_2Fe_{14}B$ grains during solidification.

It is observed that better magnetic properties (both in remanence and coercivity) appeared in MA12 (1 at% of ZrB_2) rather than in MA4 (0.6 at% of Zr) and MA1 (Zr-free) (Figure 5.31 and 5.32).

The magnetisation curves from the first quadrant show that the magnetisation of MA1 is greater than that of MA12 or MA4, indicating a greater proportion of $Nd_2Fe_{14}B$ phase in MA1 when comparing with MA12 and MA4. This result is in agreement with the result from the area

fractions of phases in Table 5.19.

There is a slight difference in the remanence but a large difference in coercivity due to the grain refinement resulting from Zr or ZrB_2 additions. The coercivity of both NdFeB and NdFeB-Zr sintered magnets is relatively poor when compared with commercial magnets [15-20% area fraction of Nd-rich phase, Liu et al, 2007] due to the lack of grain boundary-Nd-rich phase (3-4 % area fraction, as shown in Table 5.20).

Considering that the Nd-rich phase in both the sintered NdFeB and NdFeB-Zr magnets was not much different in terms of both area fraction and average size (Tables 5.19 and 5.20), the difference in coercivity of the NdFeB and NdFeB-Zr sintered magnets may result mainly from the size of the $Nd_2Fe_{14}B$ grains. Since both Zr-containing sintered magnets have smaller and more uniform grain sizes (~6.5 μm), this would therefore lead to a better coercivity when compare with MA1 (~11 μm).

The coercivity of the NdFeB-Zr sintered magnets can be improved to some extent by the ZrB_2-type needles in the Nd-rich phase when comparing the Zr-free with the Zr-containing NdFeB sintered magnets, which is in a good agreement with Kim et al. who reported that the coercivity of NdFeB magnets can be improved by small amount of Zr (~1 at%) (Kim and Camp, 1997).

The coercivity difference between the two Zr-containing sintered magnets (MA4 and MA12) may be due to the detrimental effect of the ZrB_2–type needles, which are larger and sharper in MA4. Differences may also be due to lower B content affecting the proportions of the phases.

Although some ZrB_2-type needles in the MA12 act as nuclei for $Nd_2Fe_{14}B$ grains during

the processing and remain in the centres of the grains and may therefore act as nucleation sites for reverse magnetic domains, the fact is that the small segments of ZrB_2-type needles (~0.5 µm) with the Nd-rich phase of MA12 compensate for the lack of grain boundary phase and hence obstruct better the domain wall movement. However, ZrB_2-type needles in MA4 appear in the eutectic-like phase (~3-4 µm) with Nd-rich phases with some of them wedging into the matrix phase. Nucleation of the reverse magnetic domains resulting from the ZrB_2-type needles in MA4 may therefore result in a higher demagnetisation factor. Hence, the N_{eff} of the MA4 would be larger than for MA12, resulting a detrimental effect on the coercivity when compared with MA12.

References for Chapter 6

Bram M., Aubertin F., Venskutonis A. & Breme J. 1999. Kinetics of the phase transformation and wear resistance of in-situ processed titanium matrix composites based on Ti-Fe-B. *Materials Science and Engineering A,* 264**,** 74-80.

Branagan D. J., Kramer M. J. & McCallum R. W. 1996. Transition metal carbide formation in the Nd2Fe14B system and potential as alloying additions. *Journal of Alloys and Compounds,* 244**,** 27-39.

Davies B. E., Mottram R. S. & Harris I. R. 2001. Recent developments in the sintering of NdFeB. *Materials Chemistry and Physics,* 67**,** 272-281.

Elsner N. B. & Norman J. H. 1998. *Metal infiltrated ceramic electrical conductor*.

Fidler J. 1992. Two types of dopant with different microstructural effects leading to an improvement of rare earth-iron based magnets. *7th Int. Symp. on Magnetic Anisotropy and Coercivity in RE-TM Alloys*.

Funke V. F. & Iudkovskii S. I. 1962. Structure and Properties of the alloys of Zirconium Diboride with Iron, Cobalt and Nickel. *Russian Metallurgy and Fuel,* 4.

German R. M. 1985. *Liquid Phase Sintering*, New York: Plenum Press.

Gutfleisch O., Drazic G., Mishima C. & Honkura Y. 2002. Texture inducement during HDDR processing of NdFeB. *IEEE Transactions on Magnetics,* 38**,** 2958-2960.

Jones G. & Pearson J. 1976. Factors affecting the grain-refinement of aluminum using titanium and boron additives. *Metallurgical and Materials Transactions B,* 7**,** 223-234.

Kim A. S. & Camp F. E. 1997. Microstructure of Zr containing NdFeB. *IEEE Transactions on Magnetics,* 33**,** 3823-3825.

Kirby K. A. 2007. *The role of casting conditions and heat treatment on the permanent magnetic properties of selected Sm$_2$(Co, Fe, Cu, Zr)$_{17}$ and NdFeB-Type magnets.* PhD., University of Birmingham.

Kuz'ma Y. B., Lakh V. I., Voroshilov Y. V., Stadnyk B. I. & Markov V. Y. 1965. Constitution Diagram of the Zr-Fe-B System. *Russian Metallurgy, Translated from Izvestiya Akademii Nauk Sssr, Metally,* 6.

Kwon H. W. 1997. Study of the effect of Zr-substitution on the HDDR characteristics of Nd-Fe-B-type alloys. *IEEE Transactions on Magnetics,* 33**,** 3826-3828.

Liu W. L., Liang Y. L., Ma B. M. & Bounds C. O. 1992. Effects of Nb addition and/or casting method on the amount of precipitated Fe in NdFeB alloys. *IEEE Transactions on Magnetics,* 28**,** 2154-2156.

Liu X. & Zhou S. 2007. Grain Growth Behavior in Sintered Nd-Fe-B Magnets. *Journal of Rare Earths,* 25**,** 329-335.

Ottavi L., Saint-Jours C., Valignant N. & Allibert C. H. 1992. Phase equilibria and solidification of Fe-Ti-B alloys in the region close to Fe-TiB$_2$. *Zeitschrift fuer Metallkunde,* 83.

Shurin A. K. & Panarin V. E. 1974. Phase Equilibria and Structure of Alloys Fe-TiB$_2$, Fe-ZrB$_2$, Fe-HfB$_2$. *Russian Metallurgy, Translated from Izvestiya Akademii Nauk Sssr, Metally,* 5.

Xiao Y., Liu S., Mildrum H. F., Strnat K. J. & Ray A. E. 1988. The effects of various alloying elements on modifying the elevated temperature magnetic properties of sintered NdFeB magnets. *Journal of Applied Physics,* 63**,** 3516-3518.

7 Conclusions and Future Work

7.1 Conclusions

The following conclusions can be drawn:

7.1.1 NdFeB-Zr Cast Alloys

1. Three major phases exist in the conventionally cast NdFeB alloy: $Nd_2Fe_{14}B$, Nd-rich and α-Fe. When 0.6 at% of Zr or 1.0 at% of ZrB_2 are melted together with the alloys, an additional phase - ZrB_2 needles - is formed mainly at the grain boundaries.

2. α-Fe dendrites observed in the Zr-free ingot are formed by a peritectic reaction during cooling. In the cast NdFeB alloy, the addition of 1 at% ZrB_2 has a much larger effect in removing the α-Fe dendrites than the addition of 0.6 at% Zr. This could be due to the shift of overall composition in the melt and hence the change of solidification behaviour in the Zr-containing NdFeB alloys. In a conventionally cast ingot, the different sequences of forming ZrB_2 needles via the addition of Zr to A4 and of ZrB_2 to A12 may also result in different solidification paths.

3. ZrB_2 needles occupy mainly the Nd-rich phase in both A4 and A12. However, ZrB_2 needles also play a role as nuclei for the $Nd_2Fe_{14}B$ during cooling and therefore are also observed in the centres of the matrix grains in A12.

4. The shape of the ZrB_2 needles is slightly different in A4 and A12. In A4, needles form as a loose cluster. In A12, however, they form as a tightly-knit sheaf within the Nd-rich area but as a tight bundle in the matrix phase. The ZrB_2 needles are both sharper and more curved in the latter case.

5. With regard to chemical analysis of the Zr-containing NdFeB alloys, there was no trace of other Zr-containing phases either in the matrix or within the α-Fe dendrites or the Nd-rich phase. It was found that in both Zr-containing NdFeB alloys, the Zr-containing needles are composed mainly of B (~70 at%) and Zr (~20 at%) with a small but significant amount of Fe (~7 at%). The formula can thus be expressed as $(Zr_{1-x}, Fe_x)B_2$ (x~0.3). This small amount of Fe in the ZrB_2 probably originates when ZrB_2 needles form at high temperature within a high Fe content liquid.

7.1.2   NdFeB-Zr Homogenised Alloys

1. In the present study, those α-Fe dendrites remaining in A1 and A4 can be removed by isothermal homogenisation in a vacuum of 10^{-3} atm at 1100°C for 20 hours.

2. In the Zr-free NdFeB alloy, the elimination of α-Fe dendrites occurs in stages: Fe diffuses to the grain boundaries, reacts with Nd- and boron-rich phases and forms new $Nd_2Fe_{14}B$ grains. The reaction becomes more difficult with increasing time, as the grains grow larger and the amount of Nd-and B-rich materials diminishes.

3. During heat treatment, the mechanism for limiting the grain growth in both Zr-containing NdFeB alloys is different. In A12H (1.0 at% of ZrB_2), the grain growth was suppressed by the presence of the ZrB_2 needles at the grain boundaries of the $Nd_2Fe_{14}B$ phase during coalescence, which makes the ZrB_2-type needles form into curved shapes, with some of them penetrating the $Nd_2Fe_{14}B$ grains. However, the grain growth in A4H may be dominated by the narrow grain size distribution of $Nd_2Fe_{14}B$ in A4.

4. Neither heat treatment nor the addition of Zr or ZrB_2 changes the chemical composition of the matrix phase.

5. The existence of the ZrB_2 needles degrades the efficiency of the Fe diffusion in the Nd-rich phase during the heat treatment and may then obstruct the $Nd_2Fe_{14}B$ grain growth during sintering.

6. WDX analyses from the ZrB_2-type needles in homogenised NdFeB-Zr alloys suggest the existence of a small amount of α-Fe (~2-5 at%), but less than that in the cast alloys.

7.1.3   NdFeB-Zr Sintered Magnets

1. α-Fe dendrites are not observed in all the Zr-free or Zr-containing NdFeB magnets.

2. The grain refinement by the ZrB_2 needles in the NdFeB sintered magnets might be due to blocking of diffusion pathways at the grain boundaries by the ZrB_2 needles, which restricts the grain growth via solution-reprecipitation of $Nd_2Fe_{14}B$ grains during sintering.

3. The existence of the ZrB_2-type needles decreases the solubility of Fe in the Nd-rich phase of the sintered magnets.

4. Comparing the Zr-free with the Zr-containing NdFeB sintered magnets, the coercivity of the NdFeB sintered magnets can be improved to some extent by adding Zr or ZrB_2 with the composition $Nd_{12.68}Fe_{77.91-80.91}B_{6.41-8.41}Zr_{0-1}$ (at%). Both Zr-containing sintered magnets have smaller and more uniform grain size (~6.5 μm) and would therefore lead MA12 and MA4 to have a better coercivity when compared with MA1 (Zr-free) (~11 μm).

7.2 Future Work

1. DTA studies on Zr and ZrB_2 doped NdFeB alloys should be carried out in order to elucidate the crystallisation sequence of $Nd_{12.68}Fe_{77.91-80.91}B_{6.41-8.41}Zr_{0-1}$ (at%).

2. In order to understand the solubility of the small amount of Fe in ZrB_2 needles, it is suggested to investigate the ZrB_2-rich side of the Fe-ZrB_2 system.

3. The SEM observations strongly suggest that the magnetic properties of the Zr-containing sintered NdFeB magnet are influenced by the location of the ZrB_2 needles. In order to understand the mechanism of the coercivity enhancement by the ZrB_2 needles in the NdFeB magnet, it is suggested that an investigation of the orientation relationship between the ZrB_2-type needles and other phases in NdFeB alloy be performed using TEM.

4. In order to change the morphology and distribution of the $(Zr_{1-x},Fe_x)B_2$ phase, melt spinning of the alloys should be investigated.